The Use of the Monte Carlo Technique in the Simulation of Small-Scale Dosimeters and Microdosimeters

by

Adam Richard Ernest Baker

A thesis submitted to the University of Birmingham for the degree of
DOCTOR OF PHILOSOPHY

Supervisors
Dr Richard P. Hugtenburg
Dr Stuart Green

Department of Medical Physics
School of Physics and Astronomy
University of Birmingham
August 2011

The Use of the Monte Carlo Technique in the Simulation of Small-Scale Dosimeters and Microdosimeters

Abstract

In order to understand the effects of low keV radiation upon small scales, a number of detector designs have been developed to investigate the ways energy is deposited. This research was conducted in order to investigate a number of different detector designs, looking in particular at their properties as small scale dosimeters exposed to photon radiation with an energy of 5-50 keV. In addition to this, Monte Carlo models were constructed of the different detector designs in order to ascertain the trends in energy absorption within the detectors.

An important part of the research was investigating the dose enhancement effects produced when the low Z elements present in human tissues are in proximity to higher Z metallic elements within this energy range. This included looking at dose enhancement due to the photoelectric effect, with a photon energy of 5-50 keV and through the absorption of thermal neutrons. The reason for studying the dose enhancement was twofold - looking at the increase in energy absorption for elements that are currently being investigated for medical applications as well as elements that are present in dosemeters alongside the tissue equivalent elements.

By comparing the results produced using the Monte Carlo codes MCNP4C and EGSnrc, simulations were produced for a variety of different detector designs, both solid state and gas-filled. These models were then compared with experimental results and were found to be able to predict trends in the behaviour of some of the detector designs.

Executive Summary

This is a summary of the most important conclusions reached during the course of this research on a chapter by chapter basis.

Chapter II

In this chapter dose measurements were taken for a diamond detector exposed to low keV near-monoenergetic photon energy from a synchrotron. This data was then compared with results produced using different detector models in the Monte Carlo program MCNP4C, from a simple cylinder-based geometry to a complex computer model replicating the positions and materials of the electrical contacts.

The comparison of the two data sets allowed the following conclusions to be reached:

- The MCNP models produce results that agree with the trends shown in the experimental work, for the energy range 7-28 keV.
- The design of an MCNP model can have a large effect upon the results of the simulation, with more complex models and more accurate material definitions yield a greater agreement with experimental results. Additionally dose enhancement due to the metal components of the detector can lead to an increase in the dose to the detecting element.

Chapter III

In this chapter an optic fibre-based detector system was investigated using low keV photon radiation at a synchrotron to test their use as a Thermoluminescent Dosimeter. This data was then compared with a simple MCNP model to assess whether it was possible for a TLD detector to be simulated using a standard Monte Carlo code. Two different optic fibre dopants were used, with one sample containing Erbium doping and the other Germanium.

Over the course of this research the following conclusions were reached:

- A more vigorous screening process would be needed to eliminate optic fibres that do

not contain the dopant element, producing no signal (‘dead’ fibres).

- The optic fibres irradiated produced a larger signal than those left unirradiated and showed some evidence of variation in energy absorption with changes in source energy. This suggests that the method used for the experimental work combined with screening of ‘dead’ fibres could lead to optic fibre TLDs being a useful dosemeter.
- There was a limited agreement between the MCNP models of the optic fibres and the experimental work above 20 keV, suggesting that the code may be able to predict the behaviour of the optic fibres for 20-50 keV photons.

Chapter IV

For this chapter a proportional counter dosimeter was investigated in both a near-monoenergetic photon field produced by a Synchrotron radiation source and a neutron field from a Dynamitron. The photon results were modelled using the Monte Carlo codes MCNP4C and EGSnrc allowing the two codes to be compared with each other and the experimental data. The aim of the neutron-based work was to look at the dose enhancement effects of adding boron and gadolinium to the wall material, and look at the difference in the energy absorption characteristics caused by their addition.

The research conducted lead to the following conclusions:

- The EGSnrc code can produce a good approximation of the energy absorption spectrum produced within this type of detector for photon energy at energies of 15, 28 and 33 keV.
- The MCNP and EGS codes produce comparable results, although the results from EGS seemed to underestimate the total energy absorption compared with the MCNP code.
- Boron doping in the walls of a proportional counter leads to a substantial increase in energy absorption above 100 keV that is absent in the gadolinium-doped and TEP detectors. Gadolinium lead to an increase in energy absorption below 10 keV compared with the other detectors. This demonstrates that both elements lead to an increase in energy absorption through different mechanisms.

Chapter V

In this chapter a number of different variations in the proportional counter were tested using a mixture of experimental and Monte Carlo methods to determine the effect this would have on the detector. These variations were the size of the radiation field, the pressure of the gas in the gas cavity within the detector and the influence of dopant elements within the filling gas. All of the different detector designs were exposed to photon radiation of various energies.

The conclusions reached in this section were as follows:

- If the radiation field a detector is subjected to is smaller than the detecting element, it will lead to a change in the absorption spectrum for a proportional counter due to changes in the scatter within the radiation.
- Decreasing the gas pressure of a proportional counter allows it effectively act as a detector with a smaller cavity size, but also introduces additional difficulties in producing repeatable results due to noise.
- It was found that there is a significant dose enhancement effect when higher Z elements are added to the walls of a proportional counter when irradiated by 5-50 keV photon radiation. However, adding the high Z elements to the filling gas of the detector does not produce a measureable dose enhancement effect.

Acknowledgements

This work has been undertaken with the assistance of Dr Richard Hugtenburg and Dr Stuart Green at the University of Birmingham. They provided a great deal of assistance throughout this work, making suggestions as to the paths to follow and the methods needed to produce all of the data in this document. Without their help and theoretical knowledge none of this would have been possible.

The synchrotron-based work made use of the SRS Facility at Daresbury and the Dynamitron and radiation-based work was conducted at the University of Birmingham using the BAGINS area of the Medical Physics building. The Diamond Detector and Ionisation Chamber were provided by the Queen Elizabeth Hospital and the Proportional Counter was supplied by the University of Birmingham. The peripheral equipment, computer systems and radiation sources were supplied by the University of Birmingham.

This document was proof-read by Dr Hugtenburg, Dr Green, Charlotte Gordon-Smith and Robert Kidney. Thank you all, without your encouragement and enthusiasm this document would never have been completed.

Table of Contents

List of Figures

Chapter I - Introduction

Chapter II - Diamond Detector Dosimetry

Chapter IV - Proportional Counter Dosimetry

Chapter V - Variations in Proportional Counter Design

Appendices

Appendix I - Raw Data

Appendix VI – Gafchromic Film Dosimetry

List of Tables

List of Abbreviations

ADC	Analogue to Digital Conversion
BBB	Blood Brain Barrier
BNCT	Boron Neutron Capture Therapy
CNS	Central Nervous System
DNA	DeoxyriboNucleic Acid
EBT	External Beam radioTherapy
HV	High Voltage
LET	Linear Energy Transfer
MCNP	Monte Carlo N-Particle
NCT	Neutron Capture Therapy
RF	Radio Frequency
RNA	RiboNucleic Acid
ROI	Region Of Interest
SRS	Synchrotron Radiation Source
TEG	Tissue Equivalent Gas
TEP	Tissue Equivalent Plastic
TEPC	Tissue Equivalent Proportional Counter
TLD	Thermo-Luminescent Device

Chapter I - Introduction

1.1 – Synopsis

When a new radiotherapy-based technique is being proposed, it is essential that an accurate estimation of the ionising radiation dose to a patient can be made and any potential risks assessed. Without an adequate knowledge of the hazards and benefits of treatment there is the potential that the radiotherapy will lead to further complications for the patient, without providing a significant improvement in symptoms. Newer radiotherapy techniques have been looking at the use of increasingly small radiation fields with a range of different ionising particles. These smaller radiation fields have the potential to reduce the radiation dose to the tissues surrounding tumour sites. It is therefore essential that we quantify the dose delivered by ionising radiation on micrometer scales so that its effects upon cell nuclei are better understood. This can ensure treatments are as accurate as possible as well as leading to better radiation protection.

The primary aim of this investigation is to look at the effectiveness of the Monte Carlo technique in the simulation of different detector designs and the factors that can affect them. The detector designs studied here have been chosen for their use in the simulation of ionising events within small volumes, with the latter part of the research moving into the field of microdosimetry. This includes an assessment of the effectiveness of two different codes, MCNP4C and EGS4 (which make use of a Class I and a Class II electron algorithm respectively, discussed in Section 1.7) in the simulation of a wide variety of different types of detector. These include a diamond detector, a proportional counter and an optic fibre based TLD detector.

A second line of enquiry throughout this work looks at the dose enhancement that occurs at the low energies of 5 to 200 keV due to interaction via the photoelectric effect. This is achieved by investigating the energy absorption within a material using Monte Carlo simulations and also through experimental work. From this an assessment can be made of both the reliability of the two codes being used and of the degree to which this effect increases the dose to a region. This is useful for both the fields of detector design, for which this

research can allow more accurate detector models to be constructed, and radiotherapy, as high Z materials can then be added to tumour tissue to increase the dose to a chosen volume while reducing the dose to the surrounding tissue.

This chapter will discuss the background theory relevant to this investigation starting with how cancer occurs and the methods used to treat it. The next section deals with the Dynamitron and Synchrotron particle accelerators with which the experimental results used throughout this thesis were produced. Afterwards, the use of detectors is discussed, focussing on how dose is measured before looking in more detail at the use of microdosimetry in quantifying the dose received by a target at small scales. Finally, the Monte Carlo codes used to produce the simulations in Chapters II to V are discussed and their calculation methods summarised.

Chapter II looks at the use of diamond detectors as a radiation detector, focussing on the use of the MCNP4C Monte Carlo code to produce an accurate model of a diamond detector. This research looks at two different diamond detector models in MCNP - one a three-component cylindrical geometry, the other based upon a complex approximation of the actual detector geometry. The results taken from these models are then compared. From this, the reliability of MCNP as a simulation of detectors in monoenergetic x-ray fields is assessed and found to be a good indication of the energy absorption within the detector. Additionally the presence of gold and silver wires within the detector are investigated and shown to cause an increase in the radiation dose at energies close to the K edge of silver and the L_{III} edge of gold.

In Chapter III small-scale TLD's are considered as dosemeters, in this case based upon optic fibres. The optic fibres are exposed to monoenergetic synchrotron radiation and the energy absorption assessed over a range of photon energies. This information is then compared to an MCNP4C model of the TLD set-up to assess the accuracy of the code in simulating this situation. This research investigates the reliability of the Monte Carlo code when investigating complex situations and shows how MCNP can be used to produce a measure of the energy absorption within a TLD detector. In the end though, it was difficult to produce reliable energy absorption values for detectors that were so physically small, so the research moved on to a better characterised detector design, although some future directions for research were

considered.

In Chapter IV first the energy absorption spectra of a proportional counter is assessed using both EGSnrc and MCNP4C and the reliability of both codes are compared. This showed that EGSnrc is capable of producing accurate energy absorption spectrum models of a proportional counter, allowing variations in the detector design to be made for the following chapter. Additionally the dose enhancement found within a TEP proportional counter and similar proportional counters with low dopant levels of gadolinium and boron in the detector walls were considered within both photon and neutron fields. The research showed that there is a definite increase in energy absorption for proportional counters containing low levels of gadolinium below 10 keV, when placed in a neutron field. A similar effect leads to an increase in energy absorption at around 500 keV for a boron-doped proportional counter.

Chapter V then looked at how three different variations of the proportional counter affect the energy absorption within the detector using EGSnrc and MCNP4C. These variations were changes in the aperture size of the radiation source, a reduction in the gas pressure of the proportional counter and changes in the atomic number of the filling gas and the wall material. Looking at how the aperture size affects the energy absorption spectrum of a proportional counter, it becomes clear that when a synchrotron source is used the radiation field must be at least as large as the detector element, otherwise it will lead to a different spectrum. Reducing the gas pressure of the proportional counter allowed the detector to simulate the energy absorption of an even smaller detector cavity, changing the spectrum of the radiation absorption. This was investigated through both experimental work involving all three proportional counters and by the production of energy absorption spectra in EGS. This showed that a lower gas pressure can be effectively used to represent a smaller volume, but that it creates experimental difficulties that are difficult to overcome. The final part of this chapter looked at the effects of varying the atomic number of the filling gas and the wall. This was to investigate the degree to which the filling gas and wall affect the energy absorption within a proportional counter. This research showed that the wall material has a significantly larger effect on energy absorption than the filling gas.

Finally, in Chapter VI, the conclusions of the previous four chapters are summarised, along

with the overall conclusions reached during the research.

1.2 - Causes and Treatment of Cancer

1.2.1 - Cancerous Tissue

The main aim of research into microdosimetry, especially in the fields of tissue-equivalent detector dosimetry and dose enhancement dosimetry is to further our understanding of the effects of radiation within structures as small as a human cell. This is necessary to improve our understanding of ionising radiation energy deposition, allowing prediction of the risks such interactions possess and therefore the diagnosis and treatment of tumours. This is especially important as the effects of low keV energy radiation are only poorly understood, so any risks from exposure to, for instance, high intensity low energy radiation can only be extrapolated back from the damage caused by higher energies, modified with estimates of the capacity of human tissue to repair the damage caused. By investigating the energy that is absorbed within structures closer to the scale of individual cells, estimates can be made of the impact that energy will have upon a cell, and hence the damage that may be caused.

As well as helping to quantify the risks inherent in the use of radiation fields with energies in the region of 5 to 50 keV, microdosimetry is useful in looking at the use of radiation for the treatment of tumours. It looks for ways to increase the amount of energy deposited within a small volume, while decreasing the energy within the cells surrounding it. Coupled with the use of dose-enhancing contrast media, added to increase the energy absorption within the volume, it is possible to improve the possibility of causing irreparable damage within a tumour without killing off surrounding tissue.

It is necessary to first understand why cancer cells form in the first place, both to assess the risks of the radiation and to determine the doses necessary to kill them.

1.2.1.1 - Origins of Cancer

Cancer (also known as Neoplastic Disease), is a condition caused by damage to the nucleotides which make up the DNA used by our body for regulation and maintenance of our

bodily systems. In its most dangerous, malignant form, it possesses three key characteristics which define the disease and will occur in all cases. These are the loss of control of cell reproduction leading to abnormal growth compared with normal tissue (cell proliferation), the ability to break through boundary layers between tissues (invasiveness) and the capability to spread around the body, often in the blood or lymph systems (metastasis).

In mammals, there are approximately 30,000 to 40,000 active genes (Kong et al, 2002), of which about 100 are involved in cell division, cell regulation or cell differentiation. Damage to these can lead to cancer. Additionally, there are genes for different hormones and cell messengers that can affect the way the other genes work. A large number of these genes are involved in repairing any damage caused to the cell, but if these malfunction it can lead to a build up of errors on the DNA strand.

Most of the time, the tumour produced is unable to expand beyond a limited size, leading to a ‘benign’ tumour. These are characterised by an inability to expand beyond the boundary layers of the region of the body it has developed in, generally growing much slower and acting in a manner similar to the surrounding tissue. These generally do not lead to mortality, provided the maximum size of the tumour does not interfere with survival (either by being too large for the area of the body it grows in or by impeding with vital functions, blocking arteries and veins or limiting movement of an organ). However, sometimes they will manage to overcome their limitation, or cells may break off and spread elsewhere.

In some cases, the tumour grows rapidly and uncontrollably, often in a very different manner to the surrounding tissue, becoming what is known as a ‘malignant’ tumour. If either the cell that becomes cancerous is close enough to an artery, produces growth factors that grow new blood vessels or is contained within the blood (for instance cancerous white blood cells, or Leukaemia), it continues to grow and spread, usually resulting in the death of the patient.

There are five main mechanisms which can lead to damage to the DNA. No single event is likely to cause any form of cancer, but when successive problems occur, a cell can be damaged to the point it will become cancerous.

Radiation - When radiation is absorbed within an atom it can lead to the ionisation of the atom due to electron emissions, causing the atom to break its bonds with the other atoms surrounding it. Ionising radiation can also lead to the formation of free radicals, highly reactive atoms with unpaired electrons, such as O• and OH•. Through interaction with the DNA nucleotides free radicals can lead to changes in the structure or sequence of the DNA molecule, leading to mutation.

Chemical - A large proportion of the chemicals we encounter on a day-to-day basis (such as certain dyes used in clothing) have some carcinogenic properties, however, the vast majority do little damage, so the repair systems built into our cells can eliminate problems as they occur. The majority of chemical carcinogens are mutagens, which cause mutation to occur by promoting copy errors in the synthesis of DNA or changing the structure of the DNA strand.

Viruses - Viruses cause DNA damage due to their means of reproduction, which often involves subverting the cell's means of DNA replication. They can cause damage by either inserting itself into the DNA or by altering the productions of proteins within the cell, which can lead to damage to the DNA structure.

Inheritance - Altered genes can be inherited from parents, reducing the body's resistance to certain kinds of cancer, an example being BRCA1 and BRCA2, which both increase the risk of breast cancer. Possessing altered genes does not automatically guarantee cancer, but it does lead to an increased chance of other factors triggering cancer.

Replication Accidents - The body is extremely good at copying DNA for cell replication, but it does make copying errors, usually around 1 mistake for every 10^9 nucleotides (King, 1996; Franks, 1997). Although the body can repair the majority or problems, each diploid cell within the body contains approximately 6 x 10^9 nucleotides, and as many as 0.1% of the body's cells are replaced over every 24 hours of the average person's life (or about 10^{10} cells per day).

Due to the mechanisms within the cell nucleus, in the vast majority of cases the cell either repairs itself, is unable to continue functioning and dies or the irregularity produced by the

damage is detected by specialist proteins and genes and it is marked for programmed cell death. However, as human life expectancy has increased, so too has the chance that during that time enough damage will be caused to the DNA of enough cells for cancer to develop. Ironically, better healthcare and public hygiene has lead to cancer (once considered a rare disease that only affected the wealthy) becoming one of the biggest killers, responsible for approximately 163,500 deaths (or 272.7 deaths per 100,000 population) within the UK in 2004 (WHO Health Report, 2004). Note, that 226,200 people died in the same year from cardiovascular diseases (the largest killer in the UK), and 20,800 people died from both intended (violence, war and self-inflicted) and unintended (traffic accidents, falls, drowning, etc.) injuries.

1.2.1.2 - Gliomas

Gliomas (cancer of the glial cells) account for approximately a half of all primary types of brain cancer found in humans, with a recorded incidence of approximately 5 – 10 cases occurring per 100,000 members of the population (figure taken from Behin et al, 2003). Recent research has indicated that this figure may be increasing, possibly due to better scanning technology and classification of tumours (Legler et al, 1999). This increase in incidence has been largely negated, however, due to advances in treatment increasing the chance of survival, especially in patients under 45.

Depending on the location of the glioma within the brain tissue, complete removal of the glioma through surgical means is often impossible, radiotherapy may carry too much of a risk of damage to the surrounding brain tissue and chemotherapy may be dangerous due to the necessity of countering the blood-brain barrier's attempts to block large molecules reaching the brain. Due to this, there has been a lot of interest in dose enhancement techniques, such as BNCT, which make use of drugs containing elements with high cross-sections for the radiation being used, as these can substantially increase the dose to specific areas.

Gliomas are of interest to this research because they are a cancer that has traditionally proven very difficult to treat due to their proximity to healthy brain tissue. It is hoped that the use of high Z dose enhancement could lead to an increase in the number of successful treatments of

this type of cancer as well as reduce the potential complications caused by damage to neighbouring healthy tissue.

1.2.1.3 - Treatment of Cancer

Due to the array of different types of cancer, as well as the fact that a tumour can occur anywhere in the body, by necessity several different types of treatment have been developed to deal with the problems posed by the different tumour types. For the majority of solid tumours close to the outside of the body the most effective means of removal is to simply cut away the cancerous tissue using surgery. For tumours spread throughout the body often the only treatment possible is to use drugs which kill the cancerous cells or stop them reproducing effectively using chemotherapy. Finally, in the case of localised tumours too deep or diffuse for surgery, or ones which would lead to serious damage were they to be removed, radiotherapy can be used to kill off the cancerous cells while minimising the damage to surrounding tissue.

Each of these has their own advantages and disadvantages, summed up below, and a lot of research into cancer treatment at the present is looking into ways of improving the effectiveness of each, often through combinations of treatments, know as ‘combination therapy’. At its simplest level, combination therapy can consist of using radiotherapy and/or surgery to kill off the largest proportion of tumourous growth combined with chemotherapy to reduce or kill off those tumour cells still remaining.

Radiotherapy

Radiotherapy is the use of radiation to kill off cancerous cells within the body. Due to these cells being created due to errors in the replication of the DNA or damage to organelles, most types of cancerous cell will have a lessened ability to repair the cell compared to healthy cells. This is because the cell is at its most vulnerable to radiation during the process of replication, only part of the daily cycle of a healthy cell, totalling about 10 hours. However in cancerous cells replication is often almost constant, making it easier to damage the DNA, while allowing healthy cells to recover. Additionally, the damage that leads to a cell becoming cancerous

often results in errors in the repair mechanisms within a cell, slowing down the recovery time after irradiation. Because of this, radiotherapy is often ‘fractionated’, with the patient being exposed to a pre-calculated dose of radiation, then a set time later being exposed again, giving the healthy cells time to repair the majority of the damage caused by the radiation. Over several fractions, the healthy cells will survive, but the cancerous cells will be irrepairably damaged by the radiation.

There are two main types of radiotherapy - ‘External Beam Radiotherapy’ (EBT) in which a radiation source is targeted externally and a patient is exposed to a beam of charged particles, x-rays, gamma rays or neutrons, and that in which a source (usually gamma or beta emitting) is placed inside the body, close to the tumour, known as ‘Brachytherapy’.

The advantage of Brachytherapy over External Beam Radiotherapy is that the radiation source does not have to penetrate healthy tissue layers in order to affect the tumour, reducing the risk of either killing the tissue or causing damage that may lead to cancer. Getting the radiation sources to the areas of the body where they are needed can be difficult, however, potentially involving invasive surgical procedures. This can potentially lead to radiation exposure in other areas of the body.

The main limitation of external beam radiotherapy is that the beam has to penetrate layers of tissue to reach its target. Because of this, over the last few decades there have been many improvements to external radiotherapy, such as multi-leaf collimators, image guidance and intensity modulation allowing radiotherapists to target only the tumour and a small volume surrounding it (to kill off any cancerous cells that are branching out), reducing the dose to the surrounding tissue, and hence the risk of complications.

Chemotherapy

Chemotherapy makes use of cytotoxic chemicals to poison any cancerous cells with minimal damage to healthy non-cancerous tissue that may also be present in the same region of the body. Chemotherapy is often used in addition to radiotherapy as it increases the chance of killing all of the cancerous cells and reduces the ability of those cells to self-repair after the

damage has occurred.

Chemotherapy treatments are limited, as cancerous cells can often have very similar properties to the healthy cells surrounding them, leading to some unpleasant side effects. There can also be additional difficulties with getting drugs into the brain due to the blood-brain barrier (BBB), which filters out bacteria and large or hydrophilic molecules. This makes it difficult to get a sufficient dose to the brain without causing an overdose to the rest of the body. Weakening the BBB has the disadvantage of allowing other chemicals to penetrate the blood-brain barrier, potentially leading to dangerous complications.

Other Treatments

The simplest technique for removing cancerous tissue in a patient is simply to cut it out, often leading to quick cure times for a patient and allowing the tissue to be tested to determine the type and probability of metastasis. However, due to the need to remove the surrounding tissue to minimise risks of tumour regrowth, this can lead to deformity and scarring in a patient. The greatest limitation of surgery is the depth of cancerous tissue which makes it difficult to remove tissue from deep inside organs like the brain or liver. Additionally, if the cancerous tissue has spread throughout the body, it could be too harmful or unfeasible to remove all of the tissue.

Several therapeutic vaccines are currently in development designed to stimulate an immune response against cancer-specific characteristics, such as specific proteins produced within the tumours. These are still in the testing stages so are not in common use, however, a number of preventative vaccines, including vaccines for human papillomavirus and hepatitis B are available which can reduce the likelihood of cancer developing later on in life.

As all of the methods for treating cancer have situations in which they are very effective, most modern methods of treating cancer will rely on a combination therapy technique. It is already common for surgery to be used to excise any tumours that are easily removed followed by radiotherapy to kill any deeper tumours. This can be combined with chemotherapy to either reduce tumour growth or to attempt to kill off any metastatic tumours. A large proportion of

the research into cancer treatment at the moment is looking at ways of improving the targeting using combinations of drugs, radiotherapy and surgery to maximise the tumour death while minimising damage to healthy tissue.

Gold and platinum have been used as components in a number of chemotherapy drugs, such as Cisplatin due to their cytotoxic effects, and there has been a great deal of interest in combining the chemotherapy treatment with a course of EBT (see Biston et al, 2004). The treatment would take advantage of the dose enhancement effects caused by the high photoelectric cross-section of both gold and platinum. This would lead to an increase in the radiation dose to the tumour tissue compared with the surrounding tissue, reducing the total dose required. Similar research into the use of iodine-based drugs has demonstrated some improvement in dose distributions (see Mesa et al, 1999).

Other techniques have been tested, including encapsulated chemotherapy drugs that are then targeted by concentrated ultrasound or x-ray beams and drugs that reduce the cell repair mechanisms in cancerous cells (reducing the amount of dose they can safely repair).

1.2.2 - Other Applications of this Project

Radiation research has several areas of use outside of the medical field, and the data within this thesis has several uses, for example in fields such as Archaeology and detector design.

Uses of Radiation Techniques in Archaeology

Research into TLDs, such as that in Chapter III, offers some useful techniques that can be of use in Archaeology, especially in the dating of archaeological sites. It is established for instance that a Thermoluminescence analysis of the quartz grains found in pottery can be used as a dating tool to provide an approximate figure for the year of creation of an object. This is because the firing of the clay when the pottery is created will anneal quartz grains, allowing us to determine the radiation dose the quartz has received since its creation. If we can then determine the background radiation levels of the area the pottery was discovered in, we can estimate the date in which the object was created. As pottery shards are very common finds in

most areas lived in by humans, an estimate of date can then be applied to any other remains found in the same strata.

Uses of Radiation Techniques in Detector Design

An important conclusion reached during the course of the work contained within this thesis concerns the importance of dose enhancement in situations where higher Z materials are in proximity to tissue equivalent materials (see Section 1.5.4). This could be an important factor to consider in radiation detector design, where the electrical contacts are constructed from metals with Z numbers higher than the surrounding materials, as this could increase the radiation absorption within tissue-equivalent detectors, producing an artificially high reading. This factor is already known and accounted for, but as Chapter II shows, the model used to calculate any corrections made can have a large effect upon the accuracy of simulations produced.

Use of Radiation Techniques in Industry

Although not a direct area of investigation during the research within this thesis, wide spectrum photon radiation with energies in the region of 100 keV, such as that produced at synchrotrons, is used by a number of large companies to test for faults in technical prototypes. Companies such as Roll-Royce will test prototypes to investigate the formation of microfractures within the materials they are formed from in order to test the reliability and safety of the damage (for a brief description of some techniques used in this field see Zhang et al).

Other Applications

An important part of this thesis is improving our understanding of the effects of low keV energy radiation (especially x-rays) at scales of a few microns, this is explained in more detail in Section 1.6. A better understanding of these effects could have many knock-on effects upon most areas where low-energy scanning techniques are used, such as in the study of radiation damage to DNA.

1.3 - Dynamitron Beams

The Dynamitron is the trade name of a parallel-driven high voltage particle accelerator manufactured by IBA Industrial, formerly Radiation Dynamics Inc. (RDI) of the United States. It contains two Radiofrequency (RF) electrodes surrounding an accelerator column and an RF generator within a pressure tank, which produces a very high voltage resonance circuit with a resonant frequency of about 100 - 125 kHz.

The information in this section is based upon the descriptions of the Dynamitron published in *Biomedical Particles Accelerators* (Scharf, 1994), *Particles Accelerators and Their Uses* (Scharf, 1986) and *Principles of Cyclic Particle Accelerators* (Livingood, 1961).

1.3.1 - Dynamitron Design

The Dynamitron consists of an accelerating column positioned vertically and sealed within a vertical pressure tank filled with a spark-protecting gas, usually SF_6, to minimise the chance of a discharge occurring and damaging the capacitors, column components or rectifiers in the accelerator. SF_6 is a gas commonly used in the electronics and electricity supply industries due to its insulating properties. The upper end of the chamber contains two large D-shaped High Voltage (HV) electrodes, with a built-in electron source. This provides a source of electrons to be accelerated and the inner segments of the electron path end with a series of equipotent rings, in order to equalise the chamber. A diagram showing the layout of a Dynamitron can be found in Figure 1.01.

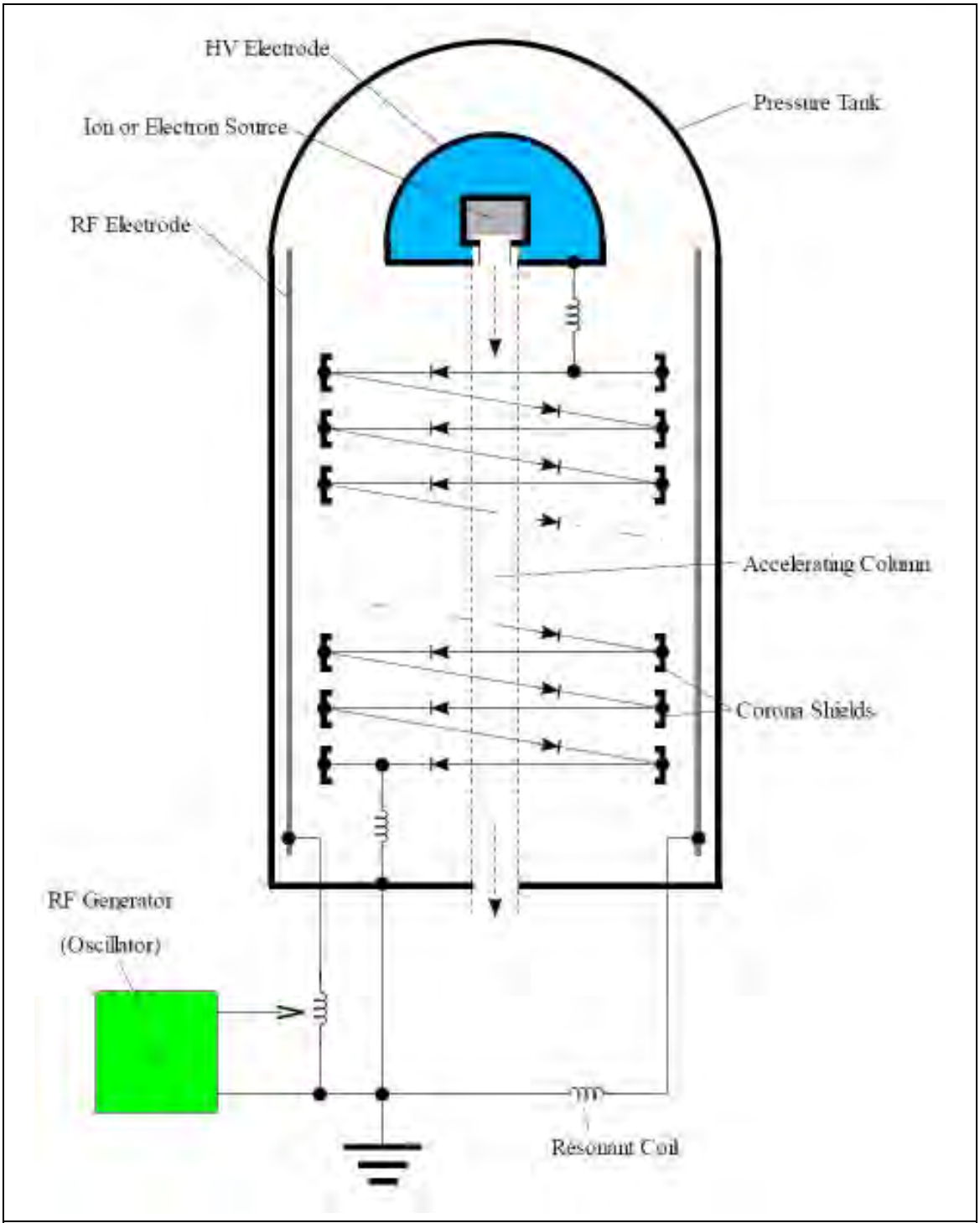

Figure 1.01 - A Typical Dynamitron

Two vertical radio frequency electrodes are mounted close to the inner surfaces of the pressure tank which provide the motive power for the acceleration of the electrons with a ring-shaped air-cored coil outside the tank. The oscillator on a Dynamitron has a very high power output, usually in the range of the tens of kilowatts, so is built as a separate water-

cooled unit to prevent it overheating.

1.3.2 - Operation of a Dynamitron

To begin operation, first the oscillator is switched on, producing a strong RF field between the two electrodes along the path of the accelerator column. The equipotential rings within the accelerating column then act as antennae, inducing voltages within the rings with the same frequency as the RF field. The equipotential rings are connected to each other in series by rectifiers, creating a chain capacitively coupled with an external resonant circuit. The partial voltages induced in each stage add together, creating an output yield of 400 kV to 4 MV, depending on the type of accelerator, with each individual segment supplying a direct voltage of about 50 kV. The rectifier chain is grounded through an RF choke on one side and an HV electrode on the other.

A Dynamitron can supply a maximum beam current of 100 mA for a 500 kV system, with a beam power ranging from 25 to 60 kW. As RF is being used to provide the acceleration, the output voltage has only a small ripple, despite the lack of smoothing capacitors.

A Dynamitron can be used for the acceleration of both electrons and positive ions. Although it is used most commonly in industry for the irradiation of items that need to be kept sterile, as it has one of the highest beam powers available for a standard accelerator, it is being used increasingly in medical applications.

1.4 - Synchrotron Beams

History and Development of the Synchrotron

A synchrotron is a cyclic-design particle accelerator in which a synchronised magnetic field and electric field are used to accelerate charged particles to a high energy. Whereas a cyclotron uses a constant magnetic field and a single-frequency electric field to accelerate ions, a synchrotron increases these values as the particles gain energy, allowing a near constant path to be maintained. This ensures that the vacuum tube the particles are accelerated through is made as thin as possible, reducing the space taken up by the system, as well as allowing more variability in the shape of the vacuum torus (many contain some straight and some curved sections).

The first synchrotrons built were the 'Cosmotron' built at Brookhaven National Laboratory, in the USA in 1953 and shortly after at The University of Birmingham in the UK, in the same year. Figure 1.02 is an aerial photograph of the SRS Facility at Daresbury, the location of the Synchrotron-based research in this document.

Figure 1.02 – Aerial Photograph of the SRS Facility at Daresbury

Figure 1.03 shows the layout of a simplified synchrotron design, showing the relative positions of the storage ring and the accelerator cavity.

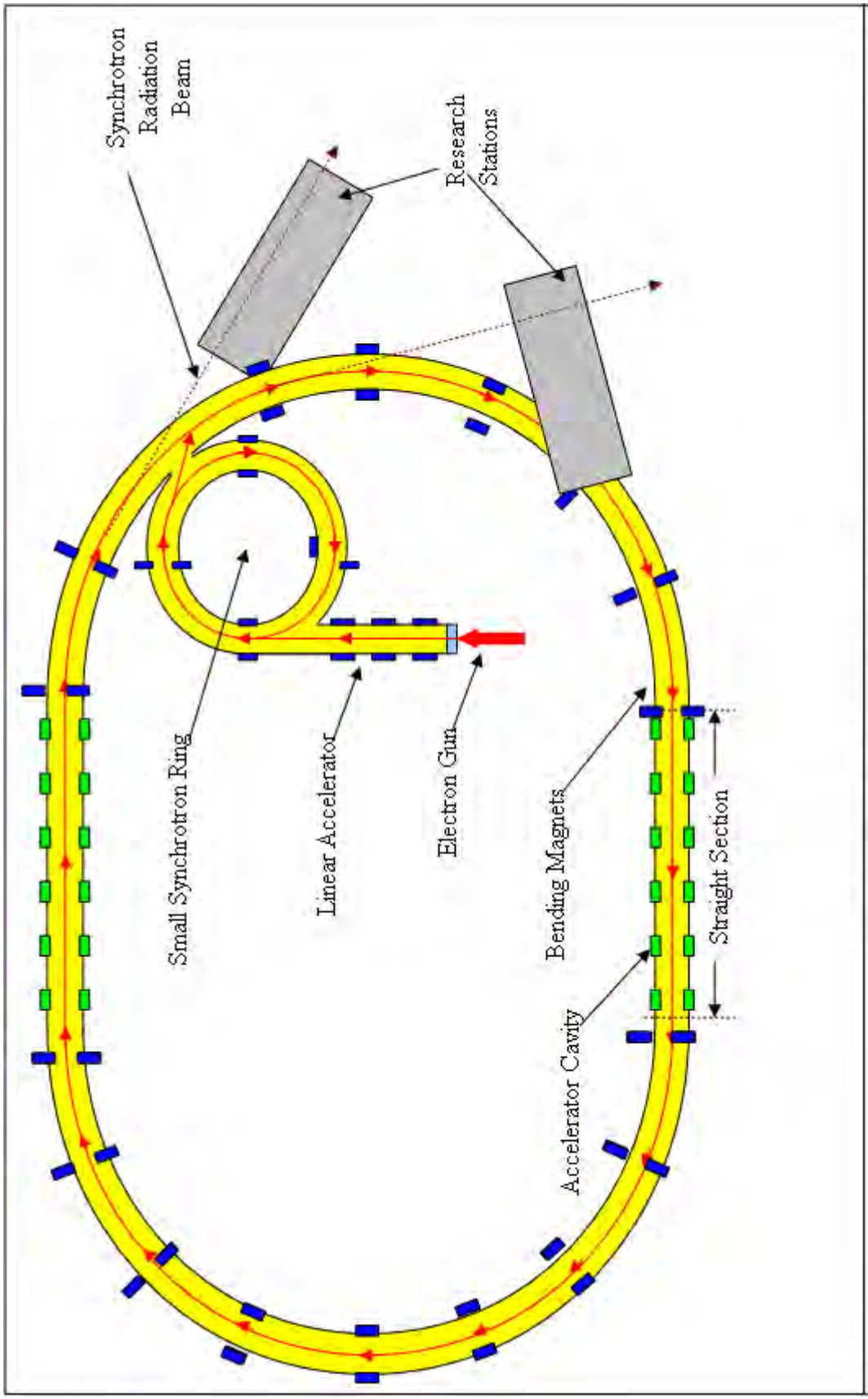

Figure 1.03 - A Typical Synchrotron

There are a few limitations as to the maximum energy that can be imparted by a synchrotron, which is caused by physical constraints for the energy input (chiefly governed by the strength of the magnetic field and the minimum curvature of the ionic path). Another factor that limits the maximum energy possible is that the particles must be charged to be accelerated using an electric field. This causes some problems, as charged particles emit photons when accelerated, causing a continuous energy loss (synchrotron radiation). This means that the maximum energy possible for any synchrotron occurs when the energy lost through lateral acceleration equals that imparted to the particle by the electric field per cycle. This value can be increased by using a large radius path (minimising the lateral acceleration), using microwave cavities to accelerate the particle beam between the corners and by using heavier ions, as lighter ions lose a larger fraction of their energy when changing direction.

The information in this section on the design and operation of synchrotrons is based upon *Electrostatic Accelerators - Fundamentals and Applications* (Hellborg et al, 2005) and *The Physics of Synchrotron Radiation* (Hoffman, 2004). Additional information on the physics and use of synchrotron radiation was found in the book *Applications of Synchrotron Radiation* (Catlow and Greaves, 1990). The information on Monochromators and Wigglers was based upon *The Science and Technology of Undulators and* Wigglers (Clarke, 2004) and *Wiggler and Undulator Magnets* (Winick, 1981).

1.4.1 - Operation of a Synchrotron

The momentum (and therefore the energy) of an accelerated ion travelling in a circular path is dependant upon the magnitude of the magnetic field deflecting it into a circular path and the radius of the path being travelled. This follows the relationship:

$$Mv = qBr$$

In which M is the mass of the ion, *v* is its velocity (dependant upon the acceleration voltage), q is its charge, B is the magnetic field of the accelerator and r is the radius of curvature.

For the majority of cyclic particle accelerators, including cyclotrons and synchrocyclotrons,

the ion being accelerated follows a spiralling path, with a constant magnetic field directing the particle from the centre of the accelerator through to the outer edge of the accelerator's chamber. This means that the maximum energy attainable is dependant upon the magnetic field of the accelerator (which governs the tightness of the spiral) and the diameter of the chamber (which sets the maximum diameter the spiral can obtain). In practical terms, these are both complex engineering issues, as building larger and larger magnets as well as greater and greater diameter evacuated tubes are complex challenges, creating a limit to the maximum energies obtainable for an accelerated particle.

The synchrotron overcomes these difficulties by varying the magnetic field containing the ions and the acceleration voltage in synch to provide an ion path with a fixed radius. This reduces a lot of the engineering issues, because the large diameter evacuated chambers can be replaced by a simpler evacuated tube. As the magnetic field can be varied along the length of the tube, it does not have to have a constant radius of curvature and it can even be built straight in places. This also reduces the engineering challenges in building the large electromagnets needed for most cyclic particle accelerators, as smaller electromagnets can be placed at intervals long the tube, so there is no need for a constant magnetic field along the entire volume of the synchrotron. As an ion is accelerated along the evacuated tube of the synchrotron, the frequency of the alternating current is raised to increase the velocity (and hence energy) of the particle at the same rate as the magnetic field is increased to confine the particle to a constant path through the tube.

As it is impossible in practical terms to accurately control a magnetic field from zero upwards, it is necessary for the ions to be inserted into the synchrotron at an energy determined by the radius of the evacuated tube and the minimum magnetic field that can be obtained reliably by the accelerator. To achieve this, a separate particle injector is used to achieve this initial energy, usually a linear accelerator.

Using classical electromagnetic theory, a charged particle travelling in a circular orbit will have to undergo acceleration if it is to travel at a constant or accelerating velocity, therefore it can be expected to emit electromagnetic energy at the expense of its kinetic energy. This emitted electromagnetic energy will be lost within a narrow cone projecting along the tangent

of the particle path in a forward direction, with a rate of emission proportional to the fourth power of the particle's energy, leading to recoil in the particle directed against the direction of motion. This energy loss is also inversely proportional to the radius of curvature (hence synchrotrons are built to as large a scale as possible) and is inversely proportional to the fourth power to the rest mass of the particle being accelerated. This means that although the energy loss is minor for proton-based synchrotrons, an electron-based system will emit a significant amount of electromagnetic energy. This loss with increasing energy must be made up before a particle can gain further kinetic energy.

Modern Synchrotrons

The synchrotrons used during this research, have been designed to maximize the intensity and spectrum of synchrotron radiation emitted, and therefore is built with a large radius (usually in the region of 30 metres) to maximise the energy achievable for the electrons (maximising the spectrum of emitted electromagnetic radiation). In order to limit the areas emitting synchrotron radiation to a few areas where research can be conducted (typically between 10 and 30 research stations), most modern synchrotrons are built with mostly straight sections (in which the particle is accelerated with minimal loss of kinetic energy), and several curved sections where the emitted radiation can be directed to sites where it can be used.

The synchrotron itself will operate as a 'storage ring' with the electrons accelerated around it at a fixed energy level. The lost energy is replaced using radio frequency radiation from a klystron, the synchrotron effectively acting as a device for converting radio frequency radiation into broad spectrum synchrotron radiation. The electron beam will be inserted to the ring as a series of 'bunches', which match the klystron frequency, accelerating around the ring at a constant rate. With each circuit some of the electrons will be lost owing to electron-electron interactions as well as collisions with the gas molecules that are present even in a hard vacuum (typically 10^{-9} Torr), so the electron current will decay exponentially and the synchrotron will need to be refilled every 12-24 hours.

The energy spread of a synchrotron beam is related to the RF voltage accelerating the electrons within the synchrotron and the size of the aperture through which the radiation is

emitted, although for a third generation synchrotron, such as the SRS facility at Daresbury, the energy spread, $\Delta E / E$ is approximately 0.1%, making the beam effectively monoenergetic.

A typical synchrotron ring will also contain insertion devices such as Wigglers or undulators to allow the peak frequency of the synchrotron radiation to be varied. A wiggler is a magnetic device that alters the radius of curvature for the beam within a specific area, allowing the energy loss of the electrons due to the change in acceleration to be increased or decreased, in turn allowing the peak wavelength of the synchrotron radiation to be varied.

1.4.2 - Monochromators

Monochromators are systems used to remove all but a narrow section of the electromagnetic spectrum produced by the synchrotron and are often combined with focussing mirrors to focus the radiation beams between the storage ring and the experimental area. Crystal monochromators are often composed of silicon or germanium, and using the high intensity and broad spectrum of a synchrotron beam allow the production of a monochromatic beam with a high enough intensity for experimental work.

The tuneable wavelength of an x-ray-reflecting crystal is given by Bragg's Law

$$n\lambda = 2d \sin\theta$$

In which d is the crystal spacing, n is the order of the reflection and θ is the angle between the x-ray beam and the reflecting crystal planes. As synchrotron radiation is white, the wavelength of the radiation, and therefore the energy of the beam, is tuneable by varying the angle of the monochromator, θ.

For a dislocation-free material, the intensity and band-pass of the monochromatic x-rays is governed primarily by the Darwin Width of the crystal. The Darwin Width is a measure of the intrinsic width of the Bragg reflection, which therefore also determines the minimum angular acceptance of the monochromator. This is given by the relationship

$$\omega_0 = 2.12 r_0 \lambda^2 CN \frac{(F(\lambda)e(-M))}{(\pi \sin^2 \theta)}$$

In this r_0 is the classical electron radius, N is the atomic density, F(λ) is the scattering factor, C is the polarisation factor and e^{-M} is the temperature factor. For a perfect crystal this can be simplified to

$$\omega_0 = \left(\frac{(d\lambda)}{\lambda}\right) \tan\theta$$

In which dλ / λ is the band constant.

To allow for the maximum intensity of the monochromatic beam, ω_0 should be made as large as possible, but this will also result in a decrease in the spectral resolution of the beam produced, as the increase in intensity is produced by increasing the energy range of the resultant beam.

1.4.3 - Synchrotron Radiation

Synchrotron radiation is produced by the acceleration of ultra-relativistic particles (that is particles travelling at close to the speed of light) through a magnetic field. For the experimental work contained in this thesis, the beams were generated at the SRS Facility at Daresbury in the UK. Apart from particle accelerators, synchrotron radiation is also produced by the acceleration of charged particles through magnetic fields found in space. A description of the SRS Facility can be found in the paper by Holland (1987).

Using a classical model, a charged particle travelling in a circular orbit through a magnetic field will emit electromagnetic radiation isotropically at the Larmor frequency of the particle, however, the electromagnetic radiation produced in a synchrotron is affected by the ultra-relativistic velocities of the particles. As the electrons producing the electromagnetic radiation are travelling close to the speed of light, to a stationary observer, the radiation appears as a beam strongly collimated in the forward direction. The photon opening angle is given as

$$\sigma_{(ph)} \propto \frac{1}{(\beta\gamma)}$$

for

$$\beta = \frac{v}{c}$$

$$\gamma = \frac{E}{(m_0 c^2)}$$

In these v is the particle velocity, E is the particle energy and m_0 is the rest mass of the particle. For a GeV electron travelling at close to the speed of light, this will give the electromagnetic radiation a photon opening angle of 0.5 milliradians or less.

Due to the ultra-relativistic velocities of the electrons within the synchrotron, the observed frequency of the synchrotron beam is effected by the Doppler effect, altering their frequency by the Lorentz Factor, γ ($\gamma = [1 - (\text{velocity of electrons}^2 / c)^2]^{-½}$). Lorentz contraction then alters the frequency by another factor of γ, thereby multiplying the frequency of the resonant cavity accelerating the electrons into the x-ray range. A third effect of the relativistic velocities is that the isotropic dipole pattern of the radiation is projected into a cone-shaped forward-pointing radiation beam. This makes the synchrotron beam one of the brightest x-ray sources known (a 3rd generation source can have a brilliance larger than 10^{18} photons / s / mm^2 / $mrad^2$ / 0.1%BW, where BW denotes a bandwidth 10^{-3} λ, centred around the frequency, λ[15]).

Synchrotron radiation can typically include different wavelengths, including x-rays, ultraviolet, optical and infra-red radiation, but is characterised by several features, many of which are useful within a medical physics environment:

- Beam has an extremely small angular divergence, is highly collimated.
- Beam is extremely intense, by many orders of magnitude compared to x-rays from a conventional x-ray tube.
- Beam is highly polarised.

- Beam can be tuned to a wide variety of different monochromatic wavelengths.
- Light emission is pulsed (pulsed at or below 1 ns) due to the bunching of electrons passing around the synchrotron ring.

In order to produce higher intensity radiation, a 'wiggler' or undulator forces the electrons within a straight section of the beam to follow a periodic magnetic structure, typically a sinusoidal or helical path. These mean that instead of producing a single bend, many tens or hundreds of 'wiggles' are produced in pre-calculated positions, adding to the total intensity seen at the end of the straight section.

1.4.4 - Synchrotron Beam Correction Factors

Note that the readings from the different detectors were not taken at the same time, so there will have been some variation in synchrotron beam intensity over the course of the time in which the readings were taken. As the only measure available of the variation in beam intensity was the current of the synchrotron ring, the results were corrected by multiplying the values obtained by the detector by a beam intensity correction factor. The beam intensity correction factor was calculated by dividing the highest synchrotron beam current (the first reading taken on a particular day, as the synchrotron beam current decreased over time) and dividing it by the beam current at the start of the reading being taken. This allowed the results to be directly compared despite the variation in synchrotron beam current. The beam intensity correction factor is included in the data used throughout this thesis.

In Figure 1.04 a picture in included of the equipment used for the experimental equipment used for the synchrotron research.

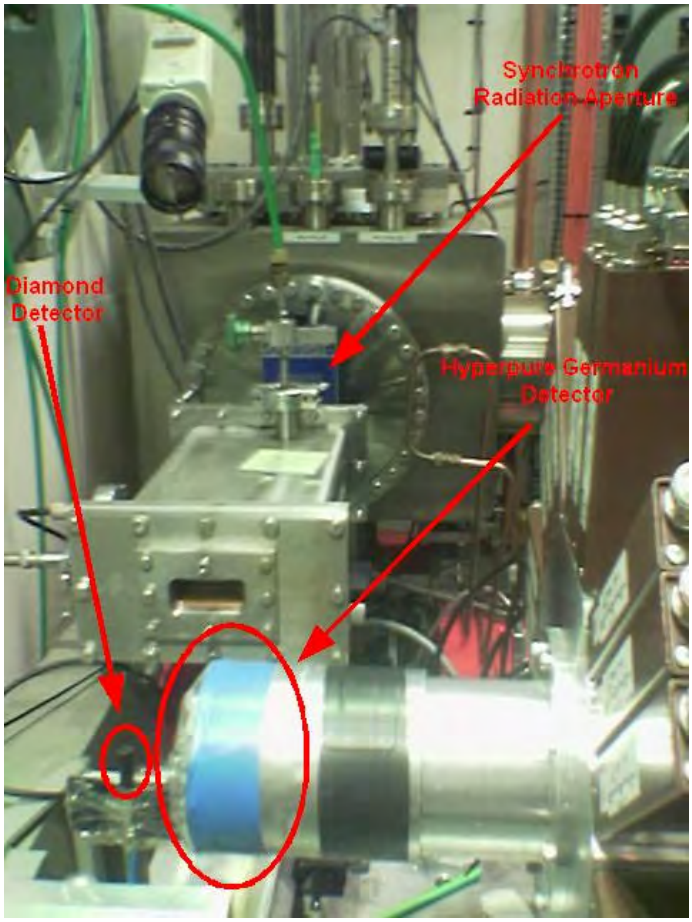

Figure 1.04 - Equipment Set-Up At Daresbury

In this picture the aperture for the radiation source is shown, as well as the experimental set-up used for the irradiation of the diamond detectors.

1.5 - Use of Dose as a Measure of Radiation Risk

When radiation is used in a workplace, whether it is being used for a course of Radiotherapy treatment or through an industrial process, it is important that the dose to the subject is quantified accurately. This is so that any risk inherent can be assessed and determined to be a necessary risk, as there is always a possibility of causing the DNA damage which may lead to the subject developing cancer. Quantifying this risk is complicated by the large number of factors involved in determining radiation risk in addition to energy absorption within a material, chiefly, the types of radiation present and the sensitivity of the tissue being irradiated. Because of this, a number of different techniques and detectors have been

developed to determine the radiation dose to a subject from any radiation source, some of which will be discussed in this section.

1.5.1 - Measurement of Radiation Dose

In order to determine the radiation risk to a patient, it is necessary that we look at the concepts used to measure the risks inherent in the exposure. An important quantity to consider with radiation fields is the Linear Energy Transfer (LET) of the beam, which describes the rate at which a beam of ionising radiation deposits energy within a medium per unit track length within the medium, as measured in units of $keV.\mu m^{-1}$. This unit is important in determining the radiation risk of different types of radiation as they will deposit their radiation in differing densities within a material. Those radiation types that deposit their energy in a more dense fashion being more likely to cause radiation damage, per unit absorbed dose. Determining the probability of cell component damage occurring has lead to the field of microdosimetry (described in Section 1.6) and nanodosimetry.

The most basic unit of radiation dose is absorbed dose, D, defined as the energy imparted to a medium per unit mass, measured in Grays, Gy, with 1 Gy equal to 1 $J.kg^{-1}$. This gives us a quantifiable unit that can produce an estimate of radiation risk that can be measured using most types of radiation detector.

One method of determining the risk to a human posed by a radiation field is to modify the absorbed dose of the radiation by the Relative Biological Effectiveness (RBE). This is defined as the absorbed dose of a reference radiation to produce a specific effect, divided by the absorbed dose of the radiation field necessary to produce the same effect, defined for the specific radiation field. This produces an accurate measure of the risks (for a specified end point) inherent from that particular radiation field, and is often used to define high doses and dose rates. This figure is dependant upon a wide range of differing factors and if one of these factors is changed, it can change the ratio significantly. These factors include the type of radiation present, the types of tissue being irradiated, the dose rate of the radiation, the temperature of the tissue, the stage of its cell cycle and the level of oxygenation present. This makes it a complicated scientific concept, only usable for situations where the radiation type

is well understood under clearly defined situations. This means two different factors are often used to provide a less accurate, but more generalised definition of radiation risk, these are the Radiation Weighting Factor and the Tissue Weighting Factor.

The Radiation Weighting Factor, W_R, is included to account for the different LETs and damage caused by different radiation fields. This value is decided by the International Commission on Radiological Protection (ICRP) based upon experimental values of the RBE by the committee. By multiplying the absorbed dose of the radiation by W_R, we obtain an estimate of the potential damage that can be caused by the radiation field, the Equivalent Dose, H, measured in sieverts, Sv, in $J.kg^{-1}$.

$$H = \sum D \cdot W_R$$

A final quantity used in determining radiation risk is the Tissue Weighting Factor, W_T. This is a factor representing the relative risk for an irradiated organ (in comparison with other organs) subject to 1 Gy of low LET radiation, designed so that the total W_T of the entire body gives a value of 1. By multiplying the Equivalent Dose, H_T, for each organ being irradiated by the tissue weighting factor, an Effective Dose, E, for that particular radiation field is reached. This is also measured in sieverts.

$$E = \sum H \cdot W_T$$

1.5.2 - Use of Detectors in Determining Dose to a Patient

There are a range of different detectors used in the determination of dose to a patient, all designed to be modified by different values to obtain a value related to the radiation risk. The reason there are a wide variety of detector types is due to the different properties needed under differing circumstances, primarily related to sensitivity vs. similarity to tissue vs. size vs. portability.

As the human body is primarily made up of carbon, nitrogen, oxygen and hydrogen, with smaller concentrations of a variety of other elements, it has been possible to design detectors

made of the same materials so as to maintain a similar radiation absorption. Many of the detectors used in diagnostic radiology are therefore made from Tissue Equivalent Plastic (TEP) and filled with Tissue Equivalent Gasses (TEG), to create a similar elemental composition to tissue. The drawback of this, however, is the low atomic number, making them less sensitive to low keV energy radiation fields, so for more sensitive designs of detector, built to detect low radiation energies in a shorter time, some detectors have a higher atomic number, to increase photoelectric absorption.

In addition it is worth considering the size of the radiation field being studied, the type and energy of the radiation as well as the type of data required (i.e. dose rate or absolute dose, to a point or to an area or volume, etc), so different detector designs are useful under different circumstances. It is also worth considering the availability of power sources, as some applications need detectors that do not require power sources, especially when they will be carried around by a patient for some time.

The detectors used in this research were chosen because of their usefulness in their relevant areas of study, these areas of use are described in details in the relevant chapters (Chapters II-V).

1.5.3 - Use of Detectors in Simulating Biological Tissue

A number of the detector designs in this research attempt to simulate the effects of radiation within human tissue through the use of tissue equivalent materials (especially in the diamond detectors and proportional counters discussed in Chapters II, IV and V), meaning that materials are used with similar interaction cross-sections and mass stopping powers to tissue. This is complicated by the differing compositions of different tissue types, such as bone, muscle, fat, etc., which has lead to the International Commission on Radiation Units and measurements (ICRU) developing models for standard tissue types (ICRU report on Microdosimetry, 1983). There are additional difficulties in obtaining materials with exact tissue equivalence that can be used for building accurate detectors. Some of the largest issues are in finding materials with the required electrical conductivity, radiation absorption, structural strength and ruggedness to build detectors, especially as these varying properties

mean that several different materials will be used, all with differing degrees of tissue equivalence.

In most cases, the deviations in the detector materials from an ideal tissue-based model can be accounted for provided the energy spectrum of the incident radiation is known, as well as the mass stopping powers of the materials used. However, this is not always possible, such as for diamond detectors, where the effects and shapes of the higher Z electrical contacts are not entirely accounted for. In these cases, approximations have been reached through comparisons between experimental and calculated values for the energy absorption distributions.

There are a number of tissue equivalent materials currently available, although most Tissue Equivalent Plastics (TEPs) are composed of a mixture known as A-150, developed by Shonka and associates. In addition there are several Tissue Equivalent Gases (TEGs) available, which are discussed below, as well as diamond crystals which are carbon-based with a low level of dopant material (discussed in Chapter II Section 2.1). Table 1.01, based on the ICRU report on microdosimetry shows the elemental composition of standard muscle, A-150 plastic and a propane-based filling gas.

	H	N	C	O	F	Na	Mg	P	S	K	Ca
ICRU standard muscle	10.2	3.5	12.3	72.9	-	0.08	0.02	0.2	0.5	0.3	0.007
A-150 Plastic	10.1	3.5	77.6	5.2	1.7	-	-	-	-	-	1.8
Propane Filling Gas	10.3	3.5	56.9	29.3	-	-	-	-	-	-	-

Table 1.01 - Elemental Composition of Tissue Equivalent Materials

A-150 is composed of polyethylene, nylon, carbon and calcium fluoride, which has a very similar level of hydrogen and nitrogen to standard muscle tissue. However, it is not an exact match, as there is some substitution of carbon for oxygen, in order to provide a practical solid plastic material that is capable of being handled and machined reliably. Due to its useful properties, allowing it to be shaped and tooled easily, it is used in the vast majority of TEP-based detectors.

A number of different gases are used for filling tissue equivalent proportional counters, chosen for their similarity to the composition of the wall material used, their tissue equivalence and their properties as filling gases. A propane-based gas was used in Chapters IV and V because of its similar elemental composition to A-150 plastic, as well as its higher gas gain. Like A-150 plastic, it possesses a similar level of hydrogen and nitrogen to standard muscle tissue, but has a drastically increased level of carbon to compensate for the low oxygen levels present.

1.5.4 - Use of High Z Materials in Dose Enhancement

The study of dose enhancement around high Z materials has existed as an area of study within radiation research for over 60 years. It was noticed that the wires used in dental surgery could lead to radiation burns and the necrosis of their surrounding tissues when a patient underwent different radiation treatments. Later, it was noticed that tissues located close to bone would also be damaged after low energy x-ray radiotherapy. Because of this initial research concentrated on ways to minimise the damage to the patient. However, over the last 30 years, research has been conducted into ways to use the dose enhancement effects to increase the radiation dose to specific areas of the body, such as tumourous tissue, while minimising the dose to the region surrounding it. Research has generally concentrated on the use of Iodine as a dose enhancement agent, as its chemistry within the body is well understood, and it has been proven to be useful in a radiotherapy context (as shown in Adam et al, 2003).

As this research is looking at detectors that can be used to improve our understanding of radiation interactions within the human body, principally concerned with a radiotherapeutical angle to cancer treatment, the primary concern of this research is to look at ways of increasing the radiation dose to specific regions of the body, while minimising the dose to the volume surrounding it. By using lower energy radiation, the shorter path lengths of the secondary electrons produced minimises the amount of tissue exposed to the effects of the radiation.

Dose enhancement media can substantially increase the radiation absorption of a localised region, principally through an increase in the flux of photoelectrons from the more absorbing

atoms, as well as increased dose from characteristic x-rays and Auger electrons. Because the main method of photon-electron interaction at low keV energies (in this case below 100 keV) is via the Photoelectric Effect, high Z materials introduced into a tumour increase the localised dose further, as the photon absorption is related to the atomic number of the materially it is passing through by the relationship: Energy Absorbed α Z^n (see Solberg et al, 1992). The value of n varies between 4 and 5 depending on the atomic number of the material.

There has been a lot of research conducted into the use of gold nanoparticles (Z = 79) to increase the radiation dose to a variety of different regions of the body (Hainfeld et al, 2004) as well as some limited research comparing the use of Gadolinium-based dose enhancement agents with iodine (Solberg et al, 1992). In the future it is very possible that some cancers will be treated by a combination of chemotherapy with drugs that include dose enhancement agents. This may prevent or slow the rate of tumour growth, which is followed by low-energy radiotherapy treatments to kill off the surviving tumour cells. This technique has been tested using synchrotron radiation in conjunction with the chemotherapy drug cisplatin (a platinum-based drug) by Biston et al (2004).

1.6 - Microdosimetry

Microdosimetry is in its simplest form the investigation of the energy distribution produced through the interaction of matter and ionising radiation on scales in the order of microns. It is important in the quantification of radiation risk, as this scale is that of the cell nucleus, where much of the damage caused by ionising radiation can lead to stochastic and deterministic effects. This is not to be confused with nanodosimetry, which looks at scales in the order of nanometres, and hence the damage done to individual DNA strands by ionising radiation.

This is important because the amount of energy imparted to a medium (per unit volume) by an ionising radiation source (the absorbed dose) is not a complete picture of the damage that will be caused by the radiation. Total energy absorption does not take into account the density of interaction of the radiation, the energy imparted per interaction or the distribution of interactions within the medium. These factors have an impact upon the quantity and nature of damage done to biological systems.

This section is based upon the *ICRU report on microdosimetry* (1983) and *Microdosimetry And Its Applications* by Rossi et al (1996).

1.6.1 - Background Theory

1.6.1.1 - Role of Microdosimetry

Within the field of ionising radiation research, microdosimetry is important because it allows the effects of the interactions between matter and a radiation field to be monitored at the scales found within the cell nucleus. This can be used to look at the interaction density of the radiation field and to determine the risks inherent to the cell nucleus and therefore the probability of that radiation field then causing damage to the DNA or organelles of a cell. Damage to the cell's internal mechanisms can lead to effects such as programmed cell death, cell mutation or uncontrollable reproduction, with the two latter effects leading to cancer.

1.6.1.2 - Applications of Microdosimetry

The main aim of microdosimetry is to provide a model with which to assess the differences associated with differing radiation fields and absorbing materials, both to aid in risk management for the use of radiation and to investigate the ways in which radiation fields interact with materials. However, the sheer complexities involved lead to any legislation produced from the research being simplified to produce a less specific measure of dose. It is therefore used to give a measure for radiation and tissue weighting factors, but is hard to apply directly to any radiation protection measures.

Outside of the field of radiation protection, microdosimetry is used in researching the causes of cancer, looking at the ways in which ionising radiation deposits its energy within the cell. This is used to assess the risks of single or double strand DNA breakages, as more densely ionising radiations tend to have a greater risk of damaging both DNA strands, and therefore causing damage that cannot be reliably repaired.

Two final fields in which microdosimetry is of use is in the investigation of dose enhancement and brachytherapy. Both of these fields are looking at maximising the radiation dose within a localised region in order to cause the maximum possible damage to surrounding tissue, while sparing tissue a short distance away. Brachytherapy looks at the distances travelled by emitted particles, whereas dose enhancement therapies rely of secondary particles produced by interactions between the ionising radiation field and the dose enhancement medium. Both, however, are looking at similar types of particle interactions over similar distances.

1.6.1.3 - Microdosimetry Definitions

Microdosimetry relies upon a number of units that are specific to the field, which are generally split into stochastic and non-stochastic values. In simple terms, we define stochastic values as representing quantities present which are subject to random fluctuations. In order to keep this section relevant to the purposes of this document, only definitions relevant to the microdosimetric work undertaken are included in this section. Other important dosimetric definitions used in other areas of radiation measurement are included in Section 1.5. The values here are generally related to the energy imparted to a medium and the statistics associated with this, following on the concept of the energy deposit, $\in_i$.

The *energy deposit*, $\in_i$, is defined as the amount of energy deposited due to a single interaction, i, at a specific point of interaction, also referred to as the transfer point, when all quantum mechanical uncertainty and detector effects are ignored. This is equal to the energy of an incident particle capable of ionisation, T_{in}, minus the total energy of all of the particles capable of ionisation that leave the interaction, T_{out}, plus any changes in the rest mass of the particles relevant to the interaction, $Q_{\Delta m}$. This includes all particles capable of interaction through primary or secondary interactions. If the value of $Q_{\Delta m}$ is greater than 0, there has been a decrease in the rest mass, whereas a value less than 0 shows an increase in rest mass. Therefore:

$$\in_i = T_{in} - T_{out} + Q_{\Delta m}$$

$\in_I$ is a stochastic quantity, measured in Joules (J), or electron volts (eV).

The *energy imparted*, $\in$, to a medium by the interaction is defined as equal to the total number of energy deposits, $\in_i$, present within the volume, also measurable in joules or electron volts. These may be due to more than one energy deposition event, and so may contain particle tracks that are statistically independent. This is written as:

$$\in = \sum \in_i$$

The imparted *specific energy*, *z*, for a medium is defined as the energy imparted by the ionising particles, $\in$, within a volume of mass *m*, written as:

$$z = \frac{\in}{m}$$

This is measured in joules per kilogram ($J.kg^{-1}$), which in radiation dosimetry is the definition of the Gray (Gy), the specific unit of specific energy.

The final important definition used within the field of microdosimetry is the *lineal energy*, *y*, which is the energy imparted within a volume by a single interaction event divided by the mean chord length within the volume, *ł*. This value is measured in joules per metre ($J.m^{-1}$), or more commonly, due to the energies and scales used for these measurements, kilo electron volts per micron ($keV.\mu m^{-1}$). Lineal energy is described as:

$$y = \in / ł$$

The mean chord length used is defined for a given volume as the mean length of different randomly-orientated chords within the volume, and is therefore dependant entirely upon the shape of the volume being studied.

As lineal energy is a stochastic value, it can be useful to consider the distribution function of *y*, *F*(*y*), showing the probability that the lineal energy of an event is equal to or less than *y*. A probability density, *f*(*y*), known as the *lineal energy distribution*, can be produced by finding

the derivative of $F(y)$ with respect to y, shown as:

$$f(y) = \frac{(dF(y))}{(dy)}$$

Note that y is only defined for single energy-deposition events.

1.6.1.4 - Interactions of Particles with Matter

It is essential to the study of microdosimetry that the interactions between the different particles capable of ionisation and the matter being ionised be understood when looking at the experimental and Monte Carlo data produced in the later chapters (Chapters IV and V).

Because of this, it is worth having a brief section detailing the different interactions that occur for the particles that will be involved in this report, namely photons, neutrons and primary/secondary electrons. Note that these interactions are not unique to microdosimetry, and will occur for any interaction between ionising radiation and matter. However, for this section, the focus is specifically upon those important in microdosimetry, and other interactions, such as pair production will be ignored.

Photons

In Section 1.7, as part of the discussion of the approximations used in the MCNP and EGSnrc codes, two means by which photons deposit their energy are discussed for the energy ranges being investigated - through the Photoelectric Effect, or through Compton Scatter. Raleigh or elastic scatter can be important in experiments or Monte Carlo models, as scatter can lead to interactions occurring within regions that would not occur otherwise. Although no energy is deposited through elastic scatter interactions, it is important in understanding radiation transport within a material, and if ignored will lead to inaccuracies in predictions of radiation dose.

In the photoelectric effect, the ionising photon interacts with an atom within the material and

transfers most of its energy to a single electron. This affects the atom as a whole, which after absorbing the photon emits an electron with an energy equal to that of the photon minus the binding energy of the electron. The binding energy is retained by the atom that emitted the electron, and may be released through the emission of Auger electrons, fluorescent radiation or low energy x-rays. Because the entire energy of the photon is absorbed, the photoelectric effect produces only a narrow distribution of electron energies, with the variance being dependant upon the binding energy of the electron shell. For relatively light elements being studied within the field of microdosimetry, the photoelectric effect dominates for photon energies up to 40 keV, which the defines the upper limit of the energy range within which the majority of the synchrotron work in this report takes place.

On the other hand, photons with enough energy to interact by Compton scatter transfer part of their energy to the electron of an atom they interact with and a Compton scattered photon is emitted with a lower amount of energy determined by relativistic momentum-energy conservation. As only a part of the photon energy is emitted through the emission of an electron, the Compton Effect produces a broad distribution of electron energies, with the energy of the Compton-scattered photon being dependant upon the emission angle with respect to the incident photon direction. As the binding energy of the electron still needs to be overcome, this binding energy is imparted to the atom as with the photoelectric effect and is released in the same manner. The Compton Effect dominates for photon energies between 40 keV and 10 MeV for the majority of the tissue-like materials being studied in microdosimetry.

Neutrons

The ionisation events in matter exposed to neutrons is mainly produced though the production of recoil protons, heavy recoil nuclei and through the products of any nuclear reactions that occur.

The interactions between a neutron and a target atom will occur through one of two mechanisms. Due to the strong atomic force and their lack of charge, neutrons may be scattered isotropically by the nucleus of an atom, with the neutron potentially losing energy in the process. The other means of interaction with an atom is through the force between the

magnetic moment of the neutron and that of the target atom, which is dependant upon the direction of the atomic moment. As neutrons are uncharged they are extremely difficult to detect directly, however, at low energies they induce nuclear reactions leading to the production of heavy ions. These lead to the production of additional tertiary charged particles which are detected directly.

The processes that will lead to the production of secondary and tertiary particles are elastic scatter, inelastic scatter, non-elastic scatter (where an interacting nucleus emits particles other than a single neutron) and capture processes. The contribution of each of these processes upon the final spectrum produced will depend upon the abundance of different elements within the material being irradiated. For example, as a large proportion of a neutron's energy can be transferred to the nucleus of a hydrogen atom, tissue-equivalent materials that have a large hydrogen content will be dominated by proton production. Because of this, it is important to ensure that the hydrogen content of different tissue-equivalent gases and plastics match that of organic tissue as closely as possible to produce accurate spectra in detectors.

Electrons

Electron interactions occur mainly with the atomic electrons present in the source atoms in a manner similar to those of photons. Due to the electrostatic forces leading to repulsion between the electrons, these scatterings and energy losses are much greater and occur much more frequently, making it extremely difficult to predict the exact behaviour of an electron.

The cross-sections of interaction for charged particles for inelastic collisions are described by the total mass stopping power, which in the case of electrons is divided into two components - the energy lost though collisions and the energy lost through radiative events. The first component describes the energy lost as the interactions of the original primary electron leads to the production of secondary electrons and the excitement of any atoms involved in the interactions. The second component includes the total energy losses to the primary electron which lead to the emission of photons. This cannot be given in a simple general form, as it is dependant upon the energy of the electron and the type material that it is interacting with. The Bethe formula describes the energy loss per unit distance for fast moving charged particles

passing through matter (as described by the stopping power of the material), however, although it applies to protons, alpha particles and atomic ions it does not work for electrons. The energy loss in electrons occurs differently due to their small mass and larger energy loss due to Bremsstrahlung radiation.

1.6.2 - Experimental Microdosimetry

In order to obtain the results found within this report, a number of experimental techniques needed to be applied, the principles of which are discussed in brief in the sections below. Some factors affecting these techniques are discussed in more depth in the relevant chapters.

1.6.2.1 - Experimental Considerations

In order to produce the measurements important in microdosimetry, an ideal detector should have the following properties: an energy absorption distribution as close as possible to that of the materials of interest (usually different human body tissues), able to measure the entire energy range of the absorbed energies. It should be capable of producing measurements over a sufficient range of volume sizes, detect low energy events with minimal distortion produced from the detector itself and the signal produced should be directly proportional to the energy imparted.

Currently, there is no simulation method or detector which fulfils all of the conditions mentioned above, so it is necessary for approximations to be made, which will place strict limits on the accuracy of any microdosimetric experimentation. Although there are a number of solutions to this problem that have been tried and a variety of different experimental procedures used (varying from low-pressure cloud chambers to different ionisation chamber set-ups), the microdosimetry experimental work reported here made use of low pressure proportional counters (the method used for simulating small cavities is discussed in Chapter IV, Section 4.1.3).

Wall Effects in Microdosimetry

Because of the differences in density between the wall of the detector and the filling gas, a number of wall effects are introduced into the results. These are present even if the wall and the filling gas have an identical elemental composition mostly due to the effects of scatter and production of secondary particles within the detector. As a small cavity is representing an even smaller region, some particles may become scattered which would not scatter into a smaller, denser volume or particles may backscatter back in. Additionally, particles produced by the same interaction may end up being absorbed far enough away from each other that they appear as two separate events or two separate ionisation events may occur close enough to each other to appear to be one event. These wall effects will lead to an increase in the energy imparted into the medium through the superposition of events that would not occur were the density uniform.

Monte Carlo calculations have been undertaken to determine the degree of inaccuracy introduced by these wall effects and the specific problems they represent. However, experimental study of these effects has been difficult to undertake at the low energies used in this research (as shown in Hugtenburg et al, 2009, and Nikjoo et al, 2010). This is due to limitations in the programs as the energy spectra are often incomplete at these energies.

1.6.2.2 - Data Analysis

The primary aim of experimental microdosimetry is to investigate the energy imparted into a specific mass of medium, giving us the dose deposition on a microscopic scale. For the purposes of this work, the pulse height spectra of the detector were converted into a y.d(y) distribution of the lineal energy, y. In this, y, the dose to the detector at a specific energy is multiplied by the dose differential at this energy, d(y).

The y.d(y) distribution is used for the analysis of this data because it shows all of the spectrum components in a manner that is clear and allows easy comparison between different sets of data. The data is modified to allow it to be shown clearly while in a logarithmic scale with the y values set to the same size. It is also useful because the biological response of a tissue,

shown in the radiation weighting factors, is linear in y for the majority of biological systems. This means that the dose differential, d(y), represents the radiation risk differential for y.

The analytical method used to calculate the y.d(y) plots used for the energy absorption spectra used in this document is included in Appendix III.

1.6.3 - Theoretical Microdosimetry

Theoretical microdosimetry is the calculation of microdosimetric spectra through theoretical models, in order to predict the behaviour of a system with a scale of microns. There are two main methods that can be used to predict this behaviour. Either the results can be predicted analytically or through the use of Monte Carlo techniques. Analytic calculation of energy deposition within microdosimetric systems is complicated for photons and is therefore only used in the calculation of neutron interactions. Therefore the techniques used in this investigation were based upon the Monte Carlo method.

1.6.3.1 - Monte Carlo Use in Theoretical Microdosimetry

As mentioned in Section 1.7, Monte Carlo is an important tool in simulating the behaviour of ionising radiation interaction systems, allowing the radiation transport equations to be solved. In this manner, it is complementary to the experimental work carried out in microdosimetry, allowing many situations to be tested across energy ranges that would be difficult or impossible to attain, providing theories that can be evaluated experimentally. This can lead to improvements in both areas of study. Experimentally, studies have shown that the average energy deposition within the filling gas of the detector is the same as for the wall itself (see Waker et al, 1995), so it is useful to be able to evaluate the difference between detector interactions and those within tissue, so a correction factor is needed.

Once a theoretical approach such as Monte Carlo simulation has been validated through comparison with experimental data, it may then be used to extrapolate detector behaviour in situations where measurements are not possible. This allows factors such as cavity size, layout, energy range and radiation type to be changed, allowing situations to be tested that

would be impossible or expensive to create experimentally. However altering the values of the variables within a computer model often leads to approximations in the layout of the detector, which combined with the simplified particle physics of the Monte Carlo codes can lead to unrealistic results. Due to this, it is essential that benchmarking be performed, where experimental results are compared to those that are computer generated in order to ascertain the accuracy of the data.

1.7 - The Monte Carlo Technique

The term Monte Carlo Method was first used in by physicists at Los Alamos National Laboratory in the 1940s, who were initially studying neutron radiation shielding problems for which analytical calculations were unable to produce a definite answer. The name was chosen as a code name for the project and is a reference to the Monte Carlo Casino in Monaco.

The Monte Carlo Method is a type of computational algorithm that makes use of repeated random sampling of a simulated object to compute a result

1.7.1 - Use of Monte Carlo in Solving Radiation Transport Problems

Radiation transport is an important component of any analysis of the behaviour of a radiation field when incident upon a material. Due to the complexity of the mathematics that describe this behaviour, solving the equations that govern radiation transport has lead to the development of Monte Carlo methods as an important tool, especially when looking at the analysis of complicated geometries.

To model the behaviour of radiation and hence to determine the effects of different radiation fields upon differing types of materials in differing arrangements, it is necessary to solve the Boltzmann Transport Equation for the situation being studied. For gamma rays, the Boltzmann Transport Equation (based upon Fitzgerald et al, 1967) may be written as:

$$\nabla \bullet \hat{\Omega} N\left(r, E, \hat{\Omega}\right) + \mu N\left(r, E, \hat{\Omega}\right) = \iint N\left(r, E', \hat{\Omega}'\right) n\sigma\left(\hat{\Omega}' \rightarrow \hat{\Omega}, E' \rightarrow E\right) dE' d\Omega' + S\left(r, E', \hat{\Omega}'\right)$$

To make use of this formula, the following quantities need to be known: *N*, the total macroscopic cross-section of the incident radiation; *n*, the number of nuclei within the interacting material per unit volume; σ, the differential cross-section of the incoming radiation from direction $\hat{\Omega}'$ to direction $\hat{\Omega}$ and energy *E'* to energy *E*; *S* (**r**, *E*, $\hat{\Omega}$), the number of source particles generated per unit time per unit volume about point **r**, moving in direction $\hat{\Omega}$ with energy *E* per unit energy range, known as the source number density; *N* (**r**, *E*, $\hat{\Omega}$), the number of particles per unit volume about **r** per unit energy interval per unit solid angle with energy *E* going in direction $\hat{\Omega}$ crossing a differential element of area normal to $\hat{\Omega}$.

Finding a solution to this equation can be difficult, as the large number of different variables within it make any solution heavily reliant upon the starting conditions of the system, something which is only possible for a narrow range of variables. Monte Carlo programs use random numbers to produce a range of variables within a pre-defined range, usually with a distribution based upon experimental work, in order to improve the accuracy of the results produced.

Monte Carlo programs provide for calculations that simulate a primary particle and all of the secondary particles produced during its passage through a medium until the primary particle has dissipated all of its energy or passed through the medium. This process consists of four distinct steps:

Step 1: The primary particle is generated. Random numbers are used to generate a particle, detailing its point of origin, energy, direction and type randomly within pre-set limits, generally designed to minimise the amount of time wasted on particles whose trajectories are non-incident with the medium.

Step 2: An interaction is selected. The random numbers are used to generate a point of interaction along the particles trajectory (calculated with regards to the medium's attenuation coefficient), the type of atom interacting and the type of interaction that takes place is often within a pre-determined area of interest.

Step 3: The angles and energies of the primary and secondary particles are calculated for after the collision. As the interaction has already been selected, the calculation then randomly determines how the energy lost by the primary particle is distributed amongst any secondary particles produced. Then the trajectories, energies and type of the primary and secondary particles are randomly selected and assigned based upon the direction and momentum of the interacting particle to preserve the conservation of energy and momentum within the system. These then continue in the same manner as the primary particle, potentially interacting with the medium and producing additional products and energy losses.

Each random probability table is based upon a histogram distribution created using experimental data to calculate more realistic directions and energies of any simulated particles. For example, high energy particles will be more likely to scatter in the direction of primary particle motion and produce higher energy secondary particles compared to low energy primary particles.

Step 4: The energy imparted to the volume of interest is calculated. The energy deposition of the resultant charged particles into the volume of interest is evaluated and can be used to produce either a spectrum of interactions within the medium or total energy absorption, and hence dose.

The particles within the simulation are all assigned a particle 'weight', which determines the importance of the particle relative to the other particles present within the simulation (i.e. a particle with a weight of 2 counts as the equivalent of 2 particles with a weight of 1). Assigning a weight to a particle allows the program to reduce the amount of histories needed to produce a relevant answer within a calculation by using variance reduction techniques such as particle splitting (dividing 1 particle into 2 identical particles with weight ½) and Russian Roulette (randomly reducing the number of particles in one area and increasing the weight accordingly). These techniques allow the number of particles within an area of interest (such as the gas cavity in a proportional counter) to be increased, while reducing the amount of time spent processing results unlikely to be of interest in the simulation (such as within the gas surrounding a proportional counter). It is especially important when there is no chance of the particles having an effect upon a specific area of interest, such as in the case of photons

interacting at a distance much greater than the electron path length of any secondary electrons that may be created.

As each interaction is heavily dependant upon the random numbers generated by the program, the accuracy of the results is directly related to the number of interactions that take place, with the accuracy being proportional to one divided by the number of particle histories ($1 / N^2$ or N^{-2}). As the number of simulated particles increases, so too does the validity of the calculation. The greatest limiting factor of this value, however, is the calculation time for the Monte Carlo simulation, so a balance has to be made between producing an accurate simulation and keeping the time required for the calculation down to a reasonable level.

1.7.2 - MCNP

1.7.2.1 - Program and Program Development

Monte Carlo N-Particles (MCNP) was originally a product of the early Monte Carlo programs created by American atomic physicists working on the development of nuclear weapons during the 1940s, although in the decades since, MCNP has developed into a general purpose Monte Carlo code useful for most nuclear applications. At present it is still owned by Los Alamos National Laboratories, but is available under license to anyone working in nuclear or radiation research, subject to approval.

The description of the MCNP physics in this section is based upon the *MCNP4C User Manual* (2005).

1.7.2.2 - Photon Physics

MCNP makes use of two different photon interaction models, utilising either a simple or complex physics model, both designed for looking at different radiation transport problems. Throughout the MCNP work done during this study, the more detailed complex model has been used, as this model uses electron transport models, which can make it more accurate for the energy ranges and applications considered within this report.

In detailed physics mode, MCNP takes into account the effects of:

Coherent Scatter
The Photoelectric Effect
Compton Scatter
Pair Production

Of these, coherent scatter and the photoelectric effect are major factors at the low photon energies being studied. Pair Production cannot occur within the detector designs studied, as the low photon energies being studied (5 to 200 keV) do not possess enough energy to form an electron-positron pair, so this effect can be ignored when discussing its implementation within MCNP. Compton Scatter is of limited importance, as its effects are independent of the atomic number of any element being ionised. Because of this it will not produce a significant difference to the energy deposition within the different detector types and so will not be a major factor at the heavy metal boundaries being studied. Also, it is worth remembering that the effects of Compton Scatter increase with photon energy, so the energy deposition is likely to be low within the energy range being studied.

This means that when looking at how the MCNP4C code works, it is important to understand the method used by the program to simulate Coherent Scatter, the Photoelectric Effect and the subsequent electron transport.

Coherent Scatter

Coherent Scatter can be an important factor within the simulations used during this investigation. This is because even though it involves no energy deposition within the volume elements used, it does involve a change in the direction of the photon, which will result in photons scattering into and out of the detector element. In MCNP4C, this is represented simply, as, a calculation of the change in angle produced. Firstly, the probability of the photon scattering is calculated for each step the photon makes, with the probability of scatter being equal to

$$Coherent \quad Scatter \quad Probability = \frac{\delta_s}{\delta_T}$$

In this δ_s is the coherent scatter cross-section of the material and δ_T is the total cross-section. A new angle is then produced using the random number generator integral to MCNP, which will make use of a preset probability distribution to determine the new direction of travel for the photon. This probability distribution is weighted to reduce the probability of backwards scatter occurring, leading to a forward-directed distribution, preventing the violation of the conservation of momentum.

Photoelectric Effect

A Photoelectric absorption process occurs when a photon is absorbed by an atom and an electron is emitted with its energy being determined by the energy of the incident photon minus the binding energy of the electron. This leaves the atom in an excited state, possessing a vacancy in its ionised shell that then relaxes by the emission of fluorescent photons and Auger electrons. The Photoelectric Effect is a far harder prospect for MCNP to simulate accurately than coherent scatter, owing to the different end points that are possible when a photon is absorbed.

Within MCNP4C, the probability of a photon capture event occurring is calculated for each photon step

$$Photoelectric \quad Capture \quad Probability = \frac{\delta_a}{\delta_T}$$

In this δ_a represents the photoelectric absorption cross-section of the material. The value of δ_T is the total cross-section of the elements present within the target volume (cell). When a photon is captured by a cell, its entire energy and particle weight are deposited within. This method of calculation is used to simulate the capture of any particle within the cell, including electrons.

After a particle has been captured within a cell, depositing its energy, E, this energy is then lost through the emission of photons and/or electrons. Electrons may then be emitted from the atom provided that E > e, the binding energy of the electron, giving the emitted electron a kinetic energy of E – e. As the capture probabilities and the kinetic energy of the emitted electron are dependant upon the binding energies of the atoms within the cell, the x-ray absorption cross-sections of the atoms will lead to an increase in energy absorption around the K and L edges, as well as at a discrete range of electron energies.

When the cell de-excites, there are 3 possible outcomes accounted for in MCNP4C, either the cell emits 0, 1 or 2 fluorescence photons, the number of which is dependent upon the energy of the captured particle and the atomic number of the cell atoms. MCNP4C defines a fluorescence photon as a photon with an emitted energy greater than 1 keV and will also produce a random number of lower energy photons and Auger electrons to dissipate any remaining energy, enforcing energy balance. Each of these possibilities and the effects it will have upon the calculation are discussed below.

At low energies, the vast majority of photoelectric interactions will result in no photons being fluoresced, as a cascade of atomic electrons quickly fill any gaps in the electron shells caused by photoelectric ejection. Any energy absorbed is therefore dissipated as a series of Auger electrons and low energy photons (the Auger effect), with a total energy equal to that of the absorbed photon.

In the case where 1 fluorescence photon is emitted, the photon energy is calculated as

$$E' = E – (E – e) – e'$$
$$= e – e'$$

In this e' is the residual excitation energy of the atom, which is then released by a series of further electron and low energy photon emissions. All fluorescence photons are assumed to carry the full fluorescent yield, determined by the higher electron orbitals of any target atoms. These are then apportioned by MCNP among the x-ray lines $K\alpha_1$ (L_{III} >> K), $K\alpha_2$ (L_{II} >> K),

$K\beta'_1$ (M_{mean} >> K) and $K\beta'_2$ (N_{mean} >> K), all of which are dependent upon the atoms present within the cell.

If e' is greater than 1 keV, it is possible for the cell to produce an additional fluorescence photon, representing an electron filling a gap in the orbital of binding energy, e'. The energy of this second fluorescence electron emission is equal to

$$E'' = e' - e''$$

In which e" represents the residual energy dissipated by the production of Auger electrons and low energy photons. As before, the energy of the fluorescent photon is maximised, with all transitions occurring in the upper shells (i.e. $K\alpha_1$ and $K\alpha_2$ transitions, resulting in L shell vacancies).

If the atomic number of the cell atom interacting is below Z = 12, all potential fluorescence energies are below 1 keV, and so there will be no emission of fluorescence photons within MCNP. For the elements 12 < Z < 31, there is a possibility of a single fluorescence photons being produced. For Z > 31, the $K\alpha_1$, $K\alpha_2$ and $K\beta'_1$ transitions become plausible, allowing a possibility of double fluorescence. When Z > 37, a $K\beta'_2$ transition becomes energetically possible.

All fluorescence photons and Auger electrons are emitted in an isotropic fashion from the point where the photon is absorbed, and the initial photon track terminates. If any electrons are produced by the photoelectric effect, they are produced using the electron physics rules, outlined below.

1.7.2.3 - Electron Physics

Although the same capture model used in MCNP4C is used for all particle captures (including photons, electrons, positrons and neutrons), there are some fundamental differences between the representations of photon and electron transport through a material. As they possess an electric charge, the transport of electrons is dominated by the long-ranged Coulomb Force,

which means that the electrons are subject to a large number of different interactions taking place, each resulting in a small change in the path and energy of the electron. This creates a problem when trying to accurately simulate the behaviour of an electron, as to model every single interaction would require a great deal of time and computing power.

MCNP4C makes use of a multi-scattering statistical technique to simplify the calculations, assuming that the loss in energy from a single interaction is small compared to the overall kinetic energy of the electron. This allows the series of small interactions to be approximated as a lesser number of 'Condensed Histories', each an estimate of the total change in direction and energy loss of the electron caused by Coulomb interactions. These are calculated from a series of probability distributions describing the major quantities in the calculation, such as the energy loss and angular deflection. The condensed histories reduce the electron transport into a several small leaps, each of which is calculated in the following manner. MCNP makes use of a Class I Condensed History algorithm for its electron transport modelling, compared to the Class II algorithm used in EGSnrc.

First, all data relevant to the steps is either pre-calculated or retrieved from a set of pre-set data files, with values interpolated as necessary from an energy grid. Relevant data at this stage includes factors such as electron energy, stopping powers, electron range, energy step ranges, sub-step lengths, angular deflection probability distributions and the generation of secondary particles.

Next, the collisional energy loss rate for the electron is sampled, based upon the non-radiative stopping power of the electron within the cell material. Every step within this stage is further subdivided into a series of sub-steps, the number of which is determined by a pre-set value based upon the stopping power of the medium. After the energy loss has been calculated for each sub-step, there is a probability that the electron will change direction, which is determined by an energy-based probability distribution. If the electron reaches a geographic or energy boundary (i.e. leaves the boundaries of the detector or is reduced to an energy below a pre-set lower threshold), the electron path is no longer followed and the electron is assumed to be lost to the system, although the importance of the particle is not changed for the purposes of error and distribution calculations.

Finally, a probability distribution is sampled to determine the nature and energies of any secondary particles produced by the loss of energy from the electron, such as through fluorescence x-ray photons, knock-on electrons or Bremsstrahlung radiation.

1.7.3 - EGSnrc

1.7.3.1 - Program and Program Development

EGS, short for Electron-Gamma Shower, is a Monte Carlo code developed by the SLAC (Stanford Linear Accelerator Centre) group primarily for the purposes of studying the interactions between ionising photons and the matter they interact with. There are several versions of the code available, most of which make use of similar techniques for calculating the interactions within the material, but allowing for differing geometries. For example; EGSxyz allows geometries to be constructed based upon joining points on x, y, z axes, producing cube-based geometries, and EGSnrc allow geometries to be created using cylindrical coordinates, based upon points at height (n), radius (r) and position along a central axis (c).

Currently, EGSnrc is maintained by the Ionizing Radiation Standards Group, a part of the Institute for National Measurement Standards in Canada.

1.7.3.2 - Photon Physics

As with MCNP, at the low energies being studied for this research, the primary methods of interaction will be through Coherent Scatter and the Photoelectric Effect, with negligible Compton Scatter occurring. This section will largely look at these interactions and how they are calculated.

Coherent Scatter

EGS handles the effects of Coherent Scatter in a similar manner to MCNP. First it calculates a

probability of interaction within the material and then an angle of scatter for the photon, both values being based upon the atomic number of the atom being interacted with.

By default, the EGSnrc code does not include Coherent Scatter within the system, and the default PEGS files do not contain the data necessary to calculate the angles of scatter. In the EGSnrc calculations contained within this work, Coherent Scattering was turned on, so the effects of coherent scatter were included in the calculations.

Photoelectric Effect

As with MCNP, the Photoelectric Effect is a harder prospect to simulate than Coherent Scatter, owing to the differing end points possible when a photon is absorbed.

The original default EGS models ignored the effects of the emission of relaxation particles; this was later modified to include the production of K_α and K_β fluorescent radiation, with the energy of incident photons below the K-shell binding energy being deposited locally. Another limitation of the EGS code is that it subtracts the K-shell binding energy from all of the emitted electrons, despite the probability that the electron may be emitted from a different shell. With high Z materials, such as those being studied, this probability can be as high as 20% (from the *EGSnrc User Manual*, Kawrakow et al, 2010).

For EGSnrc, the first step is to determine the probability of a photon capture within the material, with the probability of capture for each photon step being:

$$Capture \quad Probability = \frac{(p_i \cdot \delta_a)}{(\sum p_i \cdot \delta_a)}$$

In this p_i represents the stoichiometric index of the material, and δ_a represents the absorption coefficient of the material. To sample the element accurately, all elemental cross-sections for the material at the different energies possible are needed for the simulation. As the PEGS data set included with EGSnrc cannot contain the entirety of this data EGSnrc uses fit formulae to determine δ_a, accurate to within 1-2 %. Although these calculated values are relatively

accurate, it must be noted that the PEGS data supplied by the program is known to be inaccurate around absorption edges.

After the amount of energy absorbed has been determined, EGSnrc determines the shell the interaction has taken place with, starting with the innermost atomic shell with a binding energy lower than the energy of the incident photon and randomly determining if the photon interacts, based upon pre-defined interaction probabilities. Once the photon interacts, a photo-electron is created with a kinetic energy equal to the energy of the photon minus the binding energy of the atomic shell. This then travels through the material as a secondary electron (see section 1.6.3.3), with a direction determined from the direction of travel of the photon.

1.7.3.3 - Electron Physics

EGSnrc makes use of a condensed history technique in a manner similar to the MCNP code, with the cumulative effects of many discrete track steps being condensed into a single event in order to reduce the overall complexity of the calculations and hence the processing time. These condensed histories include both elastic and inelastic scatter events, by sampling changes in energy and direction from appropriate scattering distributions after each step.

EGSnrc makes use of a Class II Condensed History algorithm to simulate electron transport. This means that it explicitly simulates inelastic collisions that produce secondary electrons (beyond threshold energy, T_c) and photons produced as bremsstrahlung radiation (above threshold energy k_c), then simulates the paths and interactions of these secondary particles. Secondary particles that fall below these threshold values are instead grouped together to simplify the calculations.

First, a particle is selected by the program from the list of available particles and its energy, position and direction of travel calculated, either based upon the source definition or its previous values. Next, the energy loss of the electron for the next interaction is calculated from a probability distribution, based upon the total cross-sections of the material for bremsstrahlung or inelastic collisions per unit energy loss. Then the particle's position, energy and direction of travel is modified in a manner that simulates the solution of the transport

equation, in order to show the change in these values caused by the energy loss during travel.

Finally an interaction type is chosen from the total interaction cross sections of the material at the particles current position and energy then any changes to the particle's direction and energy calculated from the appropriate cross section. At this stage, any resulting secondary particles are added to the list of available particles, and the cycle of calculation then continues until all of the available particles either fall below the threshold energy or leaves the system.

1.7.4 - Comparison of MCNP and EGS

There are many different Monte Carlo codes available for detector research, therefore it is important to now consider the reasons why these codes were used and their advantages over rival codes for the research conducted during this thesis. Research has shown that there are a few differences in the ways in which these codes are implemented that can have significant effects upon the results obtained, effects which are discussed at some length in Andreo (1991) and Šídlová et al (2010). In addition to this, research has been conducted comparing the results obtained using different codes compared with experimental results (for instance in Love et al, 1998, and Jeraj et al, 1999). In most cases, these effects are slight, with general results having a statistical uncertainty of 1 to 2 %.

MCNP

MCNP was chosen for this research because it has several features that make it invaluable as a model for photon research. This is particularly evident in investigating the behaviour of complex detector designs, as a feature of MCNP is the range of different geometries that can be created using the code. This made it possible for complex models to be created for a range of detector designs, from Diamond detectors to TLDs and also gas-filled proportional counters. Another advantage of MCNP over most other codes available is the number of different particle types included, allowing photons, electrons, protons and neutrons to be modelled accurately, so, all of the particles present in any interaction could be accounted for in one code.

As a Class I electron transport algorithm, MCNP makes used of condensed histories to approximate the behaviour of electrons transported through the medium. It does not include any individual interactions along the path of the electron; this has been shown to cause a decrease in the energy absorption at the surface of the material as well as an increase in depth penetration. In more recent versions of the code, such as MCNP4C used in this research, this effect has been reduced, but can still introduce discrepancies of up to 10 % in the results obtained.

A potential disadvantage for this code is that it does not give a reliable spectrum for the interactions within the detector which can be directly compared with those taken experimentally. This is due to all of the approximations taken in particle transport by the code, meaning that although the total energy absorption within a medium predicted by the code will tend to be correct (when a large enough number of interactions are taken into account). The individual interactions do not correspond well with experimental data, leading to absorption spectra that differ greatly from those found experimentally.

Due to this, MCNP was used to investigate the behaviour of different detectors over a range of monoenergetic energies, to see the effects of the absorption edges upon the energy absorption of the detectors, especially when the detector is modified by adding a contrast medium. All of the final energy spectra produced were created using EGSnrc.

EGSnrc

As a Class II electron transport algorithm, EGSnrc includes condensed histories, but is designed to more accurately model the behaviour of interactions above a pre-determined threshold for energy loss or angular deflection. A disadvantage of the use of EGSnrc is that it is known to underestimate the electron backscatter for high Z materials, due to the Moliére theory used for its basis, which works best for small-angle deflections. This may lead to some slight discrepancies at the high Z-low Z interfaces in the detector designs being studied.

Additionally, one disadvantage of EGSnrc over MCNP is that the PEGS data tables used to calculate the cross-sections of different materials during interactions are known to be

inaccurate around absorption edges (this is discussed on p.47 of the EGS manual).

Summary

In summary it may be concluded that of the two codes, MCNP allows more detailed modelling of detector geometry. This allows complex systems to be designed, while still allowing an accurate estimation of the energy absorption characteristics to be established. However, the electron transport model used by EGSnrc is more accurate than that used by MCNP. As the accuracy of the electron transport model will largely determine the accuracy of the Monte Carlo calculation being used, EGSnrc should produce the most accurate results of radiation transport.

Chapter II - Diamond Detector Dosimetry

2.1 - Background Theory

A diamond detector is a solid state device that uses an artificial diamond to detect radiation, by looking at the effects of the interactions between the incoming ionising radiation and the crystal lattice structure of the diamond (made up of carbon and nitrogen atoms). The degree of this interaction can be used to determine the strength of the radiation field to which the diamond is exposed. Figure 2.01 shows an image of one of the diamond detectors used during the course of this investigation, for a more detailed image of the detector and its components see Figure 2.02.

Figure 2.01 - A Typical Diamond Detector

The diamond detector works within the same theoretical framework as any solid state detector. When the diamond is placed within a radiation field, the atoms within the material obtain energy through interactions with the photons within the field, which is transferred to the outer electrons of the atom, causing them to make the transition from the Valence Band to the Conduction Band. Applying an electric field to the diamond will lead to a detectable difference in the current due to the conducting electrons present, which will become larger if more energy is deposited within the material, creating more free charge carriers.

Use of Diamond Detectors in Dosimetry

Diamond detectors have a number of advantages over other detector design, some of which shall be discussed below:

The primary use of diamond detectors is in the study of high energy radiation fields, due to the detector's extreme resistance to radiation damage compared with most other detector designs, due to the stability of the carbon-carbon bonds within the crystal. However, there are a number of factors that can make them a useful tool for the study of the low intensity fields used in this research.

One very useful feature of the diamond detector is the small size of the diamond crystal (the detector housing is approximately 7.3 mm in diameter), which allows the detector to be placed in important areas within the radiation field to produce a dose distribution map. This is because the small volume allows the detector to produce a good spatial resolution. Also, the detector can be placed in areas of the field where a larger detector would be unable to fit, such as within a phantom.

For the medical applications being considered within this research, the detector also has a considerable advantage, as it is constructed largely from carbon with nitrogen contamination of less than 500 ppm (significantly lower than that of natural diamond crystals). This produces a good comparison with the chemical makeup of the human body which is composed mostly of carbon, nitrogen, hydrogen and oxygen. The advantages of a diamond crystal are discussed and tested in Fallon et al (1990). One drawback of this, however, is that the low Z number of the diamond can reduce the sensitivity of the detector to the low energy radiation being investigated, increasing the exposure times necessary to produce a result.

Finally, one more advantage of using a diamond detector for experimental work like that conducted at Daresbury is that the detector has a fast response time (an intrinsic time resolution of 30 ps is demonstrated in Griesmeyer et al), which allowed the results to be obtained in real time, making it possible to alter the conditions within the experiment to optimise the results.

2.1.1 - Detector Theory

The theory underpinning the use of solid-state detectors is discussed in some detail in the next chapter (Chapter III), as TLD theory offers a simpler scenario where the use of excitation of electrons from the Valence band to the Conduction band is used for radiation detection. As the electrons within the crystal lattice of the diamond crystal are excited from their valence band to their conduction band, the conductivity of the crystal is changed, producing a measurable change in the current proportional to the number of interactions that have occurred. A diamond crystal possesses a band gap of 5.6 eV, requiring an energy input of 5.6 eV to excite an electron from the valence to the conduction band. This is very large compared to that of silicon (1.11 eV) and Germanium (0.67 eV), which makes the detector suitable for use at high temperatures (their use at temperatures as high as 250 - 300 °C has been recorded).

Because of this, the diamond detector has been used extensively in the study of high intensity radiation fields, as it has a fast response time, is stable over long time periods and is highly resistant to radiation damage, filling a role many other detector designs can not.

2.1.2 - The Diamond Detector within the Scope of this Thesis

As has been mentioned earlier, one of the key advantages in using the diamond detector is the small size of the detector element, an important factor in using it for experimental use; however, it is insufficiently small, being millimetres in diameter, to act as a true microdosimeter.

The main purpose of investigating the behaviour of a Diamond Detector is to look at the effects of the different high Z materials used in its construction, as it has often been modelled in the past as one homogenous detecting volume mounted within a homogenous outer shell. This research will look at the effects of different detector models on the final readings obtained and see if it is possible to improve the model to get a better approximation of the behaviour of a detector during an experiment. An interesting avenue for research is looking at the effects of the gold and silver components of the detector within the electronics, as the high Z number of these metals, as well as their K and L edges should produce a measureable

difference in models designed to take them into account.

2.1.3 - Diamond Detector Design & Operation

In order to accurately simulate the behaviour of any detecting device using Monte Carlo techniques, the internal structure must first be analysed, so that the internal dimensions are accurately modelled. This simulation was therefore based upon data from the manufacturer, combined with data produced experimentally and some additional data from earlier studies (as in Bose, 2004).

The structure used initially for the productions of the MCNP diamond detector model is shown in Figure 2.02, based upon manufacturer's descriptions of the PTW-Freiburg/IPTP Dubna Diamond Detector (Serial Number 7-020). This model was refined further due to information produced during experimentation.

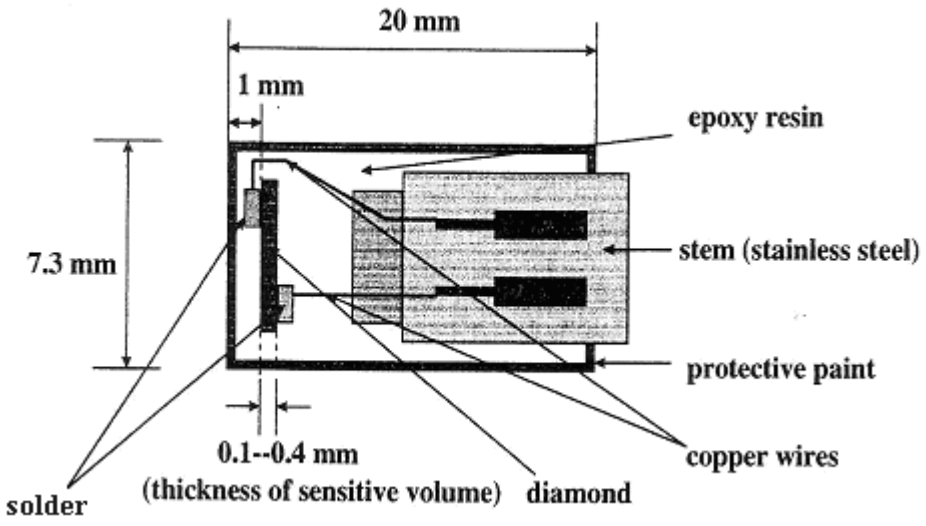

Figure 2.02 – The Internal Structure of a Diamond Detector

The manufacturer's information gave some indications of the materials used in the construction of the detector, although this was incomplete and the model was modified due to information obtained from experimental work, with slight changes made to the elemental composition of some of the components present. The main components of a Diamond

Detector are a Polyethylene outer shell, containing a diamond (mostly composed of carbon, but with some impurities), attached to two silver-plated copper wires by gold-based contacts. This is held together using an epoxy resin and mounted at the end of a stainless steel stem to increase the distance between the operator and any incident radiation fields. An important unknown in the creation of the model was the elemental composition of the solder used for the electrode-diamond contacts.

Experimental work using the Daresbury Synchrotron managed to determine the presence of Gold and Silver atoms within the detector, but the exact proportions of each were impossible to verify (and probably varied between the two detectors being used). Therefore the simulations were conducted using three different models, with three different compositions used for the contacts: one with pure gold contacts, one with pure silver contacts, and one using an industry-standard gold-based solder (described in O'Neill). It was hoped that these three models would give an idea of the effect the differing atomic masses would have upon a diamond detector's energy absorption.

2.1.4 - Gas Ionisation Chamber Design & Operation

The diamond detector used in this research was analysed relative to a gas ionisation chamber in order to investigate any changes in energy absorption at different source energies, particularly with respect to the K and L edges of the heavier elements present in the detectors. An image of the type of ionisation chamber used in this work is included in Figure 2.03. A gas ionisation chamber works by measuring the amount of charge liberated through the interaction of an ionising radiation field and a suitable gas. By passing an electric field through the gas, the free electrons are attracted towards the anode of the detector, and any positive charges migrate to the

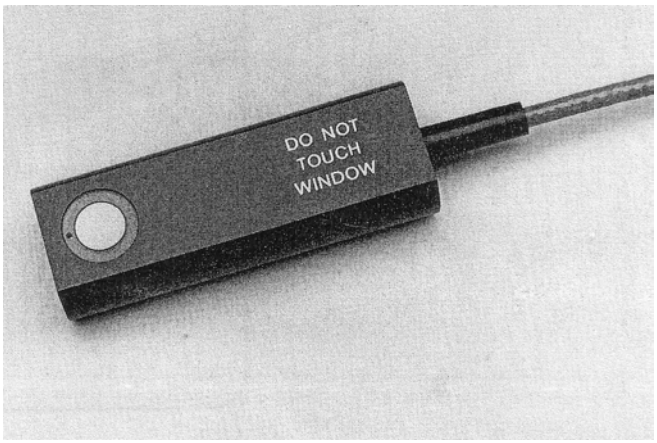

Figure 2.03 - A PTW-Freiburg Type 23342 Parallel-Plate Ionisation Chamber

cathode, creating a current, the size of which is dependant upon the quantity of energy deposited in the medium by the ionising radiation. The theory behind gas-filled detectors is discussed more thoroughly in Chapter IV, section 4.1.1.

Gas ionisation chambers are used widely in a number of different applications, especially in the field of radiation monitoring, where they are used as a standard detector design, owing to their sensitivity, stability and linearity. As a standard detector, they are often used to produce a measure of the absorbed dose to water, a standard that can then be used to calculate the effective and equivalent dose to a biological system.

The ionisation chamber used in this work was a PTW-Freiburg Ionization Chamber Type 23342, a parallel plate ionisation chamber used to measure dose over a useful range of 8 keV to 35 keV with a degree of accuracy of ±2%. This design of ionisation chamber is commonly used for the measurement of air KERMA or absorbed dose to water for radiation therapy, often being placed within a solid phantom. It consists of a rectangular plastic block containing a sensitive air-filled cavity with a diameter of 5.2 mm and a height of 1 mm, giving it a sensitive volume of 0.02 cm^3.

2.2 - MCNP Modelling of the Diamond Detector

The aim of this MCNP model was to produce the most accurate simulation of a diamond-based detector possible to allow an investigation of the effects of different complexity models and differing atomic number elements in contact with the diamond crystal. This would allow for an assessment of the MCNP4C code for use in modelling small-scale detector designs over the low keV energy ranges being studied, and if the results match well with experiments as a validation for further calculations using high Z additives to tumours.

In order to produce this data, several different models of the detector were needed, to show the effects of complexity upon the final readings produced. The first model simulated was based upon an earlier EGSnrc model used by Gunaranjan Bose (2004), which uses a simple array of cylinders to model the behaviour of a diamond detector. A second was then produced to model as accurately as possible the positions and elemental compositions of all of the

components present within the diamond detector (see previous section), which utilised three different possible solder types that could be present within the detector. To provide a baseline against which to compare the different model types, an idealised detector model was also created, where the only components were the diamond crystal itself and a simple plastic shell, without any metallic components present. Finally, to allow the different models to be compared with the experimental data obtained, an idealised gas ionisation chamber model was designed, so that correction factor calculations for the models could be made.

Common Parameters

In order to allow the different sets of data to be compared, a number of common parameters had to be established, such that the only change in the different data sets was the slight alterations to the model. As the experimental data was produced in the SRS Facility at the Daresbury Synchrotron, the MCNP4C models attempted to recreate the experimental conditions as accurately as possible.

The models all use a rectangular, strongly collimated, monoenergetic source, 8mm by 8mm, similar to that used at the SRS Facility, placed at a distance of 10 mm from the surface of the detector, which is placed within a 10 cm spherical air-filled cell. The source-to-detector distance was chosen to allow some interaction between the beam and the atoms of the surrounding air and is not representative of the distance between the synchrotron beam aperture and the detector in the experimental work. The layout of the synchrotron is described in several papers, including Collins et al (1998). Outside of this air-filled cell, all particles were assumed to be lost from the system, which helped to improve the processing speed of the calculation.

The energy absorption within the detecting element was calculated using the Pulse Height Tally *F8, which displays the energy deposition within a specified volume (in MeV), giving a close approximation of the real-life behaviour of a detector. The total energy absorption within the absorbing volume was then used in the calculation of the correction factors. The energy cut-offs used for the calculations were set to 0.1 keV and 1 MeV (based upon standard values for MCNP), as these were significantly outside the ranges being used for the

calculation. For all of the calculations, electron and photon interactions were calculated as equal importance and a total of 500,000 histories were calculated for each run.

The elemental composition of the materials used in this section is described as being pure if it is composed purely of one element (with the exception of water). All other materials are described by their elemental composition in Appendix II, Table x2.02.

The Ionisation Chamber

The ionisation chamber used for the experimental work within this thesis was a PTW Model 23342 Parallel-Plate Chamber produced by Freiburg of Germany, designed to be used to measure low energy photon interactions interacting within a small volume.

The initial MCNP Ionisation Chamber was designed to measure the energy deposited within a very thin surface layer situated within a larger phantom. The detector element was a 0.5 mm diameter by 0.01 mm depth cylinder placed on the surface of a 20 mm diameter by 30 mm depth cylinder (chosen to be deeper and wider than the electron path lengths at the highest energies used). Pure water was used as the material for both the detector element and the phantom in the first model. This design was chosen to represent an idealised ionisation chamber purely for the calculation of Correction Factor Ratios for the diamond detector models.

A diagram of the model used in the evaluation of the water and air-based gas ionisation chamber model is shown in Figure 2.04a.

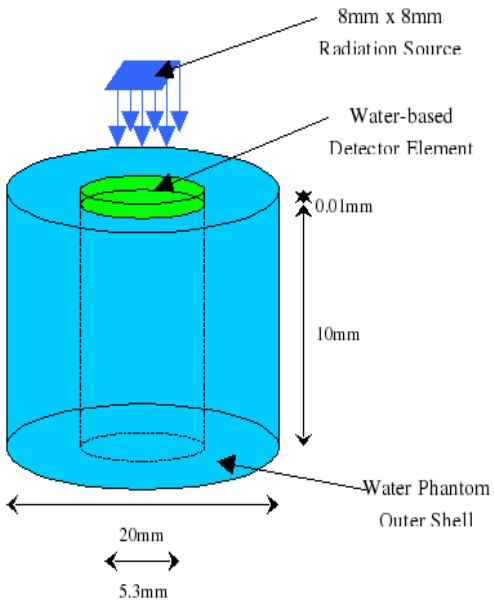

Figure 2.04a – The Basic Gas Ionisation Chamber Model

A second model was then created, which made use of the same dimensions, but

substituted air for the water. This model was designed because the research conducted was inconclusive on whether the Model 23342 ionisation chamber is designed to be air equivalent or water equivalent (see Perrin et al, 2001 and Lui et al, 2007)

Finally, a more detailed model of the ionisation chamber was produced, making use of the same dimensions and materials as the original detector used. A diagram of this model is shown in Figure 2.04b (note this diagram has been reversed in the z axis in order to better show the relative positions of the elements). In this model, the detecting element is a cavity constructed from air with a diameter of 0.25 cm and a depth of 0.1 cm. This is placed within a TEP detector housing 2.2 mm wide, 1.44 mm deep and 6.1 mm long, with the detecting element positioned 0.875 mm away from one of the lengthwise walls. Above the detecting element is positioned a pure beryllium window 1.0 cm in diameter and 0.003 cm thick. An example of an MCNP input file for the complex ionisation chamber can be found in Appendix IV Example 4.3.

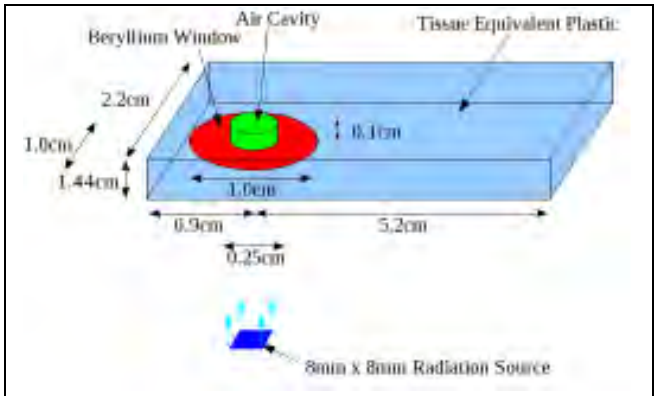

Figure 2.04b - The Complex Gas Ionisation Chamber Model

The Simple Model

The primary aim of this model was to continue work done previously at the University of Birmingham (Bose, 2004; Saeedi, 2006; Yin et al; 2004), by comparing their EGSnrc models to those constructed within MCNP4C and more geometrically complex models. Although the basic geometry of the detector model has been kept the same, the source was altered to better represent the geometry of the experimental source at the SRS Facility, as well as improve intercomparisons with the other data sets.

The detecting element is represented by a cylinder of 0.5 mm diameter, 0.03 mm thick, at a depth of 1.0 mm, based upon the dimensions of the diamond crystals within the detectors. This is housed within a 20 mm diameter by 20 mm depth polyethylene cylinder, to represent the detector housing. To test the effects of the metallic electrodes upon the photoelectric absorption of the detector, two differing models were produced using the simple geometry; one with a diamond only detecting element, and a homogenous diamond model, composed of a ratio of carbon, copper and silver chosen to represent the effects of the electrodes. The elemental composition of the homogenous crystal s included in Appendix II Table x2.01. A diagram of this model is shown in Figure 2.04c. An example of an MCNP input file for the 3 component diamond detector model can be found in Appendix IV Example 4.1.

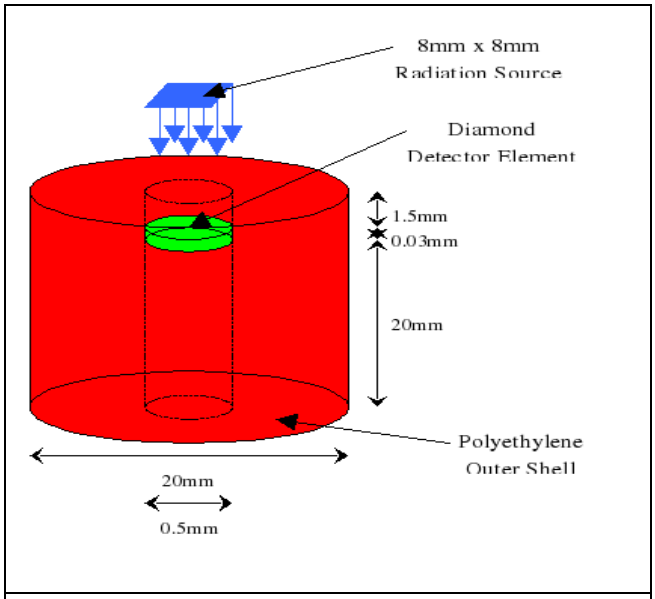

Figure 2.04c – Three Component Diamond Detector Model

The Complex Model

A final model was then created, based upon the real-life structure of the diamond detector using information from the detectors user manual, several papers on diamond detector structure (Bose, 2004; Fallon et al, 1990; Planskoy, 1980; Vatnitsky et al, 1993; Yin et al, 2004) and some experimental tests of the dimensions of the crystal, mentioned in the next section.

During the design phase for this detector some disagreements were found in the literature over the exact materials used in the electrical contacts joining the diamond crystal to the silver-coated copper wires. As some of the models investigated made use of a silver-based solder and some a gold-based solder, both designs were tested to see if they had an effect upon the final results. These contacts were constructed from pure gold and pure silver with no other

elements present. In addition, a gold-tin based solder based upon one used in the electronics industry (O'Neill, 2002) was modelled. The elemental composition of this solder can be found in Appendix II Table x2.01. A diagram of this model is shown in Figure 2.04d.

This gave a total of four different models being tested, one an idealised pure diamond model only and the other three with different composition contacts present.

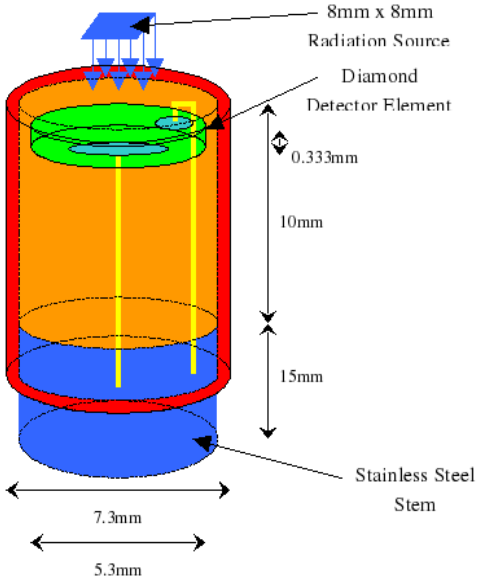

Figure 2.04d – Complex Diamond Detector Model

The detector was constructed with a 265 µm radius and 33 µm thickness diamond crystal acting as the detector element. This was placed 1 mm below the upper surface of a polyethylene outer casing, with an internal structure including two wires and their contacts. The region between the outer casing and the wires was filled with epoxy resin and the entire structure was mounted on a 15 cm pure aluminium stem. An example of an input file for MCNP created for the complex diamond detector model using Gold-Tin solder can be found in Appendix IV Example 4.2.

Errors

Based upon values generated by the MCNP4C program, the errors present in the data is summarised in Table 2.01. These calculations were run for 500,000 particle histories and the table shows the relative error calculated in intervals of 10 keV.

Monte Carlo Model	Relative Error				
	10 keV	**20 keV**	**30 keV**	**40 keV**	**50 keV**
Water-Based Ionisation Chamber	0.015	0.042	0.068	0.072	0.067
Air-Based Ionisation Chamber	0.021	0.060	0.088	0.106	0.107
Realistic Ionisation Chamber Model	0.040	0.096	0.137	0.154	0.154
3 Component Diamond Model - Diamond Only	0.006	0.017	0.029	0.035	0.034
3 Component Diamond Model - Homogeneous Model	0.003	0.008	0.010	0.013	0.015
Complex Diamond Detector - Diamond Only	0.005	0.013	0.022	0.027	0.026
Complex Diamond Detector - Silver Contacts	0.005	0.013	0.021	0.024	0.024
Complex Diamond Detector - Gold Contacts	0.005	0.013	0.021	0.025	0.025
Complex Diamond Detector - Realistic Contacts	0.005	0.013	0.021	0.025	0.025

Table 2.01 - Summary of Errors in Monte Carlo Calculations of a Diamond Detector

From these results it can be seen that the error in the calculations increased as the source energy increased, as the energy absorption decreases with increasing energy beyond ~8 keV. This means that the number of particles depositing their energy within the volume becomes less; however they are capable of depositing more energy in an event making the results less predictable. As well as this, it can be seen that the relative accuracy of the diamond detector calculations was greater than that of the ionisation chamber for all variant models due to the larger volume of the detecting element. This made it more likely that particles would interact within the detector element increasing the number of interaction events.

2.3 - Results

2.3.1 - Experimental Results

The experimental work on diamond detectors contained in this document was conducted using a PTW-Freiburg/IPTP Dubna diamond detector, serial number 7-020 using the synchrotron at Beamline Station 16.3 of the SRS Facility in Daresbury. This work was conducted to ascertain the reliability of using MCNP to simulate the behaviour of this detector design and test the assumptions made in constructing the model.

Investigation of the Diamond Detector's Properties

In order to create an accurate model of the diamond detector using MCNP, it was important that the dimensions of the detector crystal and the elemental composition of the different components be known. First the shape of the radiation field was investigated using GafChromic film to determine the optimum position to place the detector as discussed in Appendix VI. Once this had been done, the detector was positioned at a series of different heights within the radiation field and exposed to a monoenergetic beam of synchrotron radiation with an energy of 11.87 keV and 11.95 keV. These results are shown in Figure 2.05, showing the current from the detector with different source energies: a blue line represents 11.95 keV, green gives 14.35 keV and red shows 25.54 keV.

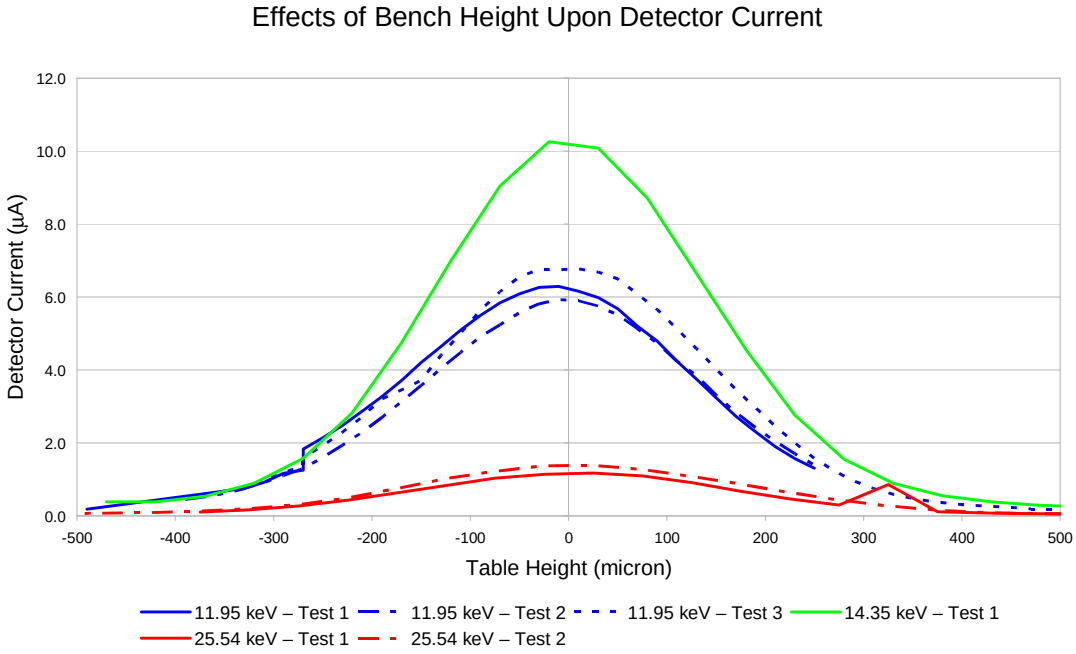

Figure 2.05 - Crystal Size in a Diamond Detector

These results show that the detector displays a peak when the radiation source is directed at the centre of the crystal, rapidly dropping away as the source irradiates less of the crystal. Taking the half value points of the graph to be a measure of the edges of the diamond crystal, it appears that the diamond has a thickness of approximately 300 μm, close to the 333 μm dimensions given by the manufacturer. This was also useful as it allowed the centre of the detecting volume to be determined, allowing all further irradiations to be directed at this point.

A second experiment was then conducted to investigate the potential presence of gold within the detector element to see whether running MCNP simulations containing gold was necessary. This was performed by investigating the fluorescence of the gold atoms in the vicinity of the L_{III} edge of gold, determining the change in energy absorption as this energy is reached. The L_{III} edge was chosen as it was an energy that the synchrotron beam could be set too easily and the K edge is at too high an energy for this setup. Table 2.01 contains the electron binding energies for the

Edge	Electron Binding Energy (keV)
K	80.725
L_I	14.353
L_{II}	13.734
L_{III}	11.919

Table 2.02 - Electron Binding Energies of Gold

relevant edges. The current recorded by the diamond detector at an energy range in the region of 11.919 keV is shown in Figure 2.06, with the red line showing the L_{III} edge.

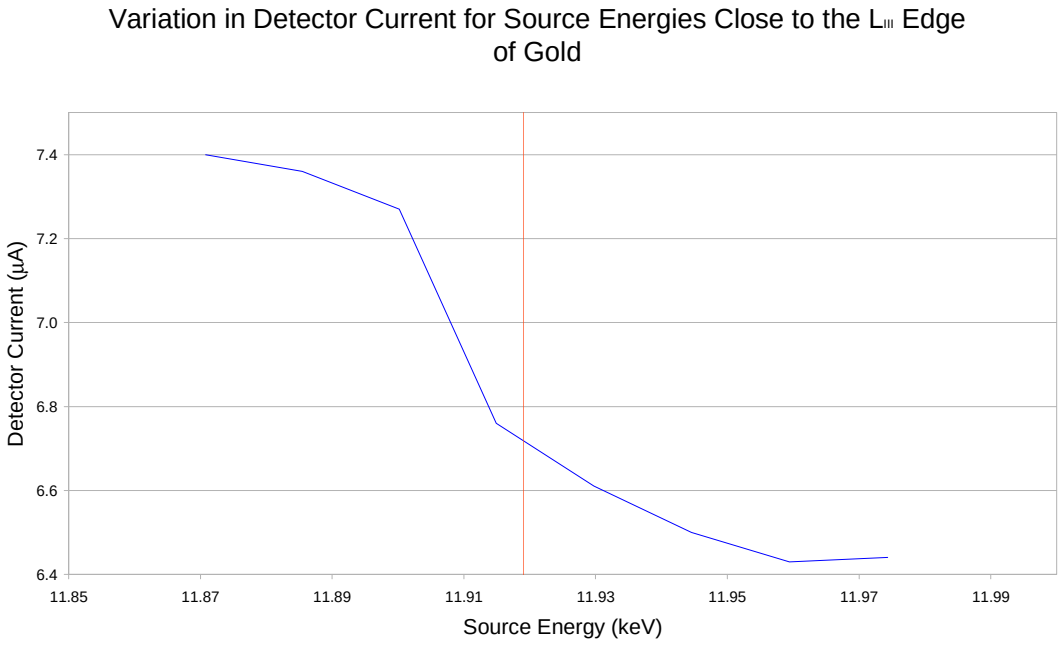

Figure 2.06 - Detector Response in the Energy Range of the L_{III} Edge

From this data, it appears that there is a strong fall in the current through the detector when the source energy is in the region of 11.9 keV, suggesting that there may indeed be gold present in the region of detector. Because of this some of the Monte Carlo models were included that contained small quantities of gold to see if this had an effect upon the energy absorption of this detector.

The final step to characterise the diamond detector was to record the current reading of the detector across a range of different synchrotron radiation energies in order to investigate the effects of source energy. This is useful data because it produces a value that can be directly compared to the energy absorption values produced by MCNP, allowing a direct comparison of the experimental and simulated results. This data is displayed in Figure 2.07.

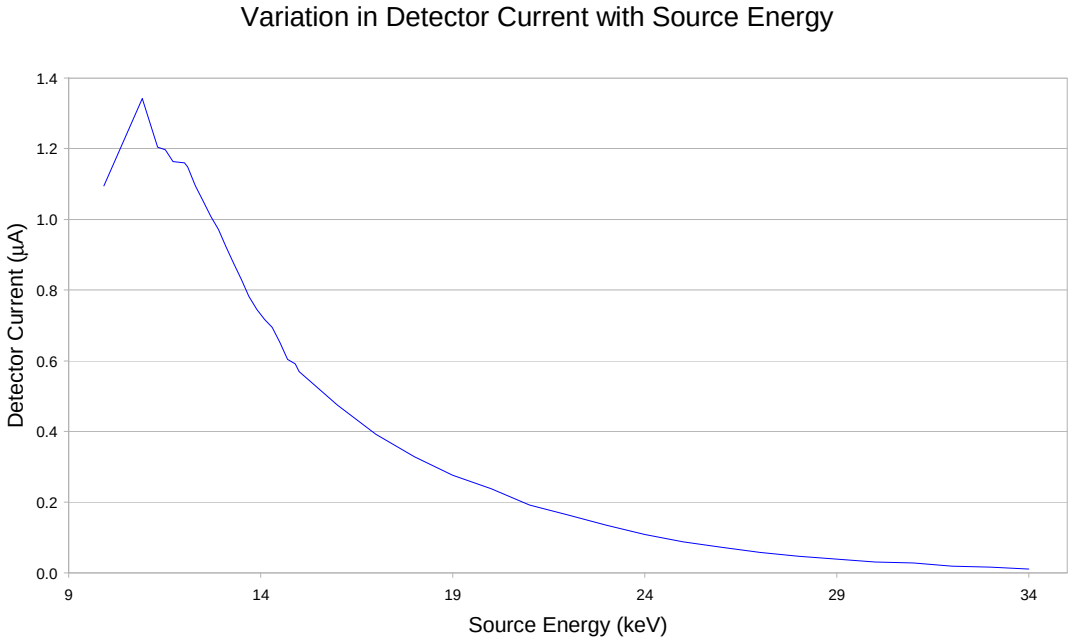

Figure 2.07 - Variation in Detector Current with Source Energy

Figure 2.07 shows that the diamond detector displays a strong absorption of energy at lower energies, with the amount of energy increasing up to a peak at 10 keV, then tailing off. This effect will be partly due to the difference in the probability of interaction between the low energies that have a high likelihood of interaction and the higher energy photons that are likely to pass through without interacting. Another factor is the increase in energy of the secondary electrons, increasing their path length and therefore making it more likely that the particles will exit the crystal and deposit their energy elsewhere.

Now that the energy absorption of a diamond detector had been tested experimentally, the next step was to determine whether MCNP could be used to accurately predict its behaviour.

2.3.2 - Monte Carlo Results

Having tested the diamond detector and its response to synchrotron radiation, the next step was to construct a Monte Carlo model using MCNP and determine the accuracy of the results produced and the effects of the model designs upon the simulated detector response.

First the simpler, homogenised diamond detector model was tested, making use of two

different setups - one with a small quantity of copper (0.15%) and silver (0.35%) present to represent the wiring surrounding the crystal, the other with a pure diamond crystal. The quantities of trace elements present are based upon previous work in this area using the Monte Carlo code EGSnrc by Fathy Saeddi (2006).

Figure 2.08 shows the total energy absorption within the detecting volume of each of the detector models for a source energy range of 5 to 50 keV.

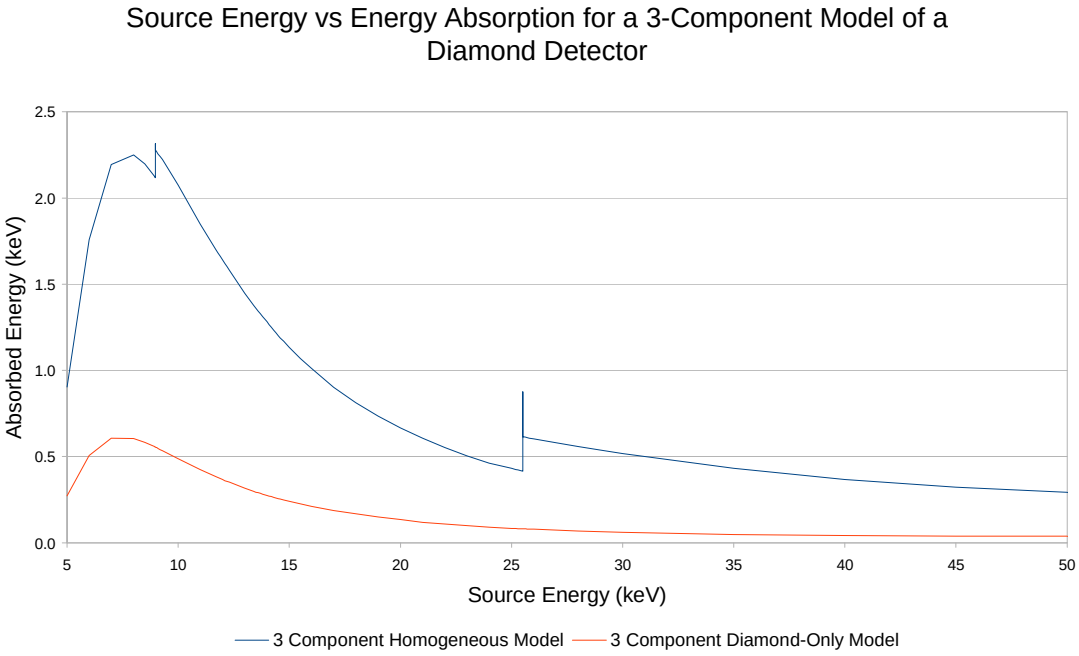

Figure 2.08 - Energy Absorption within a 3 Component Diamond Detector Model

The curves shown in Figure 2.08 show far higher energy absorption within the homogeneous model compared with the simpler diamond only model. It may be that MCNP is overcompensating for the effects of regions that contain high Z elements, as the dose enhancement peaks produced by MCNP seem a lot more exaggerated than those obtained using the more complicated model shown in Figure 2.09.

In order to ascertain the degree to which the dose enhancement observed is due to the algorithms used in MCNP to model presence of high Z elements within a diamond crystal, the complex model was then tested. If the absorption peaks appearing in Figure 2.08 are due to errors in the method used by MCNP to simulate, a complex model that separates the high Z

and low Z components should be closer to the absorption spectra of a real-life detector reading.

Figure 2.09 shows the energy absorption curves produced for a complex MCNP model making use of a range of different contact designs.

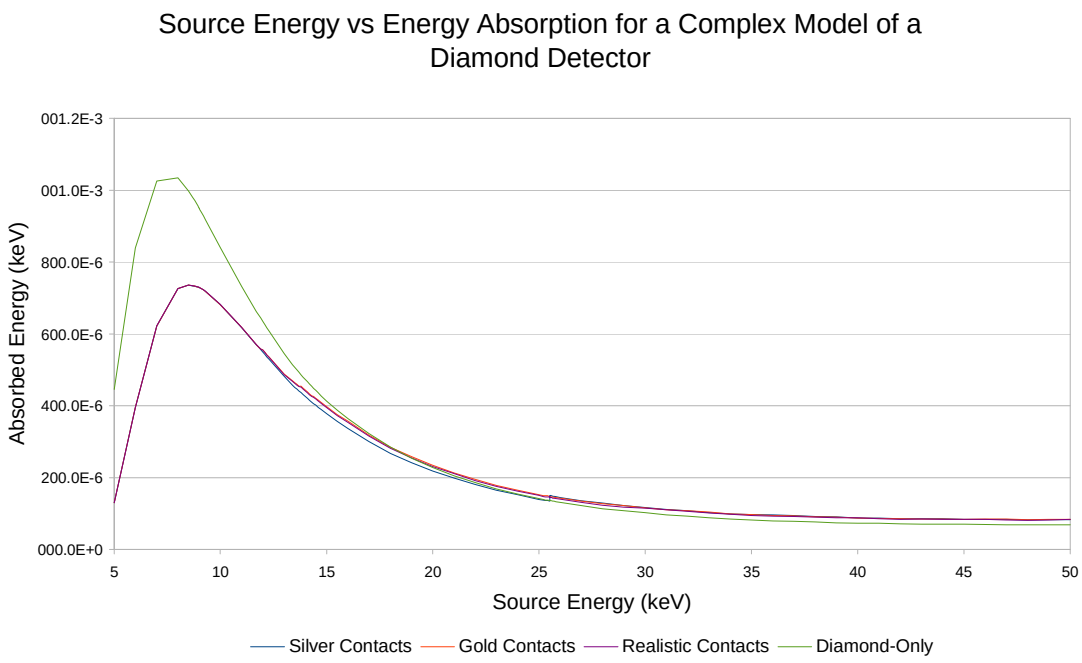

Figure 2.09 - Energy absorption within a Complex Diamond Detector Model

In Figure 2.09, the energy absorption spectra shown are for a diamond detector modelled with gold, silver, gold-tin alloy and TEP contacts. The first thing that can be seen from this curve is that the model which made use of a diamond crystal only with TEP contacts had a larger energy absorption than the other three models. The reason for this difference is that the radiation source was placed above the detector pointing down, so the higher Z contacts will produce a shielding effect on the results obtained. Despite this not being the positioning of the synchrotron beam within the experiment, this set-up allows the effects of dose enhancement caused by the high Z materials to be studied more clearly.

There are no sharp absorption peaks in the data, with no visible difference between the results for the high Z contact models at energies below about 12 keV. There is evidence of the gold contacts adjacent to the detector leading to an increase in the energy absorption within the

detector at energies of about 12 to 25 keV, a pattern also repeated for the realistic contacts. This is entirely to be expected due to the effects of the higher Z elements having a higher probability of interaction with incoming radiation due to the photoelectric effect.

There is less difference between the sets of results with high Z contacts than there is between these results and the tissue equivalent diamond detector. This is most probably because the difference between being in contact with silver (Z=47), tin (Z=50) or gold (Z=79) is less than the difference between the two and carbon (Z=6).

2.3.3 - Comparison of Results

It is essential in any research involving the use of Monte Carlo models that the simulated results be compared with experimental values in order to assess the reliability of the model being used. Figure 2.10 shows a comparison of the two different MCNP models used in this research and the experimental data acquired at the SRS facility synchrotron. Figure 2.10 only gives a rough estimate of the relationship between the Monte Carlo and experimental data, as the analysis is unable to compensate for the variation in intensity in the synchrotron beam caused by the position of the monochromator in the beamline. An attempt to cancel out this effect in the experimental data is found in Figures 2.11 to 2.14, as the diamond detector is compared with an ionisation chamber in the same synchrotron beamline.

Figure 2.10 shows the values for the total energy absorption within the diamond crystal as calculated by Monte Carlo simulation compared with the signal from a diamond detector exposed to near monoenergetic photon radiation from a synchrotron. Due to the differences in scale between the different sets of data, the energy absorption and current values have been normalised such that the largest values are equal to 1.

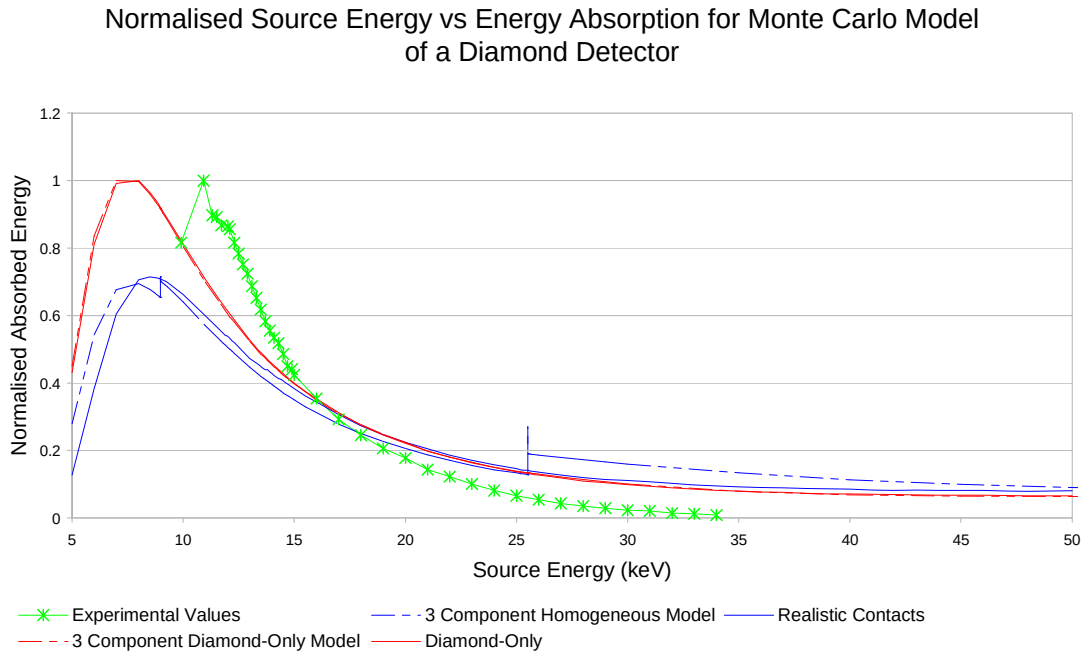

Figure 2.10 - Comparison of Energy Absorption Curves for 2 Different MCNP Models and Experimental Detector Current

Looking at this data, there are several conclusions that can be reached about the usefulness of the Monte Carlo models. First, it is clear that the two different models of a diamond detector that did not make use of high Z contacts produced an almost identical spectrum of energy absorption, with no significant difference in the curve shapes.

Secondly, there is a clear distinction between the two different metal contact models with the 3-component model showing a peak at lower energies, then tailing off at a similar rate with two clear absorption peaks, which are absent from the complex model. As there is no way to verify which of these models is more appropriate to real life situations using only MCNP, the accuracy of these absorption peaks can only be verified by comparison to experimental data.

The experimental data shows a curve of a similar shape to that produced by the different MCNP models although there are differences in the degree to which the curve drops off. This difference is most probably due to the difference in beam intensity caused by the position of the synchrotron monochromator.

It is also possible that this is due to differences in dose response between the simulation and

the experiment. The majority of Monte Carlo codes are designed for use at energies in the MeV region, so there may be some approximations used in the absorption cross-sections used for the simulations that may not be correct.

Finally, having investigated the presence of gold in the diamond detector, it could be seen that the elemental composition estimate for the MCNP model is at least justified by the experimental data, although this does not give the quantities present. Taking this into account, there should be a correlation between the results obtained from the MCNP model and from experimental work unless there are some additional metal elements present within the detector that have not been accounted for. However, trying to detect every likely element on the periodic table would be both time consuming and unnecessary, as any other elements may only be present in trace amounts.

Comparison of Diamond Detector and Ionisation Chamber

In this section the ratio of absorbed energy within a diamond detector to the energy absorption within an ionisation chamber is compared. The results obtained from an experimental investigation of the two types of detector are compared with those obtained from the MCNP models discussed in Section 2.2. The aim of this is to attempt to remove any variation in the synchrotron beamline performance through the comparison with a known detector, in this case a gas ionisation chamber. Investigations such as this can give a great deal of information on factors that need to be taken into account when using a radiation source such as a synchrotron.

In Figure 2.11, the results obtained from an experimental comparison of the two types of detector are compared with results obtained by the simpler 3-compartment model in MCNP.

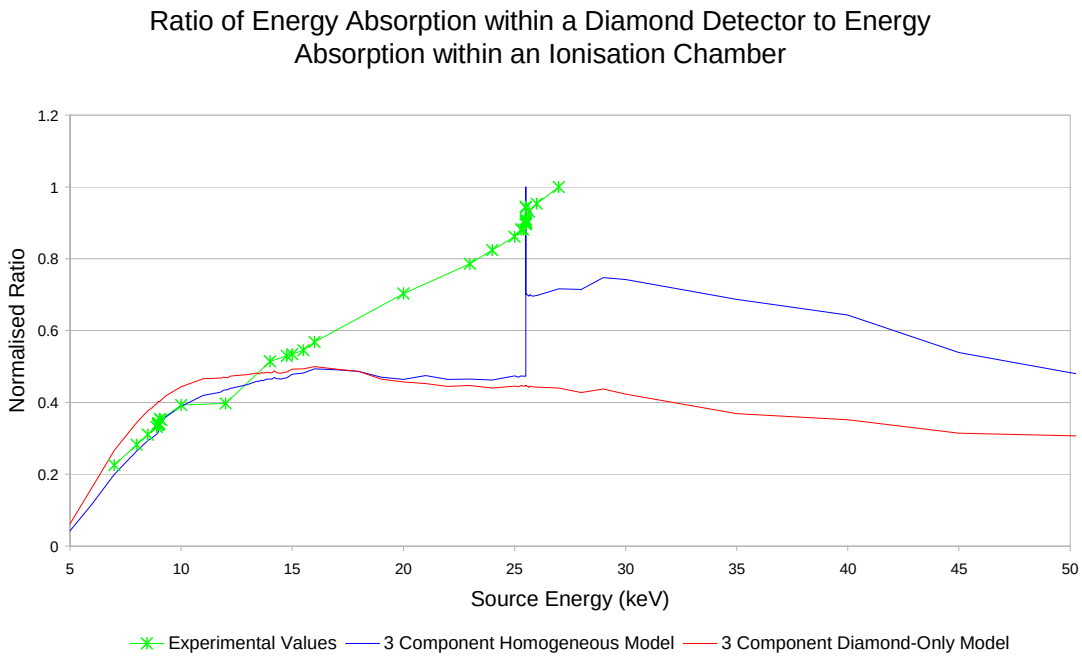

Figure 2.11 - Ratio of Energy Absorption within a Diamond Detector to that in an Ionisation Chamber for a Simple Model

Note that the experimental results have a maximum energy of 27 keV as this was the highest possible energy available from the synchrotron source. As the Monte Carlo codes had no such restriction, their readings were extended to 50 keV to investigate the variation in curve shape due to dose enhancement.

From this information, it can be seen that there is some correlation between the two sets of data, as well as some significant differences. It can be seen that there is more similarity between the experimental data and the homogeneous model (composed of diamond and TEP with some higher Z elements). Both sets of data show a similar increase in energy absorption between 5 and 10 keV as well as a peak at approximately 25 keV, at the silver K edge of 25.514 keV. There is, however, some difference in the ratio of energy absorption that becomes especially noticeable in the region of 15 to 25 keV. This may be due to non-linearities in the diamond detector that are not accounted for in this data comparison, differences in the intensity of the synchrotron beam or possibly errors in the exact elemental composition of the detector.

This set of data shows some clear similarity to earlier work conducted by Saeddi investigating

the use of EGSnrc in the simulation of the diamond detector. It was hoped that the more complex MCNP model could be used to yield a more accurate model of the behaviour of this detector, the two codes are compared in Chapter IV using a proportional counter-based model.

Originally the MCNP model of the ionisation chamber was calculated on the assumption that the detector was designed to be water equivalent. The ratio of energy absorption within a diamond detector model and a water-based ionisation chamber is shown in Figure 2.12.

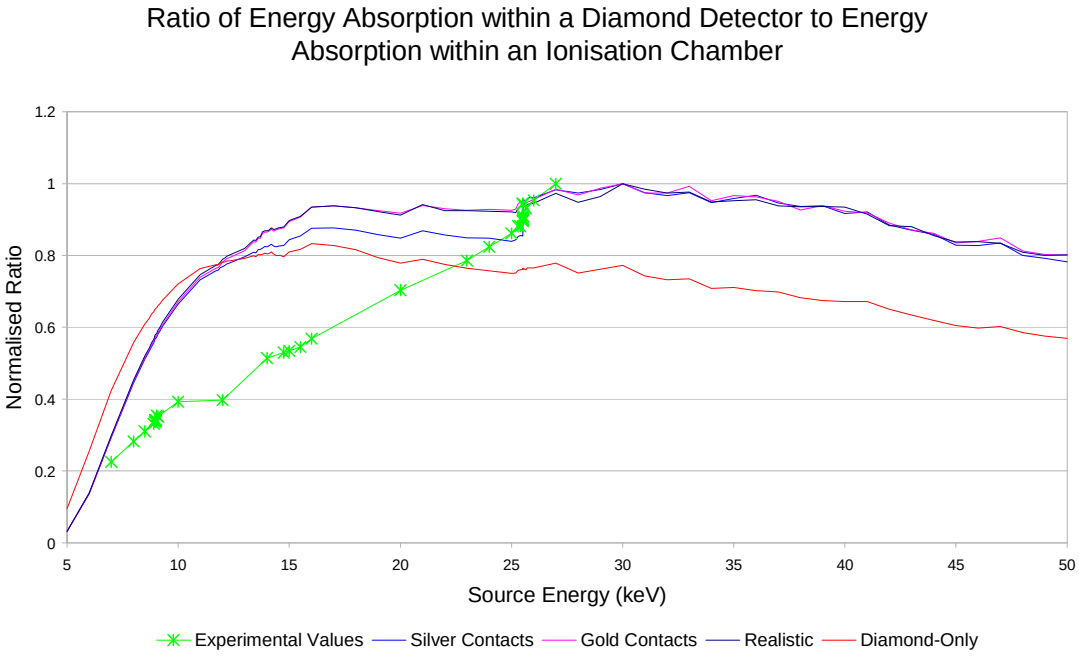

Figure 2.12 - Ratio of Energy Absorption within a Complex Diamond Detector to that in a Water-Based Ionisation Chamber

Looking at this diagram, there are clear differences between the Monte Carlo model and the experimental results. The MCNP models show greater energy absorption at low source energies compared to the water-based ionisation chamber. At first glance, there are some similarities between the two data sets, especially the increase in energy absorption at the silver edge, but the correlation between the two sets of data is less than for the simpler detector model.

Several modifications were made to the detector model to attempt to produce a better correlation between the experimental and MCNP results. These concentrated on potential

mistakes that could have been made in the models, particularly errors in crystal size, wall thickness and elemental composition of detector materials. The alterations to the diamond detector model had very little effect upon the curve produced, resulting in the same energy absorption response, suggesting that these were not the source of the error. More research into the ionisation chamber lead to the suggestion that the chamber was designed to be air equivalent as opposed to the more standard water equivalence, so two new ionisation chamber models were produced. The first model was directly based upon the previous water-based model, substituting pure air for water, with a second model based upon the manufacturer's specifications of detector.

Figure 2.13 shows the ratio of energy absorption within a diamond detector model to that of an air-based ionisation chamber.

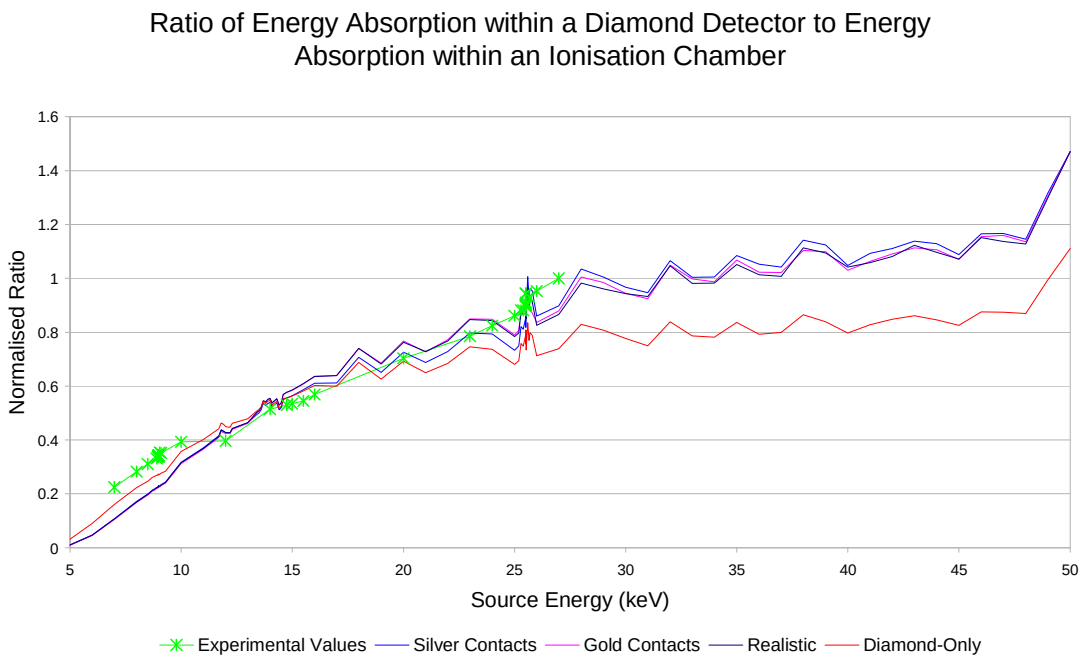

Figure 2.13 - Ratio of Energy Absorption within a Complex Diamond Detector to that in an Air-Based Ionisation Chamber

This diagram gives a much better correlation with the experimental results, showing similar energy absorption at lower source energies and a comparable increase in the number of counts due to the silver edge. There are some slight differences between the experimental results and those obtained through simulation, but they can be partially explained as due to the ionisation

chamber model. Due to the small size of the detecting volume of the ionisation chamber a large number of particles were needed to produce accurate results, leading to longer times being required for the calculations to be performed. This ionisation chamber model took 47 hours and 32 minutes to complete a calculation using the dual core Linux-based computer system available, so it was impractical for more histories to be calculated. It is possible that a model with more histories could produce a more accurate indication of the ratio between these detectors.

The ratio of energy absorption within a diamond detector model and a more complex ionisation chamber model is shown in Figure 2.14. This ionisation chamber model is based upon the materials and dimensions used in the detector.

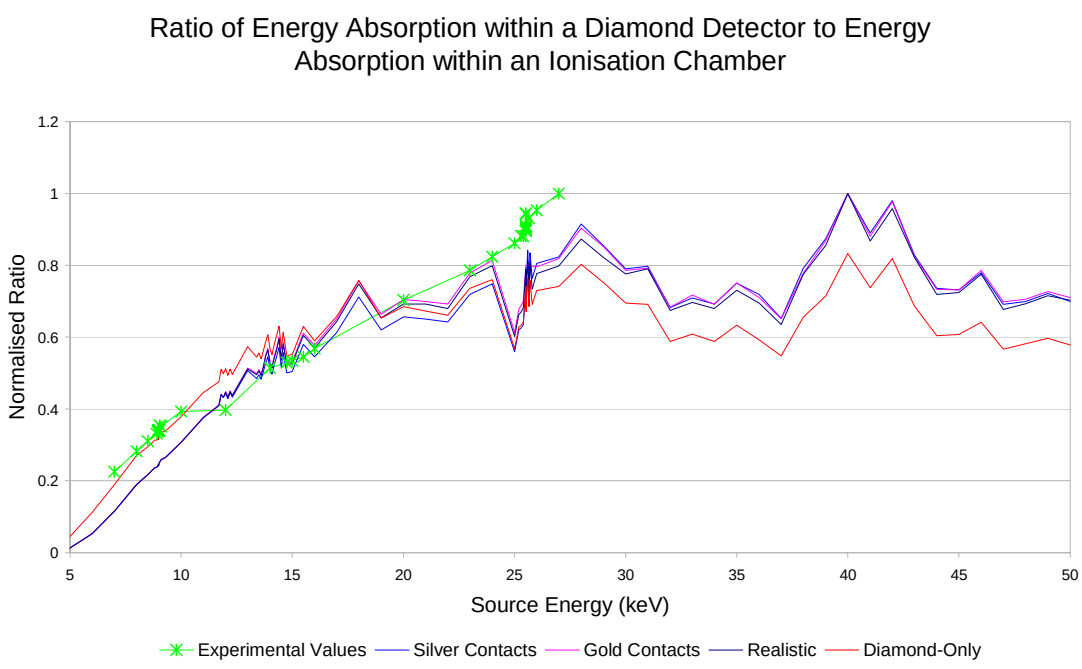

Figure 2.14 - Ratio of Energy Absorption within a Complex Diamond Detector to that in a Complex Ionisation Chamber Model

It can be seen from this figure that although there is a greater correlation between the experimental and simulated detector than obtained in Figure 2.12 with a water equivalent ionisation chamber model it is less clear than in Figure 2.13. There is some similarity between the experimental and simulation data below 20 keV, however the MCNP simulation suggests a lower energy absorption in the region of 25 keV, especially in the region of the silver K edge.

A possible reason for the discrepancy between the experimental results and the simulated models may be due to the high level of inaccuracy in the MCNP data. This was due to the extremely small volume of the detector combined with the complexity of the model leading to an extremely high calculation time. This meant that the level of accuracy possible was extremely limited.

2.4 - Conclusions

Comparing the different results gained from the MCNP modelling to those obtained from experiments there are a number of different conclusions that can be reached about the accuracy of MCNP4C in performing dose calculations at lower energies. One definite conclusion that can be reached is that the design of an MCNP model can have a dramatic effect upon the accuracy of any results obtained from it. Comparing the results from the simple and complex diamond detector models, it seems that a detailed model gives a noticeably better correlation with results produced from experimental work. This is because the effects of dose enhancement from heavy metals in contact with a detector element cannot be easily tested using homogeneous models due to the complexity of the interactions required. Producing an accurate measure of the dose enhancement due to high Z elements adjacent to low Z materials can be overly complicated when the high Z elements are only present within the material.

Also important are the exact materials used in constructing the model, although the complex model has shown that this factor does not have as great an effect upon the final results as was expected. This is because all of the models containing high Z materials produced a similar distribution of energy absorptions at the lower energies measured, only starting to diverge at around 15 keV due to the K and L edges of the metals dramatically increasing energy absorption. This is important, as this shows that any Monte Carlo model of a detector needs to include a close approximation of the real-life elemental composition.

This research also seems to show that MCNP4C is able to accurately model the effects of backscatter from high Z materials placed adjacent to lower Z detecting elements. This is

useful in simulating the types of detector used in medical applications as they are often designed to be tissue equivalent. This can be directly compared with the measurements produced using EGSnrc in Chapters IV and V. One problem with using MCNP4C in the simulation of such complex models, however, is the long calculation times required to produce accurate results. In this situation the time required for the simulation to run meant that the final results had to be of a lower accuracy than would be desirable.

In summary, it seems that MCNP can be used to produce accurate models of the diamond detector, although it is often useful to compare the energy absorption with a standard detector such as an ionisation chamber to compensate for variation in the beam intensity for a radiation source such as a synchrotron.

Chapter III - Fibre Optic Thermoluminescent Device (TLD) Dosimetry

3.1 - Background Theory

3.1.1 - Detector Theory

Inorganic Scintillators

Inorganic Scintillators are a form of radiation detector that exhibit luminescence when exposed to ionising radiation. When impinged upon by an ionising particle, the atoms within the material will absorb some of its energy and re-emit it in the form of (typically) visible light photons, a process known as scintillation. The radiation dose to the detector is determined by measuring the number and energy of the scintillation photons produced when electron-hole pairs, created by the capture of an ionising radiation photon, recombine at activation sites in a process known as prompt fluorescence. As the scintillating material captures ionising radiation, electrons are excited from the valence band to the conduction band of the material. This will happen as long as the energy captured is enough to excite the electron across the band gap, which is shown in Figure 3.01a.

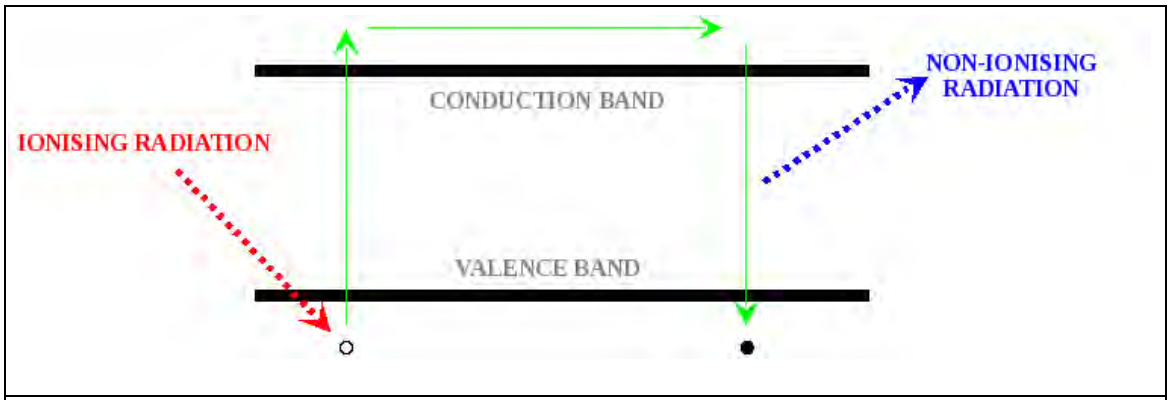

Figure 3.01a – Interaction between a Scintillating Material and Ionising Radiation

Impurities are added to the scintillating material to create electronic levels within the band gap, known as exciton bands (excitons being the loosely-bound electron-hole pairs created by the excitation of the electrons). These exciton bands allow electrons to be excited from the valence band at a lower energy and the radiation emitted from the de-excitation will have a

different, lower energy than that emitted from de-excitation from the conducting band. By adding different dopant materials, the energy of the emitted radiation can be varied to a wavelength that is more transparent within the scintillating material, as well as potentially increasing the stopping power of the scintillating crystal. The effect of dopant materials is shown in Figure 3.01b.

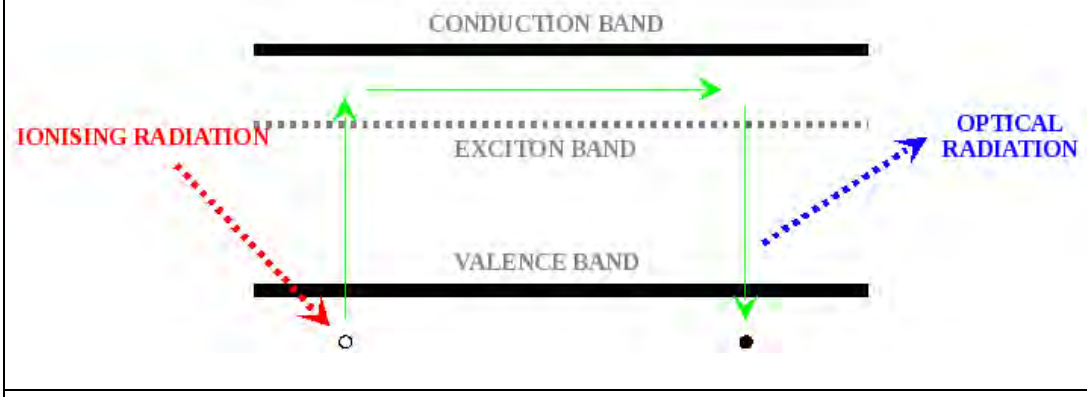

Figure 3.01b – Effects of Dopant Materials Upon A Scintillator

An important factor in choosing a material for a scintillation detector is finding a dopant which will produce prompt fluorescence with as little a delay between absorption of ionising radiation and emission of optical radiation. ThermoLuminescent Devices (TLDs) on the other hand, are designed to 'trap' the incoming ionising radiation, so that reemission can occur at a later time, usually due to thermal excitation.

Thermoluminescent Dosimeters

The optic fibre thermoluminescent devices used in this research are constructed of a silicon-based glass, which has an amorphous structure. In most silicon materials, the silicon forms four bonds with surrounding atoms, producing a regular, crystalline structure. In its amorphous form, however, the bonds form a continuous random network with some silicon atoms left with so-called 'dangling bonds' leaving them with an unsatisfied valence bond.

The behaviour of amorphous structures are less well understood than the crystalline materials, so the background information described in this section is based upon the behaviour of crystals, but the principles described here will apply to the optic fibres. This is because the

migration of electrons from the valence band to the conduction band will determine the energy absorption within the material, and thermal excitation is still used to produce a measurement.

TLDs, are designed specifically to promote electron-hole trapping within the material, using different impurities within the compound's structure to increase the concentration of trapping centres within the bandgap of the material. In the Figure 3.02a the effects of ionising radiation upon the electrons within a material are shown for a TLD.

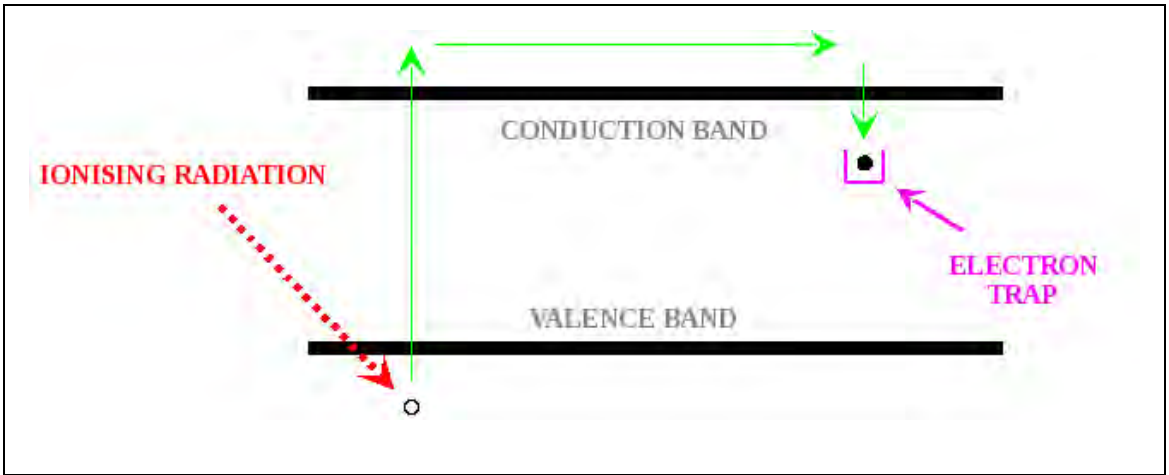

Figure 3.02a – Interaction between a Thermoluminescent Material and Ionising Radiation

As the diagram shows, in a TLD material, some of the electrons are excited from the Valence to the Conduction band through the absorption of energy from the ionising radiation. Instead of returning to the Valence band and releasing the energy they have gained, they become captured by the trapping centres in the structure of the material. This effect becomes more important when the distance between the Conduction band and the Electron Trap are greater, as the probability of the electron escaping the trap over a particular time period due to thermal excitation becomes smaller.

Because of this, a TLD exposed to a large dose of ionising radiation will only yield a proportionally small amount of scintillation light compared to an inorganic scintillator, but will build up a large number of electrons within the trapping centres of the material that is proportional to the amount of energy deposited within the material. The holes within the

material are similarly trapped within the structure through a process analogous to that of the electrons. Free holes will then migrate through the material's structure until they reach a trap with energy significantly greater than that of the Valence band, then the hole can migrate no further.

Within a TLD material, the radiation dose is proportional to the number of electron-hole pairs produced, with a relationship dependant upon the number of photons incident upon the material. The binding energy of the electrons within the TLD and the probability of photon capture, allow a calculation of the energy deposited in the material, up to a point at which the number of trapping centres within the material become saturated.

After a TLD has been irradiated, thermal excitation is used to release the electrons captured in the trapping centres of the materials, producing scintillation photons that can be measured to provide an indication of the radiation dose to the material. The material is thermally excited by gradual heating to a temperature determined by the energy gap between the trapping centres and the Valence and Conduction bands, as shown in Figure 3.02b.

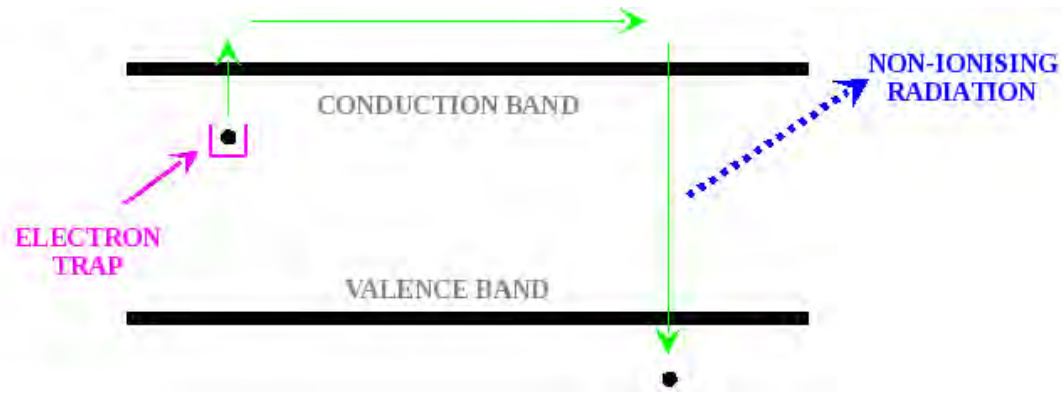

Figure 3.02b – Thermal Excitation of a TLD Material

As the electrons gain the thermal energy needed to re-excite back to the Conduction band, they become able to migrate to the site of a trapped hole - here they can become recaptured, leading to the emission of a scintillation photon. These scintillation photons are then converted into an electrical signal using a photomultiplier tube within the heater, producing a single count for every photon released from the material. The total radiation exposure of the

TLD is therefore proportional to the integral of the number of counts contained within the glow curve from this heating process. A final energy absorption figure can then be determined by comparison with calibration detectors or through Monte Carlo simulations.

For the research contained in this thesis, two types of optic fibre TLD were used - one doped with a low concentration of Erbium and the other doped with a low concentration of Germanium (both doped to levels of less than 1,000 ppm), both of which are used to a limited extent by the optic telecommunications industries. The glass which forms the basis of the optic fibres is a high purity silicon oxide, with the dopant added to increase the refractive index of the glass, reducing the attenuation of the signal as it passes through the fibre. When used as a TLD, the dopant acts as an impurity, or activator, for the material, allowing it to trap charges within the material structure.

3.1.2 - The TLD as a Dosimeter - A Summary of the Capabilities of TLDs

TLDs are widely used for radiation protection due to several advantages they possess over other dosemeter designs, these properties allow them to be used in a number of different applications, some of which will be discussed in this section.

One of the main advantages of a TLD over any other type of detector is its small size, which has allowed TLDs to be placed in a variety of useful locations. One example is on the tips of the fingers in gloves for use by radiation handlers, where a larger, electrically-powered detector design would be impractical. This lack of a need for a power source within the detector has allowed the size of a TLD to be reduced to almost any size necessary for the application, allowing radiation dose to be monitored in places that were previously inaccessible

In addition to this, TLDs are reusable, making them cost-effective as a dosemeter, especially as the lack of moving parts within the TLD itself makes their manufacture extremely simple compared to other detector designs. As the optic fibres used for this research are manufactured for use within the telecommunications industry, this means they are produced to exacting standards, but also are still relatively cheap and easy to maintain.

A final advantage of TLDs as a detector is that they are capable of dealing with a very high radiation dose without serious damage, as there is little within them to be damaged. Their only limitation in high strength radiation fields is that there is an upper dose for readings, determined by the density of the trapping centres within the material.

The TLDs investigated have their limitations, however, and have a number of factors that need to be considered compared with other radiation detection designs.

One factor, which needs to be considered in their use, is the lack of an instant readout. Each optic fibre TLD needs to be individually examined in a TLD reader after irradiation, meaning that there is no possibility of monitoring them within a real-time situation. This means that they would be of limited use for monitoring in an environment where the radiation levels were high enough to cause damage to an individual, as they would give no warning of potential risks until long after exposure. This could be a problem for some applications, such as radiotherapy or at nuclear power locations.

Another limitation of TLDs is when it comes to monitoring humans is their lack of tissue equivalence, which prevents them from giving a direct measure of the harmfulness of a radiation source. Factors can be included into the calculation to compensate for this, but they would need to be calculated for different radiation fields and tissue types.

The final major flaw of most TLDs is that the materials they are constructed from tend to be relatively soft and crystalline, making them fragile compared to some other detector designs and reducing the number of applications for which they are useful. The SiO_2-based optic fibres reduce this problem somewhat due to the relatively robust nature and high melting point (~1000 °C).

By and large, these problems can mostly be avoided by using alternate detector designs which limit their inherent problems. In uses where these problems cannot be overcome, there are usually adequate radiation monitoring tools already available that can do the job instead. Most TLDs are therefore used in applications where their potential advantages far outweigh their

disadvantages, ensuring that TLD-based dosimetry will be around for many years to come.

3.1.3 - TLD Design & Operation

For the experimental work used in this thesis, we devised a simple set-up designed to recreate the same conditions easily and keep conditions constant. Two types of optic fibre cable were used, both of which are found within the telecommunications industry, one doped with Erbium, and another doped with Germanium. These were chosen because they had shown promise in previous work (for example Abdullah et al, 2001; Yusoff et al, 2005) and were relatively easy to obtain.

The fibre optic cable was sliced carefully into approximately 10 millimetre sections using a sharp scalpel and then the outer plastic cladding was removed, exposing the silicon oxide fibre. These 10 mm sections were then arranged into groups of five and held into place using a cellulose-based adhesive tape, placed approximately 2 mm from each other. This minimised the amount of fibres lost through handling and allowed the conditions to be replicated fairly consistently. This set-up is shown in figure 3.03.

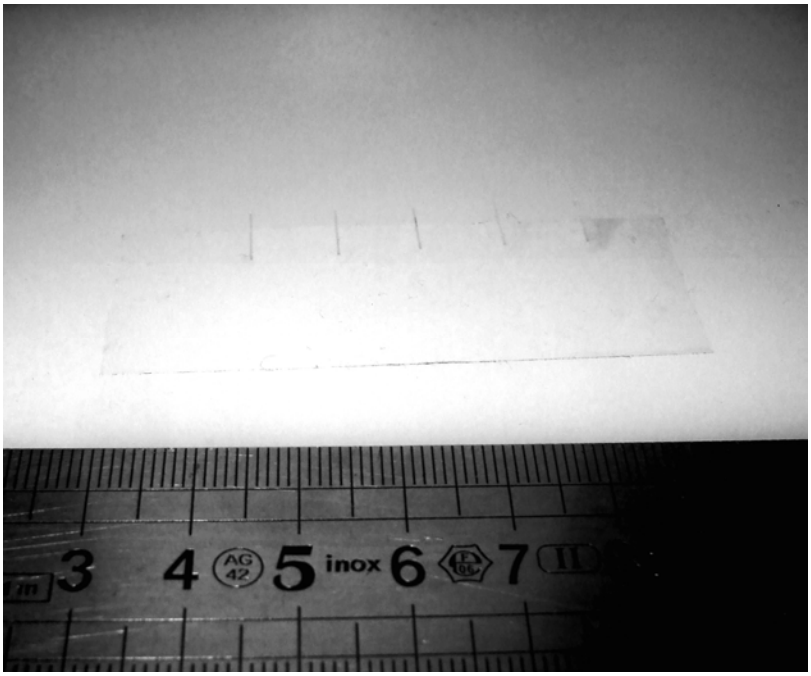

Figure 3.03 – Experimental Set-Up used for Optic Fibres

In Figure 3.03 the arrangement of the five optic fibres is shown attached to a piece of Tissue Equivalent Plastic. The rule is included to give an indication of the scale of the experimental set-up.

These strips, each containing five optic fibres, were then positioned between two 10 mm thick pieces of tissue-equivalent plastic to allow a build-up of secondary electrons before the radiation field passed through the optic fibres. This arrangement of optic fibres was then placed with the centre of the five-fibre strip in the centre of the radiation beam for a ten minute exposure.

All of the experimental work was conducted at Station 16.3 at the SRS Facility, Daresbury, using a ~12.0 mm by 1.0 mm monoenergetic synchrotron beam directed at a simple fibre optic array (for a description of the characteristics of Station 16.3 see Collins et al, 1998). The table the TLD was mounted upon was then moved vertically over a distance of 10.0 mm during the course of the irradiation to produce a uniform irradiation of the optic fibre. This data was then analysed using a ToLeDo TLD reader set to a peak temperature of 280°C with a cycle lasting 256 seconds, a ramp rate of 10°C per second and a nitrogen gas flow rate of 400cc/min. These reading were then compared to background readings obtained using the same settings, but without an optic fibre present.

Figure 3.04 shows the glow curve for Germanium-doped optic fibres subjected to a variety of different source near-monoenergetic energies at the SRS Facility Synchrotron. The data made use of the standard set-up described above, showing the time delay as the equipment heated up to a high enough temperature for thermal excitation to occur.

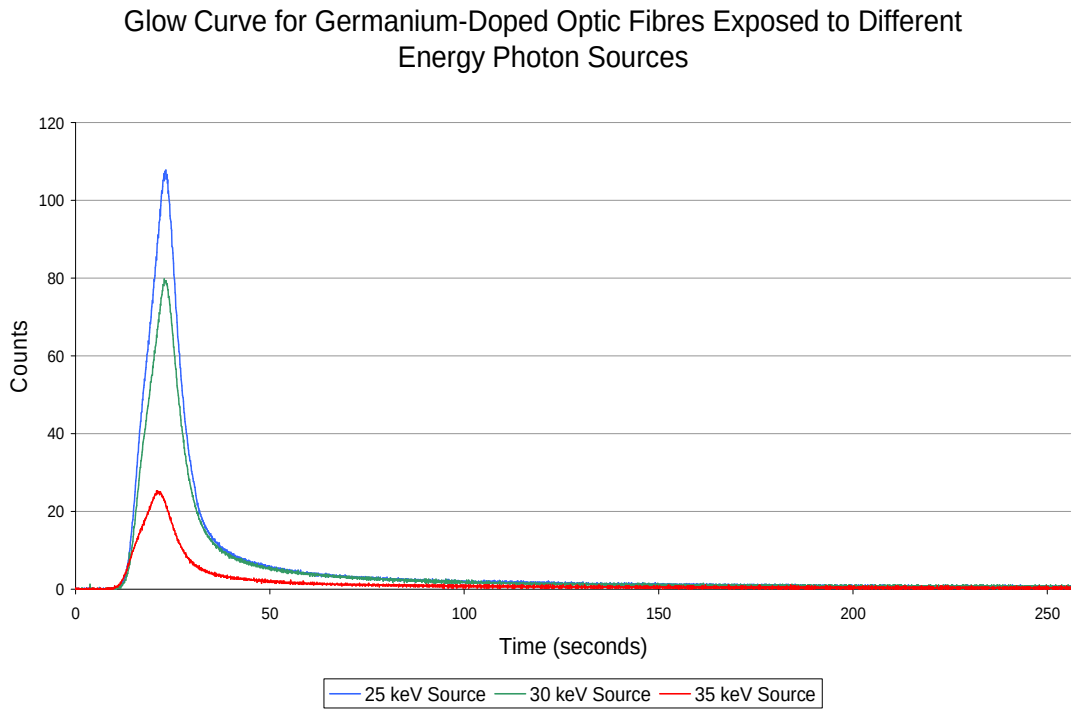

Figure 3.04 - Glow Curve for a Germanium-Doped Optic Fibre

3.2 - MCNP Modelling of the Thermoluminescent Detector

The MCNP models were designed to replicate the ideal experimental set up as closely as possible, using the dimensions shown in Figure 3.05.

This model was based upon a simplified version of the set-up used for the experimental work with five 10 mm optic fibres composed of silicon oxide, containing a low level of dopant material (either Erbium or Germanium). These were set within a block of Tissue Equivalent Plastic and contained a thin layer of cellulose covering the bottom half of each fibre. The elemental composition of the materials used is described in Appendix II, Table x2.01, and an example MCNP input file is included in Appendix IV Example 4.4.

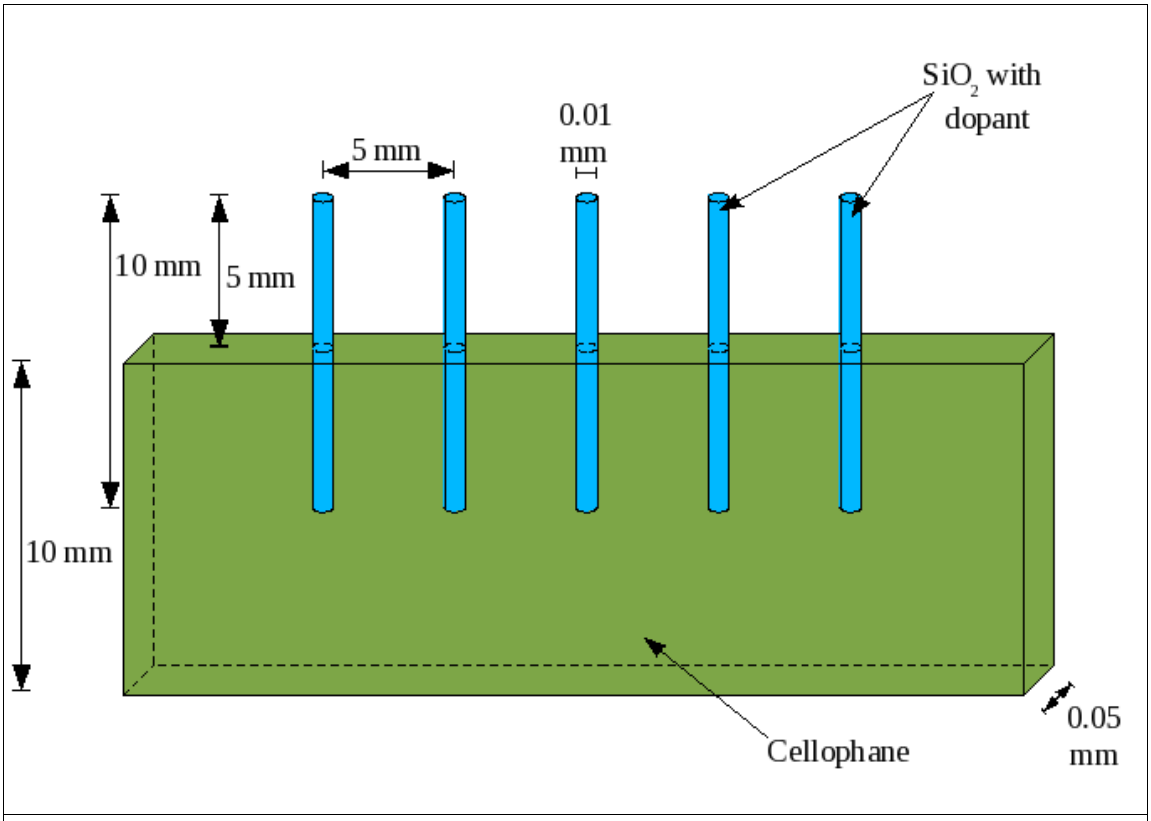

Figure 3.05 – MCNP Model of the Optic Fibre's Experimental Set-Up

The 0.1 % dopant level used in the simulations was chosen as the level of dopant within the fibres was unknown at the time the simulations were designed. Since then, further research (for example Asni et al, 2011) has suggested that a figure of 0.2% would have been closer to reality. Despite this, the patterns produced through the Monte Carlo program will give an indication of the underlying trends in energy absorption within a doped optic fibre, even if the energy absorption suggested is higher than would be received experimentally.

This was then exposed to a mono-energetic photon beam with an energy of between 7 and 30 keV to give an impression of the energy absorption to be expected within the detector over the range available at the Synchrotron where the experiment was conducted. MCNP then recorded the energy absorption of the optic fibres at each of these energies using a *F8 tally, looking at steps of 1 keV across most of the spectrum, but decreasing to 0.1 keV steps close to the K and L edges of Erbium and Germanium.

The energy absorption within the detector volume for the TLD optic fibres is a good measure

of the dose response. This is due to the fact that the number of electrons trapped within the structure of the material, as well as the number of photon emissions when heated, is also proportional to the energy absorption of the TLD material.

Errors

Table 3.01 summarises the relative errors found in the MCNP results, as calculated by the program, although the errors in the diamond detector data used for comparison purposes is included in Chapter II Section 2.2. These calculations were performed for 5,000,000 histories.

Monte Carlo Model	**Relative Error**				
	10 keV	**20 keV**	**30 keV**	**40 keV**	**50 keV**
Optic Fibre - Pure Silicon Oxide	0.062	0.240	0.461	0.664	0.554
Optic Fibre - Silicon Dioxide + Erbium	0.051	0.151	0.316	0.541	0.495
Optic Fibre - Silicon Dioxide + Germanium	0.061	0.171	0.343	0.557	0.489
Optic Fibre - Tissue Equivalent Plastic	0.083	0.277	0.489	0.450	0.469

Table 3.01 - Summary of Errors in Monte Carlo Calculations of Optic Fibre TLDs

The first thing that is noticeable about these errors is that compared with those in Chapter II Section 2.2, they are significantly higher. This is in part due to the smaller size of the optic fibres compared with the diamond detector, reducing the number of interactions within the individual fibres, making the results less accurate relative to each other. Due to the photoelectric effect the errors at lower energies are related to the atomic numbers of the material the optic fibre is composed of, due to the greater relative accuracy when there are larger numbers of particles. Because of this, the relative error is lower in the erbium-doped fibres (highest Z = 68), then the germanium-doped fibres (highest Z = 32), then the pure silicon dioxide fibres (highest Z = 14), and finally the TEP optic fibres, which are composed primarily of carbon and hydrogen.

3.3 - Results

3.3.1 - Experimental Results

The data obtained from the irradiation of the fibre optic TLDs using the SRS facility at Daresbury is shown throughout this section. Tables 3.02a and 3.02b show the raw experimental data acquired at the SRS Facility at Daresbury. The data in these tables was used to produce the figures included in this section. Figures 3.06a and 3.06b show the number of counts obtained from the TLDs as a product of synchrotron beam energy, a raw measure of the energy absorption within these detectors. Figures 3.07a and 3.07b show the normalised ratio of counts from a TLD relative to the dose obtained in a diamond detector at the same energy, with respect to the synchrotron beam energy. Finally, figure 3.08 shows the normalised results on the same axes, in order to allow the shapes of the curves to be compared.

The most noticeable feature of the experimental data is the extreme variability shown in the readings, decreasing the degree of reproducibility in the results. This seems to be due to the low count rates obtained for both sets of optic fibres, especially as their small size makes it difficult to uniformly irradiate them. Despite this, there are some clear patterns that can be observed, and it would be possible to minimise the variability in future experimental work in this field.

For tables 3.02a and 3.02b, several factors have been included, which have been used to produce the following graphs. The first column in the table shows the energy of the synchrotron beam during the irradiation in keV. The second column shows the average number of counts obtained from the five TLDs that were exposed to the synchrotron beam, with the third and fourth columns showing the maximum and minimum number of counts respectively. As the count rates obtained using the TLDs are being compared to a standard detector (in this case a diamond detector) for Figures 3.07a and 3.07b, the fifth column shows the current detected by the diamond detector whilst in current mode. The final column gives the number of counts from the TLDs divided by the current in the diamond detector and

normalised to the maximum value, giving a ratio of the detector responses. Note that the count rates for the optic fibre TLDs include the Synchrotron Beam Correction Factors described in Chapter I, section 1.4.4.

Energy (keV)	**Average Number of Counts**	**Maximum Number of Counts**	**Minimum Number of Counts**	**I_0/Diamond Detector Reading (μA)**	**Normalised Detector Response**
9	819	1,183	398	0.816	0.030
10.0	2,207	3,218	1,665	1.007	0.065
12.0	2,639	2,813	2,413	1.533	0.051
14.0	1,546	2,321	996	2.334	0.020
16.0	2,773	3,445	2,138	0.479	0.170
16.0	1,073	1,274	945	0.479	0.066
18.0	1,335	1,505	1,208	0.307	0.128
20.0	1,565	2,018	1,253	0.197	0.234
22.0	1,575	2,360	1,058	0.126	0.367
24.0	1,280	1,557	905	0.081	0.465
26.0	1,465	1,752	1,271	0.052	0.829
28.0	1,133	1,295	950	0.033	1.000

Table 3.02a – Raw Data From Erbium-Doped Optic Fibre TLD

Table 3.02a and Figure 3.06a show the results from the Erbium-doped optic fibres in relation to the energy of the synchrotron beam. The Erbium results show a maximum number of counts only twice that of the of the background readings from the TLD reader, as well as a large degree of variability, probably due to the fluctuations in the background readings from the TLD reader.

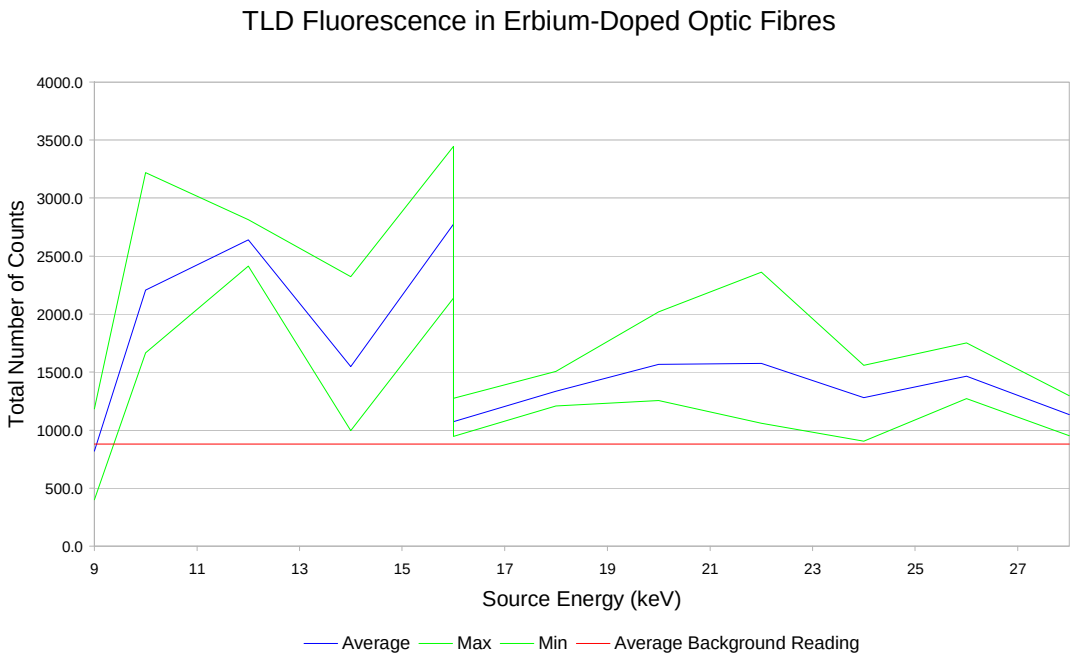

Figure 3.06a – Detector Response of Erbium-Doped Optic Fibres

The figures show the average number of counts for the TLD at that source energy in blue, with the maximum and minimum values in green either side of the average value. This method was chosen because the small numbers of results being obtained meant there were not enough values to produce a statistically valid standard deviation. This would give a visible indication of the variability inherent in the measurements. The red line shows the average background number of counts produced by the TLD reader when a fibre is not present.

Table 3.02b and Figure 3.06b show the results from the Germanium-doped optic fibres in relation to the energy of the synchrotron beam.

Energy (keV)	Average Number of Counts	Maximum Number of Counts	Minimum Number of Counts	I_0/Diamond Detector Reading (μA)	Normalised Detector Response
8.000	9,230	9,824	8,635	0.741	0.022
9.000	29,460	37,199	21,721	0.908	0.056
10.000	22,658	44,315	1,001	1.007	0.035
10.083	885	1,523	247	1.024	0.001
11.094	39,417	39,897	38,936	1.411	0.043
11.111	48,620	50,331	46,909	1.406	0.053
11.123	2,419	4,637	201	1.415	0.003
11.870	2,100	2,214	1,985	1.197	0.003
12.000	40,561	44,457	36,665	1.165	0.054
15.000	16,145	29,438	2,852	0.617	0.042
17.500	35,986	37,422	34,549	0.363	0.163
20.000	19,046	20,368	17,724	0.214	0.151
22.500	21,612	21,974	21,249	0.126	0.298
25.000	15,551	36,122	504	0.074	0.373
27.500	12,330	15,851	8,809	0.044	0.516
30.000	12,646	18,019	6,444	0.026	0.921
32.500	5,076	6,082	4,069	0.015	0.644
35.000	4,522	11,599	304	0.009	1.000

Table 3.02b – Raw Data From Germanium-Doped Optic Fibre TLD

Looking at the results for the Germanium-doped optic fibres it appears that they possess a higher count rate than those which were Erbium-doped, reaching a maximum peak with a count rate over twenty times that of the background and four times the background levels at its lowest points.

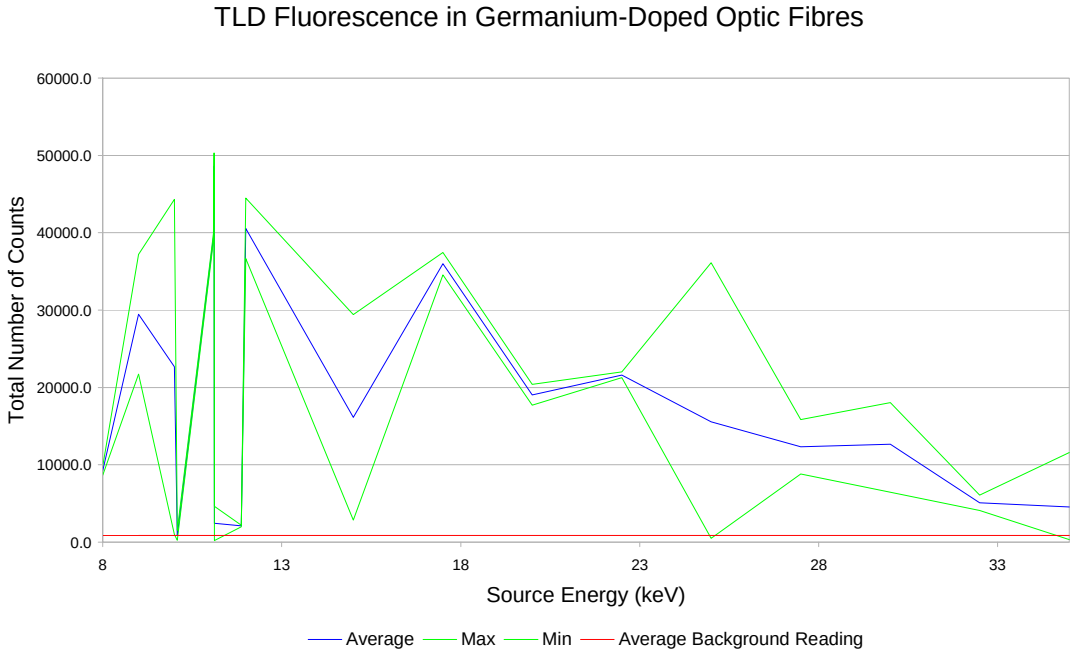

Figure 3.06b – Detector Response of Germanium-Doped Optic Fibres

Although these results are limited by the low number of readings obtained, some patterns can be seen in the data, allowing an evaluation to be made of the usefulness of this technique as a measure of radiation dose. The results show that optic fibres with Erbium and Germanium dopant yielded a larger number of counts when irradiated compared to the non-irradiated fibres, showing that they can produce readings substantially larger than background levels.

The next step is to compare the results for a TLD detector to those of a known detector (in this case the diamond detector from the previous chapter), producing a detector response curve, where the number of counts is divided by the current for the diamond detector. This will give an indication in the difference in energy absorption between the two different detector designs, specifically in this case, between a high Z and a tissue equivalent solid state detector. This is shown in Figures 3.07a and 3.07b. As well as this, a comparison with a reference detector on the same beamline will cancel out any changes in beam intensity caused by the position of the monochromator.

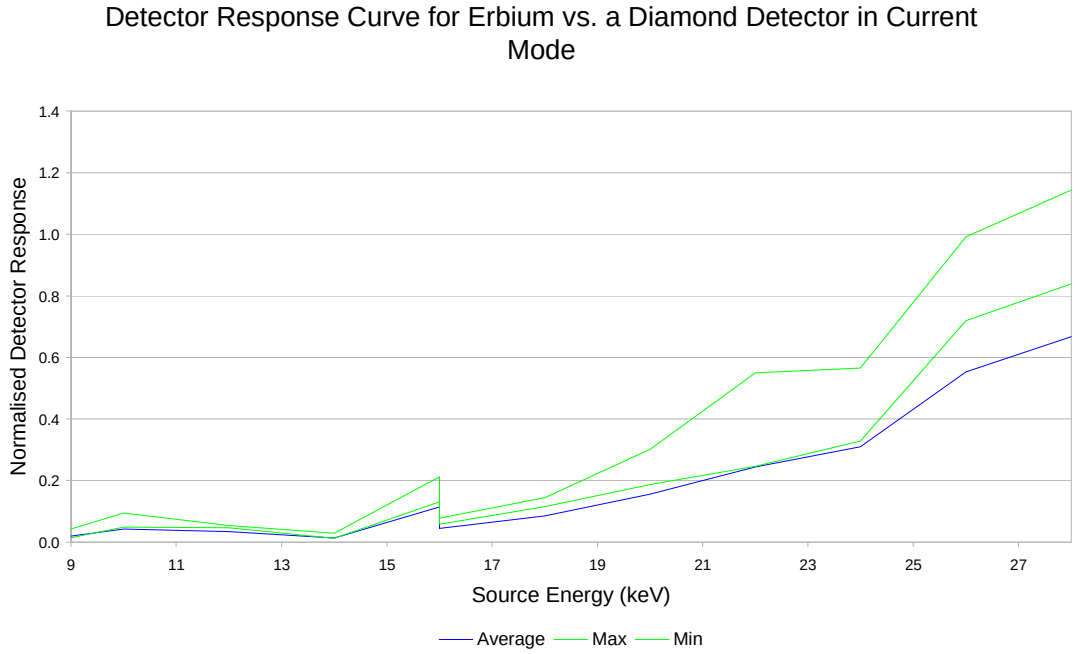

Figure 3.07a – Detector Response of Erbium-Doped Optic Fibres Compared to a Diamond Detector

Figure 3.07a shows that compared to a diamond detector, an Erbium-doped optic fibre has a significantly lower drop-off in energy absorption as the source energy increases. This may be an artefact of the low number of readings and large degree of variability in the readings, as they seem to plateau in Figure 3.06a, whereas the more accurate diamond detector readings show a definite drop-off in energy absorption as the energy increases.

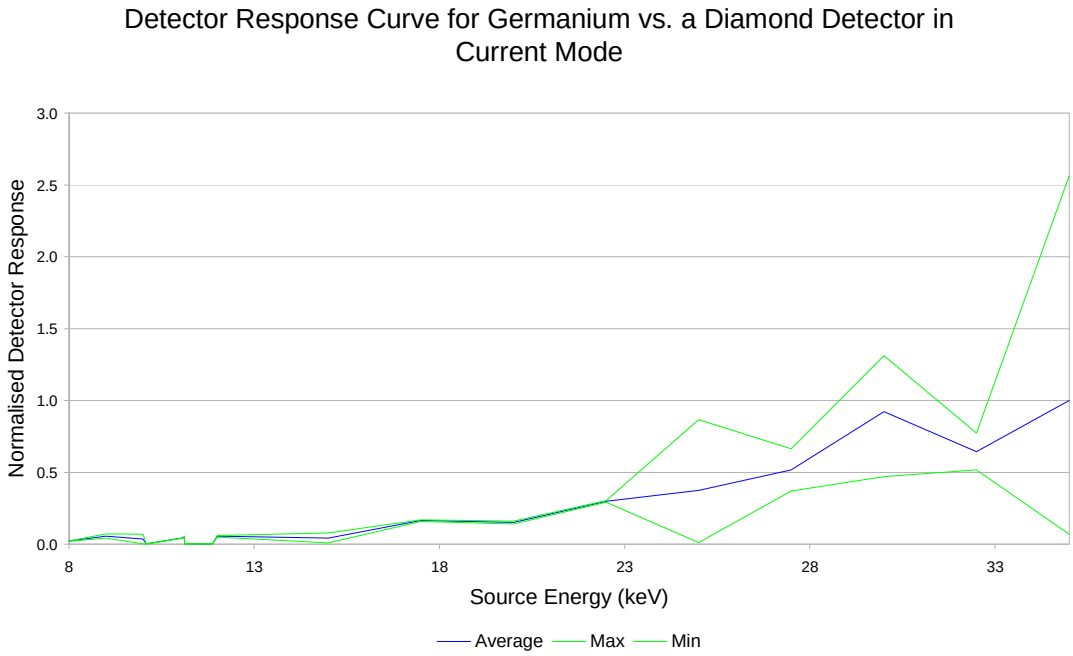

Figure 3.07b – Detector Response of Germanium-Doped Optic Fibres Compared to a Diamond Detector

Figure 3.07b shows a similar effect to Figure 3.07a, the main difference between the two sets of data being the greater degree of variability in the readings as the energy of the source beam increased. This similarity is to be expected, as the shape of the curve will largely be determined by the silicon dioxide glass present in the optic fibre.

Figure 3.08 shows a comparison of the detector responses of the Erbium-doped and Germanium-doped optic fibres, both in relation to the current recorded by a diamond detector subjected to the same source voltage.

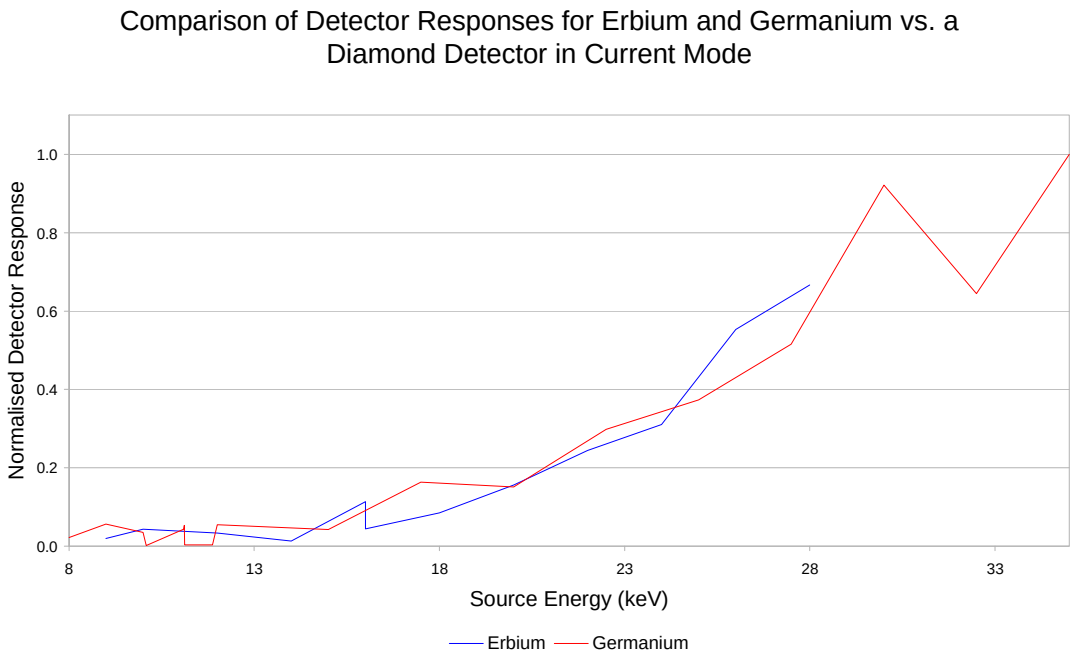

Figure 3.08 – Comparison of the Detector Response of Erbium- and Germanium-Doped Optic Fibres Compared to a Diamond Detector

From the data we have produced, it appears both sets of optic fibres have similar absorption characteristics, far too similar to be able to find any concrete differences from these readings. The much higher count rates obtained for Germanium, however, suggest that it may be more sensitive to the radiation levels being encountered in this research, despite the similarity in curve shape.

The results may suggest that the Germanium-doped fibres may be the more useful of the two for dosimetry at the dose levels being studied, but further research would be needed to find more effective dopant elements for a medical use. Even the Germanium-doped optic fibres showed a fluctuation of ± 75% in some readings. The fluctuations could also have been reduced somewhat had more readings been taken, perhaps by increasing the number of optic fibres within the array to ten or more.

Improvements could also be made to the method used for reading them as a number of optic fibres were lost within the machine, due to the nitrogen flow for the system sometimes driving the fibres deeper into the machine where they were lost. Other techniques such as making use of laser-based TLD readers could yield more reliable results.

Another factor which was not taken into account is that the production of the fibres does not result in an even distribution of dopant throughout the material. This can lead to sections of the optic fibre having no dopant present, producing ‘dead’ fibres where thermoluminescent excitement does not take place. Subjecting a large sample of optic fibres to a uniform irradiation then rejecting any fibres that produce a high enough signal would have improved the quality of the results substantially.

3.3.2 - Simulated Results

Initial Testing of the MCNP Code

The model of the components of the optic fibre used for this section is described in detail in section 3.2. This made use of the same photon energies and source position as the simulations used in Chapter II, section 2.2. This section tested the possibility that because MCNP does not simulate fluorescence within the material, the MCNP results may not be comparable to the experimental results. This technique may, however, give some indication of the trends in energy distribution, possibly offering information that can be hard to obtain experimentally.

The results obtained from this MCNP run are shown in the energy absorption spectrum in Figure 3.09, with the blue line denoting a pure silicon oxide optic fibre, the green and purple lines showing optic fibres containing a dopant element and the red line representing a Tissue Equivalent optic fibre.

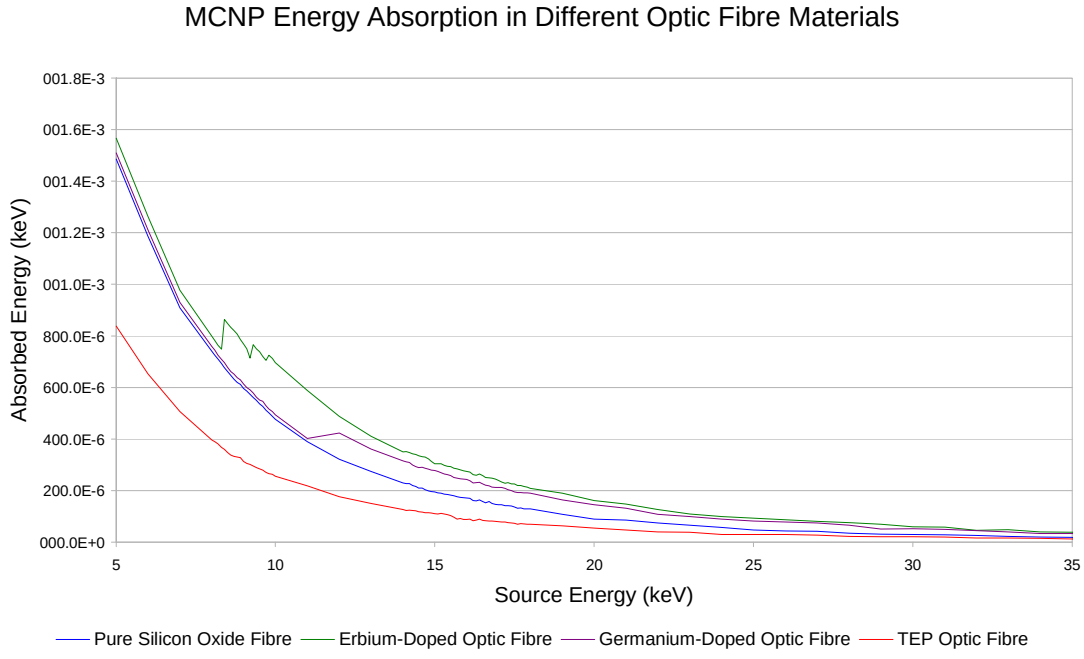

Figure 3.09 – MCNP Model of Energy Absorption Within Different Optic Fibres

Figure 3.09 suggests that Erbium has a greater energy absorption at the energies being investigated, showing maximum energy absorption below 10 keV, and then tailing off as the source energy approaches 30 keV. This result is due to the higher atomic number of Erbium making it more likely to absorb energy at energies where the main means of energy deposition is due to the photoelectric effect. An interesting result is that the dopant elements have both lead to a noticeable increase in the energy absorbed by the optic fibres, especially compared to the dose to Tissue Equivalent fibres.

Effects of Dose Enhancement

After simulating the energy absorption of the different optic fibre materials, it was clear that the dopant elements were increasing the energy absorption of the optic fibres. The next step was to quantify the degree to which this increase occurred. First, the dose enhancement caused by the silicon oxide of the optic fibres relative to a Tissue Equivalent material (in this case simulated A-150 TEP) was investigated.

Figure 3.10a shows the ratio of the energy absorption in a silicon-based optic fibre to the energy absorbed within an optic fibre with the same dimensions composed of A-150 Tissue

Equivalent Plastic.

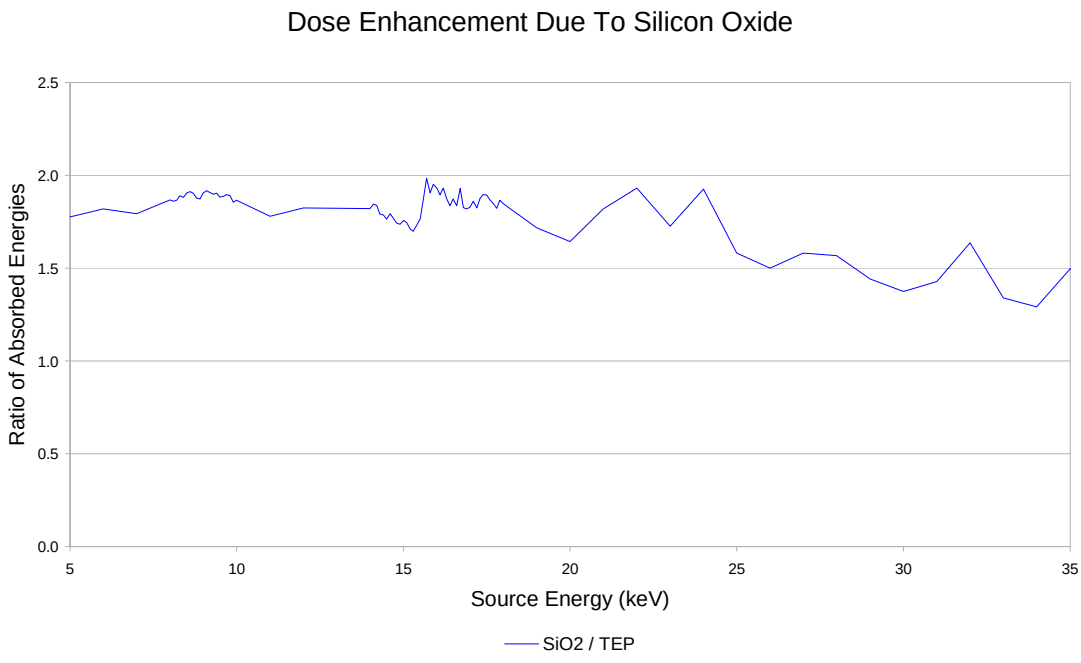

Figure 3.10a - Dose Enhancement of Silicon Oxide Compared to Tissue

Looking at Figure 3.10a, it shows an average increase of a factor of approximately 1.75 between silicon oxide and TEP-based optic fibres, with a relatively constant dose enhancement up to source energy of about 20 keV, after which it tails off slowly. This will be due to the shift in interaction between the radiation field and matter as the primary means of interaction shifts from the photoelectric effect to Compton scatter.

Having looked at the effect of the difference in atomic number between the silicon oxide optic fibres and a TEP model, the next step was to investigate the effects of the dopant materials upon the dose deposition within the optic fibre model. A comparison of the dose enhancement in the Erbium and Germanium doped optic fibres relative to a pure SiO_2 optic fibre is shown in Figure 3.10b. In Figure 3.09 it could be seen that they showed an increase in energy absorption, Figure 3.10b shows the degree to which this occurred. This figure shows the ratio of energy absorption within an optic fibre composed of 99% silicon oxide with a 1% by mass quantity of the dopant element to the energy absorption within an optic fibre of pure silicon oxide.

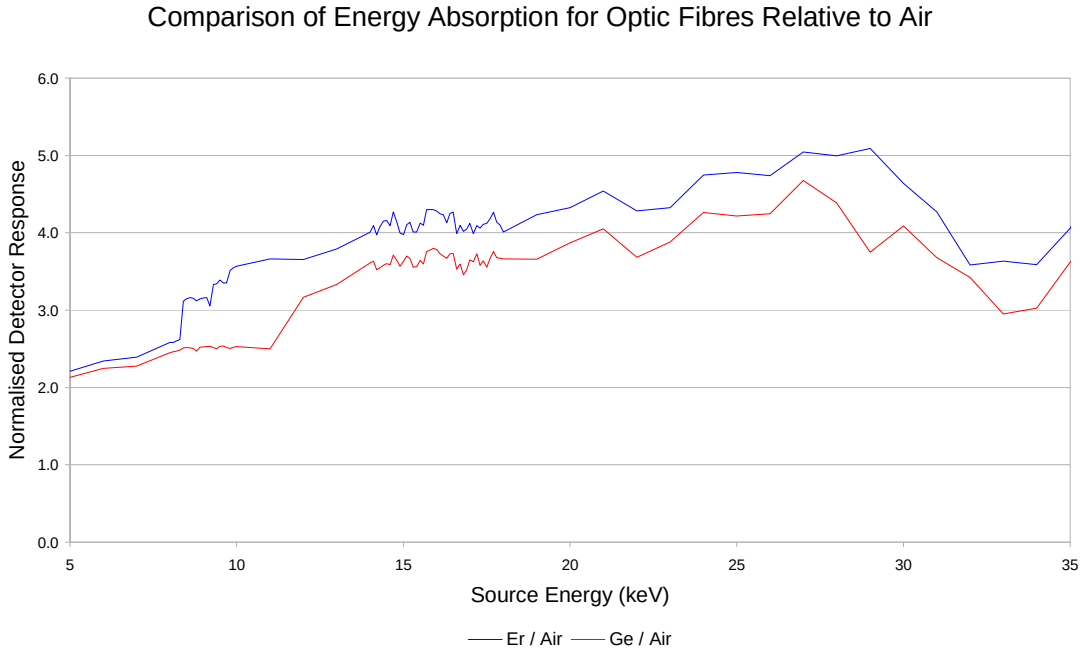

Figure 3.10b - Dose Enhancement in Optic Fibres Compared to Pure Silicon Oxide Glass

Figure 3.10b shows an increase in the energy deposited within the optic fibre due to the dopant element, with Erbium showing a greater increase than the Germanium. Interestingly, there is very little increase in dose below a point (approximately 9 keV for Erbium and 11 keV for Germanium), most probably due to shielding of the optic fibre due to the TEP and cellophane outer layers of the model. After this point, both dopant elements show a steady increase in energy absorption, rising to a factor of about 1.5.

This shows that the dopant element will lead to an increase in the dose absorbed by an optic fibre, suggesting that the radiation absorption can be maximised through the use of high Z elements, as explored in Chapters IV and V.

Simulation of Detector Response

The dose enhancement and energy absorption data is useful as it gives an indication of the energy absorption within the optic fibres. However, having produced a model for the diamond detector in Chapter II, it was worth looking at the detector response curves so that they could be compared with those produced experimentally. Figure 3.11 shows the ratio of the energy

absorption within a doped optic fibre relative to the energy absorption within the crystal of a diamond detector, giving a comparison of the two different models.

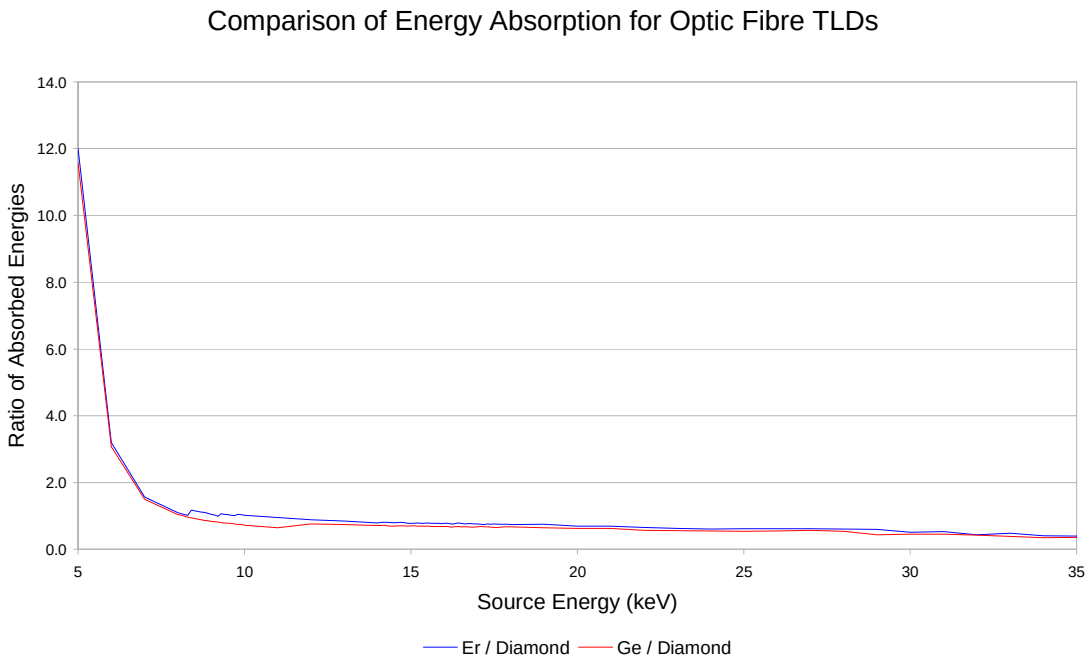

Figure 3.11 – MCNP Model of Detector Response Of Doped Optic Fibres vs. Diamond Detector

As can be seen in Figure 3.11, the ratio of energy absorption within an optic fibre to energy absorption within a diamond detector is similar for both Erbium and Germanium-doped TLDs, with the energy absorption being slightly higher in those doped with Erbium. This graph appears to show that the optic fibres are significantly more sensitive at low energies, at 5 keV absorbing 12 times the energy of the diamond (as a ratio of average energy absorption per unit mass), then falling off to reach a factor of 1.5 by 8 keV.

This is due to the higher atomic number of the components of the optic fibre compared with the diamond crystal and would produce two significant effects were this detector design to be put into general use. Firstly, it appears to show enhanced sensitivity to low energy radiation, making it a useful test for radiation fields of the energy range being investigated. As it is not tissue equivalent the dose enhancement factors would have to be studied in greater depth to provide an accurate comparison of dose.

3.3.3 - Comparison of Results

The Monte Carlo results produced can tell us a lot about the viability of using basic computer models to simulate the behaviour of real-life detectors under different circumstances. Chapter II showed some success in producing a model in MCNP that behaved in a similar manner to the real detector under experimental conditions. The principal problem in investigating the behaviour of a TLD under experimental conditions is that the TLD device does not produce a direct reading of energy absorption, as it needs to be read by monitoring the fluorescence when heated. This introduces several factors into a calculation that are not included in the Monte Carlo model and may need to be accounted for. This includes the shape of the optic fibres leading to the light being emitted in a non-isotropic manner, causing a large loss in photon absorption, although this effect should have been reduced by the reflective cavity in which the fibres were placed. Other potential problems are the band gap of the optic fibres which may be high enough that the lower energy particles are unable to excite electrons to the Valence band affecting the absorption spectrum, or the photomultiplier tube built into the TLD reader may be more sensitive to particular light emissions.

With this in mind, the Monte Carlo models were then compared with the experimental data produced from the SRS facility at Daresbury so that the accuracy of the computer model could be evaluated. Figure 3.12a shows the energy absorption of the optic fibres in the Monte Carlo model compared with the count rate for the same optic fibres obtained experimentally. Both sets of data have been normalised to allow them to the displayed on the same axes.

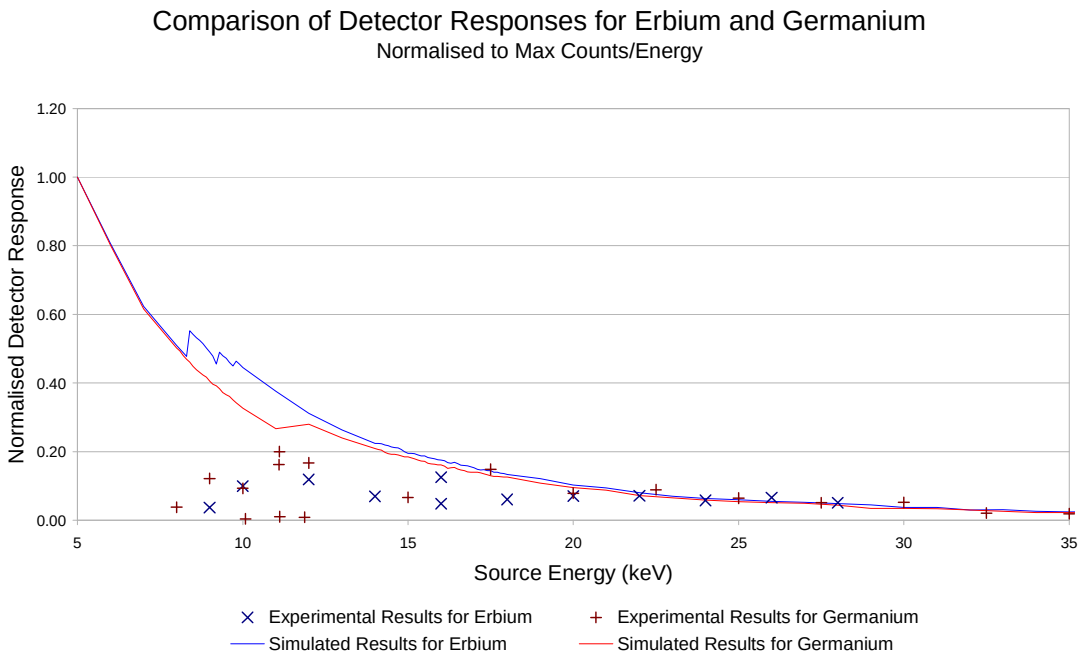

Figure 3.12a – Comparison of Energy Absorption in Experimental and MCNP Results

Looking at Figure 3.12a, it appears that the experimental data follows a similar relationship at higher energies, with the similarities becoming less as the energy decreases. The MCNP data suggests a clear pattern with a large energy absorption shown at low energies, where the path length of the electrons is shorter. However, as the energy increases, the probability of the electron being captured within the optic fibre, and therefore depositing any energy decreases. On the other hand, the experimental data show little evidence of this relationship at low energies, showing little evidence of this large energy absorption. At energies above 20 keV, however, it begins to resemble the MNCP model more closely. There are brief increases in absorption of incident radiation due to the K-edges of the Erbium and Germanium, but these are not noticeable in the experimental data.

Figure 3.12b shows the region of 20 to 40 keV in more detail, showing the similarity between the MCNP model and the experimental data. The factors that may have contributed to the difference in the results at energies below 20 keV are discussed below, but this data suggests that it is possible to use a Monte Carlo program such as MCNP to predict the behaviour of optic fibre TLDs, at least for source energies above 20 keV.

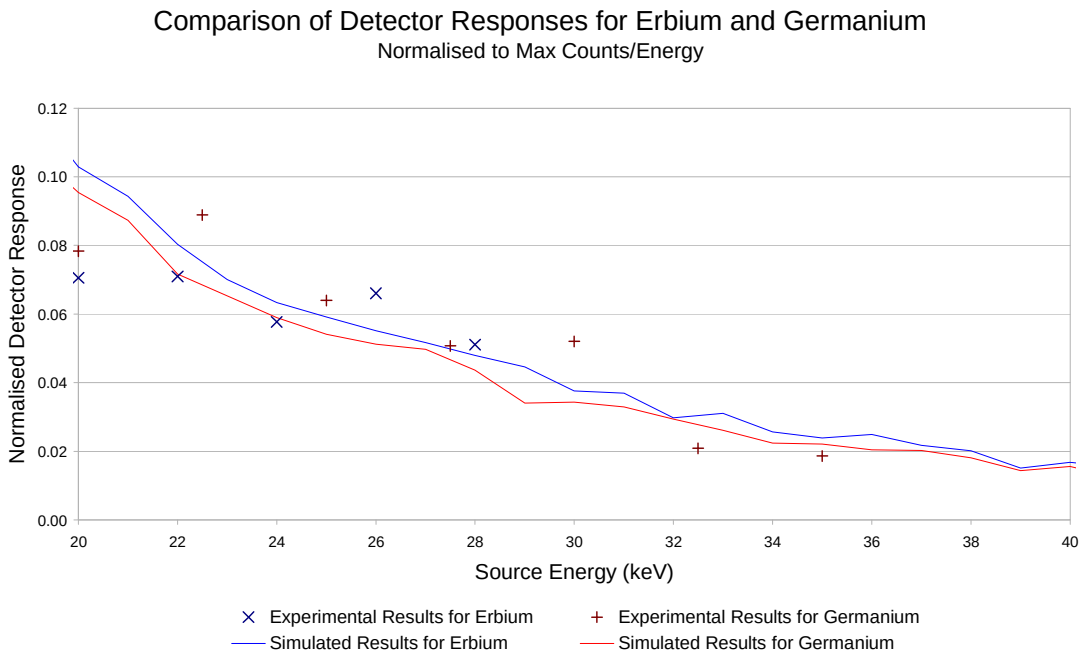

Figure 3.12b - Rescaled Comparison of Energy Absorption in Experimental and MCNP Results

It is interesting that the comparison of the experimental and simulated readings shown in Figures 3.12a and 3.12b show a similarity in the shape of the curve for energies above 20 keV. There are several reasons why they do not agree below this, which are discussed below.

There is a possibility that MCNP may be too general purpose to include the complexities of photon emission and detection that characterise TLDs (factors such as self-absorption, the effects of band gaps, and so on). The electron cut-off used by MCNP in particular may lead to absorption of low energy electrons that may not have had sufficient energy to be excited across the band gap, although pure silicon dioxide's band gap of 8.9 eV makes this unlikely but not impossible. This research shows some similarity to the results obtained for a similar TLD model tested by Asni et al (2011), which showed significant deviation in simulated and experimental data for the region of 20-100 keV.

Another possible reason may be due to differences in the idealised computer model compared to the experimental work. It was difficult to maintain a constant length and position for the optic fibres so small differences in placement and TLD length between the theoretical model and the experimental work may have reduced the accuracy of the final results. Additionally,

the thicknesses used for both the optic fibres and the cellophane backing tape were difficult to measure accurately and may have been different to the values used in the Monte Carlo simulation. Additionally, it must be noted that in reality the optic fibres only contain the dopant material within a narrower core of approximately 8 μm. This may have lead secondary electrons passing through the optic fibres without interacting or interacting in regions not present in the experimental models. This is an important factor to take into account, as the penetration distance of a 10 keV electron is of the order of 1 micron, assuming all of the energy lost by the photon is absorbed (Nikjoo and Lindborg, 2010).

3.4 - Conclusions

An analysis of the data produced from the SRS Facility in Daresbury shows that there have been several flaws in the experimental procedure, as there is too much variability in the results to obtain a statistically important conclusion. These issues may have been solvable; however, it seemed likely that the experimental problems would not be overcome without significant investment in additional equipment to improve the reliability.

A number of problems with the method used became apparent and would need to be solved before more research could continue. The first was in maintaining the consistency of the experimental set-up, as the optic fibres being used were small and difficult to handle, making it difficult to cut, strip and them position them reliably. Secondly, a number of the fibres were broken while being removed from their backing layer of cellophane, while placing two broken halves of a fibre in the TLD reader did not produce a noticeable difference in the final reading, this did lead to the loss of several readings. Finally, it was a problem that the nitrogen flows from the TLD reader lead to the loss of a number of the fibres, compounding the difficulties inherent in working with such small objects in a reliable fashion.

Despite the problems in producing reliable results, the results in this chapter show definite evidence of Thermoluminescence occurring within the optic fibres. This was shown by the increase in the number of counts in those fibres which were irradiated, compared to those that were not. Additionally, there is some evidence of differences in energy absorption within the two fibre type due to the dopant materials present, suggesting that dopant materials could be

chosen to make the readings obtained from the optic fibres more sensitive to specific energies of radiation.

The results show a definite advantage in using Germanium-doped fibres for the energy ranges studied here, as the count rates for Germanium-doping were significantly higher than the background count rates of unirradiated optic fibres of the same type. As is mentioned in section 4.3.3, the count rates for Germanium were approximately twenty times those of unirradiated fibres, compared to Erbium, which showed a count rate four times higher. This makes it less likely that the results for Germanium will be affected by random fluctuations in count rate due to the design of the optic fibre used, the TLD reader or background radiation, making the readings more reliable.

One thing that has been shown clearly by this work is that Monte Carlo modelling using MCNP may be able to produce an accurate simulation of the behaviour of a TLD although it has limitations at source energies below 20 keV. This is consistent with other research conducted in this field, such as the work by Nunn et al (2008).

From this data, it was concluded that although there was a definite indication that optic-fibres may be of use in monitoring radiation exposure, and can function effectively as a TLD, the variability in the readings obtained was too great to be reliable. In addition to this, evidence was produced that the Germanium-doped fibres show a greater difference in count rate between irradiated and unirradiated, this will produce more reliable results. Further research into this field would be desirable, however, more sensitive equipment and better access to a monoenergetic radiation source (such as a Synchrotron) would be needed to continue investigating their characteristics. As neither of these were a possibility at the time, the research was moved onto other fields where the equipment was readily available.

Also, from the results presented, it appears that MCNP can be used to predict the results that will be obtained for an optic fibre TLD, but only at photon energies greater than 20 keV.

3.5 - Future Directions for Research

For further research to be conducted in this field, the methods used for gathering results will need to be refined substantially, probably through improvements in the design of the equipment. This could be achieved by altering a TLD reader such as that used, so that the fibres themselves are less likely to be lost within the machine, or by looking at completely different techniques such as laser heating the fibres.

One simple improvement that could be applied to the experimental techniques would be to pre screen the fibres in order to eliminate those that have a low detector response. This would involve uniformly irradiating the optic fibres beforehand, then passing them all through the TLD reader, removing those that have a response below an arbitrary value then annealing and reusing those that produced reliable readings.

Were it possible for a technique to be found that could reliably read the fibres, additional research could be conducted, looking at different compositions, thicknesses and dopant materials to produce a TLD that can be reliably used in the monitoring of radiation dose. If this is achieved, there will be several areas of dosimetry where they would be of use, such as the radiation protection of extremities such as the hands, where they could be attached to a radiation workers gloves to monitor the level of exposure they undertake.

There are several applications for which optic fibre TLDs would be useful as dosimeters, however, more research needs to be conducted into the best methods of setting them up and obtaining readings.

Chapter IV - Proportional Counter Dosimetry

Proportional counters were first introduced in the late 1940's, where they were largely used for the detection and spectroscopy of low energy x-rays and neutrons. This chapter discusses the use of proportional counters in the detection of low energy x-rays from a synchrotron, primarily testing the detectors and assessing the effects upon dose caused by differing dopant materials in the walls of the detector. In the following chapter, variations in the set-up and design of these detectors are assessed, testing some of the assumptions made.

This chapter will begin by explaining the ways in which a gas filled detector quantifies an ionising radiation field, before going into more detail about the specifics of the proportional counter and how they were used to obtain the data included at the end of the chapter. The experimental data will also be compared with the data produced from Monte Carlo models of the detector produced using MCNP and EGSnrc, and its reliability as a predictor for future experimental work assessed.

4.1 - Background Theory

4.1.1 - Gas Filled Detector Theory

A gas filled detector is designed to detect the ion pairs created by the interactions of an ionising radiation field losing energy within a volume of gas. The ion pairs produced are a free electron (e^-) and a positive ion. If an electric field, ε, is applied, the electrons will migrate to the anode, while the positive ions will migrate towards the cathode, producing a pulse of electric current. The characteristics of the resultant pulses are dependant upon the strength of the electric field across the gas, which will affect the rate of recombination or gas multiplication of ions.

Figure 4.01 shows the gas ionisation curve for a gas filled detector, with the labelled regions showing the differing behaviour of the detector due to different applied voltages. The characteristics of the different regions are discussed in more detail below (based upon *Radiation Detection and Measurement*, Knoll, 2000).

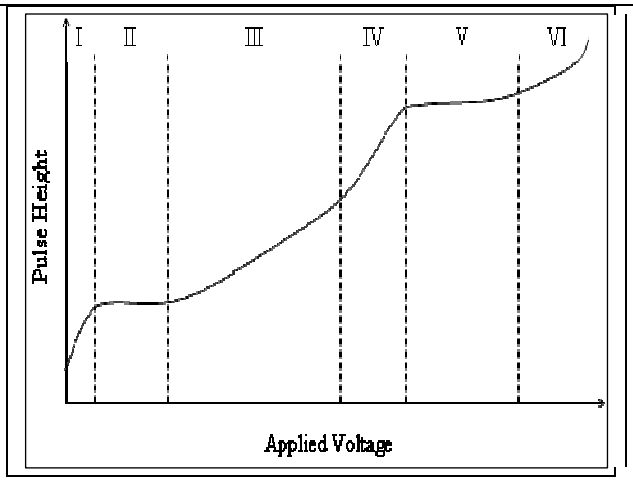

Figure 4.01 - Effects of Voltage Upon Pulse Height In A Gas Filled Detector

If the applied voltage is within region I, the drift velocity of the ions is very low, so the ions tend to recombine before reaching the anode or cathode. This reduces the pulse height of the signal, making it largely dependant upon the position the ion is created in and therefore unreliable as a radiation detector.

In region II, all the ion pairs created are collected at the anode and cathode of the detector, producing a voltage range where an increase in applied voltage does not lead to an increase in pulse height. With the pulse height being related only to the quantity of ionised particles produced by the incident radiation, this is in turn related to the energy absorbed within the gas from the ionising radiation. An ionisation chamber was used as a standard detector for comparison with a diamond detector in Chapter II.

Below ~600V, in region III, the electrons produced from ionisation may acquire enough energy between collisions to create secondary ion pairs. This leads to a Townsend Avalanche, where electrons produced through ionisation create additional ion pairs. This may in turn create more ion pairs, leading to gas multiplication. As the number of secondary ion pairs produced is related to the energy acquired by the electrons between impacts, the amount of gas multiplication within the proportional counter is largely linear as the applied voltage is increased. A proportional counter was used as a basis for experimental and Monte Carlo work in this chapter and Chapter V.

In region IV, beyond about 600V, the electrons produced within the gas are quickly absorbed, leading to higher concentrations of the slower moving positive ions produced by the gas multiplication. This high concentration of positive ions leads to a reduction in the strength of the electric field, distorting the effects of gas multiplication, leading to non-linearities in the results.

As the voltage across the gas becomes greater, the number of electrons produced in Townsend Avalanche continues to increase and more of the secondary ions return to their ground state through the emission of UV or visible photons as seen in region V. These photons are absorbed by either another gas molecule or by the cathode of the detector, creating another free electron. This is then accelerated by the detector's electric field, triggering additional avalanches, leading to a Geiger discharge. As the positive ions created in this process move significantly slower than the electrons produced, their concentration around the anode increases rapidly until the space charge effect reduces the electric field strength, terminating the discharge. As this termination is dependant on the creation of a fixed amount of positive charge, the number of initial ion pairs created through interaction with the incident radiation is irrelevant, creating only pulses with a fixed amplitude.

Beyond region V, the electric field becomes such that it is able to ionise the gas directly, with the amount of ionisation directly related to the electric field between the anode and cathode. As the pulse of electric current is no longer related to the amount of energy absorbed from the ionising radiation, a gas filled detector with a voltage in this region is no longer useful as a radiation detector.

4.1.2 - Proportional Counter Theory

For the research contained within this chapter a tissue equivalent proportional counter was used to obtain the results. Proportional counters have several significant advantages over other gas filled detectors, making them ideal as a microdosimeter for the research conducted at the Daresbury synchrotron, foremost of which is the large voltage pulse due to the gas multiplication of the original ion pair.

The fractional increase in the number of electrons per unit path length is given by the Townsend Equation:

$$\frac{(\mathrm{d}n)}{n} = \alpha \mathrm{d}x$$

In this n is the number of electrons, x is the path length of the electrons within the gas and α is a constant called the first Townsend coefficient for the gas which is dependant on the electric field. The electron multiplication at the proportional counter region voltages is linear, with the charge collected by the detector having a linear relationship with the number of ion pairs created by the incident radiation, and therefore the energy of the radiation.

Tissue equivalent proportional counters are widely used in microdosimetry to simulate the effects of radiation upon a sub-cellular sized volume of tissue and to investigate the degree to which different qualities of radiation will deposit their energy. These designs are composed of a spherical cavity composed of a tissue equivalent plastic (in this case doped with different higher Z elements) and filled with a low pressure tissue equivalent gas). When an x-ray or neutron source irradiates the detector, secondary charged particles are created within the walls of the chamber. This produces a condition of equilibrium in which the number of particles emitted from the wall is characteristic of the particle flux produced within the wall material, as long as the wall thickness is greater than the range of the secondary particles.

The biggest advantage of a tissue equivalent proportional counter is that it allows the LET distribution of the secondary particles to be determined, as the pulse amplitude recorded will depend on the ion pairs created by the LET of the particle and the path length through the gas. This occurs as long as the fill gas pressure is kept low enough, such that the particles entering the gas lose a negligible amount of their energy as they pass through to the opposing wall. With a spherical chamber, the approximation can be made that the paths are straight lines, so the chord distribution can be determined analytically. Knowing the pulse height distribution and the distribution of the chord lengths, an LET analysis of the particles can be determined, a feature of the detector which is especially useful in the analysis of neutron fluxes

(investigated in Section 4.1.4 and 4.3.3).

Figure 4.02 shows the layout of a tissue equivalent proportional counter (as a note on the scale of the image, the diameter of the detector including the wall was 1.33 cm for the experimental research):

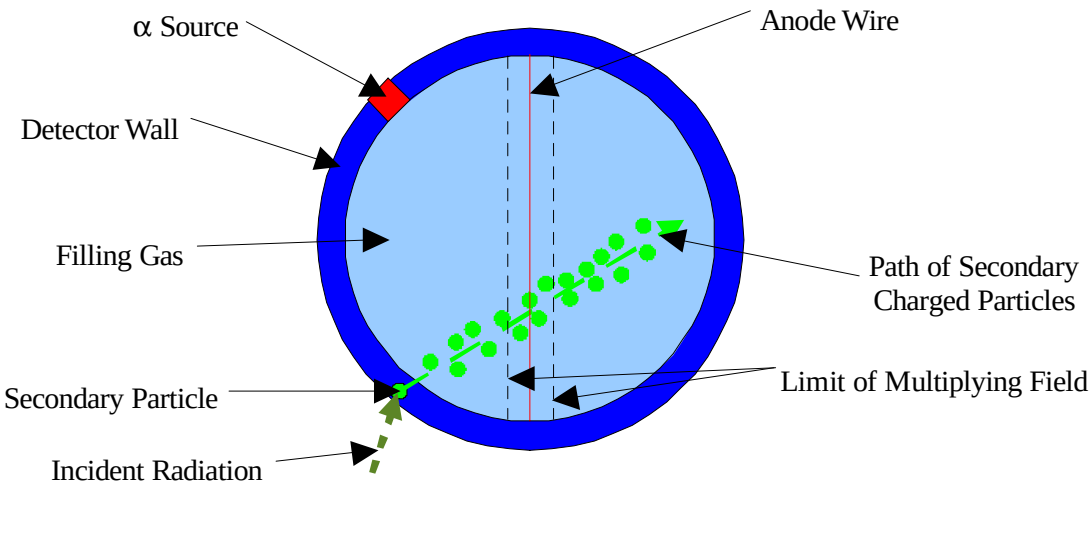

Figure 4.02 - A Diagram of a Tissue Equivalent Proportional Counter

The detectors used for this work are Single Wire design, with only a central anode wire, which has only a limited region in which the electric field is strong enough to accelerate electrons. This effectively constrains the multiplying region to a cylinder, this preserves the pulse height resolution of the detector at low gas pressures. The electric field at a given radius, r, is given by the equation:

$$\varepsilon(r) = \frac{V}{\left(r \ln\left(\frac{b}{a}\right)\right)}$$

In this V is the applied voltage, a is the anode wire radius and b is the inner radius of the cathode tube. This makes the value of ε extremely large when r is small, so the electric field strength increases as the electrons move closer to the anode, reducing the applied voltage needed for gas multiplication significantly.

The advantage of using an effectively cylindrical geometry for the detector is that it reduces the region in which gas multiplication can take part, as there is a threshold for ε below which the kinetic energy of the secondary charged particles is insufficient for further excitation to occur. This region can be reduced to a fraction of a percentage of the radius of the detector, meaning that the Townsend Avalanche will occur in the same region of the detector regardless of which region of the detector wall the original ion pair was created.

4.1.3 - The Proportional Counter as a Microdosimeter

As mentioned in Chapter I, the low pressure proportional counter is chosen as a compromise between a number of different factors that describe a perfect microdosimetry detector. However, the proportional counter itself operates at a different scale, with a cavity size of millimetres representing a volume of tissue microns across.

Simulating Small Cavities Using Gas Cavities

In order to experimentally determine the distribution function, f(y), of lineal energy, y, within a proportional counter for a microscopic volume of tissue, a larger volume proportional counter is used, with a low density filling gas to simulate a smaller volume cavity, the effects of this approximation and the problems inherent are discussed in this section.

For a spherical detector, such as those used in this experiment, to apply this principle, it is necessary that the amount of energy lost by a passing particle is identical for a sphere of tissue and a sphere of gas for equivalent trajectories, as described in the equation below:

$$\Delta E_t = \left(\frac{S}{\rho}\right)_t \rho_t d_t = \left(\frac{S}{\rho}\right)_g \rho_g d_g = \Delta E_g$$

This represents a tissue sphere of diameter d_t and a gas sphere of diameter d_g where $d_g = k_{gt}.d_t$, with ΔE_t and ΔE_g representing the mean energy losses from charged particles within the tissue and the gas, ρ_t and ρ_g are the material densities and $(S / \rho)_t$ and $(S / \rho)_g$ are the stopping

powers. Although this equation is written for a particle travelling across the diameter of a sphere, the relationship should hold true for any equivalent trajectory. In a situation where the tissue and gas components have an identical atomic composition, assuming that the mass stopping powers are independent of the density of the medium, the following equation can be reached:

$$\rho_g = \frac{\rho_t}{k_{(gt)}} = \frac{1}{k_{(gt)}}$$

This applies if the tissue has a unit density. This indicates that the mean energy loss by a charged particle passing through a sphere is equal for two different spheres as long as the ratio of the two different diameters, k_{gt}, is the same as the ratio of the two different densities of the gases. This allows us to use a larger gas-filled sphere to simulate a smaller tissue-filled sphere as long as the density of the gas within is reduced by the ratio of the two different diameters, k_{gt}, with an increase in diameter by factor k_{gt} resulting in a reduction in pressure by a factor of k_{gt}. Geometrically, this means that the mass of the gas present within the expanded diameter sphere increases by a factor k_{gt}^2 and the volume of the gas sphere is increased by a factor k_{gt}^3, with the absorbed dose remaining constant. Additionally, the number of charged particles present within the gas sphere will increase by a factor k_{gt}^2.

In a real-life microdosimeter, it is often not possible to find a tissue equivalent plastic and gas with identical atomic compositions, producing an incomplete homogeneity in the materials. However it has been shown experimentally that the differences in effect between a homogenous detector and the detectors commonly used in microdosimetry applications is slight (as discussed experimentally in ICRU Report 36 Chapter 5, Section 5.2.3, 1983).

Proportional counter microdosimeters produce a reading by measuring a charge proportional to the number of ions pairs produced by incident ionising radiation, with a value, W. This gives the relationship between the number of ion pairs produced through the interaction and the amount of energy imparted to the material, allowing a spectrum to be produced. W, as a measure of the amount of gas multiplication in a specific detector at a given voltage, is related to the lowest limit of the diameter of a proportional counter. This is because as the pressure is

reduced within the detector, the starting region for the electron avalanche within the detector also increases. As the size of the starting region increases it starts to become a non-negligible part of the volume of the sphere and so will no longer function as a cylinder. This makes the point of interaction important in determining the numbers of secondary electrons produced (thereby making it impossible to ascertain the energy of the interacting ionising radiation). Although the degree of inaccuracy introduced depends on the geometry of the detector, the voltage applied and the necessary degree of accuracy for the experiment, there have been few successes in carrying out experiments with a simulated volume below 0.3 μm.

4.1.4 - Neutron Therapies

The method used for Boron Neutron Capture Therapy (BNCT) is a form of radiotherapy first suggested as a theory in 1936, shortly after the discovery of neutrons (Lochler, 1936). BNCT makes use of the high neutron capture cross-section of Boron-10 nuclei to increase the radiation dose from a thermal neutron beam to a specific volume (usually a tumour). A Neutron Capture Therapy (NCT) creates a binary system where two components, neither of which are lethal in themselves are combined to create a strongly cytocidal effect. Since the 1930s, a lot of research has been conducted into NCT, looking at ways to improve the dose enhancement within the Boron-containing volume, as well as other elements with a high neutron cross-section that could provide a more effective dose to cancerous tissue without killing the healthy tissue surrounding it (including some research into Uranium-231 until the amounts needed were discovered to be lethal in the late 1950s).

This research is designed to look at the dose enhancement to a detector volume produced by the doping of a proportional counter with both Boron and Gadolinium. This research is then taken further by looking at the same detectors, but with a reduction in their fill pressure, in order to allow their behaviour to be investigated at a smaller scale.

Neutron Interactions in a Proportional Counter

The neutron beam used for this experiment was produced by a Dynamitron accelerating protons into a lithium target, creating a neutron beam which is targeted at the detector. First

the beam is shaped to energies that are useful for BNCT, and then the beam is collimated to a narrow beam shape.

The neutron interacts with the Boron-10 nuclei to form a compound nucleus, excited Boron-11, which decays into Lithium-7 and an α-particle, both of which produce a series of ionisations within a distance of 5-9 microns from the reaction. As this distance is extremely short (approximately the diameter of a typical cell), any effects produced by the Boron Neutron captures are very localised, but useful in a radiotherapy treatment as it reduces any potential damage to surrounding tissue. This reaction is summarised as:

$$^{10}B + n_{th} \rightarrow {}^{4}\alpha + {}^{7}Li + 2.8 \text{ MeV (occurs 6\% of the time)}$$
$$^{10}B + n_{th} \rightarrow {}^{4}\alpha + {}^{7}Li^{*} + 2.3 \text{ MeV (occurs 94\% of the time)}$$
$$\text{then } {}^{7}Li^{*} \rightarrow {}^{7}Li + \gamma\,(0.475 \text{ MeV})$$

Note that for a detector, due to the conservation of momentum, *either* the alpha particle or the lithium ion will enter the gas cavity.

Gadolinium has attracted a lot of interest as a neutron absorber owing to its extremely high neutron cross-section of 255,000 Barns for Gd-157 (Boron's cross-section is 3,835). This would mean that at an equal dopant level a significantly lower external neutron dose would be required to produce an equal dose to a target, the longer-ranged photons produced, however, will lead to an increase in the dose to the surrounding tissue which offsets some of the sparing from the lower external dosage. The interactions of the neutron beam with the Gadolinium are more complex and therefore less predictable than those of Boron, owing to its larger atomic mass and therefore more complex atomic structure. In general, however, neutron-rich isotopes of Gadolinium tend to decay through the emission of photoelectric emission, with energy being lost through the production of x-rays and Auger electrons.

There are several important interactions for natural Gadolinium in a thermal neutron field when considering dose enhancement effects, however due to its incredibly high neutron cross-section the interaction with Gd-157 is one of the more common:

$$^{157}Gd + n_{th} \rightarrow {}^{158}Gd^*$$

The Gd-158 then relaxes to a ground state through the emission of gamma radiation and atomic electrons through internal conversion, followed by x-rays and Auger cascades. This produces a mixture of short-ranged (micron-scale) electrons and longer-ranged (centimetre-ranged) photons. The gadolinium used to dope the detector consists mainly of the isotope Gd-157, which makes up 15.65% of naturally occurring gadolinium (Blasy, 2008; Goorley, 1998).

4.1.5 - Dose Enhancement

The aim of Neutron Capture Therapy is to greatly increase the radiation dose to a defined volume with a dose-enhancing material contained within, without risking an increase in the dose to the surrounding materials.

Table 4.01 shows the thermal neutron capture cross-sections of some of the elements contained within a typical proportional counter design (from EnvironmentalChemistry.com website, last checked 2010).

Element	**Atomic Number**	**Thermal Neutron Capture Cross-Section (Barns)**
Boron	5	767
Gadolinium	64	49,000
Hydrogen	1	0.3326
Carbon	6	0.0035
Nitrogen	7	1.91
Oxygen	8	0
Fluorine	9	0.0096
Calcium	20	0.43
Gold (present in anode wire of detector)	79	98.7

Table 4.01 - Neutron Cross-Sections of Elements Present Within Detectors

From this table, it can be seen that the neutron capture cross-sections of boron and gadolinium are significantly greater than those of any of the other elements present within the detector, even including the gold-coated anode wire. This means that the neutron absorption should be much greater within those detectors that contain boron and gadolinium than within the Tissue Equivalent-only detector.

4.2 - Monte Carlo Modelling of the Proportional Counter

During the course of this research several different Monte Carlo models were used to produce results, all of which were based on a simplified model of the tissue equivalent detectors used. Owing to the limited geometries of both MCNP and EGSnrc, the models were idealised to a spherical Tissue Equivalent Plastic (TEP) wall composed of A-150 plastic placed within a pure aluminium detector housing. This was filled with a low pressure Tissue Equivalent Gas (TEG) containing a small diameter gold wire anode, ignoring the electrical components and cathode. The gaps between the gas-filled spherical volume and the cylindrical walls of the detector case were filled with propane-based TEG with a density of 1.617×10^{-6} g.cm^{-3}. The elemental compositions of the materials used in the construction of the MCNP model of the proportional counter can be found in Appendix II Table x2.01, and the materials used in the EGS model are summarised in Appendix II Table x2.02.

The two codes were used to take advantage of their differing strengths and weaknesses to create a more complete understanding of the behaviour of this type of detector, as well as allowing the usefulness of the codes to be evaluated in simulating this type of detector. MCNP was used to measure the total energy absorption within the gas volume within the detector using its more complex geometry functions. EGSnrc was used to look at the energy absorption spectra within the same gas volume, allowing its more complex photon and electron physics models to be used.

4.2.1 - MCNP Model of the Proportional Counter

The MCNP model used to simulate the proportional counter that was used in this chapter is shown in Figure 4.03.

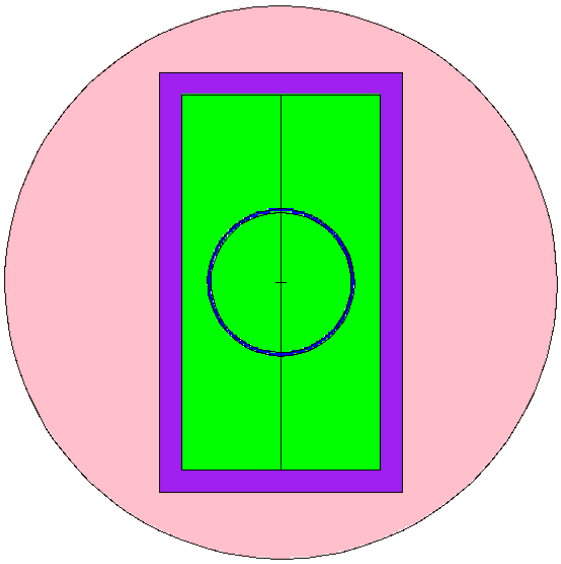

Figure 4.03 - MCNP Model of a Proportional Counter

This model is made up of seven components. The first component is the detector housing, constructed from Aluminium, which represents the outer shell of the detector. Within this there are 2 gas layers, one encompassing the interior of the detector housing, the other inside the detector wall, both of which were composed of a standard propane-based TEG. A detector wall was added to the model, composed of A-150 TEP based upon previous work on these detectors (such as by Saeddi, 2006). Next, a narrow pure gold wire was added running along the centre of the detector, representing the detector anode wire. The final two components consisted of the inside and outside of a large air-filled sphere, which represented the limits of the simulation. This was made 10 centimetres in diameter, as any particles which moved outside these limits were lost to the system.

The dimensions of the different components of the detector are listed in Table 4.02. These dimensions are based upon those used by Dr Mark Gainey (2002) in earlier work conducted at Birmingham University and were used in the construction of the MCNP and EGS Monte

Carlo models.

Detector Component	Dimensions
Detector Housing	3.8 cm length x 1.1 cm radius cylinder
Outer Gas Layer	3.4 cm length x 0.9 cm radius cylinder
A150 Wall Material	0.665 cm radius sphere
Inner Gas Layer	0.635 cm radius sphere
Gold Wire	3.4 cm length x 0.00023 cm radius cylinder

Table 4.02 - Dimensions of the Proportional Counter Components

This shows that the detector itself had dimensions of only 3.8 by 1.1 centimetres, with a detecting element 0.635 cm in diameter and a wall thickness of 0.03 cm. An example input file for one of the simulations performed is included in Appendix IV Example 4.5.

4.2.2 - EGSnrc Model of the Proportional Counter

To produce energy spectra that would allow the investigation of the effects of gas pressure and dose enhancement due to high Z materials, an EGSnrc model had to be produced that resembled the detectors being used for the experimental work. This would allow easy comparisons to be made of the results obtained, allowing the computer model to be easily validated or rejected.

In this chapter, EGSnrc was used to produce the Monte Carlo simulations because it is capable of simulating accurate spectra for detectors of this design, instead of having to rely on just total energy absorption. In Section 4.3.1 the spectra produced by EGSnrc was compared to several spectra obtained from experiments using a synchrotron and the results were found to be a good approximation. In this chapter, the accuracy of EGSnrc calculations can be seen at lower gas filling pressures, allowing the accuracy of the approximations in both the experimental and Monte Carlo results to be compared.

Because EGSnrc is not designed to deal with shapes other than cylinders, the modelling of a

spherical detector was problematic. This was dealt with by constructing the spherical detector element from a series of 12 cylinders of equal height, with the radius of each chosen to ensure that the volume within was the same as the equivalent section within a sphere. This was achieved through the use of the formula for determining the volume of a spherical cap to determine the mass of a section of a sphere.

$$V = \pi d^2 \left(R - \frac{d}{3} \right)$$

In this formula, V is the volume of the sphere, d is the depth of the cap and R is the radius of the sphere.

The energy absorption in each of these cylinders was then summed to give the total energy absorption within a sphere of equivalent mass. This approximation should yield similar results, however there is the problem that the ‘stepping’ of the walls caused by their construction will lead to variation in the path lengths of the secondary particles.

A visual representation of this model is shown in Figure 4.04, produced by the EGSnrc program. This shows a cross-section of the model, with the centre of the detector on the left hand side and the outer shell on the right, with the rectangular sections representing the radius and height of the component cylinders. In this model, the propane-based TEG is represented by the orange-coloured regions, A-150 TEP is yellow, the pure aluminium outer shell is the grey region and the air outer region is red. An example input file for EGSnrc can be found in Appendix V.

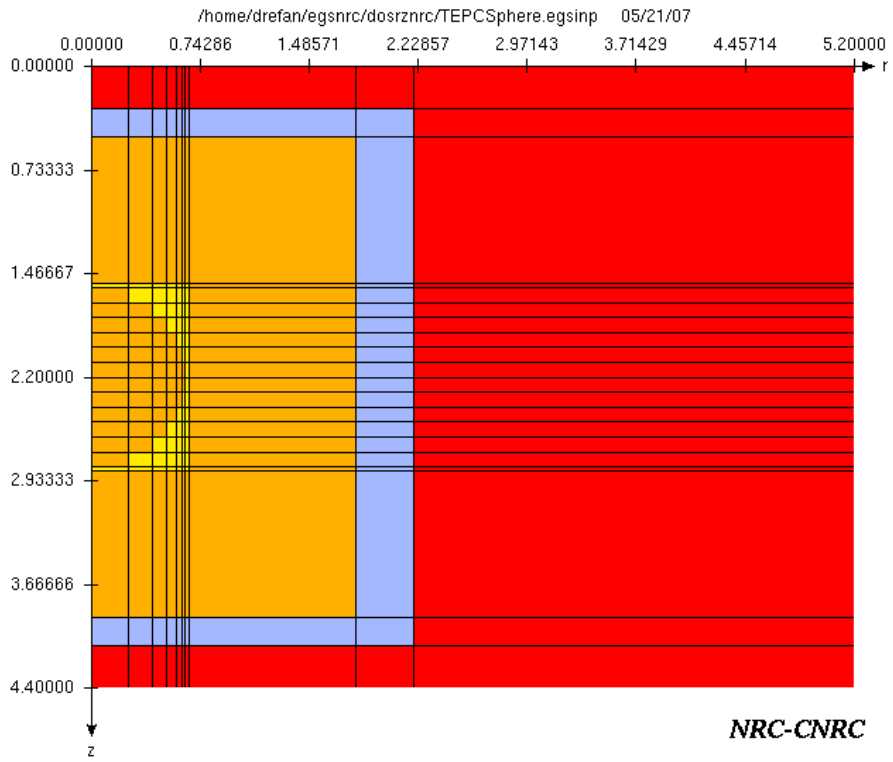

Figure 4.04 - EGS Output Demonstrating the Layout of the EGSnrc Proportional Counter Model

4.3 - Results

Please note that for the experimental work included in this section the results are presented as a y.d(y) plot, the method used to obtain this data is explained in Appendix III.

4.3.1 - Monoenergetic Radiation Results

The following section is based upon results obtained using monochromatic synchrotron radiation produced at the SRS Facility in Daresbury compared to results produced using an EGSnrc model, designed along similar parameters. This research was undertaken to compare the accuracy of the EGSnrc model used and determine whether it is an accurate model of the behaviour of this type of detector.

To allow an accurate comparison of the two gain settings used to produce the experimental results and check for any non-linearities that might occur, a signal generator was used to

record the signal generated at each setting. The results of this are included in Appendix I Figure x1.01.

4.3.1.1 - Experimental Results

In Figure 4.05 below is a summary of the results obtained with a tissue equivalent proportional counter for a range of different synchrotron energies for a proportional counter with an internal radius of 0.635 cm and a gas density of 1.617×10^{-6} g.cm^{-3}, representing a volume of tissue with a 2 μm diameter.

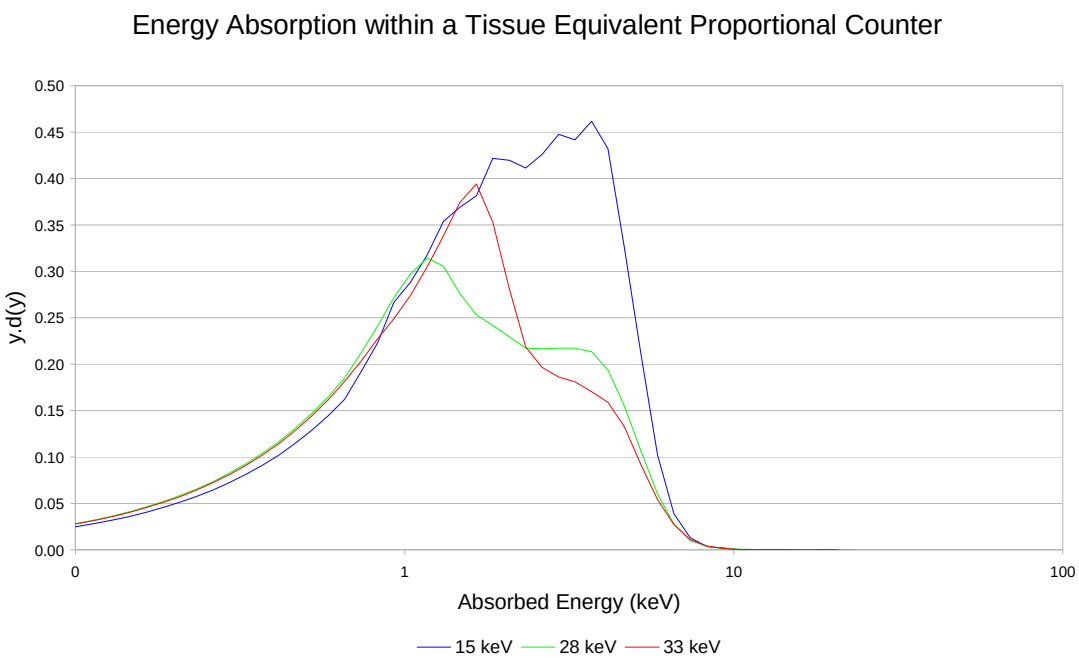

Figure 4.05 - Comparison of Dose Spectra for a Proportional Counter Exposed to Synchrotron Radiation at a Range of Different Source Energies

In Figure 4.05, at lower source energies the proportional counter shows increased energy absorption, due to the lower path length of the secondary electrons produced by the radiation ionisations. The reason for the reduction in energy absorption within the detectors as the source energy increases is due to the higher energies transmitted to the secondary electrons resulting in greater path lengths. These result in the secondary electrons passing through the gas cavity without interacting with the gas and depositing their energy. This shows up in the graph as a greater energy absorption peak for the larger energies as proportionally more

secondary particles created with the maximum path length (equivalent to ~8.25 keV) are absorbed by the detector. As the path length of the secondary particles increases due to a higher source energy, the detector becomes less likely to absorb the photons leading to a reduction in the total energy absorption, as shown for the 28 and 33 keV sources.

4.3.1.2 - Monte Carlo Simulation Results

Figure 4.06 below shows the energy spectra obtained from the EGSnrc model of the tissue equivalent proportional counter.

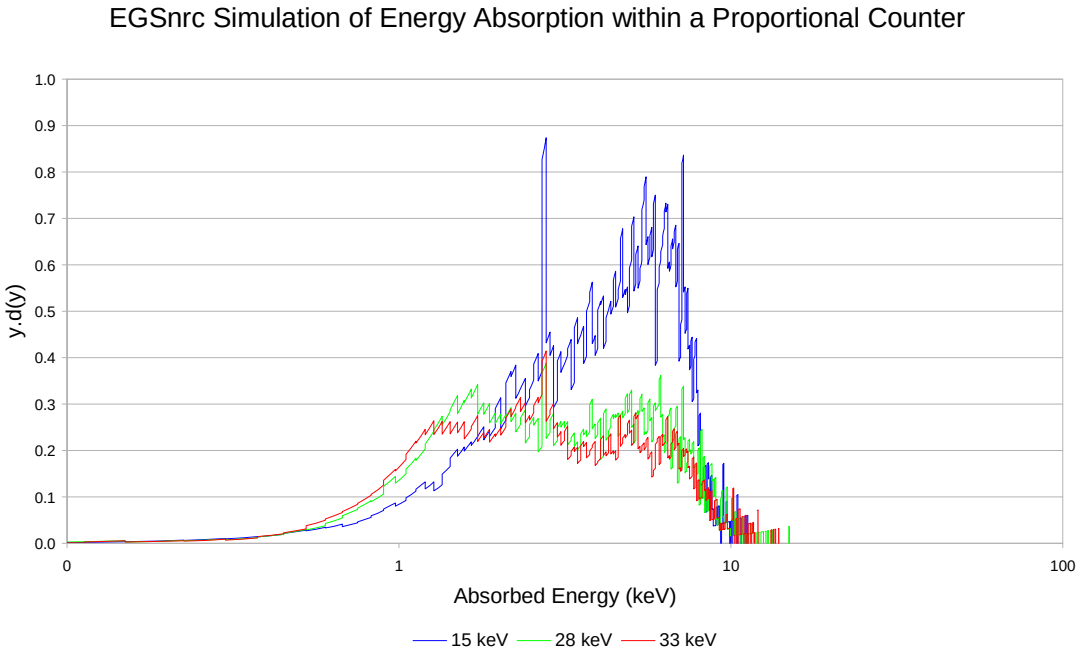

Figure 4.06 - Comparison of Dose Spectra for Monoenergetic Photons Calculated Using EGSnrc

These results show a large degree of variability between lower and higher energies, as is expected of detectors representing such small volumes. However, a similar relationship can be seen in this graph to that produced from the experimental data. As in Figure 4.05, the above diagram shows a significantly larger energy absorption for the 15 keV source energy than for the higher source energies due to the path lengths of the secondary particles produced. This gives some confidence to the use of EGSnrc as a simulation of the behaviour of a detector of this type, although a source energy by source energy comparison will yield a better measure

of the differences, as is shown in the next section.

These results show a large degree of variability due to the complex EGSnrc input used for this research taking a long time to complete its calculation, limiting the number of histories that were simulated. With a more powerful computer or a longer processing time the accuracy of these readings could be increased, however the accuracy supplied here gives at least an indication of the distribution of the energy absorption spectrum.

Errors

Table 4.03 summarises the relative errors found in the Monte Carlo simulations as calculated by the EGSnrc program.

Source Energy	EGS Maximum Relative Error	EGS Average Relative Error
15 keV	0.999	0.076
28 keV	0.999	0.084
33 keV	0.999	0.081

Table 4.03 - Summary of Errors in EGSnrc Simulations of a TEP Proportional Counter

This shows a great deal of variation, with some of the energy bins demonstrating a variability of approximately 100% for some of the results. Despite this, the average relative error within the simulation was extremely low, in part due to the large number of energy bins that did not contain any interactions.

4.3.1.3 - Comparison of Results

Having tested the proportional counter experimentally and run a simulation of its response at several different source energies it is then useful to compare the results to determine the accuracy of the Monte Carlo model.

Figures 4.07a, 4.07b and 4.07c compare the energy absorption in a tissue equivalent

proportional counter as obtained by experimentation compared to data derived from a Monte Carlo simulation. The experimental data used in this section was obtained using synchrotron radiation from the SRS Facility (as shown in Figure 4.05), whereas the Monte Carlo data was calculated using EGSnrc (as summarised in Figure 4.06). In Figure 4.07a the experimental and Monte Carlo results for a 15 keV source energy are compared.

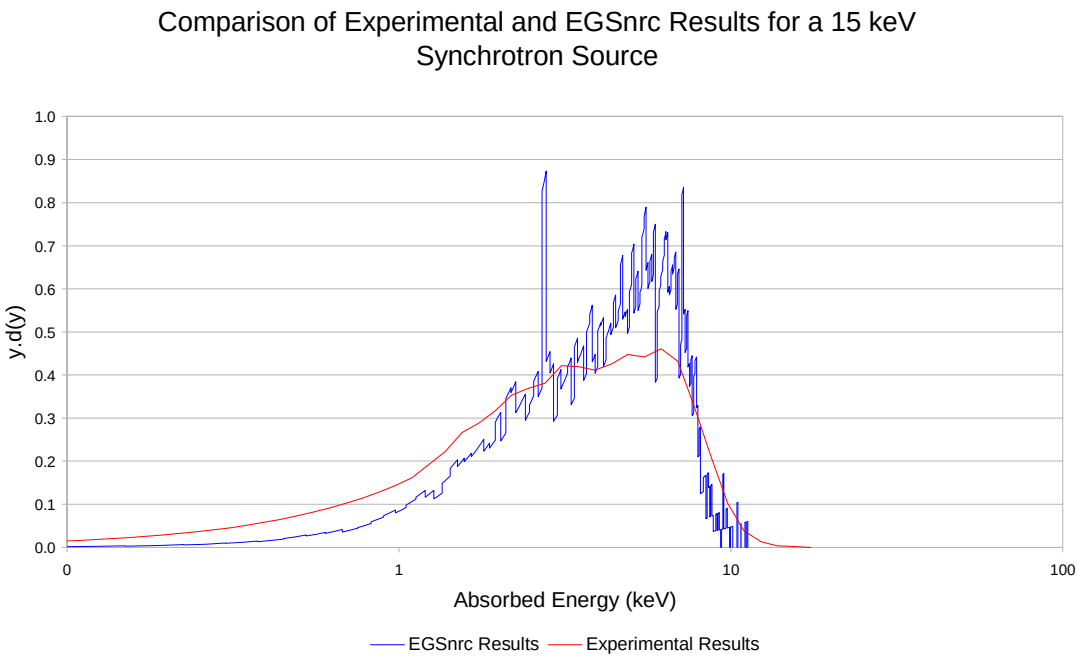

Figure 4.07a - Comparison of Dose Spectra for 15 keV Monoenergetic Photons

In Figure 4.07a it can be seen that EGSnrc has produced a good estimate of the energy absorption of the detector, producing a similar energy absorption curve. There are some differences, with the EGS model producing a larger peak at the higher energies and a lower energy absorption at lower energies. This may be due to a slightly lower sensitivity in the detector used to obtain the experimental data, compared to the simulation, which records the exact energy absorption within the volume. This appears to show that despite the relative error in the EGSnrc calculations it is capable of producing a good approximation of the behaviour of this type of detector.

Next, in Figure 4.07b, the experimental results obtained for a proportional counter from the SRS Facility are compared with those produced by an EGSnrc simulation of the same detector for a 28 keV monoenergetic source.

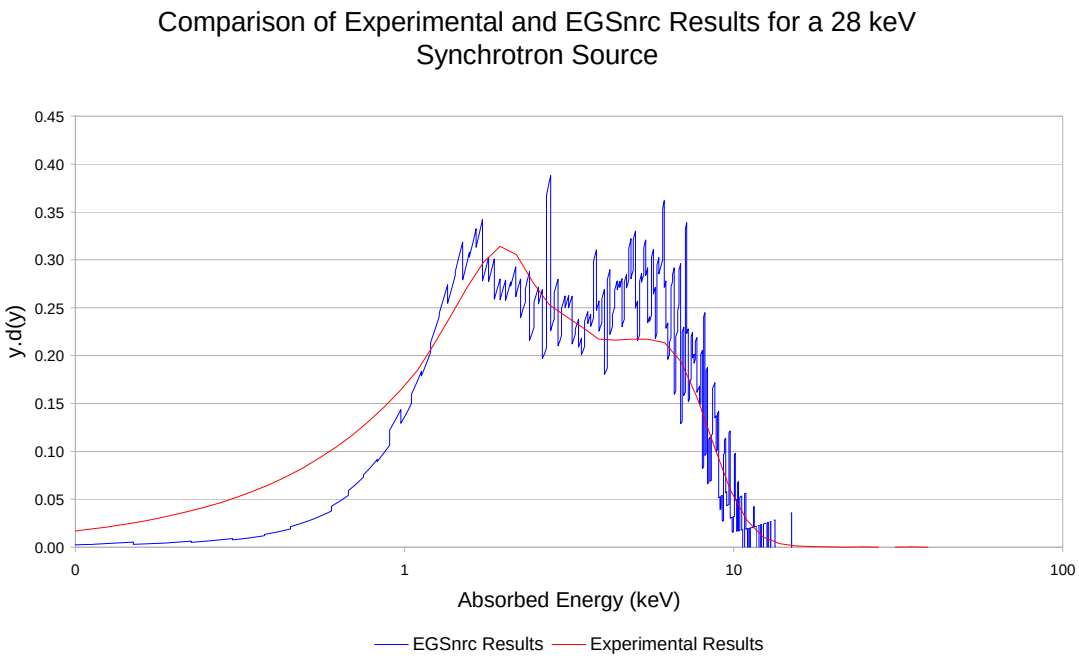

Figure 4.07b - Comparison of Dose Spectra for 28 keV Monoenergetic Photons

In Figure 4.07b, the two sets of results appear to show a similar degree of agreement to that obtained in Figure 4.07a, showing a great deal of similarity in the height and appearance of the first peak. However, this figure shows a slightly lower absorption at lower energies and greater absorption at high energies in the simulation compared with the experimental results. These differences are almost identical to those in the previous figure and may be due to the sensitivity of the detector used in the experimental work.

Finally, in Figure 4.07c, the results obtained experimentally are compared with those produced using EGSnrc for a 33 keV monoenergetic source.

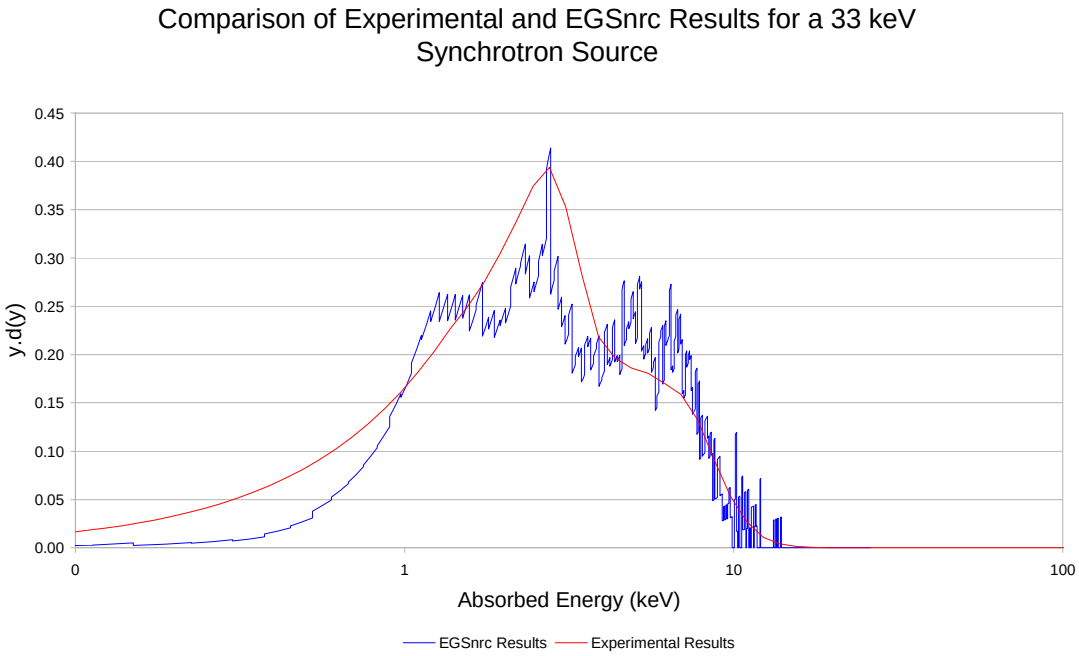

Figure 4.07c - Comparison of Dose Spectra for 33 keV Monoenergetic Photons

Figure 4.07c shows a similar pattern to the results in the previous two figures, this shows a very similar shape to the curve in both the experimental and simulated results. There is, however, a larger energy absorption at the higher energies in the simulations and less absorption at low energies.

Looking at the results obtained comparing the results produced using EGSnrc and comparing them with those produced in an experiment it appears that EGSnrc can be used to produce an accurate model of the proportional counter. The accuracy of the results, however, is limited by differences caused by the sensitivity of a real life detector being a product of an electrical signal, but there is a significant amount of agreement between the two sets of data.

This agreement between the experimental and EGSnrc results allows the Monte Carlo code to be used to predict the behaviour of this detector design under conditions that are difficult to achieve through experimental means. This technique is used in Chapter V Sections 5.2.1 and 5.2.2 to investigate the effects of changing the source radiation aperture size and the gas pressure within the detecting volume.

4.3.2 - Dose Enhancement from Photon Radiation

The next stage of the research looked at the effects of dose enhancement within a proportional counter due to the presence of low concentrations of Boron and Gadolinium. The use of Boron as a neutron absorber is well known and used extensively for applications such as shielding and detector design as well as clinical techniques like BNCT. In addition to this, Gadolinium has shown promise as a neutron absorber and research is being conducted into its effectiveness for similar medical uses to BNCT, where it will increase the neutron dose to regions infused with Gadolinium. In this research, the effectiveness of both of these dopants was assessed for photons, as the high atomic number of gadolinium should lead to an increase in radiation absorption due to the photoelectric effect.

4.3.2.1 - Experimental Work

The work in this section details an investigation into the dose enhancement displayed in two detectors with low concentrations of Gadolinium and Boron. Although the work involved was ultimately unsuccessful it did demonstrate some underlying trends that could be investigated further in the future.

As access to the SRS Facility is limited, this research made use of several different isotopes available in the laboratory to investigate the dose enhancement effects. These isotopes were chosen because they possess major photon emissions at low energies that are close to being monoenergetic, summarised in Table 4.04. Note that emissions with a relative intensity of less than 1 % were left out of the table to reduce the size.

Source Isotope	Energy of Photon Emission (keV)	Intensity of Major Emissions (%)
Am-241	13.90	37
	26.34	2.27
	59.54	35.9
Co-60	1,173.23	99.85
	1,332.49	99.98
Cs-137	31.82	54.28
	32.19	100
	36.30 36.38 36.65	29.4
	661.66	84.99

Table 4.04 - Energy of Emissions for Isotopes used in Dose Enhancement Research

As Table 4.04 shows, the majority of the isotopes used for this research have only a small number of emissions with a large intensity, with the majority within the range of energies used within this research (specifically 5-100 keV).

Unfortunately the results obtained using the radioactive sources were not consistent with those that would be expected from the photon energies they were exposed to. This information has been included in Appendix I Section x1.4.3 along with a table detailing the levels of dose enhancement. As it proved difficult for experimental results to be produced for this set-up, the investigation of the dose enhancement caused by the presence of boron or gadolinium in a tissue equivalent proportional counter moved on to Monte Carlo simulations. This section in Appendix I also considers some of the factors that may have lead to the errors in the data.

4.3.2.2 - Monte Carlo Simulation Results

A ratio of the energy absorption within a TEP proportional counter compared to the energy absorption within a similar detector with trace amounts of Gadolinium or Boron was

produced using MCNP. The aim of this was to give an indication of the dose enhancement within the detector at a range of different energies to provide a model for further work in this area. This section summarises the results of this Monte Carlo investigation, discussing the parameters used for the Monte Carlo input file then displaying the figures produced as a table.

The MCNP model used was based upon the proportional counter model described in Section 4.2.1, however, to produce a measure of the dose enhancement that will occur in a detector with low levels of gadolinium or boron, A-150 TEP doped with the elements was used. The elemental composition of these materials is found in Appendix II Table x2.01. These MCNP results were calculated for 2,500,000 histories, the level of relative error in the calculations is included in brackets under the total energy absorption value in Table 4.05.

In Table 4.05 the total energy absorbed by the detector volumes for the TEP detector and the Boron-doped and Gadolinium-doped detectors is compared and the dose enhancement factor calculated.

Detector Design	**Total Energy Absorption at 15 keV (in keV)**	**Total Energy Absorption at 33 keV (in keV)**	**Dose Enhancement Factor at 15 keV**	**Dose Enhancement Factor at 33 keV**
TEP	1.730 x 10-7 (0.157)	1.955 x 10-6 (0.063)	-	-
TEP + Boron	1.484 x 10-7 (0.142)	1.846 x 10-6 (0.119)	0.857	0.944
TEP + Gadolinium	2.759 x 10-7 (0.241)	2.592 x 10-6 (0.051)	1.595	1.326

Table 4.05 - Comparison of Energy Absorption and Dose Enhancement Factors in MCNP Models of the Proportional Counter

This data shows a dose enhancement effect at both energies for a TEP proportional counter doped with gadolinium, although there should be a reduction in the number of counts for a boron-doped detector. This is fits in very well with the results that would be expected from a

theoretical approach, as gadolinium has an atomic number significantly greater than boron or any of the elements present in TEP. It is a little surprising that the results for boron showed such a reduction in the energy absorption, however, it must be noted that boron's low atomic number decreases the average Z of the atoms within the TEP, reducing the effects of elements such as calcium (Z=20). This will lead to a reduction in the photon absorption, especially at lower energies.

This suggests that the MCNP code is able to simulate the high Z to low Z interfaces studied here, as the results show a clear dose enhancement effect. Appendix I Section x1.4.3 contains the results obtained from an attempt to simulate the dose enhancement within a proportional counter using EGSnrc. This research was unsuccessful due to an error in the entry of the material composition data; however, it does contain a measure of the dose enhancement for a boron-doped proportional counter that can be compared with the MCNP model.

4.3.2.3 - Comparison of Results

Unfortunately the research in this section was unsuccessful due to errors in both the experimental technique and the EGSnrc model. The MCNP model shows clear evidence of a dose enhancement effect in a proportional counter doped with gadolinium, which could offer some evidence that its use in future low energy radiotherapy treatments would lead to an increase in the dose deposition within a target area. However, experimental evidence and a more effective model of the degree of dose enhancement would be necessary before any concrete conclusions could be reached.

After investigating the dose enhancement caused by gadolinium and boron in a TEP proportional counter using different radioactive sources, the next step was to find an experimental set-up that could be used to investigate this effect. Without access to a synchrotron facility, experimental work was conducted using the BAGINS Dynamitron facility at the University of Birmingham (Culbertson et al, 2004). The Dynamitron is discussed in Chapter I Section 1.3, discussing the way in which a Dynamitron produces a radiation field, and Section 4.1.4 of this chapter looks in depth at how the beam interacts with the detector to produce a signal.

4.3.3 - Dose Enhancement from a Neutron Field

This area of research looked at the dose enhancement within a proportional counter produced by the radiation field of a Dynamitron. Although the use of a Dynamitron to investigate the energy absorption characteristics of these detectors, and hence the dose enhancement, was a compromise it does show useful information on the effect of placing boron and gadolinium within these detector designs.

The aim of this research was to investigate the dose enhancement within the different detectors when subjected to a neutron-based radiation field. This is useful, because this work is aiming to look at ways in which the techniques first used with neutrons in BNCT can be applied to photon fields as the introduction of Boron and Gadolinium to cancerous tissue has already been proven in a BNCT context. By providing a measure of the dose enhancement within these specific detectors to a neutron field, it is hoped that the effectiveness of the photon-based dose enhancement can be put into context. The interaction of the neutrons with the materials within the detectors will also lead to the production of photons within the proportional counters, possibly giving an indication of the increase in energy absorption associated with the presence of these elements.

4.3.3.1 - Experimental Work

For this research, the detectors were placed in a water phantom within a Dynamitron beam for a period of 10 minutes with the particle accelerator running at a current of either 10 μA or 100 μA. This research was conducted using the 3MV Dynamitron based at the University of Birmingham Medical Physics Building, formerly the University of Birmingham Radiation Centre.

Figure 4.08a shows the energy absorption spectrum produced for the three detectors when exposed to the Dynamitron beam operating at a current of 10 μA.

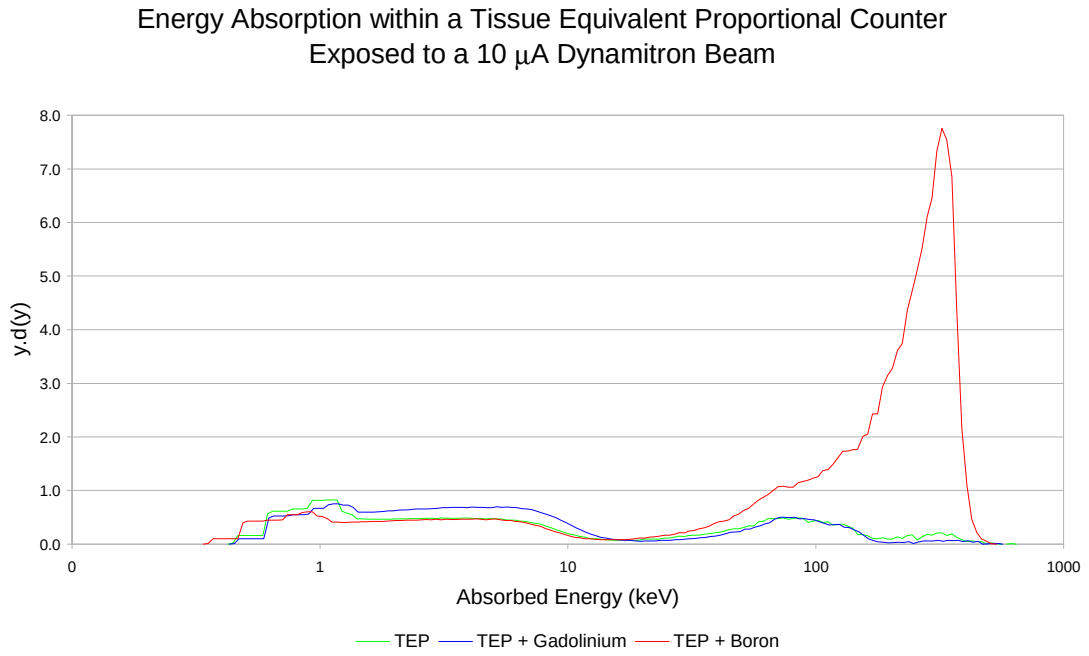

Figure 4.08a - Energy Absorption in Proportional Counters Exposed to a 10 μA Dynamitron Beam

This figure shows the increase in dose associated with the two different dopant elements. In this, there are two sets of peaks associated with the energy absorption spectra of the detectors, which have been affected in different ways by the beam components.

Below approximately 10 keV, there is a clear peak produced in all of the sets of data. This is due to the relaxation of the detectors after neutron capture has occurred, producing low energy photons, which are then captured through the photoelectric effect. For this peak there is clear evidence of dose enhancement due to the presence of gadolinium atoms within the detector, shown by an increase in energy absorption, with little difference in the spectra of the TEP and boron-doped detectors.

At energies above about 100 keV, there is a second peak in the data sets. This is due to the production of alpha particles and lithium ions within the detector, which deposit more energy within the detecting volume due to their shorter path lengths. It is clear that the presence of boron within a proportional counter has lead to an extremely large increase in the energy absorbed within the detector. The dose enhancement factor of the boron detector compared with the TEP detector reaches 38.8 at an energy of 323 keV, compared with the dose

enhancement of the gadolinium detector which is 0.25. The figures for boron show a large increase in energy absorption at higher energies due to the alpha particles and lithium ions created from the neutron capture as would be expected. Similarly the gadolinium results show an increase in energy absorption below 10 keV due to the emission of low energy photon and electrons due to the absorption of thermal neutrons. As is discussed in Section 4.1.4, the energy of the captured neutrons is released through the emission of internal and Auger electrons and low energy photons.

Figure 4.08b shows a close-up of the energy absorption spectra produced for the three different proportional counters below 100 keV.

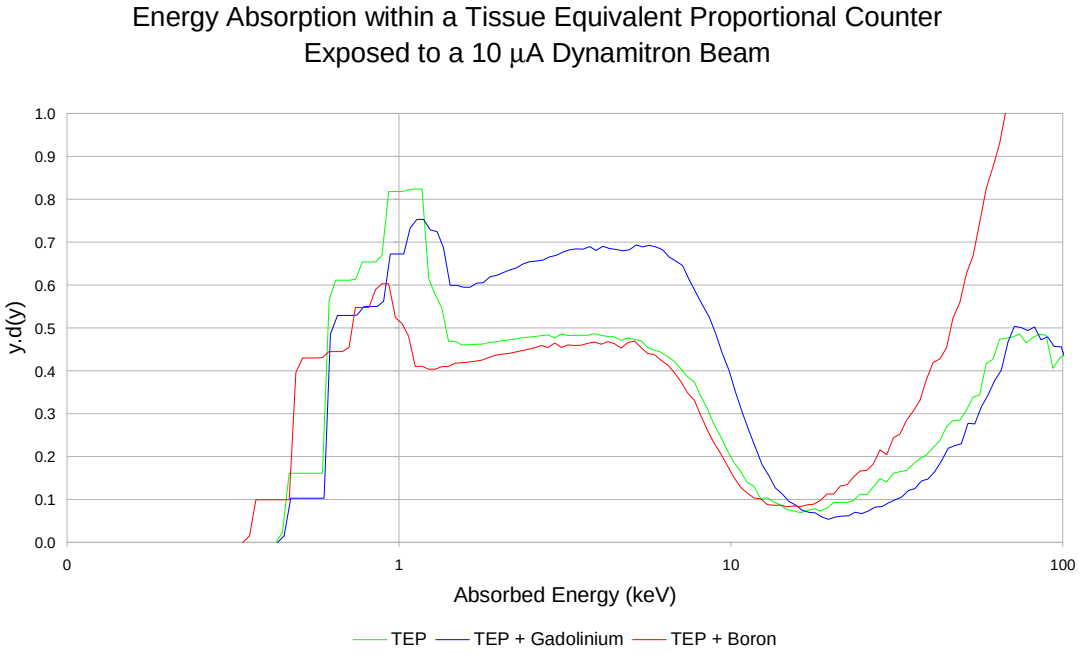

Figure 4.08b - Close-Up of the Energy Absorption Spectra for Proportional Counters Exposed to a 10 µA Dynamitron Beam

In this figure the dose enhancement caused by the presence of gadolinium atoms is clearly shown, with the dose enhancement for the gadolinium-doped detector being 1.42 at an energy of 5 keV and 1.84 at an energy of 10 keV, compared to the TEP detector. For the boron-doped proportional counter, there is no noticeable increase in the energy absorption of the detector at this energy range, with the detector showing a dose enhancement of 0.98 at an energy of 5 keV and 0.79 at an energy of 10 keV.

Figure 4.09 shows a comparison of the three detectors when exposed to a 100 µA Dynamitron beam.

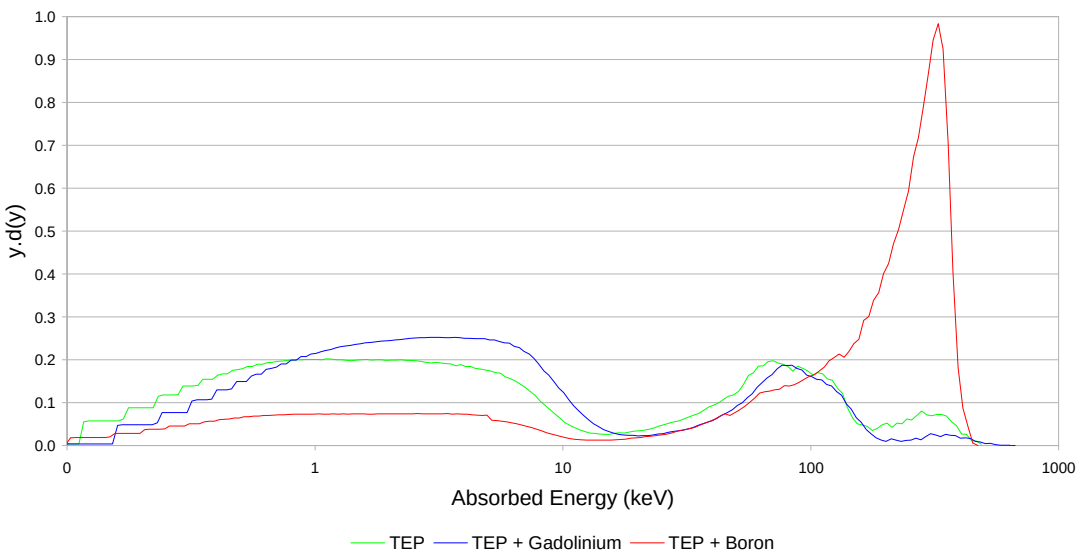

Figure 4.09 - Energy Absorption in Proportional Counters Exposed to a 100 µA Dynamitron Beam

In this graph, a similar pattern is obtained to that in Figure 4.08, with a clear peak in the spectra below 10 keV, due to the photon emission in the detector from the relaxation of atoms after neutron capture, and another peak above 100 keV due to the capture of alpha particles and lithium ions.

Compared with the MCNP results produced in the previous section, these results seem reasonable, with the presence of gadolinium leading to an increase in the energy absorption within a detector, but the presence of boron leading to a slight decrease. Although these two sets of data are not a direct comparison of the same experimental set-up, it is encouraging that the same pattern of energy absorption is found in both.

Although the greater neutron fluence of the beam allowed a more interactions to occur within

the same space of time, it did also lead to an increase in the dead-time of the detector. It is this increase in dead-time that is likely to have contributed to the difference between the spectra in Figure 4.09 and those in Figure 4.08a. Despite this, the two sets of results show similar trends in the data, showing that boron produces a large dose enhancement effect within a TEP proportional counter exposed to neutrons. Similarly, it appears that a low level of gadolinium in a TEP proportional counter will lead to an increase in the detector's absorption of gamma radiation through the photoelectric effect.

After limited success in demonstrating an increase in energy absorption within a gadolinium-doped proportional counter using a range of radioactive isotopes, the use of a Dynamitron neutron field has shown a definite increase in energy absorption within the detector at low energies. This suggests that introducing low levels of gadolinium into a tumour can lead to an increase in the dose to the targeted region when it is exposed to photon-based radiation.

A final area of interest in this chapter is the difference (if any) in the results obtained from the two different Monte Carlo codes used in this chapter. EGSnrc was used to produce an accurate measure of the energy absorption spectra for the TEP proportional counter, whereas MCNP has been used to model the geometry of the detector and investigate the effects of the high Z elements on the total energy absorption.

4.3.4 - Comparison of the MCNP and EGSnrc Codes

Having made use of both EGSnrc and MCNP4C in the simulation of the behaviour of a proportional counter, it is useful to compare the relative accuracy of the two different codes. Both MCNP4C and EGSnrc have their own advantages and uses, which will affect the choice of code for a specific problem.

MCNP4C has the advantage of being able to produce a variety of different geometries, a feature which make it possible for extremely complex arrangements of detector to be designed. Also, despite it being the slower of the two, it has proven easy to create short codes to slightly alter the input files and start the next run, allowing 'chains' of results to be produced over an energy range. Although MCNP lacks the level of accuracy in its electron

and photon models compared with EGSnrc, it has proven high enough to give an indication of the trends in all of the work undertaken in this thesis.

EGSnrc on the other hand has a much simpler set-up, with a geometry model solely composed of cylinders, although Section 4.3.1 shows that this can be used to produce an accurate model of some different shapes with a little thought. The big advantage of EGSnrc over MCNP4C, apart from its more complex electron and photon models, is its ability to produce an accurate spectrum for the energy absorption. This allows EGSnrc to simulate the spectrum that will be observed using the detector, allowing the model to be directly checked against the experimental results with a minimum of additional processing.

The results used in this section are based upon a TEP-based proportional counter model identical to that used throughout this chapter. The MCNP output file used for these results produces a value for the total energy absorption within the detector volume. The program ran for 500,000 counts as standard throughout this chapter.

EGSnrc as standard produces a spectrum of the energy absorption within the detecting volume so the absorption at a particular energy was integrated to obtain the total energy absorption for a particular source energy. The detector model used for the EGSnrc section of this section was the standard spherical approximation used throughout this chapter, again run for a total of 500,000 counts.

Figure 4.10 shows a comparison of the total energy absorption within the detector as calculated using the EGSnrc and MCNP codes. The error bars in the figure have been included to give a measure of the relative error of the two different codes.

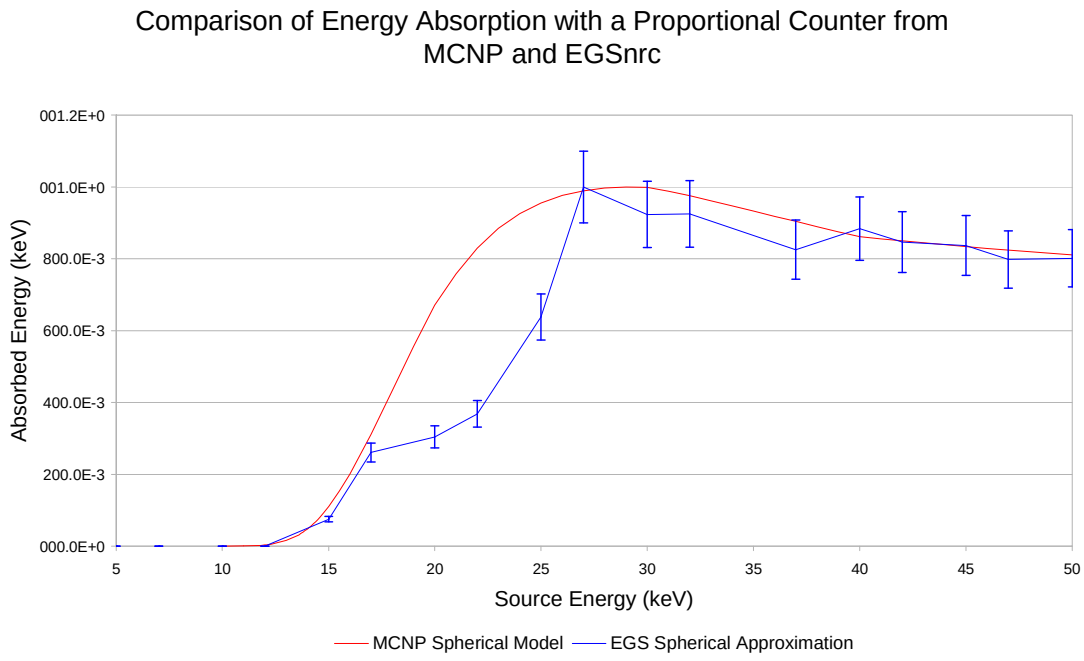

Figure 4.10 - Comparison of Energy Absorption as Calculated by MCNP and EGSnrc

As can be seen from these simulations, MCNP shows less relative error in its measure of the energy absorption within this energy range. This may show more variability in the more complex calculations run in EGS, despite the MCNP programs simulating 2,500,000 histories, compared to the 200,000,000 histories simulated in EGS. The EGS data contains error bars showing an error of ±10%.

Also worth noting is that, as mentioned in Chapter I Section 1.7.4, the run times for the EGSnrc code were on average significantly shorter. With the proportional counter model it took 0.57 minutes for EGS to simulate a million particles, and MCNP taking 10.62 minutes to perform the same calculation. Because of this, the EGS programs were set up to perform the same calculation using approximately 10 times the numbers of particles. These are purely approximations of the run times, as there were significant differences in the models used for both simulations.

4.4 - Conclusions

In this chapter, the main aim has been to look at the results obtained for a proportional counter under a range of different conditions and compare them with similar results obtained using Monte Carlo simulations. The aim of this has been to investigate whether or not the Monte Carlo programs are able to accurately predict the results obtained from a proportional counter under a range of different conditions for which the programs were not necessarily designed. These look at issues such as energy absorption at low keV energies and the differences in energy absorption due to interfaces between high Z and low Z materials.

Comparing the experimental results to the computer models allows a number of conclusions to be made about the accuracy of the computer simulations that will be relevant to the investigations in Chapter V, where modifications to the detectors are investigated. If a computer simulation can produce an accurate indication of the energy absorption within a detector it allows variations in the design to be tested by a computer simulation first and then reproduced so experimental readings can be obtained. This allows a number of different factors to be tested without expensive and time consuming modifications to the detectors that may not produce useful results.

In Section 4.3.1, experimental results obtained from the SRS Facility were compared with those produced by a Monte Carlo simulation using the program EGSnrc for a monoenergetic photon source at energies of 15, 28 and 33 keV. From this data it can be concluded that EGS is capable of producing an accurate measure of the energy absorption spectra in a proportional counter, with a good degree of agreement between the two sets of data at all of the energies tested.

There were, however, some differences in the energy absorption, with EGSnrc suggesting a larger absorption at the higher energy end of the absorption spectrum than was observed. This may be due to issues in the sensitivity of the detector itself, as opposed to problems with the simulation. As the detectors used for the experimental work had to deal with issues such as the carrying of charge through the gas and slight impurities and variations in the materials, there are bound to be some slight differences with Monte Carlo data which deals with an

idealised detector model.

In Section 4.3.2, the effects of dose enhancement upon the detector were first investigated and although the methods used proved challenging for producing reliable results, an MCNP model did suggest that there is a dose enhancement effect within a gadolinium-doped detector. Unfortunately, errors in the EGSnrc model and the experimental set-up meant that more definite conclusions were not possible. As it was difficult to gain reliable readings using different radioactive isotopes, a different method of investigating the dose enhancement in a proportional counter containing gadolinium or boron was attempted in the next section.

In Section 4.3.3, the energy spectrum produced within the three detectors when exposed to a Dynamitron beam was investigated. These results showed a clear increase in the dose deposited within a boron-doped proportional counter, due to the greater production of alpha particles and lithium ions. More interesting was the larger dose found in the gadolinium-doped proportional counter at the lower energies associated with the generation of low energy photons through the relaxation of atoms that had captured neutrons. This demonstrated that the presence of gadolinium in the detector leads to a dose enhancement effect that could potentially be used in the planning of radiotherapy treatments.

Finally, in Section 4.3.4, the total amount of energy absorbed by the two Monte Carlo codes was compared for a photon source of different energies. In this situation, the EGS code managed to calculate at about 20 times the speed of the MCNP code, allowing a larger number of particles to be simulated. On the other hand, however, the results produced showed a higher relative error, with MCNP producing a smoother energy absorption curve.

Both Monte Carlo programs showed a steady increase in absorption within the detecting volume as the source energy increased up to approximately 25 keV, before steadily decreasing above this value. This is due to the greater source energies leading to more energetic secondary particles that then deposit more energy within the detecting volume. This trend continues until the path length of the secondary particles becomes great enough to pass through the detector, leading to a steady decrease in dose deposition from that point on.

From the work contained in this chapter, it has been shown that EGSnrc can be used to accurately model the behaviour of a proportional counter, allowing it to be used to test the effect of changing the layout and design of the detector. As well as this, a clear dose enhancement effect has been found for a TEP proportional counter doped with low levels of gadolinium when exposed to a low keV photon field. In contrast, there is no increase in energy absorption in a similar detector doped with boron when exposed to the same radiation field, although when a exposed to neutrons, the boron leads to a large increase in the energy deposited within the same detector.

Chapter V - Variations in Proportional Counter Design

Having assessed MCNP and EGSnrc Monte Carlo models for the simulation of a proportional counter in Chapter IV, the next step of the investigation was to look at the effects of several different factors upon the detector characteristics. These cover a range of different areas of detector design, primarily looking at the accuracy of the Monte Carlo calculations compared to experimental results.

The first part of this chapter investigates the effects of varying the radiation field size in a manner based upon the aperture of a synchrotron. The radiation field sizes investigated were 1.0 mm by 1.0 mm, 10.0 mm by 10.0 mm and 100.0 mm by 100.0 mm, giving a field size smaller than, the same size as and significantly larger than the detecting element. EGSnrc was used for this research because it is capable of producing accurate simulations of the energy absorption spectrum of a proportional counter.

Another area of interest in this research was the effect of using low gas pressures in a proportional counter to simulate smaller cavity sizes. This was tested both experimentally and through Monte Carlo modelling, looking at the differences in energy absorption between a detector with an effective cavity size of 2.0 μm and one with further reduced gas pressure yielding an effective cavity size of 0.8 μm. As the effect of the gas pressure upon the energy absorption spectra for the proportional counter was important, EGSnrc was used to produce the Monte Carlo simulations in this section.

The final part of this chapter looks at the effects of different filling gases upon the energy absorption of a proportional counter. This was undertaken as the Boron and Gadolinium-doped models make use of dopant materials in the walls of the detector, with the detector element (filled with TEG) simulating a doped region. It seemed logical to test whether this approximation had an effect upon the energy absorption characteristics of the detector. As this was looking at the total energy absorption within a proportional counter across a range of source energies, MCNP4C was used to produce the simulation data for this section.

5.1 - Variations in Monte Carlo Models of a Proportional Counter

A number of different variations of the proportional counter models used in Chapter IV Section 4.2 were created for this chapter. This section discusses the differences between these and the previous chapter's models as well as the reasoning behind the changes and the effects these may have upon the results.

5.1.1 - EGSnrc Modelling of Aperture Size Variation

This series of simulations makes use of the standard proportional counter model developed in Chapter IV, using a model with pure TEP walls. The only difference between these simulations and those included in Section 4.2 is the changes in the field size of the source radiation.

It is hoped that this variation will test whether or not it is necessary for the synchrotron source to make use of a slot beam when irradiating a proportional counter. This is of interest because the experimental source at the SRS Facility scanned across the detector element in order to irradiate the detector evenly across its volume. It is worth investigating whether this was necessary, as this has an effect upon potential experimental set-ups that could be used in the future. The simulation compared the results of a narrow radiation source directed at the centre of the detector, a wider source covering the detector element only and a flood field.

5.1.2 - EGSnrc Modelling of Changes in Cavity Size

The next area of investigation looked at reducing the gas pressure within the proportional counter in order to simulate the effects of a smaller cavity size. For this the standard EGSnrc model used in Chapter IV Section 4.2.2 was used, with the only significant difference being a reduction in the density of the TEP within the gas-filled regions of the detector.

The was to offer a Monte Carlo model that could be compared with the experimental work to show whether EGSnrc could be used to accurately predict the results for a complex system like this. It was expected that the reduction in gas pressure would reduce the number of

interactions at lower energies, leading to the spectrum of energy absorption being skewed towards lower energy interactions.

5.1.3 - MCNP Modelling of Variation in Wall and Filling Gas

The final part of this chapter deals with an investigation into the effects of different filling gases upon the energy absorption of the detector. The reason for investigating this effect is to confirm an assumption made in proportional counter microdosimetry - that by adding dopant to the walls of the detectors we can simulate the energy absorption of doped small volumes. This work was undertaken to confirm that the lack of dopant materials in the filling gases themselves had no effect upon the energy absorption. Additionally it was looking to show that the important element in these detectors is the dopant elements within the detector walls. If this was shown to be untrue it could be an avenue for further research.

The detector models used in this section were based upon the standard spherical model of the proportional counter developed for MCNP in the previous chapter, with the only difference being the materials used in its construction. In this case, gadolinium-doped TEP was used for the construction of the walls in some of the models and gadolinium-doped TEG was used in some others. One model did not contain any gadolinium, one contained gadolinium in the detector walls, one had a gadolinium-doped filling gas and the final model had gadolinium within both the filling gas and the walls. The elemental composition of these materials is described in Appendix II Table x2.01. As there was no experimental component of this section, the accuracy of the final results is entirely dependent upon the accuracy of MCNP itself, which has been tested in Chapters II to IV. Through these chapters the accuracy shown has been high enough to at least suggest that an MCNP model can indicate a trend that will occur in experimental data.

5.2 - Results

5.2.1 - Effects of Aperture Size upon Energy Absorption

This section looks at the difference that changing the aperture size of the radiation source has upon the energy absorption spectra within a proportional counter. The results here were theoretical and intended to test the supposition that a source placed close to the detector would produce a similar effect to a slot beam irradiating the entire detector element.

Simulated Results

In Figures 5.01a and 5.01b EGSnrc was used to produce an energy spectrum to investigate the effects of aperture size upon the dose within a proportional counter. Figure 5.01a shows the energy absorption spectrum produced by a proportional counter exposed to a 15 keV monoenergetic source energy of varying aperture sizes.

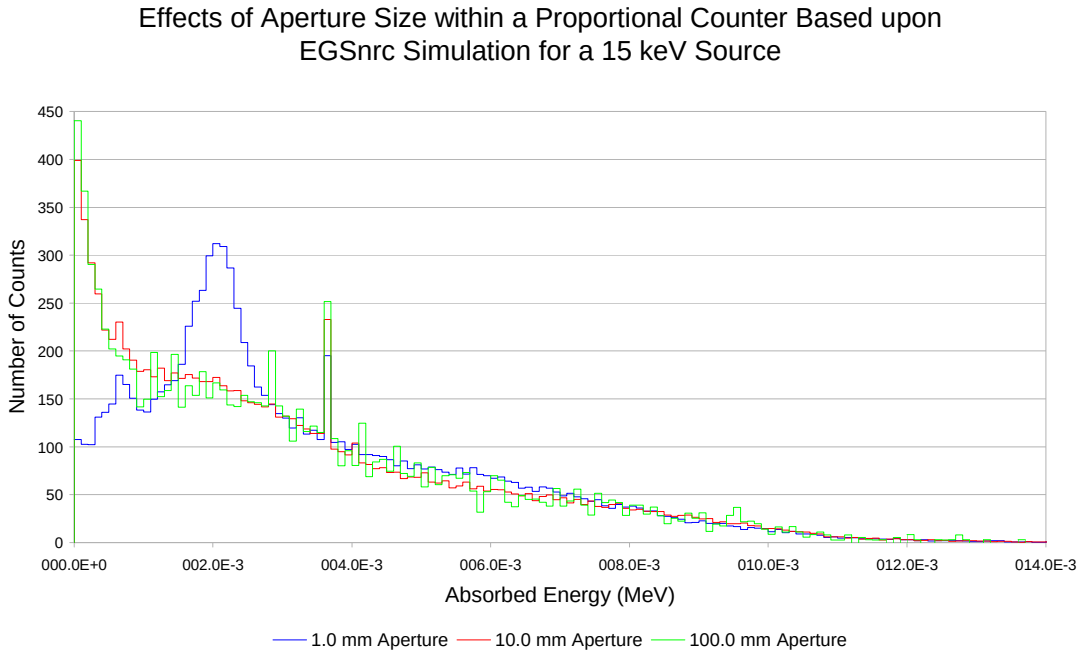

Figure 5.01a - Effects of Aperture Size upon Energy Absorption within a Proportional Counter for a 15 keV Source Energy

Looking at this figure, it is apparent that there is little difference in the energy spectrum

between the two larger aperture sizes. This suggests that there is little difference in the spectra produced by a radiation field that covers the detector and one that floods the detector and the surrounding area. This is expected as a large component of the energy absorption spectrum is made up of scatter in the detector, which will occur whether the source is larger than the detector or exactly the same size. The reason for choosing a narrower field is often more of a safety issue than one of experimental design.

What is interesting is the effect the narrowest aperture size has had upon the dose deposition within the detector, leading to a decrease in the absorption of extremely low energy secondary particles. This is presumably because less scatter occurs due to the radiation source being directed towards the centre of the detector volume. There is then an increase in energy absorption at around $2x10^{-5}$ keV, probably caused by more radiation being directed to the centre of the detecting volume and less lost to the other parts of the detector. In Figure 5.01b the same three aperture sizes are compared, but making use of a 33 keV monoenergetic photon source.

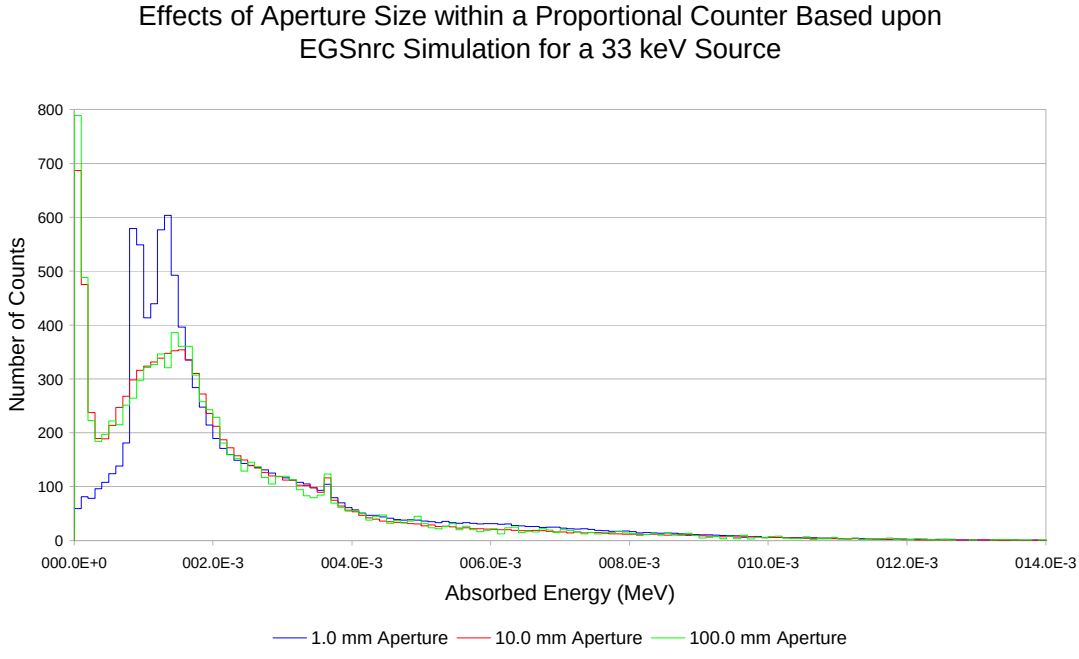

Figure 5.01b - Effects of Aperture Size upon Energy Absorption within a Proportional Counter for a 33 keV Source Energy

Figure 5.01b shows a similar relationship between aperture size and the energy spectra

produced. As before, there is little difference in energy absorption for the two larger aperture sizes. The smallest size leads to a decrease in the low energy absorption, which increases significantly at $1x10^{-5}$ to $2x10^{-5}$ keV before dropping off to produce a very similar distribution at higher energies.

These results show that when making use of a tightly collimated radiation source, such as that produced by a synchrotron, the radiation field needs to be the same size as the detecting element or larger. If the beam field size is smaller than the detecting element it will lead to a change in the shape of the radiation spectrum due to beam hardening caused by the reduction in beam scatter.

Errors

Table 5.01 below summarises the relative error in the EGSnrc calculations used to produce the data within this section. The EGSnrc calculations in this section simulated the behaviour of 2,500,000 particle histories.

EGS Model Source Energy	EGS Model Effective Cavity Size	EGS Maximum Relative Error
15 keV	1.0 mm	0.743
15 keV	10.0 mm	0.768
15 keV	100.0 mm	0.897
33 keV	1.0 mm	0.853
33 keV	10.0 mm	0.799
33 keV	100.0 mm	0.856

Table 5.01 - Relative Error in the EGSnrc Models Used to Investigate the Effects of the Radiation Source Aperture

These results yielded a larger relative error than would have been desirable, however the design of the detector, with a very small cavity size within a larger system, tends to lead to more variability in the readings.

5.2.2 - Effects of Cavity Size upon Energy Absorption

The aim of this part of the investigation was to look at how the internal cavity size would affect the ability of a proportional counter to act as a photon detector. Specifically this looked at whether the gas pressure could be reduced further without compromising the quality of the results produced. As the initial experimental work had been conducted with a tissue equivalent gas density of 1.63×10^{-4} g.cm^{-3}, producing an effective cavity size of 2 μm, these experiments compared the previous results with those obtained from a gas density of 6.55×10^{-5} g.cm^{-3}, with an effective cavity size of 0.8 μm.

Compared to the results produced previously, it would be expected that the numbers of particles interacting with the walls of the detector would not be affected by the pressure (or density) of the fill gas. However, the probability of producing an interaction that would be detected by the proportional counter would decrease due to the lessened stopping power of the detector gas cavity. This decrease in the probability of the fill gas interacting with the secondary particles produced by photon interactions will effectively increase the path length of these secondary particles. This will make the gas filled cavity act in the same manner as a smaller-sized cavity as discussed in Chapter I Section 1.6. This should lead to a decrease in the probability of detection, as well as a decrease in the average energy of the particles interacting (as the higher energy particles will pass through the cavity without interacting).

Experimental Results

Figure 5.02 shows the energy absorption within the three proportional counters at a low gas pressure exposed to a Cobalt-60 radiation source. Although the energies emitted by this source are a lot higher than would be ideal for this research, the source was easily of a high intensity and had previously shown a good consistency in experimental tests compared with the other sources available. The data comparing the energy absorption spectra of the proportional counters to three different radiation sources is included in Appendix I Section x1.4.3.

Note that although all of the results showed a large amount of noise at the lower end of the

spectrum (which has been removed from these results), the results for the TEP detector showed a very large amount of noise in the signal. This made it very difficult to distinguish the signal from the background signals, so Figures 5.03a and 5.03b look only at the results obtained for the detectors dosed with Gadolinium and Boron.

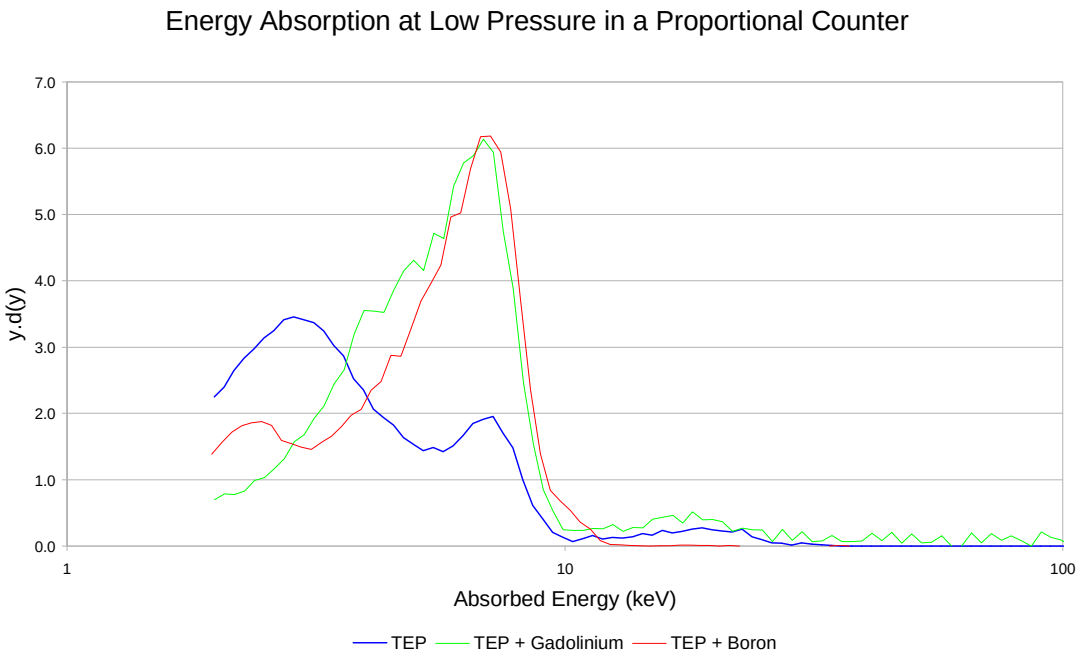

Figure 5.02 - Energy Absorption Spectra for Three Different Proportional Counters at Low Gas Pressure

From this figure, it appears that the energy absorption within the detector was the same for the detectors doped with boron and gadolinium, with little difference in the energy absorption or the spectrum shape. This is because the high energy of the photon source leads to the primary interactions within the detectors being via pair production, which is affected by the atomic number of the elements present by a Z^2 relationship.

The energy absorption spectrum from the TEP detector would be expected to follow the same pattern, as the densities of the materials present is the same. The differences in the spectra are most likely due to the problems found with obtaining a strong signal with a proportional counter at this gas pressure. This is because the amount of signal to noise produced is smaller, therefore making it harder to filter out, making it necessary to ignore the spectra below ~2.0 keV leading to a significant loss in count rate. It is worth noting that the results obtained at

this gas pressure are extremely close to the limit of the proportional counters' accuracy as it is beyond the minimum pressure the detectors were designed for.

In Figure 5.03a the energy absorption spectra produced by a gadolinium-doped detector are compared under the two different gas pressures are compared.

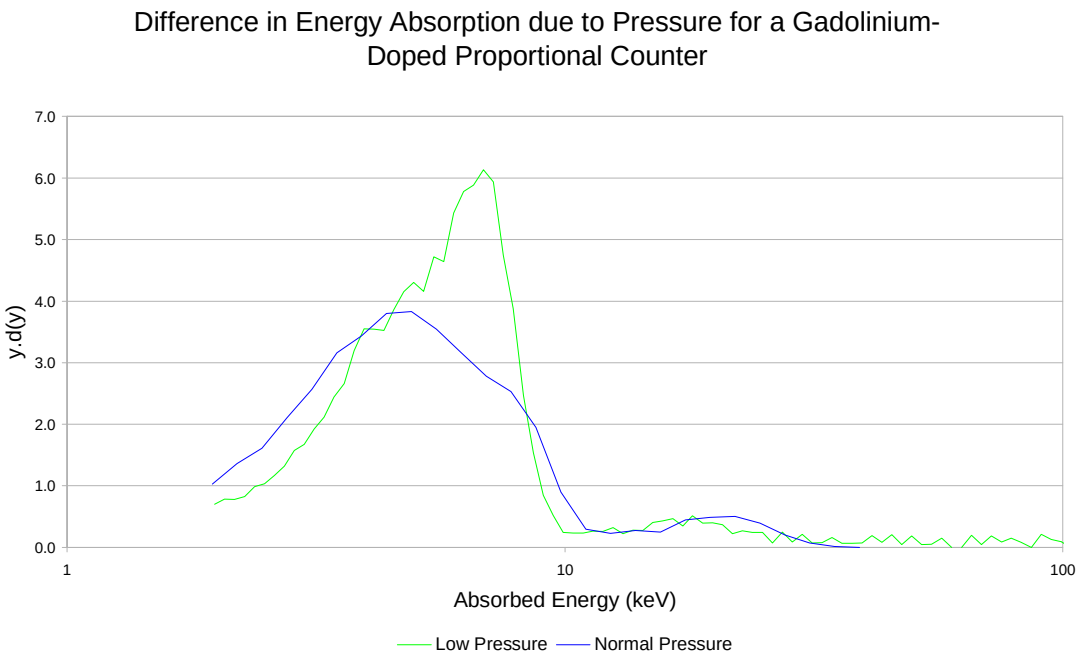

Figure 5.03a - Comparison of Energy Absorption in a Gadolinium-Doped Proportional Counter at Different Gas Pressures

In this figure, the effect of the lower pressure can be seen by a shifting of the energy spectrum, with a greater amount of the dose within the detector being due to higher energy. Some of the difference in the spectrum may be due to the normalisation of the data, as the proportional counter results are normalised such that the drop-off region of the curve is centred on 8.25 keV, the maximum energy of a secondary electron within the detector.

In Figure 5.03b the energy absorption within a boron-doped proportional counter is compared for the two different gas pressures.

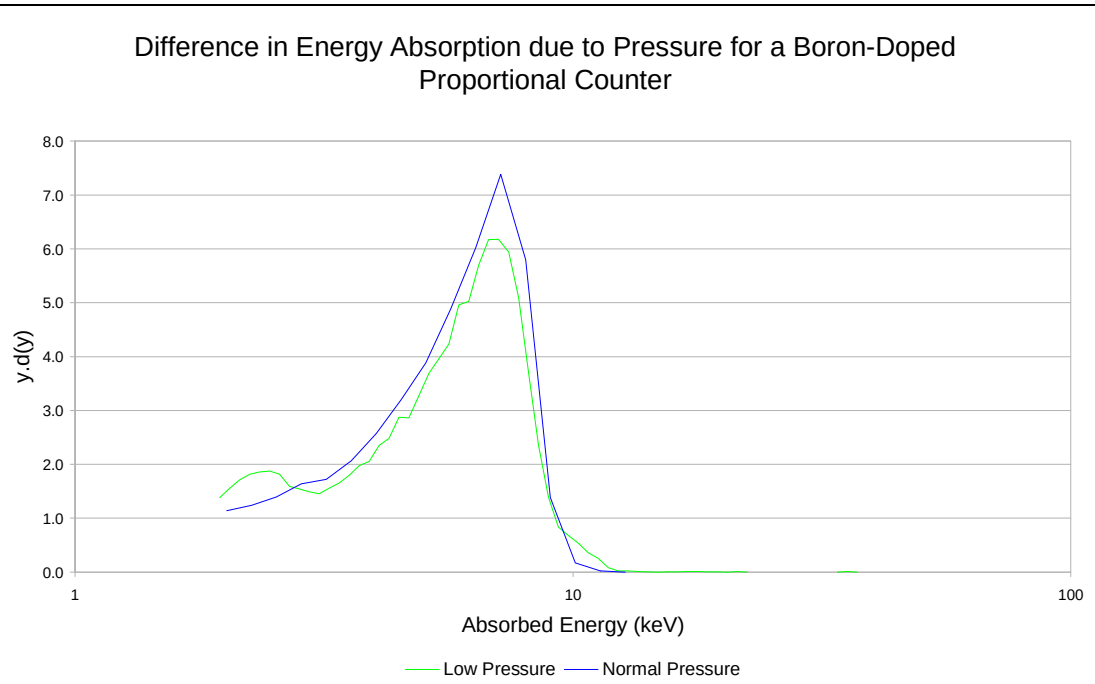

Figure 5.03b - Comparison of Energy Absorption in a Boron-Doped Proportional Counter at Different Gas Pressures

This figure is interesting, as the detector shows little difference in the energy absorption spectrum for the two different gas pressures. The only really noticeable difference is a lack of definition in the spectrum obtained for the lower pressure readings, probably due to the noise in the signal rather than a change in the dose deposition.

It is unclear why there is such a difference in the two comparisons in Figures 5.03a and 5.03b, it would be expected that the results for the boron-dosed detector would mirror those of the gadolinium-doped one. The reason for the similarity in the two sets of results may be due to one of several factors. First, there is the possibility that there was a flaw in the method used to measure the pressure in the detector, leading to both sets of results being produced from similar detectors. This seems unlikely as the gas filling rig has a pressure meter built into it and this same rig was used to fill the gadolinium-doped and pure TEP proportional counters. Therefore any errors that occur would probably appear in both data sets. Secondly, there may be an error in the data analysis used, which may have lead to an error being included in the final set of results. The data has been checked several times, however, and the same results have been obtained every time. Finally, it is possible that the large amounts of noise in the data sets may have created errors within the data that it may be difficult to account for. Again,

this seems unlikely, as the results for the two doped detectors seem relatively consistent single peak, whereas those of the TEP proportional counter shows several peaks, at least one of which is due to noise.

Without further study, it would be impossible to tell which pattern of response is most representative of the detector under this pressure. It is hoped that a Monte Carlo study of the same effects will allow the underlying trend to be determined.

Simulated Results

The results produced by EGSnrc looked at the spectra produced by two different photon source energies, 15 keV and 33 keV. These energies were chosen because they were used to produce experimental results during the research at the SRS facility, so could be easily compared to existing results. The results obtained for a TEP detector at both an effective diameter of 2 μm and 0.8 μm are included in this section.

These data sets were simulated using the Monte Carlo model produced for EGSnrc and characterised in the previous chapter in Chapter IV Section 4.2. The EGSnrc models were simulated for the TEP proportional counter and for two variations which contained small concentrations of gadolinium and boron in the detector walls. These were compared at the standard gas pressure and again at a lower gas pressure used in the experimental data for the detectors. Figure 5.04a summarises the energy absorption spectra for the proportional counter models when subjected to a monoenergetic source energy of 15 keV.

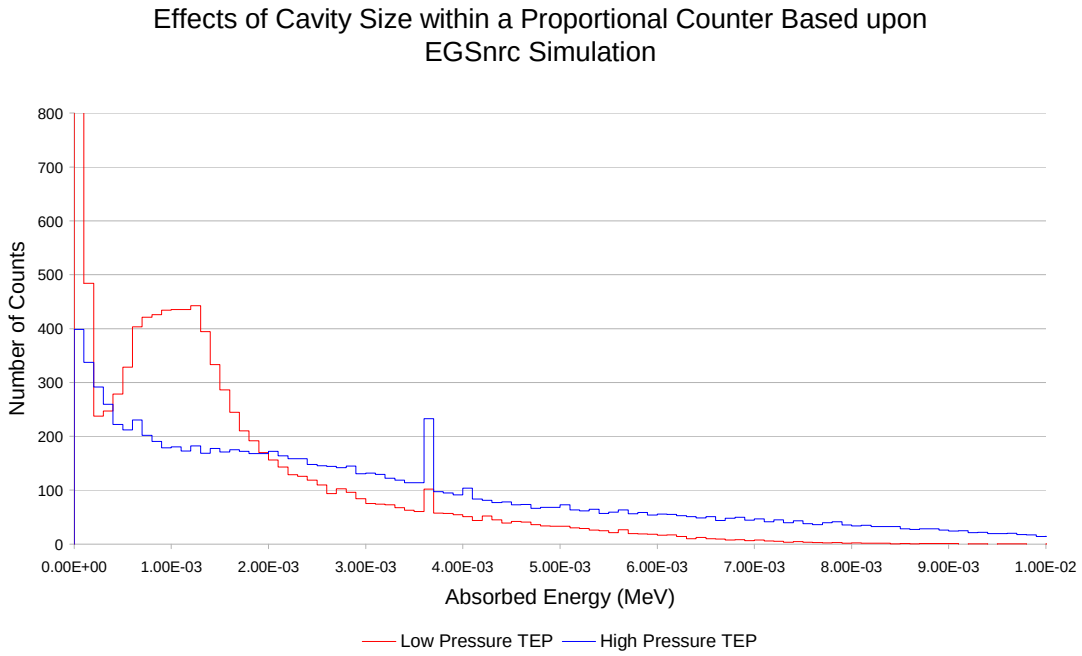

Figure 5.04a – EGSnrc Model of Energy Absorption in a Proportional Counter at Different Gas Pressures Exposed to a 15 keV Source

In this figure, it is apparent that the principal effect of the lower gas pressure has been a reduction in the amount of energy deposited at higher energies, coupled with an increase in absorption at lower energies. This occurs because the smaller effective cavity size reduces the probability of the fill gas capturing the secondary particles produced within the wall of the detector as their energy increases, effectively increasing their path length within the detector element. Despite this, the lower gas pressure shows the same characteristic peak at 3.60 to 3.70 keV.

In Figure 5.04b, the energy absorption spectra are shown for the different proportional counter models when subjected to a monoenergetic photon source with an energy of 33 keV.

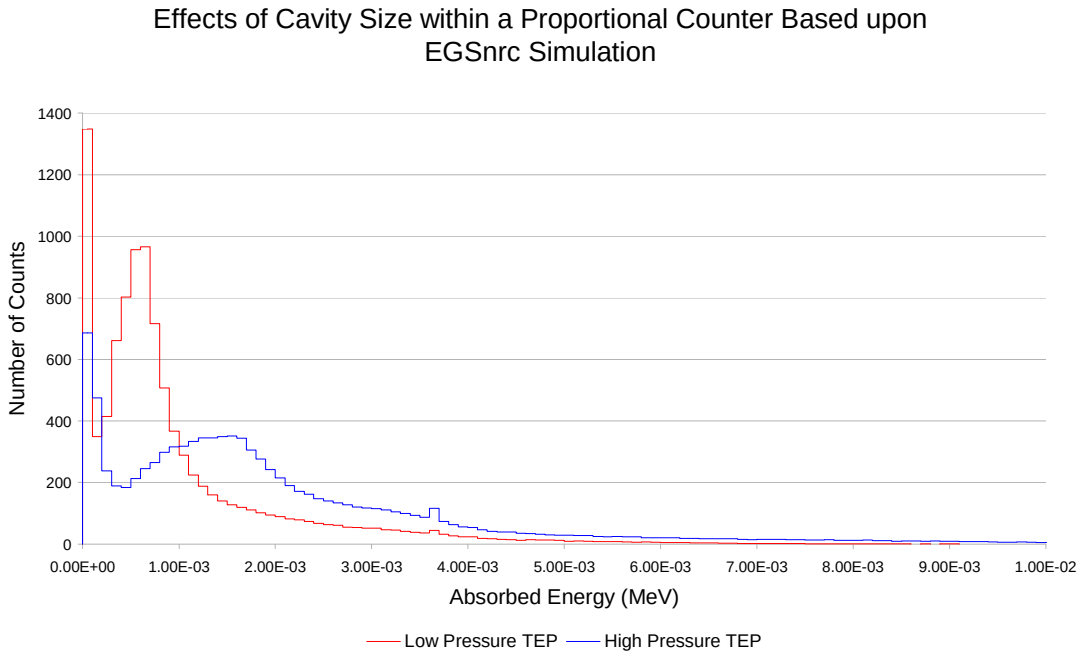

Figure 5.04b – EGSnrc Model of Energy Absorption in a Proportional Counter at Different Gas Pressures Exposed to a 33 keV Source

In this figure the same pattern occurs as that found in Figure 5.04a. Again, it can be seen that the proportional counters with the lower filling pressure display a peak absorption at a lower energy, with less absorption of high energy secondary particles, as would be expected from an analysis of the problem.

Also of interest is the similarity between the three sets of proportional counter models, using a TEP detector, one doped with gadolinium and one doped with boron. This further suggests that EGSnrc is unable to adequately simulate the effects of dose enhancement within a detecting volume adjacent to a higher Z material.

Errors

Table 5.02 below summarises the relative error in the EGSnrc calculations used to produce the data within this section. These calculations were run for a total of 200,000,000 histories. The maximum relative error is based upon the highest error value across the energy spectrum for the proportional counter model.

EGS Model Source Energy	EGS Model Effective Cavity Size	EGS Maximum Relative Error
15 keV	2.0 μm	0.768
15 keV	0.8 μm	0.778
33 keV	2.0 μm	0.799
33 keV	0.8 μm	0.732

Table 5.02 - Relative Error in the EGSnrc Models Used to Investigate the Effects of the Filling Gas Pressure

From this table, it appears that the maximum relative error in the simulations was reasonably consistent across the energy and pressure ranges. In the simulations the 33 keV source energy yielded the largest variation in error, but this is consistent with random fluctuations in the energy absorption caused by the modelling of the particle interactions.

5.2.3 - Effects of Filling Gas upon Energy Absorption

The aim of this section was to look at whether it is an acceptable approximation to assume that the dose enhancement within a detector will be unaffected by the lack of a high atomic number materials in the filling gas. During the course of this research, a proportional counter with a low concentration of gadolinium in the detector walls has acted as a representation of the behaviour of a small volume of gadolinium-doped tissue. As the detector gas does not contain any gadolinium at all, it is worth investigating whether or not this has an effect upon the energy absorption of a theoretical detector that contains gadolinium. These results were calculated using MCNP4C, as this code has shown a good approximation of the dose enhancement within a detector in past research. Additionally, as only the total energy absorption within the detecting element was required in order to see whether it has an effect or not, MCNP seemed the logical choice for this area of research.

The MCNP proportional counter model described in Chapter IV Section 4.2.1 was used for this research, with each simulation being run for 500,000 histories across a range of source energies from 5 to 50 keV in 1 keV intervals. The aim of this section is to see whether including gadolinium in the filling gas of a proportional counter has an effect upon the total

energy absorption of the detector and how big an effect this is compared to adding gadolinium to the detector walls.

Simulated Results

Figure 5.05 shows the total energy absorption of a proportional counter which contains a tissue equivalent medium with gadolinium included at a low concentration in some situations. The red line represents a detector that does not contain any gadolinium at all, the orange line is a detector with gadolinium present only in the filling gas, the blue line shows a detector with gadolinium present in the detector walls and the green line shows a detector with gadolinium present in both the walls and the filling gas.

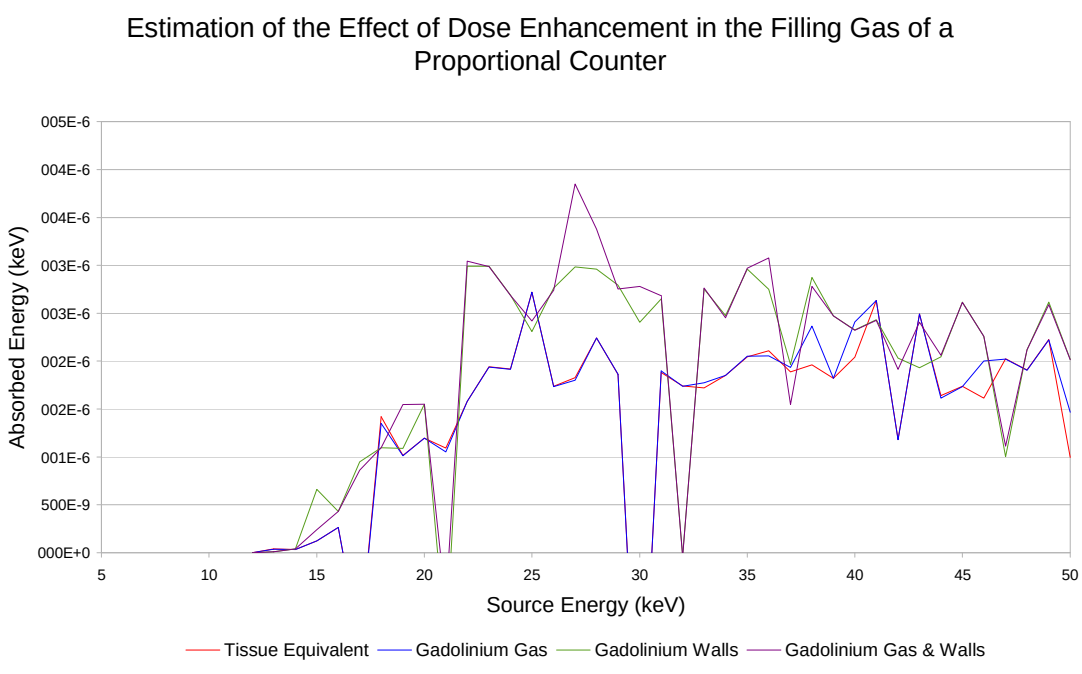

Figure 5.05 - MCNP Model of Effects of Gadolinium as a Component of the Filling Gas in a Proportional Counter

This figure shows that there is little impact upon the results when gadolinium is added as a filling gas, with the results being heavily dominated by the wall material. When the wall material is tissue equivalent, the filling gas has almost an almost negligible effect upon the energy absorption of the detector, to the extent that it is difficult to even work out the position of the orange line. A similar pattern is observed for the simulations where there is gadolinium

present in the wall material.

One point of concern in these readings, however, is the presence of negative energy absorptions in some of the results. This could potentially be due to particles being ionised within the detecting element and then scattering outside the volume, effectively taking their energy with them. This, however, seems unlikely and seems to have been repeated at several points in all of the data sets, repeating in both the TEP wall and gadolinium-doped wall results. It would be worth repeating this simulation, possibly with a significantly extended number of histories, in order to see if this error is an issue with the program or something more fundamental.

Errors

Based upon values generated by the MCNP4C program, the errors present in the data is summarised in Table 5.03.

Monte Carlo Model	**Relative Error**				
	10 keV	**20 keV**	**30 keV**	**40 keV**	**50 keV**
Tissue Equivalent Walls and Filling Gas	0.707	0.167	1.000	0.281	0.635
Tissue Equivalent Walls and Gadolinium-Doped Filling Gas	0.707	0.168	1.000	0.326	0.606
Gadolinium-Doped Walls and Tissue Equivalent Filling Gas	0.707	0.529	0.130	0.256	0.146
Gadolinium-Doped Walls and Filling Gas	0.707	0.530	0.198	0.256	0.146

Table 5.03 - Summary of Errors in Monte Carlo Calculations of the Wall Effect

These calculations were run for 500,000 particle histories and the table shows the relative error calculated in intervals of 10 keV. The total time required to produce these results was

116 hours and 23 minutes. This data shows that the error in the results was a lot greater than would have been desirable; however, the long processing time limited the accuracy that could be achieved. In the first two sets of errors, the results for 30 keV source energy coincided with a point in which the energy absorption dropped to a negative value, and similarly the relative error shown for these results is 1.000.

5.3 - Conclusions

This chapter lacked a single aim in the same manner as Chapters II to IV, which investigated the use of a detector and then produced a Monte Carlo model that could accurately simulate the characteristics of that detector. Instead this chapter looked at how variations in particular detector parameters affect the results obtained. These parameters were chosen because they are difficult to adjust in an experimental set-up but easy to modify in a Monte Carlo simulation. Because of this there is no one conclusion that can be drawn from this data, so this section will be forced to look at each investigation in turn and draw conclusions based upon the research undertaken.

Looking at the effects of variation in the aperture of a radiation source directed at a proportional counter it was shown that of the three simulations produced, those with an aperture size of 10.0 mm and 100.0 mm were almost identical. This suggests that for an aperture the same size as the detecting element or larger, there is no difference in the energy absorption. Potentially there may be a difference introduced through variation in the fluence of the radiation beam, but that may be accounted for by the inverse R^2 rule, which states that as the distance to a source increases, the quantity of radiation reaching a detector will decrease at a rate proportional to R^{-2}. More interesting is the difference in the energy absorption spectrum between the two larger aperture sizes and the 1.0 mm aperture.

The difference in the energy absorption that was noted for the smaller aperture size was most likely due to the lack of scatter into the detecting element from the walls of the detector, except along the very centre. This shows that even small differences in the set-up of an experiment like this can lead to large differences in the final results obtained.

In the second part of this chapter, the effects of lowering the gas pressure to simulate a smaller cavity size was investigated. The Monte Carlo results obtained showed very clearly that the reduction in cavity size would result in the detector being unable to absorb secondary particles with an energy above a certain threshold, changing the shape of the spectrum obtained. The experimental work, however, was unable to conclusively recreate this effect, most probably due to the problems with the levels of noise in the signal, as seen in Figure 5.02.

In the final section of this chapter, the effects of adding higher Z materials into the filling gas of a detector was investigated and compared to those obtained through just having the same elements in the same concentrations only in the walls. For the energies being studied it appears that adding higher Z elements to the filling gas to make them similar to the atomic numbers present in the walls is unnecessary. This would be a product of the proportion of secondary particles produced in the walls compared with those produced in the filling gas. From these results, it appears that such a small proportion of the secondary particles present are produced in the filling gas that any small differences in atomic number between it and the wall material is largely irrelevant and can be ignored. A far more important factor to account for is the density of the filling gas, as it can have a significant effect on the energy absorption characteristics seen.

Chapter VI - Final Conclusions

The work conducted through this thesis has investigated different detector designs and the dose enhancement within those detectors for low energy photon beams, particularly through the use of simulation using the Monte Carlo programs EGSnrc and MCNP. The energy absorption characteristics of a wide range of detectors, from the solid state (Diamond Detectors and TLDs) to gas filled proportional counters have been investigated and compared with Monte Carlo simulations. This has included looking at the dose enhancement effects of different high Z elements within the detector designs both directly and indirectly. The research has looked at the simulation of different detector designs using the Monte Carlo technique, as well as looking at dose enhancement effects that could lead to future radiotherapy methods.

During this investigation a large amount of data was accumulated and a number of conclusions were reached, which are summarised in this chapter.

6.1 - Summary of Chapters

Chapter II - The Diamond Detector

The diamond detector investigation in Chapter II looked at a detector already used in Radiation physics and looked at methods for improving the Monte Carlo predictions of its behaviour when exposed to low energy photons. The research looked in particular at the effects of the type of model used and the dose enhancement caused by the electrical contacts.

From the results in this chapter, it was concluded that a more complicated model produces a greater agreement with experimental data. The research compared the results obtained from a cylinder-based model of the detector with a more complex model that included the positions of the electrical contacts and internal wiring. Although both models showed some agreement with the experimental results, the more complex model had a better agreement with the energy absorption spectra produced.

Another conclusion reached was, having proved the existence of gold and silver within the

detector, that the presence of these elements has a significant effect upon the energy absorption of the detector, although the exact proportions of each had little effect. This shows that the presence of high Z materials leads to an increase in the energy absorbed by the detector due to the photoelectric effect within the energy range investigated.

Chapter III - Optic Fibre TLDs

In Chapter III, the use of optical fibres as a means of measuring the dose produced by a low energy ionising photon field was investigated. After studying the energy absorption characteristics of this detector using both experimental and Monte Carlo techniques, several conclusions were reached.

The most important discovery was the difficulty of using such small volume detectors. The technique used involved such small volumes of material, the results proved too variable, with too low a level of consistency in the readings. Despite this, evidence was found of thermoluminescence occurring in the fibres used, suggesting that an improvement in technique may be possible that could make these detectors a viable TLD design.

In addition to this, there were some intriguing similarities between the MCNP-based model of the optic fibre TLDs and the results obtained experimentally, but only for an energy greater than 20 keV. This suggests that MCNP could be a useful tool in the investigation of these radiation detectors, but a lot more work will need to put into their use before they can reliably be used as a radiation dosimeter at the photon energies tested.

Chapter IV - Proportional Counter Dosimetry

In this chapter, the behaviour of a proportional counter when exposed to both photons and neutron was assessed and compared with results obtained using the Monte Carlo codes MCNP and EGSnrc. A model was produced of the proportional counter using EGSnrc, and a comparison between the experimental work and the simulations showed a definite agreement between the two sets of data.

The research then looked at the dose enhancement effects of including gadolinium and boron within a proportional counter, although a direct measure of the dose enhancement from these detectors proved difficult. Using the MCNP4C code, a measure of the dose enhancement effect was produced showing that adding gadolinium to a TEP proportional counter should lead to an increase in the energy absorption of the detector at energies below 10 keV. A similar comparison for a boron-doped proportional counter showed a small decrease in the energy absorption.

When exposed to a neutron beam produced by a Dynamitron, a gadolinium-doped detector showed an increase in absorption due to the emission of low energy photons within the detector material. This suggests that gadolinium could be a useful avenue of research for low energy photon-based radiotherapy. The boron-doped data showed no significant increase in energy absorption due to the low energy photons but demonstrated a much higher neutron capture compared with the other two detectors leading to dose enhancement.

Finally, a comparison between the EGS4 and MCNP4C codes was produced, to see if the results produced by both codes were similar. Plotting the two sets of data on the same axes showed that both codes produce a similar energy absorption curve, however EGS4 produces its results more rapidly but with a greater degree of relative error.

Chapter V - Variations in Proportional Counter Design

Finally, in the last chapter, the effects of modifications in the parameters of the detector were investigated to see the effect they had upon the dose deposition.

The first section showed that there was little difference in the energy absorption spectra of a proportional counter between a radiation field the same size as the detecting element and one ten times the size. On the other hand, the lack of scatter found the shape of the spectrum changed with the narrow beam due to the reduction in scatter within the detecting element. This means that when using a heavily collimated source such as a synchrotron, the beam profile must be larger than the detecting element, otherwise it will change the spectrum of the energy absorption. This is due to beam hardening produced by the more directed source

having a smaller scatter component.

The next section then looked at the effects of gas pressure upon the energy absorption characteristics of the proportional counter. This showed that for an EGSnrc model, the spectrum produced showed the effects expected, with the higher energy secondary particles being lost due to their longer path lengths as the gas pressure was reduced. The experimental work, however, proved difficult due to the detectors operating at such a low gas pressure, making the noise in the signals much larger and the energy absorption less. Despite this the results showed some promise and the results for the gadolinium and boron doped detectors suggest that given more time it is possible to produce more accurate results for the proportional counters at these low gas pressures.

In the last section, the wall effect was investigated, looking at whether adding gadolinium to the filling gas has a noticeable effect upon the energy absorption characteristics of the detector. Using MCNP4C the total energy absorption for a proportional counter with and without gadolinium in the walls and/or filling gas was simulated for an energy range of 5 to 50 keV. The results suggested that adding a 0.1 % concentration of high atomic number elements to the filling gas has little effect upon the energy absorption characteristics of a proportional counter. A much more important factor affecting the energy absorption is the atomic number of the elements present in the walls.

6.2 - Overall Conclusions

Comparing the results from the different chapters in this document, three very different detector designs can be compared and their simulation using two different Monte Carlo codes evaluated.

The experimental work allowed several different approaches for the field of small-volume dosimetry to be investigated. Although the work in Chapter II investigating the effects of modelling a diamond detector was successful, there are limits to its usefulness in looking at the dose distributions over small scales. The research was followed by smaller designs of radiation detector being investigated. The use of optic fibres as TLDs as detailed in Chapter

III would have been a useful avenue of research as they are small enough to be placed in locations such as the fingertips or inside the body. As the research continued, however, it was found that the reliability of such small devices was limited using the equipment and techniques applied. Despite some promising data a new avenue of research was undertaken to look at dose deposition on small scales. Proportional counters were investigated as a method of producing a simulation of a micron-scale detector, as the gas pressure could be altered producing a range of effective cavity sizes. Chapter IV looked at characterising the proportional counter and comparing it to Monte Carlo models, before Chapter V looked at the effects of different factors upon the accuracy of the readings produced.

From this, it can also be concluded that there is a great deal of potential in the use of gadolinium as a dose enhancement agent. Through both experimental work and MCNP simulations it has been shown that the presence of low levels of gadolinium leads to a significant increase in energy deposition within a detector. This could lead to a new contrast medium for use in radiotherapy, as gadolinium is non-toxic and could potentially be added to chemotherapy drugs to increase the radiation absorption in a targeted region. Additionally, Chapter II shows that the presence of gold or silver in the region of a detecting element can lead to a noticeable increase in energy deposition, showing two more elements that could be of use in this field.

Looking at the use of Monte Carlo in the simulation of different detector designs, it has become clear that there are several factors that need to be appreciated when designing the model. Both MCNP and EGSnrc showed advantages in different areas of the investigation and limitations in other areas.

First, the Monte Carlo code used should be chosen with respect to the aims of the investigation. The MCNP code is unable to produce an accurate energy absorption spectrum for specific source energies, so the research in Chapters IV and V were produced in EGSnrc. Both codes were used in this research to produce an accurate indication of the total energy absorption across a range of different source energies, as well as allowing more complicated geometries to be constructed. Of the two codes MCNP4C proved useful due to its complex geometry model which allowed a range of different detector geometries to be modelled

accurately. It was, however, limited by its simpler electron and photon models as well as an inability to produce an accurate energy absorption spectrum. EGSnrc on the other hand only allowed the construction of geometries based upon cylinders on a single axis but is able to produce an accurate energy absorption spectrum that can be directly compared with experimental results.

Looking at the complexity of the computer model used compared to the results produced experimentally, it was clear that a model should have a geometry similar to the detector being used and similar materials. It was shown in Chapter IV and V that the EGSnrc code was able to produce very accurate spectra for the proportional counter and do so in less time than MCNP. On the other hand, MCNP4C was used in all of the chapters to produce detailed models of the detector geometries that proved to be an accurate measure of the total energy absorption.

6.3 - Further Research

As with all scientific research, this document is only a stepping stone, providing a few lines of enquiry that can later be built upon to advance our knowledge in this field. It has shown that Monte Carlo modelling can be used to produce accurate simulations of a range of different detector designs and suggested some of the limitations in this method. As well as this, it has looked at the increase in dose deposition associated with some high Z elements, including gadolinium in some depth as well as gold and silver. From the conclusions reached in Section 6.2, there are some clear avenues for future research that can be seen in this document.

The first area which could provide a valuable opportunity for further research is in the work described in Chapter III. The data suggested that there is a definite thermoluminescent effect found in germanium and erbium-doped optic fibres, although the equipment used meant that it was impossible to produce reliable readings. It is possible that further research could overcome the problems found with the method used in this chapter, possibly through the use of laser thermodosimetry. It is also probable that more research into the optimum dopant materials to introduce into an optic fibre, as well as research into the best length and diameter for the individual fibres could produce a significant increase in the accuracy of the results

produced.

A second area of research that could follow on from this work is in the field of dose enhancement, as this has shown that the presence of low levels of gadolinium in a proportional counter leads to an increase in energy absorption. Further experimental work could look at quantifying this dose enhancement through the use of synchrotron radiation fields, determining the optimum source energy for producing dose enhancement. Additional investigations could also ascertain the levels of gadolinium required for an effective increase in energy absorption. This would give an indication of the levels required to make a radiotherapy treatment using gadolinium dose enhancement effective. Similar experiments could also look at other non-toxic high Z materials and determine how much of an increase in dose deposition is possible. In this thesis the dose enhancement effects of silver and gold were investigated indirectly and an increase in energy absorption was detected. Further investigations could be conducted in this direction.

Finally, it was shown that gas-filled proportional counters can be used to simulate even smaller cavity sizes. Although the attempts to use the different proportional counters to achieve an effective cavity size of 0.8 microns were only partially successful, the research showed that EGSnrc can be a useful tool in evaluating these detector modifications. Further work could identify and eliminate the problems found in producing data using these proportional counters and allow them to be evaluated at a range of different source energies using a synchrotron.

Appendices

Appendix I - Raw Data

This section is included to allow an evaluation to be made of some of the results that were not included in the main text for reasons of space. This includes the calibration of the proportional counter as well as results that did not produce the expected results. In the case of results that did not follow the trends expected, comments on what the source of the error may be are included.

This section is not numbered in the same manner as the previous chapters; the sections are numbered in relation to the chapter they have been taken from, in order to allow an easy comparison between the different sets of data.

x1.4 - Raw Data from Chapter IV - Proportional Counter Dosimetry

x1.4.1 - Calibrating the Proportional Counter

Before readings can be taken using a proportional counter, it is first necessary that the detector be calibrated and characterised. As the readings taken made use of both low and high gain settings, in order to produce an accurate spectrum that when processed would allow analysis of the spectrum across the energy range. In Figure x1.01, the signal produced through the detector electronic when a signal generator is added is shown for both high and low gain data. The figure shows the signal height produced with both the gain settings.

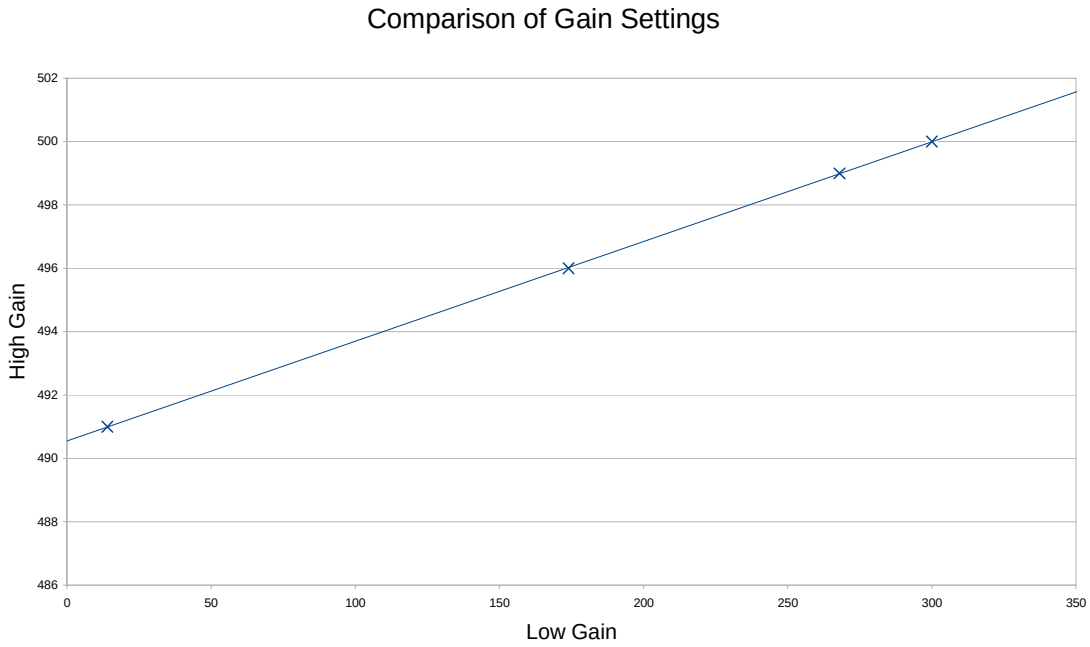

Figure x1.01 – Test of Gain Settings

These results show a linear relationship between the two settings, allowing the data sets from a low setting to be compared with the high gain.

x1.4.2 - Synchrotron Radiation Readings

The following data was obtained experimentally at the SRS Synchrotron facility based at Daresbury. The different sets of results are summarised in Table x1.01 below, followed by a series of graphs summarising the distribution spectra for each reading.

Filename	*Operating Voltage (V)*	*Source Energy (keV)*	*Beam Type*
dl001	710	27.928	Small Spot Beam (~0.1 mm by 0.1 mm)
dl002	710	27.928	No Change
dl003	710	27.928	50 % Reduction In Intensity
dl004	710	33.164	No Change
dl005	710	20.002	No Change
dl006	710	15.200	No Change
dl007	710	27.928	No Change
dl008	750	27.928	No Change
dl009	750	27.928	Slot Beam (~0.1 mm by 3.0 mm)
dl010	750	27.928	No Change
dl011	750	27.928	Slot Beam (~1.0 mm by 12.0 mm)
dl012	750	27.928	Reduced Beam Height (Reduced count rate to 50%)
dl013	750	27.928	Reduced Beam Height (Reduced count rate to 33%)

Filename	*Operating Voltage (V)*	*Source Energy (keV)*	*Beam Type*
dl014	750	27.928	Reduced Beam Height (Reduced count rate to 50%)
dl015	750	27.928	Scanned Detector (effective beam size ~16.0 mm by 12.0 mm)
dl016	750	27.928	Detector Position Changed
dl017	750	33.000	No Change
dl018	750	20.000	No Change
dl019	750	15.000	No Change

Table x1.01 – Table of the Different Settings Used for the Microdosimeter

As shown in the table, a wide range of different slot sizes and beam energies were used in order to produce results that were detailed enough for comparison with the other detector designs, but without the beam saturating the small detector element. This was largely due to the use of a millimetre-sized cavity filled with a low density Tissue Equivalent Gas approximating the behaviour of a micron-scale higher density fluid within tissue. This can mean that the small quantities of atoms within the detector are more easily saturated by a high dose of radiation than a larger detector design would be. This produces a larger dead time in the signal, making the results less reliable.

Figures x1.02a and x1.02b show the energy absorption spectra obtained using the TEP proportional counter at voltages of 710V and 750V. They show a range of readings described in Table x1.01. Figures x1.02c and x1.02d show the energy absorption spectra for the same detector at a range of different energies at operating voltages of 710V and 750V.

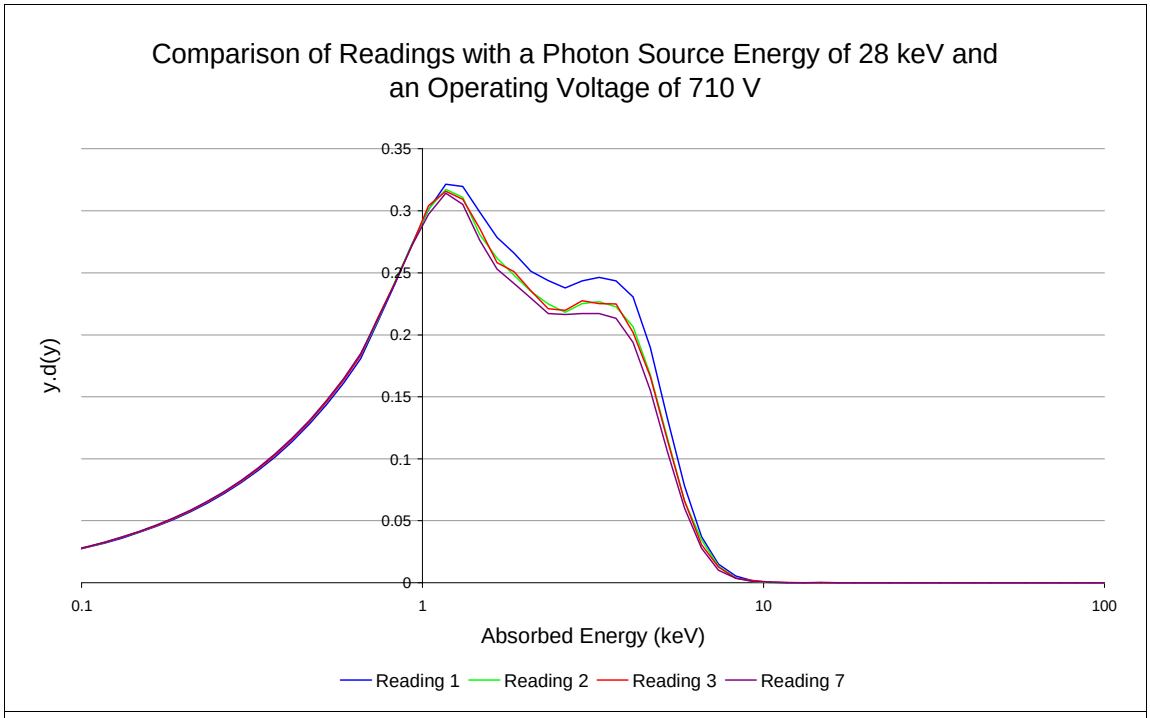

Figure x1.02a - Comparison of Readings for a Tissue Equivalent Detector with a Source Energy of 28 keV at an Operating Voltage of 710 V

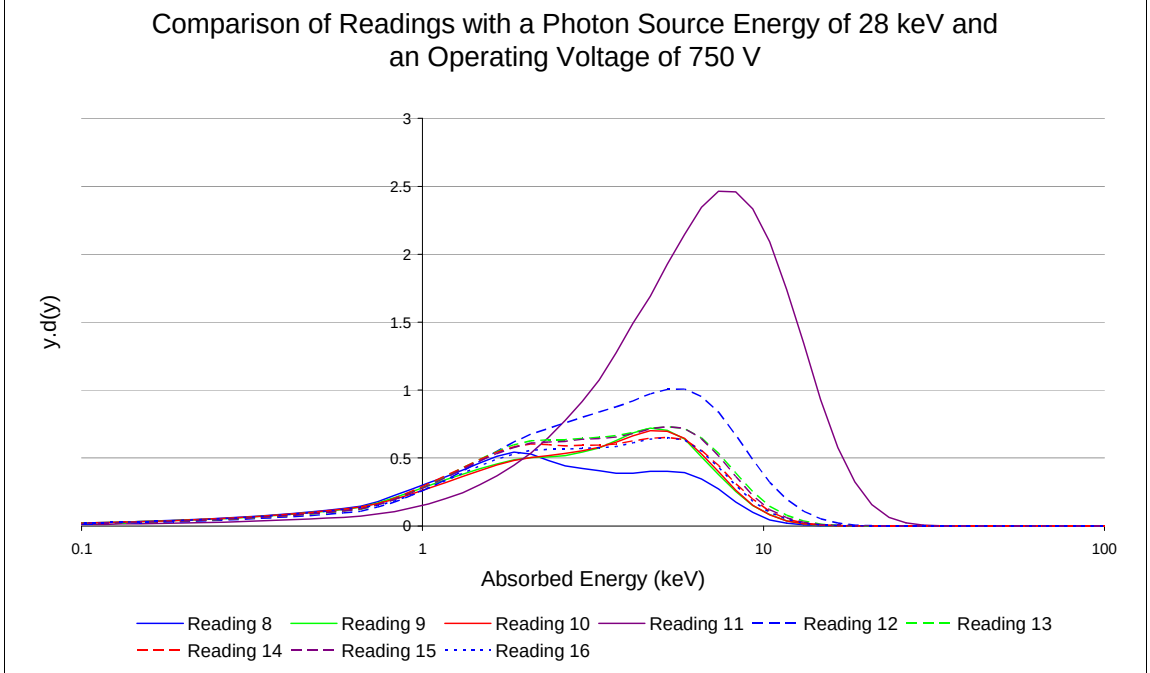

Figure x1.02b - Comparison of Readings for a Tissue Equivalent Detector with a Source Energy of 28 keV at an Operating Voltage of 750 V

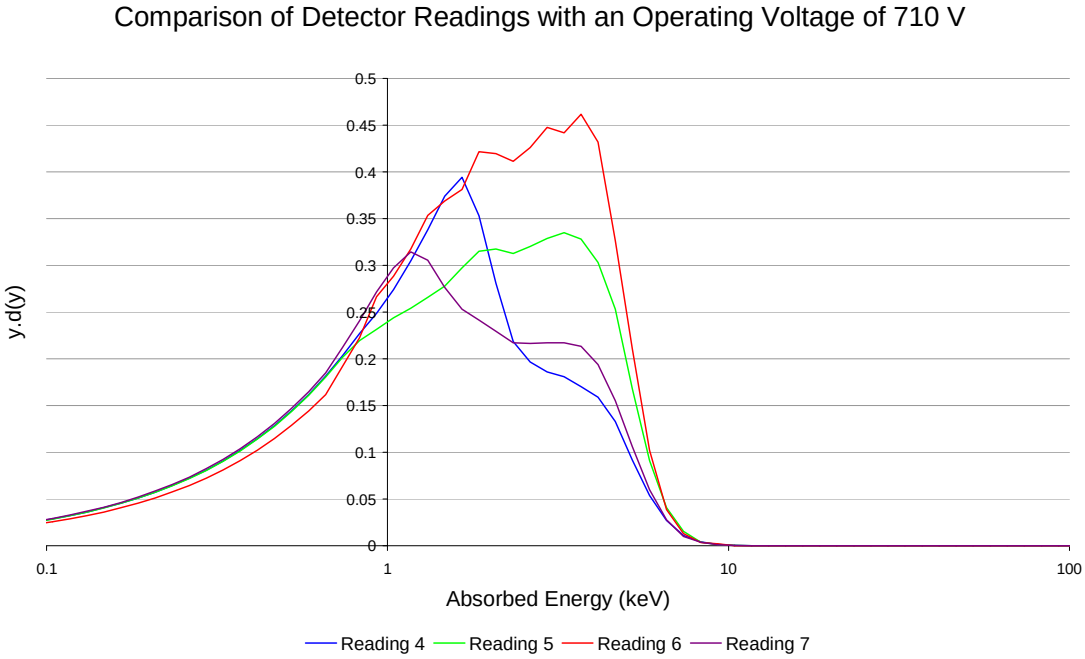

Figure x1.02c - Comparison of Readings for a Tissue Equivalent Detector with a Range of Source Energies at an Operating Voltage of 710 V

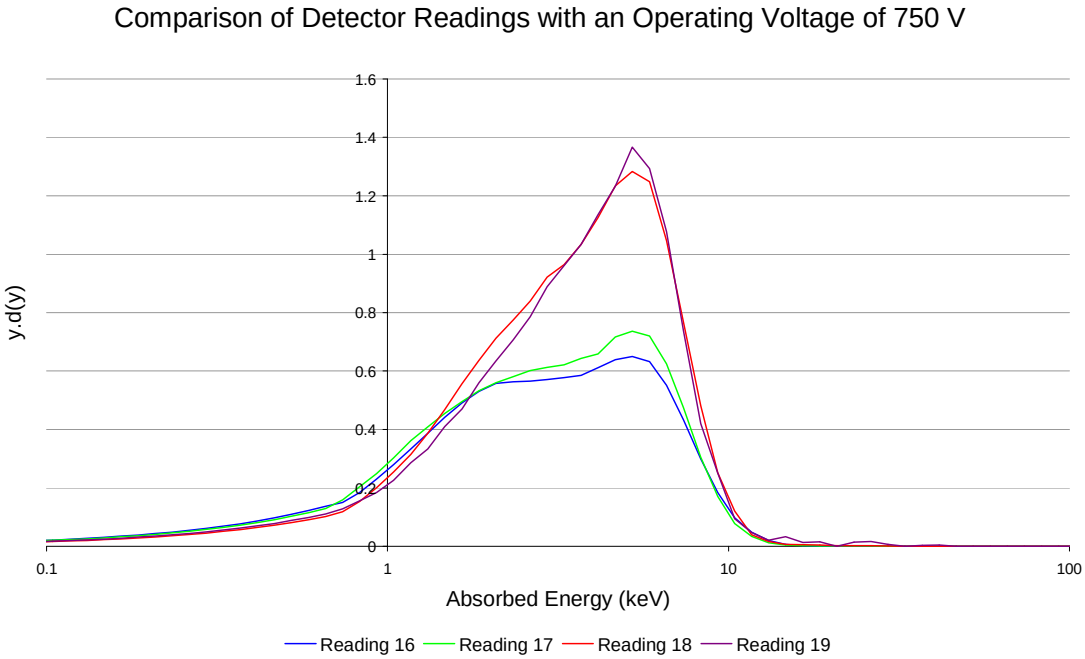

Figure x1.02d - Comparison of Readings for a Tissue Equivalent Detector with a Range of Source Energies at an Operating Voltage of 750 V

Based upon the results presented here it was decided that the 710V applied voltage was more

consistent, with less noise present in the results compared with those at 750V. Figures x1.02c and x1.02d show more variation in the spectra produced by different source energies, demonstrating that the higher voltage may not display the level of sensitivity required for this research.

x1.4.3 - Dose Enhancement from Photon Radiation

Using the isotopes listed in Chapter IV Table 4.04, energy absorption spectra were created for the three different proportional counters being investigated to show the variation in energy absorption produced by the high Z dopant elements. Because a synchrotron radiation source was not available, the research attempted to make use of different radioactive sources to achieve similar results. Although the results were not consistent enough to be included in the main text, they are included here along with some thoughts on what the problems may have been with the experimental methods used. Figure x1.03a shows the energy absorption within the detectors when exposed to an Americium-241 source over 1 hour.

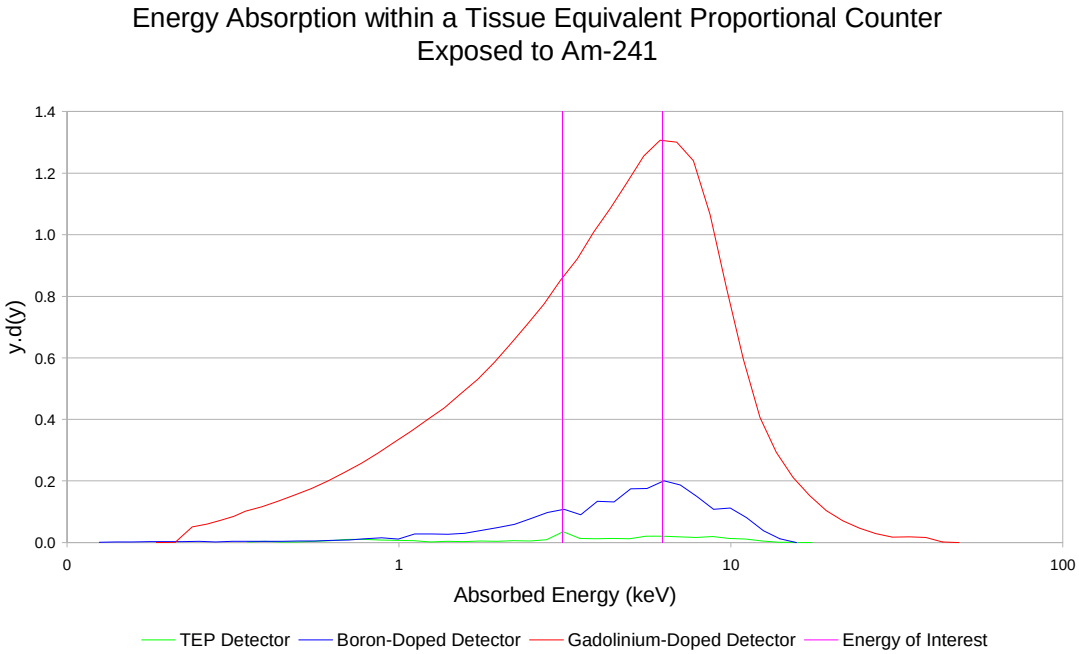

Figure x1.03a - Energy Absorption in a Proportional Counter Exposed to Americium-241

In this figure, at first there appears to be evidence of an increase in the amount of energy

deposited within the two detectors containing high Z elements in the detector walls. This would be due to the greater capture cross-section of high Z elements at energies where the primary interaction between photons and matter is through the photoelectric effect. This is demonstrated by the higher energy absorption within the Gadolinium-doped detector compared with the Boron-doped detector, which may be explained by Gadolinium having a higher capture cross-section for photons than Boron, owing to its higher atomic number.

The effects seen here are different to those that would be expected, as the atomic number of boron is lower than the majority of the elements used in the TEP proportional counter there should be little difference in energy absorption of the two detectors. Although gadolinium has a higher atomic number than the other elements present in the different detectors, MCNP modelling of the detector (shown in Chapter IV Section 4.3.2.2) suggests that it should be less absorption than shown here. This is discussed at the end of this section.

In Figure x1.03b the same three detectors were exposed to radiation from a Cobalt-60 source for 1 hour.

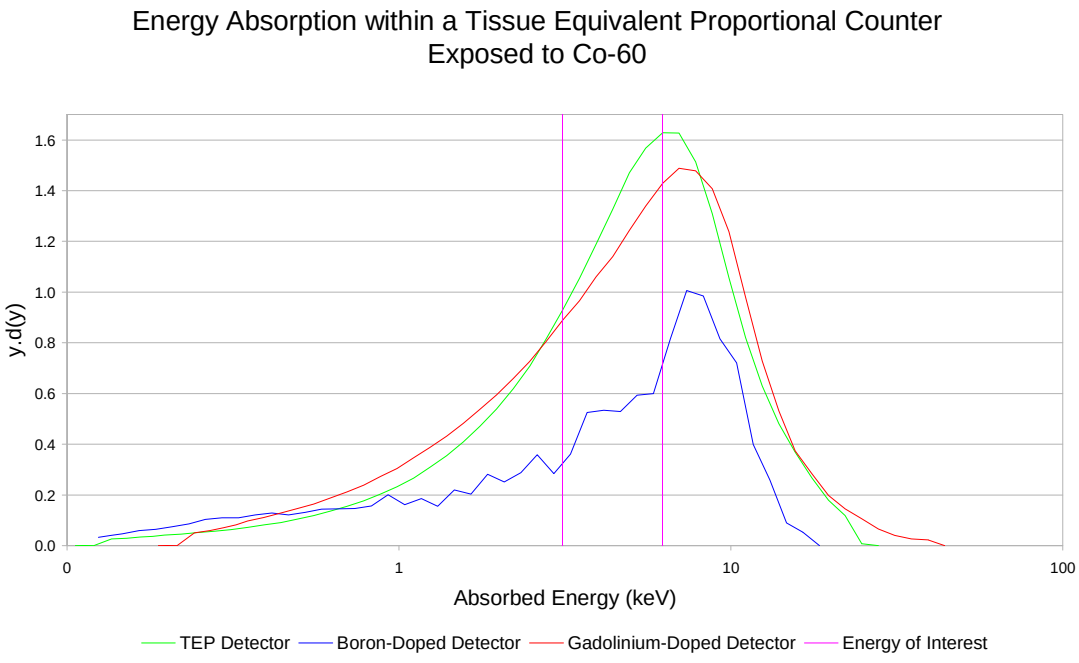

Figure x1.03b - Energy Absorption in a Proportional Counter Exposed to Cobalt-60

From this figure there is little difference in the energy absorption in the TEP proportional

counter and that doped with gadolinium, although there is a lower energy absorption for the boron-doped detector. This is due to the much higher energy of the radiation source, as the photon energy is more than 1.02 MeV, which is high enough for the interactions to occur through Pair Production. This is affected by the atomic number of the element it is interacting with less than energies low enough to be governed by the photoelectric effect, so the spectra produced should be very similar.

Although it was not apparent at the time, it is likely that there was a problem with the results obtained using the boron-doped detector, maybe due to variation of the position of the radiation source relative to the detector cavity. Theoretically it would be expected that there would be little difference between the results for boron and the other two detectors. Cobalt-60 was later used as a radiation source to investigate the effects of varying the gas pressure within a proportional counter in Chapter V Section 5.2.2. Finally, in Figure x1.03c, the proportional counters were exposed to radiation from a Caesium-137 source for 1 hour, producing the following spectrum of energy absorption.

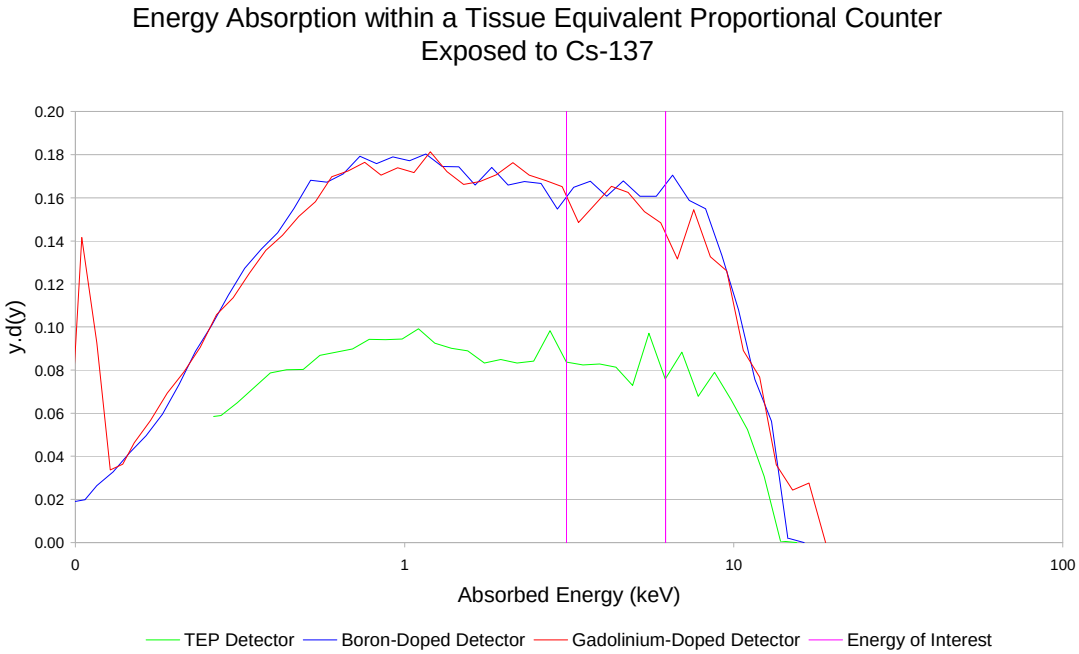

Figure x1.03c - Energy Absorption in a Proportional Counter Exposed to Caesium-137

This figure clearly shows an increase in absorbed dose for the two detectors with high atomic number elements present. As Caesium-137 has a high intensity emission at an energy of 661

keV, this means that the majority of the interactions will occur via Compton Scatter. As the probability of interaction via Compton scatter is linearly proportional to atomic number, it would be expected that the energy absorption within the detector would not show a significant amount of difference from the addition of a dopant. However, the source shows some emission at lower energies, which will be absorbed by the means of the photoelectric effect, so there may be some dose enhancement present.

As with Figure x1.03a, it would be expected that there would be little difference between the results of the TEP proportional counter and a proportional counter with low levels of boron present, so the large difference between these peaks suggests that the experimental work contained an error.

The dose enhancement for the proportional counters used in this experimental work was calculated by dividing the number of counts absorbed at a particular energy in the TEP walled detector by the same figure obtained for a detector with a dopant in the walls. Table x1.02 shows a comparison of the dose enhancement within a detector at specific energies on the spectra for the three sources used to produce the graphs (Americium-241, Cobalt-60 and Caesium-137). Note that due to differences in scaling between different sets of results it was very difficult to produce a clear graph of the dose enhancement at a set point, so these values are included for only specific energies. The energies from which these values are derived are marked on Figure x1.03a to x1.03c as a purple line.

Isotope	Energy of Dose Enhancement (keV)	Dose Enhancement in a Boron-Doped Detector	Dose Enhancement in a Gadolinium-Doped Detector
Americium-241	3.1	3.08	24.29
	6.2	9.91	64.42
Cobalt-60	3.1	0.39	0.95
	6.2	0.50	0.88
Caesium-137	3.1	1.97	1.97
	6.2	2.25	1.96

Table x1.02 - Dose Enhancement in Proportional Counters due to Radioactive Isotopes

Table x1.02 gives an indication of the degree of dose enhancement produced for each radioactive source, the values of which show that there must have been a flaw in the experimental work. In this table, the differences between the energy absorption spectra of the different proportional counters are numerically ascertained. The overly high values for the gadolinium-doped detector for the AM-241 and Cs-137 sources heavily suggests an error in the data, as does the similar dose enhancement found for a boron-doped detector.

Possible Sources of Error

When a set of data provides a set of results that appear unlikely, it is worth checking it again to try to ascertain the source of the errors. For these results, the most likely reason for the difference between the expected values and those obtained is probably that the gain settings were recorded incorrectly. This would have lead to some of the values being higher or lower than the figures would suggest, and a repeat of the experiment would correct this problem.

Another potential source of error could be a misreading of the gas pressure when one of the detectors was filled. This seems unlikely, however, as none of the detectors consistently produced an unexpected result, rather they all showed a higher or lower energy absorption than expected at some point. Similarly this removes the possibility that a small quantity of air may have leaked into one of the detectors, as it would be expected that that detector would

show results that were consistently different.

A final source of potential error was in the data analysis used to produce the comparisons. This has been discounted, however, as despite repeated reanalysis the results have stayed the same, showing that the error is in the proportional counter output data itself.

EGS Simulation Results

In Figure x1.04, the ratio of energy absorption within a pure TEP proportional counter to that within a detector with the wall material doped with low levels of Gadolinium or Boron. Although the geometry used for each of these was identical, they had detector walls constructed from TEP, with one would have contained low levels of Gadolinium, one had low levels of Boron and the other had only pure TEP.

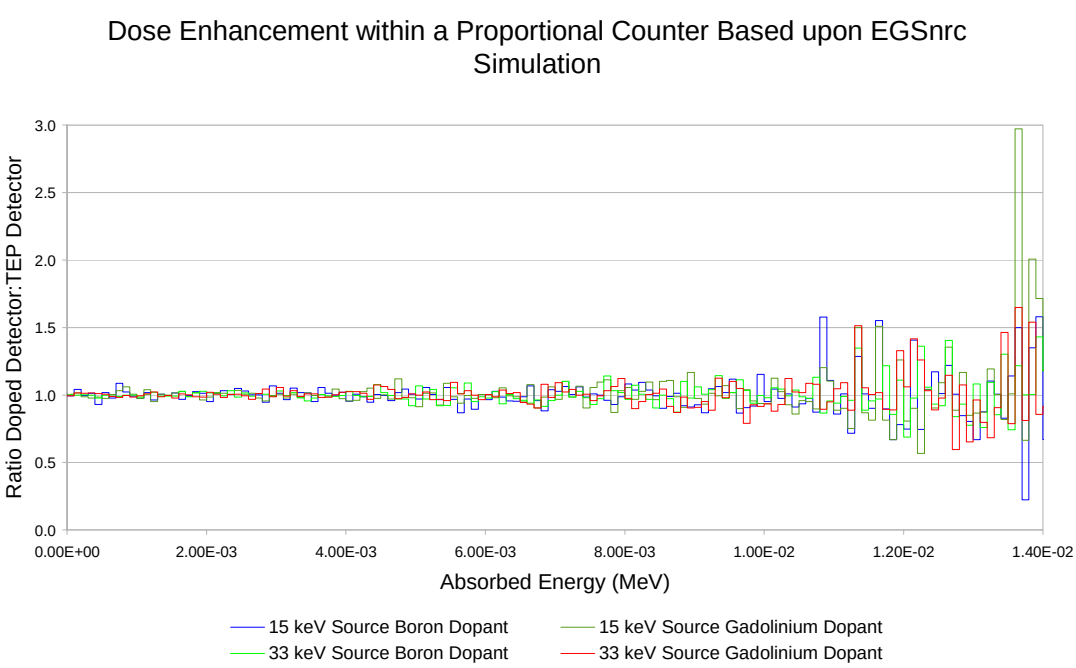

Figure x1.04 - Ratio of Energy Absorption within a Proportional Counter with Doped Walls and a Proportional Counter with TEP Walls

If we compare the dose enhancement effects in Figure x1.05 it is apparent that there is little increase in energy absorption occurring within the detector. This is due to the boron present in the detectors having a very similar atomic number to the elements present in the TEP-based

models. Without the presence of gadolinium in any of the detectors, there was no noticeable dose enhancement effect.

Unfortunately an error in the input of the material source data lead to the gadolinium-doped TEP model being constructed with boron instead of gadolinium. As this mistake was not noticed at the time it was not possible for the simulation to be repeated in order to remove this error. As boron has a similar atomic number to the elements preset in the TEP proportional counter, there was no noticeable dose enhancement effect observed in the EGSnrc simulations.

Although these simulations were unsuccessful in attempting to investigate the dose enhancement effects of adding gadolinium to a TEP proportional counter, they did help to prove that the presence of boron in a similar detector will have no effect upon the energy absorption characteristics for this energy range.

Appendix II - Standard Materials Used in the Monte Carlo Models

This section is included as a summary of the different materials used throughout the Monte Carlo studies. This is in order to provide an effective interpretation of the models produced and how they compare with each other. The majority of the material compositions listed in this section are for the MCNP4C code, as EGSnrc made use of its own PEGS data files containing standard material types. For EGSnrc new materials were only needed in situations where non-standard elemental compositions were needed, such as doped TEP used in the proportional counters. Any components that contained only one element such as the aluminium casings of some of the detectors, gold or silver wires, or the beryllium window used in the ionisation chamber, are not included in the tables. These components are noted in the descriptions of the detector models.

This section will include the materials used in chapter order where possible, although some, such as a-150 Tissue Equivalent Plastic were used in several sections. The descriptions of Monte Carlo models in the chapters of this document will describe the materials used and include any specifically produced for that model. Table x2.01 contains those used by the different MNCP 4C models.

Material	Elemental Composition	Elemental Abundance (by Weight)	Elemental Abundance (Absolute)
Air	Carbon (6)	0.000124	0.0001
	Nitrogen (7)	0.82	0.7750
	Oxygen (8)	0.179487	0.1937
	Argon (18)	0.012827	0.0312
Pure Water	Hydrogen (1)	0.941177	0.6667
	Oxygen (8)	0.058823	0.3333
Stainless Steel	Chromium (24)	0.193206	0.1800
	Iron (26)	0.733192	0.7400
	Nickel (28)	0.073602	0.0800
Polyethylene	Hydrogen (1)	0.501739	0.1437
	Carbon (6)	0.498261	0.8563

Material	Elemental Composition	Elemental Abundance (by Weight)	Elemental Abundance (Absolute)
Epoxy Resin	Hydrogen (1)	0.364025	0.0810
	Carbon (6)	0.503343	0.6720
	Nitrogen (7)	0.015408	0.0240
	Oxygen (8)	0.111792	0.1990
	Chlorine (17)	0.000264	0.0001
	Calcium (20)	0.005168	0.0230
Diamond	Carbon (6)	1.000000	1.0000
Homogenous Diamond Model	Carbon (6)	0.999239	0.9950
	Copper (29)	0.000312	0.0015
	Silver (47)	0.000449	0.0035
Silver-Coated Wire	Copper (29)	0.618421	0.5000
	Silver (47)	0.381579	0.5000
Gold-Tin Solder	Tin (50)	0.283154	0.3000
	Gold (79)	0.716846	0.7000
Cellulose	Hydrogen (1)	0.062162	0.0093
	Carbon (6)	0.444462	0.3995
	Oxygen (8)	0.493376	0.5912
Optic Fibre (SiO_2)	Oxygen (8)	0.777778	0.6667
	Silicon (14)	0.222222	0.3333
Erbium-Doped Optic Fibre (SiO_2 + Er)	Oxygen (8)	0.775609	0.6533
	Silicon (14)	0.221599	0.3267
	Erbium (68)	0.002792	0.0200
Germanium-Doped Optic Fibre (SiO_2+Ge)	Oxygen (8)	0.773178	0.6533
	Silicon (14)	0.220904	0.3267
	Germanium (32)	0.005918	0.0200
A-150 Tissue Equivalent Plastic	Hydrogen (1)	0.413613	0.1013
	Carbon (6)	0.527595	0.7755
	Nitrogen (7)	0.020442	0.0351
	Oxygen (8)	0.026696	0.0523
	Fluorine (9)	0.007903	0.0174
	Calcium (20)	0.003751	0.0184

Material	Elemental Composition	Elemental Abundance (by Weight)	Elemental Abundance (Absolute)
A-150 TEP + Boron	Hydrogen (1)	0.412787	0.1011
	Carbon (6)	0.526542	0.7736
	Nitrogen (7)	0.020401	0.0350
	Oxygen (8)	0.026643	0.0522
	Fluorine (9)	0.007887	0.0174
	Calcium (20)	0.003744	0.0183
	Boron (5)	0.001996	0.0024
A-150 TEP + Gadolinium	Hydrogen (1)	0.413548	0.1011
	Carbon (6)	0.527513	0.7736
	Nitrogen (7)	0.020438	0.0350
	Oxygen (8)	0.026692	0.0522
	Fluorine (9)	0.007902	0.0174
	Calcium (20)	0.003749	0.0183
	Gadolinium (64)	0.000156	0.0024
Propane-Based Tissue Equivalent Gas	Hydrogen (1)	0.429286	0.1027
	Carbon (6)	0.396468	0.5689
	Nitrogen (7)	0.020918	0.0350
	Oxygen (8)	0.153328	0.2934
Propane-Based TEG + Gadolinium	Hydrogen (1)	0.429219	0.1024
	Carbon (6)	0.396406	0.5676
	Nitrogen (7)	0.020915	0.0349
	Oxygen (8)	0.153304	0.2927
	Gadolinium (64)	0	0.0024

Table x2.01 - Description of Materials used in MCNP4C Models

In Table x2.02 the materials used in the EGS4 models are summarised. If the simulation has used the standard PEGS libraries of materials this is noted and the elemental composition is not included. Note that the inclusion of Boron in the A-150 TEP Doped with Gadolinium entry was due an error made when creating the PEGS data. This error meant that all of the results for the EGSnrc model of the gadolinium-doped TEP proportional counter were incorrect, and is discussed in Appendix I Section 1.4.3.

Material	Elemental Composition	Elemental Abundance (Absolute)
Air	PEGS Data File	
TEG (Propane-Based)	PEGS Data File	
A-150 TEP	PEGS Data File	
A-150 TEP Doped with Boron	Hydrogen (1)	0.100324
	Carbon (6)	0.767822
	Nitrogen (7)	0.034711
	Oxygen (8)	0.051798
	Fluorine (9)	0.017249
	Calcium (20)	0.018196
	Boron (5)	0.009900
A-150 TEP Doped with Gadolinium	Hydrogen (1)	0.101248
	Carbon (6)	0.774895
	Nitrogen (7)	0.035030
	Oxygen (8)	0.052275
	Fluorine (9)	0.017408
	Calcium (20)	0.018364
	Boron (5)	0.000780

Table x2.02 - Description of Materials used in EGS4 Models

The presence of boron in the gadolinium-doped A-150 TEP material description is marked in the table above.

Appendix III - The Proportional Counter Spreadsheet

In order to calculate a y.d(y) distribution for the proportional counter it was necessary that each point on the distribution be plotted in an appropriate manner. This data analysis was undertaken in a series of steps summarised below using an OpenOffice spreadsheet to automate the process and speed up data analysis.

Step 1 - Reformatting and Calibrating the Data

Initially the data recording software produced two different output files, one for the low gain setting and one for the high gain. In these files, the data was recorded as a series of counts corresponding to a range of different energy channels. An example data file is included below:

Example 3.1 - Example Proportional Counter Output File

The example below shows a proportional counter's low gain output file produced for dl001 data file produced during the research a the SRS Facility (listed in Table x1.01). Note that this example has been shortened in order to save space, as the original file contains data for 1024 channels.

```
                  ------------------------------------------------------------
Channel Data Report             10/17/05  3:30:54 PM              Page  1

          ****************************************************
          *****   S P E C T R A L   D A T A   R E P O R T   *****
          ****************************************************


          *****          Sample ID:                          *****

          Elapsed Live time:       300
          Elapsed Real Time:       345

Channel|------|-------|-------|-------|-------|-------|-------|-------|
    1:       0       0       0       0       0       0       1       0
    9:      96 1008448 2374666 2110130 1841200 1609841 1362399 1128329
   17:  920463  768579  647198  545753  460994  385433  315554  254097
   25:  200751  156707  121553   95617   75986   62166   51457   44106
   33:   37665   33093   29261   25941   23614   21392   19788   18489
   41:   16879   15699   14720   14012   12941   12061   11731   10859
   49:   10432    9930    9464    9015    8519    8130    7784    7513
                  ------------------------------------------------------------
```

Because this data is recorded in an unwieldy format, the first stage is to reformat the data into a simple list of results and cut out the nonessential data, such as timing information. The number of counts for a specific energy channel was then converted into an absorbed energy value by multiplying it by the energy of the channel squared. This value was obtained by calculating the point at which the curve dropped off - in other words the maximum path length, which is known to be 8.25 keV for photons in this detector design. These values were calculated by eye, finding the mid-point in the detector drop-off for the low gain data and then using the gain calibration curve in Figure x1.01 to determine the energy of the high gain values.

Step 2 - Combining and Merging the Data

The problem with this result is that it presents the data on a linear scale but the graphs are plotted on a logarithmic scale to allow an easier comparison of the curve shape across the entire spectrum. The next step was to replot the data onto a logarithmic scale and combine the data from multiple channels together into 80 logarithmic bins. In order to ascertain the absorbed energy within each bin, the output file data was treated as a histogram and all of the energies within the range of the bin were automatically included. For channels which were within two bins, the energy absorption within the channel was split between the two bins proportionally.

Step 3 - Combining the Low Gain and High Gain Data

The final step to producing the data analyses shown in this document was to plot the low gain and high gain data on the same set of axes. A comparison was then made of the two sets of data, determining at which points the two curves followed the same relationship and at which points they diverged. Then high gain data was used to construct the lower part of the energy absorption curve, the low gain used to construct the high energy part of the curve and the two data sets averaged in the central part. Finally, the area under the energy absorption curve was calculated and each of the bins divided by this value in order to obtain a y.d(y) curve for the energy absorption within the proportional counter.

Appendix IV - Example MCNP Inputs

Example 4.1 - Example MCNP Input for the 3 Component Diamond Detector Model

The example below shows an MCNP input file produced to simulate the behaviour of a simple 3 component diamond detector. In this example a homogenous diamond crystal containing traces of silver is exposed to 6 keV photons.

```
MESSAGE:

FS Diamond Detector for MCNP
C    Series of 2 cylinders, a large cylinder, with a smaller detector
within it
C    Source is 6 - 30 kev photons
C
C
C    CELL CARDS
1    1  -0.93   -1 +2 -3 #2                  $ Polythene Phantom
2    2  -3.52   -5 +6 -7                     $ Detector
50   0          -100 #1 #2                  $ Outside Detector
100  0          +100                        $ Outer Space

C    SURFACE CARDS
C    Polythene Phantom
1    PZ    0.0
2    PZ   -2.18
3    CZ    1.0
C    Detector
5    PZ   -0.10
6    PZ   -0.13
7    CZ    0.5
C    Outer Sphere
100  SO    10.0
C    Source
500  PZ    1.0

C    MODE CARD
MODE P E
C
C    Cell photon importances
IMP:P,E 1 1 1 0
C
C    SOURCE DEFINITION
C    Irradiation of cylinder with a rectangular, directional surface source
SDEF SUR=500 X=D1 Y=D2 Z=1.0 VEC=0.0 0.0 1.0 DIR=-1 ERG=6.000e-3
SI1  H  -0.4  0.4
SP1  D   0.0  1.0
SI2  H  -0.4  0.4
SP2  D   0.0  1.0
C
C
C    TALLY CARDS
```

```
C    Pulse height in MeV within inner cylinder
*F8:P,E 2
C
C    ENERGY BINS FOR TALLIES
E8   0 1e-5 1e-4 1e-3 0.01 0.1 1 10
C
C
C    MATERIAL CARDS
M1   1001  0.501739                          $ Polyethane
     6000  0.498261
M2   6000  0.999239622                       $ Diamond + Heavy Metals
     29000 0.000311666
     47000 0.000448712
C
C
PHYS:P 0.1 0 0
C    NUMBER OF HISTORIES TO RUN
NPS  500000
```

Example 4.2 - Example MCNP Input for the Complex Diamond Detector Model

The example of an MCNP input file shown below was produced to simulate the behaviour of a complex-model diamond detector. In this example a pure diamond crystal is adjacent to wires containing silver and copper as well as gold-tin alloy electrical contacts is exposed to 5 keV photons.

```
MESSAGE:

Basic Diamond detector geometry for MCNP
C    Started with a basic tube of water within a radiation field
C    Source is 5-50 kev photons
C
C
C    CELL CARDS
1    1  -0.93   -1 +2 -3 #2 #3 #4 #5 #6 #7 #8 $ Outer Casing
2    2  -3.51   -4 +5 -6                      $ Diamond
3    3  -16.902 -5 +7 -8                      $ Contact 1
4    3  -16.902 -9 +4 -10 #6                  $ Contact 2
5    4  -9.705  -7 +2 -11 +12 -13 +14         $ Wire 1 (Ribbon)
6    4  -9.705 ((-15 +4 -11 +12 -16 +17) :    $ Wire 2 (Ribbon)
               (-15 +18 -11 +12 -19 +16) :
               (-18 +2 -11 +12 -19 +20))
7    5  -7.92   -51 +52 -53 #5 #6              $ Stem
8    6  -1.02   -61 +51 -53 #2 #3 #4 #5 #6     $ Inner Casing
50   10 -1.2e-3 -100 #1 #2 #3 #4 #5 #6 #7 #8   $ Outside Detector
100  0          +100                           $ Outer Space

C    SURFACE CARDS
C    Outer Casing
1    PZ    1.0
2    PZ   -1.0
3    CZ    0.365
```

```
C    Diamond
4    PZ    0.9
5    PZ    0.8667
6    CZ    0.315
C    Contact 1
7    PZ    0.86
8    CZ    0.125
C    Contact 2
9    PZ    0.91
10   C/Z   0.0 0.15 0.06
C    Wire 1 (Ribbon)
11   PX    0.01
12   PX   -0.01
13   PY    0.005
14   PY   -0.005
C    Wire 2 (Ribbon)
15   PZ    0.92
16   PY    0.155
17   PY    0.145
18   PZ    0.91
19   PY    0.29
20   PY    0.28
C    Stem
51   PZ    0.0
52   PZ   -1.5
53   CZ    0.32
C    Inner Casing
61   PZ    0.95
C    Outer Sphere
100  SO    2.0
C    Source
500  PZ    1.0

C    MODE CARD
MODE P E
C
C    Cell photon importances
IMP:P,E 1 1 1 1 1 1 1 1 1 0
C
C    SOURCE DEFINITION
C    Irradiation of cylinder with a rectangular, directional surface source
SDEF SUR=500 X=D1 Y=D2 Z=1.0 VEC=0.0 0.0 1.0 DIR=-1 ERG=5.000e-3
SI1  H  -0.4  0.4
SP1  D   0.0  1.0
SI2  H  -0.4  0.4
SP2  D   0.0  1.0
C
C
C    TALLY CARDS
C    Pulse height in MeV within inner cylinder
*F8:P,E 2
C
C    ENERGY BINS FOR TALLIES
E8   0 1e-5 1e-4 1e-3 0.01 0.1 1 10
C
C
C    MATERIAL CARDS
M1   1001  0.501739                        $ Polyethylene
     6000  0.498261
```

```
M2   6000  1.0                              $ Diamond (Carbon)
M3   50000 0.283154                         $ Solder (Au/Son)
     79000 0.716846
M4   29000 0.618421                         $ Wire (Cu and Ag)
     47000 0.381579
M5   26000 0.733192                         $ Stem (Stainless Steel)
     24000 0.193206
     28000 0.073602
M6   1001  0.364025                         $ Epoxy Resin
     6000  0.503343
     7000  0.015408
     8000  0.111792
     17000 0.000264
     20000 0.005168
M10  8016  0.179487                         $ Air
     7014  0.820513
C
C
PHYS:P 0.1 0 0
C    NUMBER OF HISTORIES TO RUN
NPS  500000
```

Example 4.3 - Example MCNP Input for the Complex Ionisation Chamber Model

The example below is an MCNP input file produced to simulate the behaviour of a complex ionisation chamber. In this example an air-filled cavity with a germanium window is exposed to 5keV photons.

```
MESSAGE:

Basic Ionisation Chamber phantom for MCNP
C    Started with a basic tube of water within a radiation field
C    Source is 5-50 kev photons
C
C
C    CELL CARDS
1    1  -1.0    -1 +2 -3                    $ Beryllium Window
2    10 -1.2e-3 -2 +5 -6                    $ Detector
3    2  -1.0    -7 +8 -9 +10 -2 +11 #2      $ Detector Housing
50   10 -1.2e-3 -100 #1 #2 #3               $ Outside Detector
100  0          +100                        $ Outer Space

C    SURFACE CARDS
C    Beryllium Window
1    PZ    0.003
2    PZ    0.0
3    CZ    1.0
C    Detector
5    PZ   -0.1
6    CZ    0.25
C    Detector Housing
7    PX    1.1
8    PX   -1.1
```

```
9    PY    0.9
10   PY   -5.2
11   PZ   -1.44
C    Outer Sphere
100  SO    100.0
C    Source
500  PZ    1.0

C    MODE CARD
MODE P E
C
C    Cell photon importances
IMP:P,E 1 1 1 1 0
C
C    SOURCE DEFINITION
C    Irradiation of cylinder with a rectangular, directional surface source
SDEF SUR=500 X=D1 Y=D2 Z=10.0 VEC=0.0 0.0 1.0 DIR=-1 ERG=5.000e-3
SI1  H  -0.4  0.4
SP1  D   0.0  1.0
SI2  H  -0.4  0.4
SP2  D   0.0  1.0
C
C
C    TALLY CARDS
C    Pulse height in MeV within inner cylinder
*F8:P,E 2
C
C    ENERGY BINS FOR TALLIES
E8   0 1e-5 1e-4 1e-3 0.01 0.1 1 10
C
C
C    MATERIAL CARDS
M1   4000  1.000000                          $ Beryllium
M2   1001  0.501739                          $ Polyethylene
     6000  0.498261
M10  8016  0.179487                          $ Air
     7014  0.820513
C
C
PHYS:P 0.1 0 0
C    NUMBER OF HISTORIES TO RUN
NPS  5000000
```

Example 4.4 - Example MCNP Input for the Fibre Optic Dosemeter Model

This example shows the MCNP input file used to simulate the fibre optic dosemeter model for an erbium-doped optic fibre, exposed to a source energy of 8 keV.

```
MESSAGE:

FS Fibre Optic Detector for MCNP
C      Series of 2 cylinders, a large cylinder, with a smaller detector
within it
C    Source is 6 - 30 kev photons
```

```
C
C
C    CELL CARDS
1    1  -2.40     -5 +6 -11                    $ Optic Fibre 1 Top
2    1  -2.40     -5 +6 -12                    $ Optic Fibre 2 Top
3    1  -2.40     -5 +6 -13                    $ Optic Fibre 3 Top
4    1  -2.40     -5 +6 -14                    $ Optic Fibre 4 Top
5    1  -2.40     -5 +6 -15                    $ Optic Fibre 5 Top
6    1  -2.40     -6 +7 -11                    $ Optic Fibre 1 Bottom
7    1  -2.40     -6 +7 -12                    $ Optic Fibre 2 Bottom
8    1  -2.40     -6 +7 -13                    $ Optic Fibre 3 Bottom
9    1  -2.40     -6 +7 -14                    $ Optic Fibre 4 Bottom
10   1  -2.40     -6 +7 -15                    $ Optic Fibre 5 Bottom
11   2  -1.44     -6 +7 +21 -22 +24 -25        $ Sellotape
                  #6 #7 #8 #9 #10 #12
12   3  -0.0012   -6 +7 +22 -23 +24 -25        $ Metal
20   4  -1.2e-03  -1 +2 -3 #1 #2 #3 #4 #5      $ Outer Air System
                        #6 #7 #8 #9 #10 #11 #12
50   0            -100 #1 #2 #3 #4 #5 #20      $ Outside Detector
                       #6 #7 #8 #9 #10 #11 #12
100  0            +100                         $ Outer Space

C    SURFACE CARDS
C    Outer Air System
1    PZ    0.0
2    PZ   -1.5
3    CZ    1.5
C    Optic Fibre Limits
5    PZ   -0.25
6    PZ   -0.75
7    PZ   -1.25
C    Optic Fibres
11   C/Z   0.0 -1.0 0.001
12   C/Z   0.0 -0.5 0.001
13   CZ    0.001
14   C/Z   0.0  0.5 0.001
15   C/Z   0.0  1.0 0.001
C    Metal and Sellotape
21   PX    0.0
22   PX    0.005
23   PX    0.010
24   PY   -1.0
25   PY    1.0
C    Outer Sphere
100  SO    10.0
C    Source
500  PX    1.0

C    MODE CARD
MODE P E
C
C    Cell photon importances
IMP:P,E 1 1 1 1 1 1 1 1 1 1 1 1 1 0
C
C    SOURCE DEFINITION
C    Irradiation of cylinder with a rectangular, directional surface source
SDEF SUR=500 X=1.0 Y=D1 Z=D2 VEC=1.0 0.0 0.0 DIR=-1 ERG=8.0e-3
SI1  H  -1.1  1.1
SP1  D   0.0  1.0
```

```
SI2  H  -0.7 -0.3
SP2  D   0.0  1.0
C
C
C    TALLY CARDS
C    Pulse height in MeV within inner cylinder
C    Optic Fibre 1
*F18:P,E 1
C    Optic Fibre 2
*F28:P,E 2
C    Optic Fibre 3
*F38:P,E 3
C    Optic Fibre 4
*F48:P,E 4
C    Optic Fibre 5
*F58:P,E 5
C
C    ENERGY BINS FOR TALLIES
E18  0 1e-5 1e-4 1e-3 0.01 0.1 1 10
E28  0 1e-5 1e-4 1e-3 0.01 0.1 1 10
E38  0 1e-5 1e-4 1e-3 0.01 0.1 1 10
E48  0 1e-5 1e-4 1e-3 0.01 0.1 1 10
E58  0 1e-5 1e-4 1e-3 0.01 0.1 1 10
C
C
C    MATERIAL CARDS
M1   8000  0.775609                        $ Si O2 + Er
     14000 0.221599
     68000 0.002792
M2   1001  0.062162                        $ Sellotape (Cellulose)
     6000  0.444462
     8000  0.493376
M3   7000  0.501739                        $ Metal
     8000  0.498261
M4   6000  0.000124                        $ Air
     7000  0.755267
     8000  0.231781
     18000 0.012827
C
C
C
PHYS:P 0.1 0 0
C    NUMBER OF HISTORIES TO RUN
NPS  5000000
```

Example 4.5 - Example MCNP Input for the Proportional Counter Model

In the example below an MCNP input file is shown that was produced to simulate the behaviour of a proportional counter. In this example a proportional counter containing TEP-based detector walls is exposed to 100 keV photons.

```
MESSAGE:

Basic Proportional Counter geometry for MCNP
C    Started with a basic generic microdosimeter
C    Source is 5-50 kev photons
C
C
C    CELL CARDS
1    1  -2.70      -1 +2 -3 #2 #3 #4 #5   $ Detector Housing
2    3  -1.617e-6  -4 +5 -6 #3 #4 #5      $ Outer Gas Layer
3    2  -1.12      -7 #4 #5               $ A150 Wall Material
4    3  -1.617e-6  -8 #5                  $ Inner Gas Layer
5    4  -19.3      -4 +5 -13              $ Gold Wire
50   10 -1.2e-3    -100 #1 #2 #3 #4 #5    $ Outside Detector
100  0             +100                   $ Outer Space

C    SURFACE CARDS
C    Detector Housing Outer Edge
1    PZ    1.9
2    PZ   -1.9
3    CZ    1.1
C    Outer Gas Layer Outer Edge
4    PZ    1.7
5    PZ   -1.7
6    CZ    0.9
C    A150 Wall Outer Layer
7    SO    0.665
C    Inner Gas Layer Outer Edge
8    SO    0.635
C    Gold Wire
13   CZ    0.00023
C    Outer Sphere
100  SO    2.5
C    Source
500  PZ    2.00

C    MODE CARD
MODE P
C
C    Cell photon importances
IMP:P 1 1 1 1 1 1 0
C
C    SOURCE DEFINITION
C    Irradiation of cylinder with a rectangular, directional surface source
SDEF SUR=500 X=D1 Y=D2 Z=2.0 VEC=0.0 0.0 1.0 DIR=-1 ERG=100.0e-3
SI1  H  -0.04  0.04
SP1  D   0.00  1.00
SI2  H  -0.04  0.04
```

```
SP2  D   0.00  1.00
C
C
C    TALLY CARDS
C    Pulse height in MeV within inner cylinder
F6:P 4
C
C    ENERGY BINS FOR TALLIES
E6   0 1e-5 1e-4 1e-3 0.01 0.1 1 10
C
C
C    MATERIAL CARDS
M1   13000 1.0               $ Aluminium
M2   1001  0.413613          $ A-150 Tissue Equivalent Plastic
     6000  0.527595
     7000  0.020442
     8000  0.026696
     9000  0.007903
     20000 0.003751
M3   1001  0.429286          $ Propane-Based Tissue Equivalent Gas
     6000  0.396468
     7000  0.020918
     8000  0.153328
M4   79000 1.0               $ Gold
M10  8016  0.179487          $ Air
     7014  0.820513
C
C
PHYS:P 0.1 0 0
C    NUMBER OF HISTORIES TO RUN
NPS  500000
```

Example 4.6 - Annotated Proportional Counter Model

This example of an MCNP input file was used to model the behaviour of a proportional counter based upon the detector used for the experimental work. Due to slight variations in the exact layout of the different models used, the design was somewhat simplified, so that the results produced by MCNP could be compared with each other and different detectors used. It consists of a series of cylinders representing the different layers of the proportional counter, surrounded by air.

This raw input file is annotated in *italics* with a simple explanation of what each part of the file does; note that the spacing of the original file has been altered to allow annotation.

```
MESSAGE:

Basic Proportional Counter geometry for MCNP
C     Started with a basic generic microdosimeter
C     Source is 5-50 kev photons
```

Statement of the purpose of the input

```
C
C
C     CELL CARDS
```

Describes which surfaces make up each volume within an object, what material they made of and their relative densities.

```
1     1     -2.70 -1 +2 -3 #2 #3 #4 #5          $ Detector Housing
2     3     -1.617e-6   -4 +5 -6 #3 #4 #5       $ Outer Gas Layer
3     2     -1.12 -7 #4 #5                      $ A150 Wall Material
4     3     -1.617e-6   -8 #5                   $ Inner Gas Layer
5     4     -19.3 -4 +5 -13                     $ Gold Wire
50    10    -1.2e-3     -100 #1 #2 #3 #4 #5     $ Outside Detector
100   0                 +100                    $ Outer Space
```

The first number on the line is a label for the volume, which is used for defining which areas to focus on in the calculation. For the first cell, it has been labelled cell 1.

The second number tells the program which material (defined in the material cards below) to use in all calculations relating to that cell. For the first cell, material 1 (Aluminium) is used.

The third number defines the density of the material.

The final series of numbers define the different surfaces (defined in the surface cards below) that form the boundaries for the cell. A positive value is used when the cell volume is above the surface on the axis (or outside a bound volume), and a negative value represents values below

the surface on the axis (or inside a bound volume). A hash before a number tells the program to ignore the cell numbered. For the first cell, the description is less that plane 1, more than plane 2 and inside cylinder 3, but ignoring cells 2, 3, 4 and 5.

After the dollar sign is a quick description of the cell, for the programmer.

```
C     SURFACE CARDS
```

Describes which surfaces make up the object being modelled. It is based on a simple x y z grid system for planes. For cylinders and spheres they are assumed to be lying along the origin of the axis described, with the diameter given..

```
C     Detector Housing Outer Edge
1     PZ     1.9
2     PZ    -1.9
3     CZ     1.1
C     Outer Gas Layer Outer Edge
4     PZ     1.7
5     PZ    -1.7
6     CZ     0.9
C     A150 Wall Outer Layer
7     SO     0.665
C     Inner Gas Layer Outer Edge
8     SO     0.635
C     Gold Wire
13    CZ     0.00023
C     Outer Sphere
100   SO     2.5
C     Source
500   PZ     2.00
```

The first number labels the surface so it can be used to produce a cell.

The letters define what shape the surface follows, P# representing a plane perpendicular to the axis defined by the #, C# representing a cylinder lying along axis # and S0 representing a sphere centred at the origin.

The final number is either the position at which a plane intersects axis # or is the diameter of the cylinder or sphere.

```
C     MODE CARD
```

Describes which particles are being used for the calculation and therefore the behaviour of any incident radiation (any radiation types not mentioned here are ignored for the calculation). MCNP supports several different types of particle, but of interest to this research were photon (P), electron (E) and neutron modes (N).

```
MODE P
C
C     Cell photon importances
```

Describes which cells need to have an increase or decrease in the relative importance of their

interactions, for instance; if a cell is listed as importance 0, all interactions within that cell are ignored, or if a cell is listed as importance 2, in any interactions the numbers of particles interacting is multiplied by 2. All of the cells are listed in order of entry in the cell cards section.

```
IMP:P 1 1 1 1 1 1 0
C
C     SOURCE DEFINITION
```

Describes the type of incident radiation, its energy and the shape of its field.

```
C     Irradiation of cylinder with a rectangular, directional surface
source
SDEF  SUR=500 X=D1 Y=D2 Z=2.0 VEC=0.0 0.0 1.0 DIR=-1 ERG=100.0e-3
```

This defines the shape of the beam being used between X axis planes 1 and Y axis planes 2, at a point 2.0 cm along the Z axis, travelling along the Z axis only, moving in the negative direction, with an energy of 100 x10^{-3} MeV.

```
SI1   H     -0.04 0.04
```

For planes 1, the source is emitted between the positions of -0.04 and 0.04 on the X axis.

```
SP1   D      0.00 1.00
```

Additionally, the energy range between these points of the entire energy range of the source.

```
SI2   H     -0.04 0.04
```

For plane 2, the positions along the Y axis and the energies are identical to those used in the X axis.

```
SP2   D      0.00 1.00
```

For the majority of these calculations, a rectangular, well-collimated monoenergetic photon beam with a side-length of 8mm was used in the calculations, to simulate a synchrotron beam similar to that at Daresbury.

```
C
C
C    TALLY CARDS
```

Describe what is being looked for in the output files, whether the amount of flux across a surface, the fluence through a volume, or the amount of energy deposited within a volume.

```
C     Pulse height in MeV within inner cylinder
F6:P 4
```

This example is looking at the amount of energy deposited within cell 4.

```
C
C     ENERGY BINS FOR TALLIES
E6    0 1e-5 1e-4 1e-3 0.01 0.1 1 10
```

This defines the energy ranges used in the output file.

```
C
C
C     MATERIAL CARDS
```

Describes what elements each cell is made of and their relative abundance.

```
M1    13000 1.0                    $ Aluminium
M2    1001        0.413613         $ A-150 Tissue Equivalent Plastic
      6000        0.527595
```

```
      7000        0.020442
      8000        0.026696
      9000        0.007903
      20000       0.003751
M3    1001        0.429286          $ Propane-Based Tissue Equivalent Gas
      6000        0.396468
      7000        0.020918
      8000        0.153328
M4    79000       1.0               $ Gold
M10   8016        0.179487          $ Air
      7014        0.820513
```

The first part of each material description is a label to allow the program to know which material is used in which cell.

The second part defines the element and isotope present, with the first part being the atomic number of an element followed by the atomic mass, for example; 8016 represents an atomic number of 8 and an atomic mass of 16, or $^{8}_{16}O$.

```
C
C
      PHYS:P 0.1 0 0
```

Defines the physics mode to use for the calculation, with the exact mode being a balance between the accuracy of the final results and the time taken by the computer to produce the data. As these results were produced on a computer cluster, time was less of an issue than it would have been if a single computer had been used, so a higher level of detail was used

```
C     NUMBER OF HISTORIES TO RUN
NPS   500000
```

Describes the number of source particles to simulate before ending the simulation.

In addition to the input files created to model the different detector designs, a number of simple programs were created to speed up the data analysis of the output files or to increase the speed at which input files were created. The computer system these programs were designed for is Fedora 8, so the programs were designed to work within the Linux architecture. The next few examples are examples of these simple programs.

Example 4.7 - Program to Chain MCNP Runs

This program was designed to find an existing MCNP input file and then change the energy value of the radiation source and run the resultant input through MCNP. This allowed sets of simulations to be ‘chained’, with one output being created for a range of different energy

values. Different programs were created for a different energy ranges, and the example included here is shortened to save space, producing only output files for file r005 over a range of 5 to 10 keV removing the temporary runtpe storage file from the previous simulation.

```
rm runtpe
./mcnp4c2.exe inp=r050 outp=r050.o
sed -e s/ERG=5.0/ERG=6.0/ r050 > r060
rm runtpe
./mcnp4c2.exe inp=r060 outp=r060.o
sed -e s/ERG=6.0/ERG=7.0/ r060 > r070
rm runtpe
./mcnp4c2.exe inp=r070 outp=r070.o
sed -e s/ERG=7.0/ERG=8.0/ r070 > r080
rm runtpe
./mcnp4c2.exe inp=r080 outp=r080.o
sed -e s/ERG=8.0/ERG=9.0/ r080 > r090
rm runtpe
./mcnp4c2.exe inp=r090 outp=r090.o
sed -e s/ERG=9.0/ERG=10.0/ r090 > r100
rm runtpe
./mcnp4c2.exe inp=r100 outp=r100.o
```

Example 4.8 - Output Amalgamation Program

As the series of MCNP simulations would produce a large number of different output files this program was created to speed up the data analysis. This program sorts through all of the files within a folder with the extension *.o and places a specific line into a single file marked as combined.o. This allowed the data to then be imported into an OpenOffice spreadsheet and converted into a y.d(y) plot.

```
grep total *.o > combined.o
```

Appendix V - Example EGSnrc Input

The following is an example of the EGSnrc input files used for the creation of the proportional counter model used in Chapters IV and V, in this case subjected to a monoenergetic photon beam with an initial energy of 27 keV.

```
TITLE= Tissue Equivalent Proportional Counter Data
##########################
:start I/O control:
IWATCH= off
STORE INITIAL RANDOM NUMBERS= no
IRESTART= first
STORE DATA ARRAYS= yes
OUTPUT OPTIONS= long
ELECTRON TRANSPORT= normal
DOSE ZBOUND MIN= 1
DOSE ZBOUND MAX= 61
DOSE RBOUND MIN= 0
DOSE RBOUND MAX= 60
:stop I/O control:
##########################
##########################
:start Monte Carlo inputs:
NUMBER OF HISTORIES= 1000000
INITIAL RANDOM NO. SEEDS= 1, 3
MAX CPU HOURS ALLOWED= 20.000
IFULL= pulse height distribution
STATISTICAL ACCURACY SOUGHT= 0.0000
SCORE KERMA= no
:stop Monte Carlo inputs:
##########################
##########################
:start pulse height distribution input:
REGION OF SENSITIVE VOLUME= 5
SLOTE= 0.01
DELTAE= 0.005
:stop pulse height distribution input:
##########################
##########################
:start geometrical inputs:
```

```
METHOD OF INPUT= groups
Z OF FRONT FACE= 0.
NSLAB= 1, 1, 1, 1, 1, 1, 1, 1, 1
SLAB THICKNESS= 0.3, 0.2, 1.035, 0.03, 1.27, 0.03, 1.035, 0.2, 0.3
RADII= 0.00046, 0.635, 0.665, 0.9, 1.1, 3
MEDIA= Air,
 Aluminium,
 TEGPropane,
 A-150,
 Gold;
DESCRIPTION BY= planes
MEDNUM= 1, 2, 3, 4, 3, 5
START ZSLAB= 1, 2, 3, 4, 5, 3
STOP ZSLAB= 9, 8, 7, 6, 5, 7
START RING= 1, 1, 2, 2, 2, 1
STOP RING= 6, 5, 4, 3, 2, 1
:stop geometrical inputs:
##########################
##########################
:start source inputs:
INCIDENT PARTICLE= photon
SOURCE NUMBER= 0
SOURCE OPTIONS= 5, 0, 0, 1
INCIDENT ENERGY= monoenergetic
INCIDENT KINETIC ENERGY(MEV)= 0.027
:stop source inputs:
##########################
##########################
:start MC transport parameter:
Global ECUT= 0.521
Global PCUT= 0.001
Global SMAX= 1e10
ESTEPE= 0.25
XImax= 0.5
Skin depth for BCA= 3
Boundary crossing algorithm= EXACT
Electron-step algorithm= PRESTA-II
Spin effects= on
Brems angular sampling= KM
Brems cross sections= BH
Bound Compton scattering= On
Pair angular sampling= Simple
Photoelectron angular sampling= On
Rayleigh scattering= On
Atomic relaxations= On
```

```
Set PCUT= 0
Set PCUT start region= 1
Set PCUT stop region= 1
Set ECUT= 0
Set ECUT start region= 1
Set ECUT stop region= 1
Set SMAX= 0
Set SMAX start region= 1
Set SMAX stop region= 1
:stop MC transport parameter:
##########################
##########################
:start variance reduction:
BREM SPLITTING= off
NUMBER OF BREMS PER EVENT= 1
CHARGED PARTICLE RUSSIAN ROULETTE= off
ELECTRON RANGE REJECTION= off
ESAVEIN= 0.0
RUSSIAN ROULETTE DEPTH= 0.0000
RUSSIAN ROULETTE FRACTION= 0.0000
EXPONENTIAL TRANSFORM C= 0.0000
PHOTON FORCING= on
START FORCING= 1
STOP FORCING AFTER= 1
CS ENHANCEMENT FACTOR= 1
CS ENHANCEMENT START REGION= 1, 1
CS ENHANCEMENT STOP REGION= 1, 1
:stop variance reduction:
##########################
##########################
:start plot control:
PLOTTING= on
LINE PRINTER OUTPUT= off
EXTERNAL PLOTTER OUTPUT= on
EXTERNAL PLOT TYPE= Histogram
PLOT RADIAL REGION IX= 1, 2
PLOT PLANAR REGION IZ= 10
:stop plot control:
##########################
```

Appendix VI – Gafchromic Film Dosimetry

This part of the research was conducted during experimental work at the SRS Facility at Daresbury. It was decided that it would take too much time to follow on with this work and that this would interfere with the other research in this thesis. Because of this, I am including the results and background information I wrote on this area of investigation in this Appendix instead of in the main body of the thesis as it has relevance to the other work conducted.

The data in this section shows the shape of the synchrotron radiation beam. This information was used during the work at the SRS Facility to determine the centre of the beam and the detectors were positioned based on this data. Although the data analysis was never completed it provides information on the shape of the beam and was an early attempt at using MCNP4C to simulate a detector.

x6.1 - Background Information

Radiographic Film

The use of photographic film in radiation dosimetry has been about since the first discovery of X-ray radiation at the turn of the 20th Century and still remains an important technique today. Although the technology has been around for a long time, the use of photographic films has remained largely unchanged, apart from the need for radiographic information to be digitised to allow more complex data analysis and distribution.

Radiographic films are based upon the ionisation of a layer of silver halide (AgBr) emulsion subjected to a radiation field. Two layers of silver halide are sandwiched between layers of protective coating separated by a thicker polyester base, which supports and protects the reactive layer.

The dominant theory on the formation of an image through radiographic film is the Gurney and Mott Theory (see Chaal, 2009). According to this theory, each silver halide grain contains imperfections in the lattice structure caused by the presence of silver sulphide, which are

known as ‘specks’. When a silver halide molecule is exposed to ionising radiation the bromine is ionised, producing a free electron. The free electrons are then attracted to the speck in the grain, leading to the migration of positive silver ions to the region, forming a latent image. Although a silver halide grain may contain 10^{10} silver ions, only a small percentage will constitute the latent image, which is not visible until it is fixed by the development process.

In the development process, the small numbers of silver atoms present are used as a catalyst for the reduction of all of the silver ions within a grain, darkening the film through the formation of metallic silver. Although the majority of the reduction reactions will occur within grains where silver atoms are present, a small minority of the silver ions will also act as catalysts, leading to ‘fog’. The resolution of a film varies depending upon the manufacturing process used, but is dependant upon the size of the silver halide grains present, not the specks within them.

Radiographic films have been used less frequently over the last ten years due to the processing time required for the film, as well as the silver halide’s lack of tissue equivalence. With an atomic number of 45, silver can be too sensitive to low energy radiation to be a reliable indicator of dose.

Radiochromic Film

Radiochromic films are a relatively recent addition to the field of radiation film dosimetry, developed initially in the 1960’s, designed to avoid some of the disadvantages of radiographic film. In terms of design, the film has a similar structure, with two active layers of organic dye layered between polyester sheets to provide rigidity and structure to the film.

Radiochromic films contain a dye with a low atomic number that undergoes a colour change from a colourless (or less-coloured state) to a darker blue when ionised, due to the polymerisation of microcrystals of organic monomer. The active components of the film are needle-shaped particles with a diameter of 1-2 μm and a length of 15-25 μm.

Radiochromic films offer a number of advantages over the more established radiographic versions, principally that the reaction occurs within the film in real-time with no requirement to fix or develop the film to produce a final image. This eliminates the need for dark rooms, developing equipment and also reduces the sensitivity of the film to non-ideal environmental conditions. In addition, the grainless nature of the film improves the resolution, making it more useful for microdosimetric applications.

The radiochromic film type which was used in the experimental work was GafChromic film, a colourless film with near tissue equivalence (9.0% hydrogen, 60.0% carbon, 11.2% nitrogen, 19.2% oxygen), that turns blue upon radiation exposure. This is a useful tool in radiation dosimetry, owing to the large amount of literature available that assesses its performance over a wide range of energies (for example Butson et al, 2002; Cheung et al, 2001; Thomas et al, 2003), showing that under the correct environmental conditions a precision of greater than 3% can be achieved.

Dose Enhancement

One of the primary aims of the work in this thesis was to investigate the dose enhancement effects of placing higher Z materials in proximity with lower Z materials. Because of this, an aim of the radiochromic film work was to investigate the variation in radiation dose associated with a film in contact with a metal foil above and below the binding energy of an electron shell within that metal. Due to the increase in the absorption of radiation within the atoms within the foil, there should be an increase in the electron emission above the binding energy of the atomic shell, and hence an increase in the energy deposited within the film.

Table x6.01 summarises the electron binding energies of the different elements used in the experimental and Monte Carlo simulations in this chapter.

Element	Edge	Electron Binding Energy (keV)
Gold	L_I	14.353
	L_{II}	13.734
	L_{III}	11.919
	K	80.725
Indium	L_I	4.238
	L_{II}	3.938
	L_{III}	3.730
	K	27.940

Table x6.01 - Electron Binding Energies of Elements Studied

Of these, the K edge of gold and the L edges of indium are outside of the range of energies that were available from the synchrotron source. For this research, the electron binding energies of the gold L_{III} and indium K edges were investigated as they were within the range of energies available at the synchrotron where the research was conducted.

x6.2 - MCNP Model

The MCNP models produced was designed to investigate the difference in energy absorption when a thin foil of gold or indium is placed over a piece of gafchromic film. To this end, a basic model was produced, making use of a rectangular piece of GafChromic film embedded within a block of tissue equivalent plastic with a thin film of gold placed at one end. The film section was constructed such that it was split into a series of cells, each positioned to measure the energy absorption within the film using the same *F8 tally system used for the other MCNP simulations in this document.

An MCNP model was designed to look at the distribution of energy across a piece of GafChromic film placed normal to the direction of the synchrotron beam (modelled using the same MCNP synchrotron beam described in Chapter IV), concentrating on the distribution of the energy at the metal-detector interface. This was intended partly to see how the distribution of energy absorption is affected by passing through a layer of tissue equivalent plastic in

contact with a metal foil. This also allows a comparison of these simulations with readings produced from experimental work. The piece of GafChromic film was the same dimensions as the previous piece, but split up into 40 cells, to give an indication of the dose distribution in one dimension.

The model was then tested using a monochromatic photon beam at energies 5 keV above and below the L III edge of gold, at 11.819, 11.919 and 12.019 keV, in order to investigate the effects of the increased energy absorption due to the gold foil. By testing the variation in dose enhancement with energy it was hoped that data could be produced to be compared with that obtained experimentally, partly to test the experiment and partly to test the Monte Carlo code.

These two different models are shown in Figures x6.01.

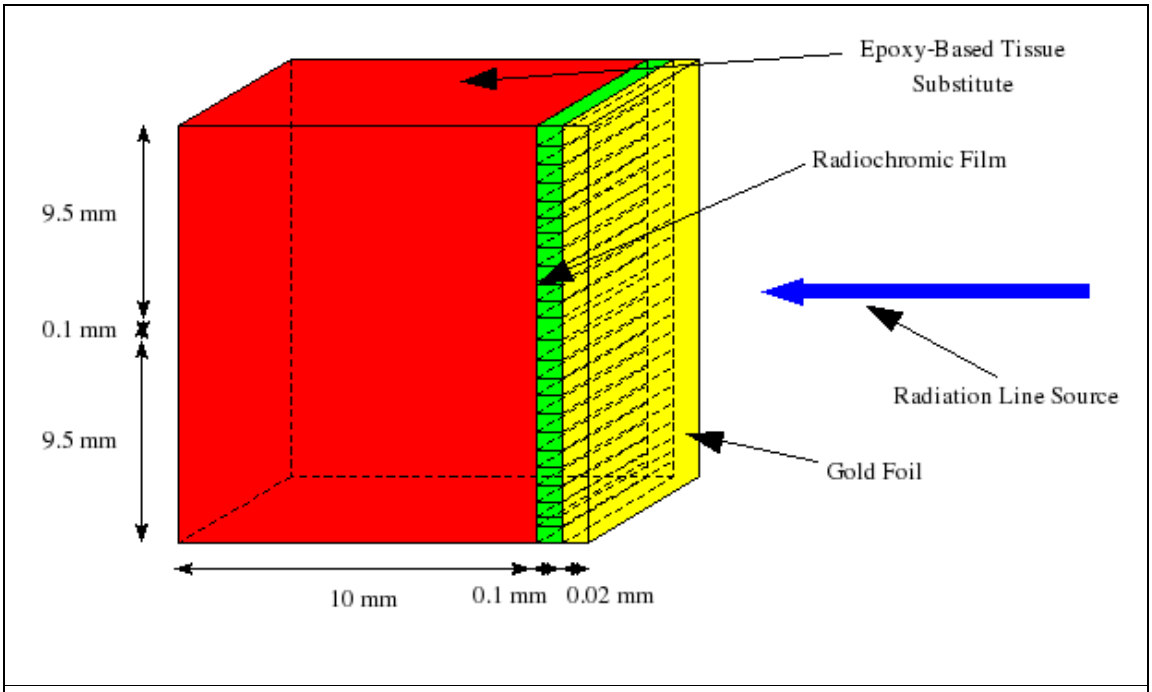

Figure x6.01 - MCNP Model of a GafChromic Film Set-Up

x6.3 - Results

x6.3.1 - Experimental Results

The results in this section are based upon gafchromic film irradiated at the SRS Facility in Daresbury using both a slot beam of 10 mm by 1 mm and a point beam of 1 mm by 1 mm. These sections of film were then scanned into a computer using a high definition slide scanner set to the highest resolution settings.

The experimental results obtained are split into two sections, the first shows the images produced from the synchrotron beam, giving an indication of the type of results obtained. This is then followed by a section detailing the analysis of the images using ImageJ. This analysis was performed to allow a quantitative comparison of the results, allowing any dose enhancement effects to be determined. This also allowed the data to be compared to the results of the Monte Carlo simulations detailed in the next section.

Raw Data

Results x6.02a to x6.02e show the raw images produced using the film when it was irradiated at thee SRS Facility synchrotron beam.

For the work used elsewhere in this thesis, the beam was set to scan across the detector volume creating an effective aperture size of 8 mm by 8mm. The line profiles here were obtained for the largest aperture size available of 16 mm.

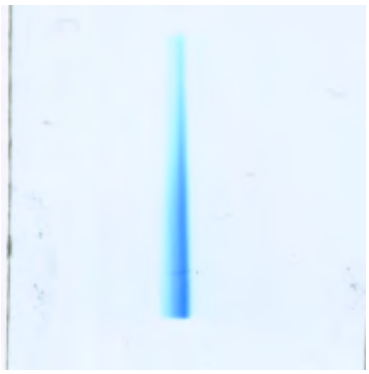

Figure x6.02a – Unfocused Line Profile

Figure x6.02b – Unfocused Line Profile

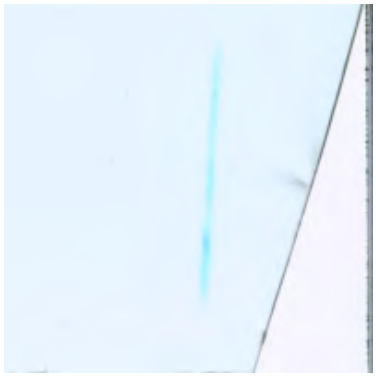

Figure x6.02c –Below L_{III} Edge of Gold

Figure x6.02d –Above L_{III} Edge of Gold

Figure x6.02e –K Edge of Indium

For the unfocused line profiles, it is clear that there is a difference in beam strength between one side of the beam aperture and the other, probably due to a slight flaw in the collimator. However, this does not seem to have had an effect on the focused readings, so is presumably due to the collimator being opened further than it is designed to.

Figures x6.03a and x6.03b summarise the results obtained from exposing the GafChromic

film to a point source at a source energy above and below the L edge of gold:

	
Figure x6.03a – Point Profile Below L_{III} Edge of Gold	Figure x6.03b – Point Profile Above L_{III} Edge of Gold

From these results, it can be seen that there has been an increase in the dose to the film just above the L_{III} edge, showing that the gold foil has lead to an increase in the photoelectric absorption of the incident radiation. It is also interesting to note the way the beam has blocked out the lower dose fringes from the source, demonstrating beam hardening and creating a more rectangular impression of the beam.

ImageJ Analysis

The raw images of the film section were then analysed using ImageJ, an open source image analysis program. A Region of Interest (ROI) was defined separately for each image, centred upon the exposed area of the film and sized such that any marks upon the film not caused by irradiated were avoided. The colour information within the ROI was then converted into an ADC (Analogue to Digital Conversion) value, a numerical value used to define the shade of the colour. For the 8-bit images used, the ADC value has total colour saturation (white) defined as 256 (the maximum possible value) through to 1 for a complete absence of signal (black). These values were then subtracted to produce an inverse ADC value so that the pixels with the highest radiation absorption produced a larger signal than those which were unirradiated.

To produce the ADC values, the images were split into their component colour channels,

based upon recommendations made by Boyd et al (2009), Chaal (2009) and Marder (2010), in order to perform the analysis upon the red colour channel. This was necessary because the film itself is not colourless and absorbs the blue region of the visible light spectrum, reducing the ADC value of the image. The image was then rotated so that the line within the profile was vertical, allowing the ADC of the image to be averaged over a larger region, improving the statistics of the results. ImageJ was then used to calculate the ADC value of the ROI using the plot profile function. The pixels were then centred by eye so that the peak was at the origin and the ADC values inverted in the manner described above.

In Figure x6.04 the inverted ADC values for gafchromic film with a thin foil of gold or indium placed on the surface is shown for energies at 5 keV above and below the L_{III} energies of gold and 5 keV above the K energy of Indium.

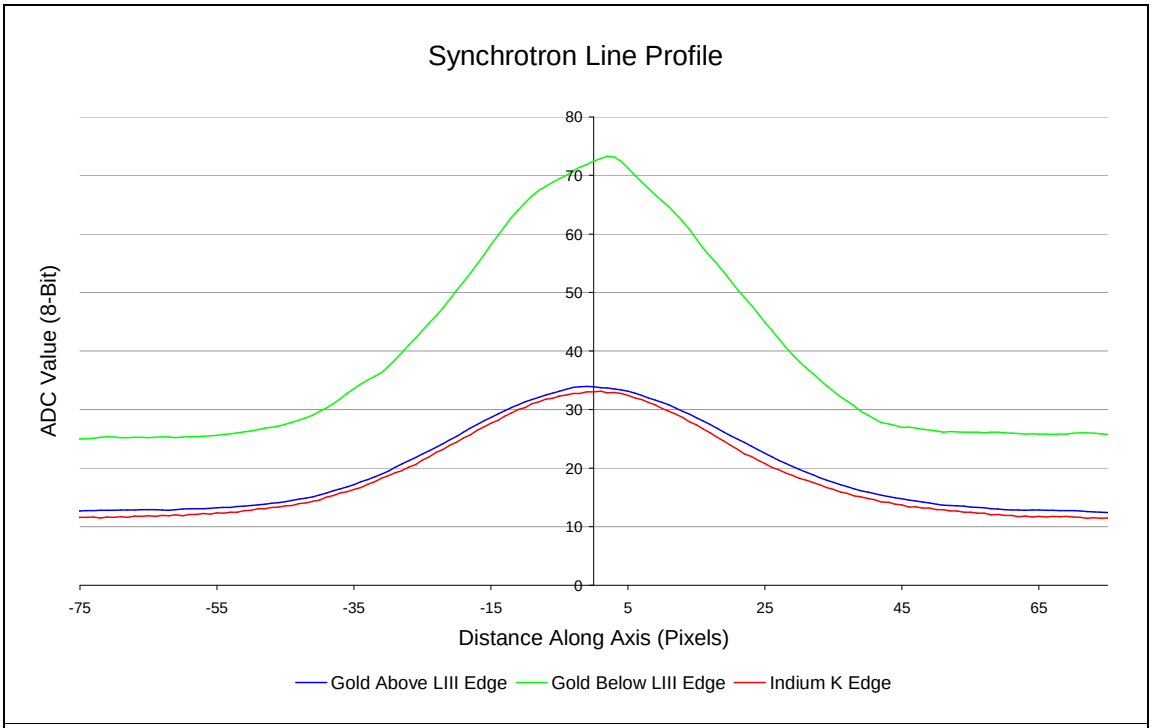

Figure x6.04 - Variation in ADC Value for Different Energy Synchrotron Beams Incident Upon Different Dose Enhancing Media Using a Slot Beam

This shows a dose reduction effect for the film due to the gold foil, with the inverse ADC value decreasing by a factor of more than 2. This effect is mirrored in the results for Indium which shows similar values to those of gold above the L_{III} edge. This suggests a decrease in

the energy absorption of the film below the L_{III} edge of gold, suggesting the beam may have been more intense for that part of the research or that the gold foil used was thinner than that used for the other results.

Note that all of the images show a reduction in the inverted ADC value compared to the regions of the film which were not under the foil due to shielding effects.

In Figure x6.05, the inverted ADC values for a point beam 5 keV above and below the L_{III} edge of gold are compared.

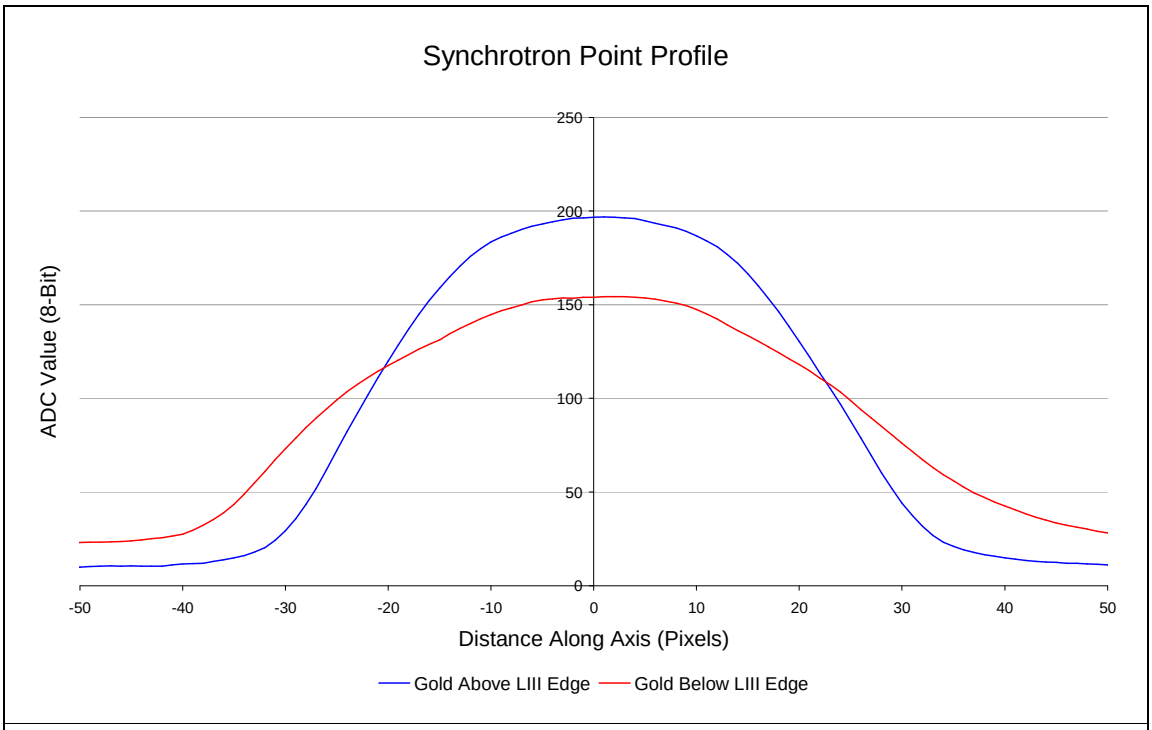

Figure x6.05 - Variation in ADC Value for Different Energy Synchrotron Beams Incident Upon Different Dose Enhancing Media Using a Point Beam

These results show an increase in the inverted ADC value for gold above the L_{III} edge, suggesting a dose enhancement effect of a factor of nearly 1.25. An additional effect of the increase in energy above the binding energy of the L_{III} shell is a decrease in energy absorption on the periphery of the synchrotron beam. This may indicate a geometric widening of the synchrotron beam as the energy was changed or greater emission of electrons on the periphery of the beam.

Without further research it is difficult to tell whether either of these two data sets are reliable, however it is hoped that the Monte Carlo results can at least support one of the experimental results.

x6.3.2 - Monte Carlo Simulation Results

Figures x6.06 summarise the results produced by the MCNP models looking at the total energy absorption in a series of cells placed along the x axis.

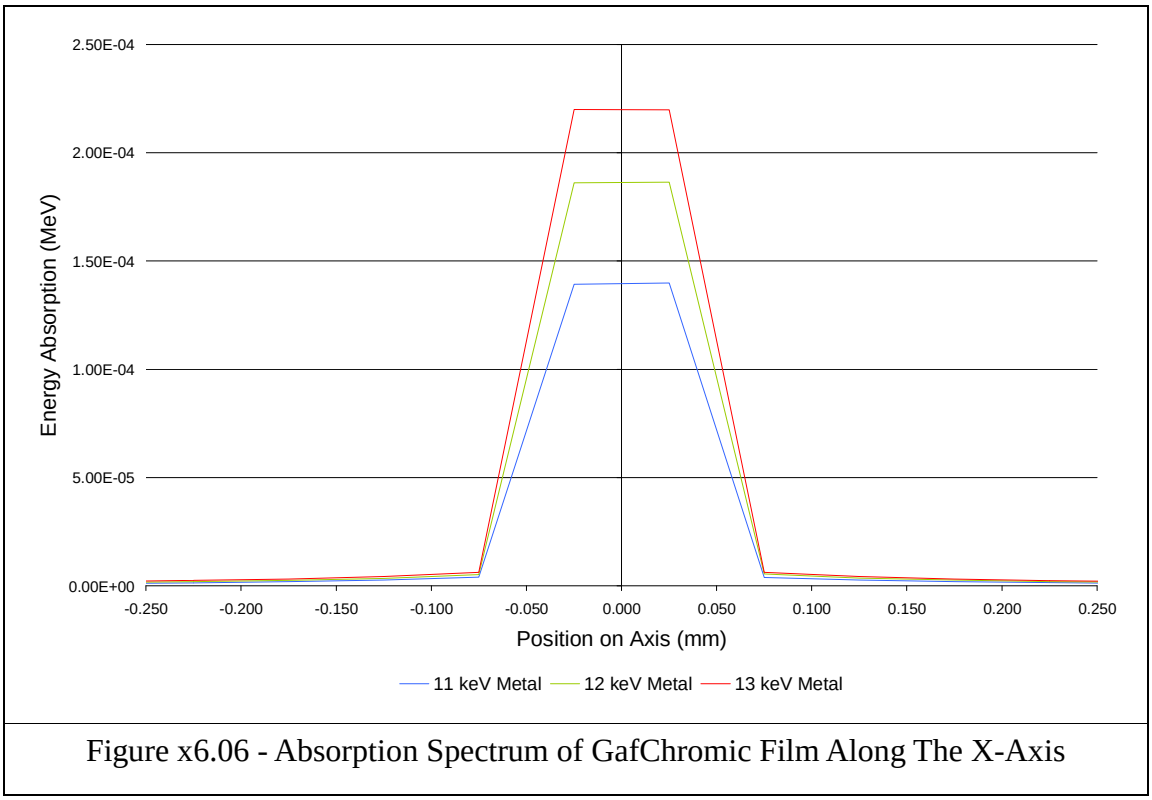

Figure x6.06 - Absorption Spectrum of GafChromic Film Along The X-Axis

Figure x6.06 resembles the results in Figure x6.05, showing an increase in energy absorption as the source energy increases from 11 to 13 keV with a factor of approximately 1.5. This is slightly higher than for the experimental data, but the dimensions of the gold foil was calculated as an average from several different foils, so there may be some slight difference in the thickness of the gold sheet.

x6.4 - Conclusions

Although the data produced from the experimental work at the SRS Facility was inconclusive, the Monte Carlo model produced of the experimental setup appears to validate one of the sets of results. This suggests that placing a gold foil on the surface of a piece of gafchromic film will increase the energy deposition within the film above the L_{III} edge of gold. This agrees with the research conducted in Chapter IV looking at the diamond detector which had similar findings.

It must be assumed that the difference between the dose enhancement factors of the line beams and the point beams is due to a mistake being made, leading to two different thicknesses of gold foil being used. This is because in the line profile, the gold foil seems to have drastically reduced the dose to the film, shielding it from the radiation. With a point profile, however, it appears to have enhanced the dose. If there had been time, it would have been useful for additional readings to be taken to ascertain which of the two sets of data is more typical.

From some of the results, it appears that the thickness of the gold foil can have a large effect upon the dose within the detector elements, with an increase in source energy leading to an increase in the dose in the film. This is because the foil will absorb energy through photoelectric absorption much more effectively than the film due to its higher atomic number and emit energy as Auger electrons. If the foil is thin compared with the electron path lengths it will lead to an increase in the energy absorption along the direction of the beam. However, if its thickness is greater than the electron path length it will lead to a reduction in the beam fluence. This is important when attempting to simulate the behaviour of these kinds of dosimeters, as a small difference in the thickness of these high atomic number elements can lead to a large difference in the results.

Appendix VII – Published Papers

The following papers were published using data produced for this thesis.

Monte Carlo modelling of the influence of boron microdistribution on BNCT microdosimetry

The first paper was published in Applied Radiation and Isotopes in 2009 and makes use of the experimental data in Chapter IV. This paper uses the energy absorption spectra for a TEP proportional counter and a Boron-doped TEP proportional counter found in Chapter IV Section 4.3.2.

X-ray synchrotron microdosimetry: Experimental benchmark of a general-purpose Monte Carlo code

This second paper was published in Applied Radiation and Isotopes and is based upon work conducted at the SRS Facility near Daresbury. This paper makes use of the energy absorption spectra obtained for the TEP proportional counter during exposure to synchrotron radiation with an energy of 15 keV and 33 keV. This data is included in this document in Chapter IV Section 4.3.1.

Bibliography

Chapter I - Introduction

Adam Jean-François, Ph.D., Elleaume Hélène, Ph.D., Joubert Aurélie, M.Sc., Biston Marie-Claude, M.Sc., Charvet Anne-Marie, Ph.D., Balosso Jacques, M.D., Ph.D., Le Bas Jean- François, M.D., Ph.D., Estève, M.D., Ph.D., Synchrotron Radiation Therapy of Malignant Brain Glioma Loaded with an Iodinated Contrast Agent: First Trial on Rats Bearing F98 Gliomas. *Int. J. Radiation Oncology Biol. Phys.*, **Vol. 57 No. 5**, 1413-1426, 2003.

Andreo P, Monte Carlo Techniques In Medical Radiation Physics. *Phys. Med. Biol.*, **36**, 861-920, 1991.

Behin Anthony, Hoang-Xuan Khe, Carpentier Antoine F, Delattre Jean-Yves, Primary Brain Tumours in Adults. *Lancet*, **361**, 323-331, 2003.

Biston M-C, Joubert A, Adam J-F, Elleaume H, Bohic S, Charvet A M, Esteve F, Foray N and Balosso J, Cure Of Fisher Rats Bearing Radioresistant F98 Glioma Treated With Cis-Platinum And Irradiated With Monochromatic Synchrotron X-Rays. *Cancer Res.*, **64**, 2317-2323, 2004.

Catlow Richard, Greaves G. N., Applications of Synchrotron Radiation. Springer, 1990.

Clarke James A., The Science and Technology of Undulators and Wigglers. Oxford Series on Synchrotron Radiation, 2004.

Fitzgerald J. J., Brownell G. L., Mahoney F. J., Mathematical Theory of Radiation Dosimetry. Gordon and Breach Science Publishers, Inc., 245-247 and 440, 1967.

Franks C. M., Teich N. M., Introduction To The Cellular And Molecular Biology Of Cancer (3rd Edition), Oxford University Press, 1997.

Hainfeld James F, Slatkin Daniel N, Smilowitz Henry M, The Use Of Gold Nanoparticles To Enhance Radiotherapy In Mice. *Phys. Med. Biol.*, **49**, N309-N315, 2004.

Hellborg R. (Editor), Electrostatic Accelerators - Fundamentals and Applications. Springer, 2005.

Hofmann Albert, The Physics of Synchrotron Radiation. Cambridge University Press, 2004.

Holland D. M. P., The Daresbury Synchrotron Radiation Source. *Physica Scripta*, **36**, 22-35, 1987.

Hugtenburg R. P., Baker A. E. R., Green S., X-Ray Synchrotron Microdosimetry: Experimental Benchmark of a General Purpose Monte Carlo Code. *Appl. Rad. and Isot.* **67**, 433-435, 2009.

ICRU (International Commission On Radiation Units and Measurements), Microdosimetry, ICRU Report 36, Bethesda, MD, USA, 1983.

Jeraj Robert, Keall Paul J, Ostwald Patricia M, Comparisons Between MCNP, EGS4 And Experiment For Clinical Electron Beams. *Phys. Med. Biol.*, **44**, 705-717, 1999.

King RJB, Cancer Biology, Addison Wesley Longman, 1996.

Kong Augustine, Gudbjartsson Daniel F., Sainz Jesus, Jonsdottir Gudrun M., Gudjonsson Sigurjon A., Richardsson Bjorgvin, Sigurdardottir Sigrun, Barnard John, Hallbeck Bjorn, Masson Gisli, Shlien Adam, Palsson Stefan T., Frigge Michael L., Thorgeirsson Thorgeir E., Gulcher Jeffrey R., Stefansson Kari, A High-Resolution Recombination Map Of The Human Genome. *Nat. Gen.*, **31**, 241-247, 2002.

Kawrakow I., Mainegra-Hing E., Rogers D. W. O., Tessier F., Walters B. R. B., EGSnrc User Manual. NRCC Report PIRS-701, 2010.

Legler Julie M., Gloeckler Ries Lynn A., Smith Malcolm A., Warren Joan L., Heineman Ellen F., Kaplan Richard S., Linet Martha S., Brain and Other Central Nervous System Cancers: Recent Trends in Incidence and Mortality. *J. Nat. Can. Inst.*, **Vol. 91, No. 16**, 1382-1390, 1999.

Livingood John J., Principles of Cyclic Particle Accelerators. Van Nost. Reinhold, 1961.

Love P A, Lewis D G, Al-Affan I A M, Smith C W, Comparison of EGS4 and MCNP Monte Carlo Codes When Calculating Radiotherapy Depth Doses. *Phys. Med. Biol.*, **43**, 1351-1357, 1998.

MCNP4C User Manual, 2005.

Mesa A V, Norman A, Solberg T D, Demarco J J, Smathers J B, Dose Distributions Using Kilovoltage X-Rays and Dose Enhancement From Iodine Contrast Agents. *Phys. Med. Biol.*, **44**, 1955-1968, 1999

Nikjoo Hooshang, Lindborg Lennart, RBE of Low Energy Electrons and Photons. *Phys. Med. Biol* **55**, R65-R109, 2010.

Rossi H H, Zaider M, Microdosimetry and its Applications. Springer-Verlag Berlin Heidelberg, New York, 1996.

Scharf Waldermar H., Biomedical Particle Accelerators. American Inst. of Physics, 1994.

Scharf Waldemar, Particle Accelerators and Their Uses - Part 1. Harwood Academic Publishers, 1986.

Šídlová Věra, Trojek Tomáš, Testing Monte Carlo Computer Codes For Simulations Of Electron Transport In Matter. *Applied Radiation and Isotopes*, **68**, 961-964, 2010.

Solberg T D, Iwamoto K S, Norman A, Calculation of Radiation Dose Enhancement Factors For Dose Enhancement Therapy of Brain Tumours. *Phys. Med. Biol.*, **37**, **No. 2**, 439-443, 1992.

Waker A. J., Principals of Experimental Microdosimetry. *Rad. Prot. Dosimetry*, **61 (4)**, 297-308, 1995.

WHO Health Report, The Global Burden of Disease, Annex A: Deaths and DALYs 2004 Anex Tables, published 2008. Available at www.who.int/healthinfo/global_burden_disease/ 2004_report_update/en/index.html. Last checked: 21/04/2010.

Winick Herman, Brown George, Halbach Klaus, Harris John, Wiggler and Undulator Magnets. *Physics Today*, **Volume 34**, **Issue 5**, 50-63, May 1981.

Zhang Shu Yan, Vorster Willem J. J., Jun Tea-Sung, Song Xu, Golshan Mina, Laundy David, Walsh Michael J., Korsunsky Alexander M., High Energy White Beam X-Ray Diffraction Studies Of Residual Strains In Engineering Components. *Proceedings of the World Congress on Engineering*, **Volume II**, WCE 2007.

Chapter II - Diamond Detector Dosimetry

Bose Gunaranjan, Dose Response of Diamond Detectors with Synchrotron X-Rays, MSc. Thesis, University of Birmingham, 2004.

Collins S P, Cernik R J, Fell B, Tang C C, Harris N W, Miller M C, Oszlanyi G, Station 16.3: A High-Resolution Single-Crystal Diffraction Facility at the SRS, Daresbury. *J. Synchrotron Rad.* **5**, 1263-1269, 1998.

Fallon P. J., Nam T. L., Keddy R. J., Burns R. C., Grobbelaar J. H., Synthetic Diamonds Used As Pulse-Counting Gamma-Ray Detectors. *Appl. Radiat. Isot.* **Vol. 41 No. 1**, 35-39, 1990.

Griesmeyer E., Dehning B., Effinger E., Dobos D., Pernegger H., Diamond Detectors as Beam Monitors. *Proceedings of BIW 10*, 49-52, 2010.

Lui Derek Man Chun, Characterization of Novel Electronic Brachytherapy System. Medical Physics Unit McGill University, Montreal, 2007.

O'Neill Brian, Solder Selection for Photonic Packaging. AIM Speciality Materials website, published 2002, *www.aimsolder.com/techarticles/Solder Selection for Photonic Packaging.pdf*, last checked 11:28, 19/09/2006.

Perrin B A, Whitehurst P, Cooper P, Hounsell A R, The Measurement of k_{ch} Factorsfor Application with the IPEMB Very Low Energy Dosimetry Protocol. *Phys. Med. Biol.* **46**, 1985-1995, 2001.

Planskoy B, Evaluation of Diamond Detector Radiation Dosemeters. *Phys. Med. Biol.*, **Vol. 25**, **No. 3**, 519-532, 1980.

Saeddi Fathy, High Resolution Dosimetry in Radiation Oncology. Thesis (PhD.) - University of Birmingham, 2006.

Vatnitsky Stanislav, Järvinen Hannu, Application of a Natural Diamond Detector for the Measurement of Relative Dose Distributions in Radiotherapy. *Phys. Med. Biol.* **38**, 173-184,1993.

Yin Z, Hugtenburg R P, Green S, Beddoe A H, Dose Responses of Diamond Detectors to Monoenergetic X-Rays. *Nucl. Instr. and Meth. in Phys. Res. B* **213**, 646-649, 2004.

Chapter III - Fibre Optic Thermoluminescent Device (TLD) Dosimetry

Abdulla Youssef. A., Amin Y. M., Bradley D. A., The Thermoluminescence Response of Ge-Doped Optical Fibre Subjected To Photon Irradation. *Rad. Phys. and Chem.* **61**, 409-410, 2001.

Asni H., Wagiran H., Saripan M. I., Ramli A. T,. Yaakob N. H., Thermoluminescence Energy Response of Germanium Doped Optical Fibre Using Monte Carlo N-Particle Code Simulation. *AIP Conf. Proc.* **1250**, 420-423, 2011.

Collins S P, Cernik R J, Fell B, Tang C C, Harris N W, Miller M C, Oszlanyi G, Station 16.3: A High-Resolution Single-Crystal Diffraction Facility at the SRS, Daresbury. *J. Synchrotron Rad.* **5**, 1263-1269, 1998.

Nikjoo Hooshang, Lindborg Lennart, RBE of Low Energy Electrons and Photons. *Phys. Med. Biol* **55**, R65-R109, 2010.

Nunn A. A., Davis S. D., Micka J. A., DeWerd L. A., LiF:Mg,Ti TLD Response As A

Function of Photon Energy For Moderately Filtered X-Ray Spectra In The Range Of 20-250 kVp Relative to ^{60}Co. Med. Phys. **35** (5), 1859-1869, May 2008.

Yusoff A. L., Hugtenburg R. P., Bradley D. A., Review Of Development Of A Silica-Based Thermoluminescence Dosimeter. *Rad. Phys. and Chem.* **74,** 459-481, 2005.

Chapter IV - Proportional Counter Dosimetry

Blasy, Bryan D., Neutron Detection Utilizing Gadolinium Doped Hafnium Oxide Films. Thesis (MSc) - Air Force Institute of Technology, USA, 2008.

Culbertson Christopher N., Green Stuart, Mason Anna J., Picton David, Baugh Gareth, Hugtenburg Richard P., Yin Zaizhe, Scott Malcolm C., Nelson John M., In-Phantom Characterisation Studies as the Birmingham Accelerator-Generated epIthermal Neutron Source (BAGINS) BNCT Facility. *Appl. Rad. and Iso.* **61**, 733-738, 2004.

EnvironmentalChemistry.Com, Periodic Table of Elements, Sorted by Cross-Section (Thermal Neutron Capture), http://environmentalchemistry.com/yogi/periodic/ crosssection.html last checked 12/03/10

Gainey Mark Bedford, Dosimetry and Microdosimetry of the Birmingham BNCT Programme. Thesis (PhD.) - University of Birmingham, 2002.

Goorley John, A Comparison of Three Gadolinium Based Approaches to Cancer Therapy. Thesis (PhD.) - Massachusetts Institute of Technology, 33-36, 2002.

ICRU (International Commission On Radiation Units and Measurements), Microdosimetry, ICRU Report 36, Bethesda, MD, USA, 1983.

Knoll Glenn F, Radiation Detection and Measurement, John Wiley Sons, New York, Third Edition, 2000.

Lochler G. L., Biological Effects and Therapeutical Possibilities of Neutrons. *Am. J. Roentgenol. Radium Ther.* **36,** 1-13, 1936

Saeddi Fathy, High Resolution Dosimetry in Radiation Oncology. Thesis (PhD.) - University of Birmingham, 2006.

Appendices

Boyd J, Sandford P, Commissioning of Epson 10000XL Scanner for Use in IMRT Film Dosimetry. Report No. TP/PAH 2009-05, ROS, 2009.

Butson Michael J, Cheung Tsang, Yu Peter K N, Corresponding Dose Response of Radiographic Film with Layered GafChromic Film. Phys. Med. Biol. 47, 285289, 2002.

Chaal Kahena, Film Dosimetry of Intensity Modulated Beams. MSc Thesis, McGill University, Quebec, 2009.

Cheung Tsang, Butson Michael J, Yu Peter K N, Use of Multiple Layers of GafChromic Film to Increase Sensitivity. Phys. Med. Biol. 46, 235240, 2001.

Marder Dietmar G, Absolute Pre-Treatment IMRT Verification in External Beam Therapy. MSc Thesis, Swiss Federal Institute of Technology, Zurich, 2010.

Thomas G, Chu R Y L, Rabe Frank, A Study of GafChromic XR Type R Film Response with Reflective-Type Densitometers and Economical Flatbed Scanners. J. App. Clin. Med. Phys. 4, 307314, 2003.